DEPARTAMENTO DE ASTROFÍSICA

Universidad de La Laguna

Massive stars in Cygnus OB2

Memoria que presenta
Sara Rodríguez Berlanas
para optar al grado de
Doctora por la Universidad de La Laguna.

INSTITUTO Đ ASTROFISICA Đ CANARIAS
junio de 2019

Examination date: July, 2019
Thesis supervisor: Prof. Artemio Herrero Davó

DEDICADO A LOS NADIES

Los nadies: los hijos de nadie, los dueños de nada.
Los nadies: los ningunos, los ninguneados, corriendo
la liebre, muriendo la vida, jodidos, rejodidos:
Que no son, aunque sean.
Que no hablan idiomas, sino dialectos.
Que no hacen arte, sino artesanía.
Que no practican cultura, sino folklore.
Que no son seres humanos, sino recursos humanos.
Que no tienen cara, sino brazos.
Que no tienen nombre, sino número.
Que no figuran en la historia universal,
sino en la crónica roja de la prensa local.
Los nadies, que cuestan menos que la bala que los mata.

Eduardo Galeano.

Agradecimientos

A Artemio.
Gracias por hacer que Cygnus OB2 sea ahora parte de mí. Has sido un jefe maravilloso, enseñándome y motivándome en cada paso que he dado, siempre con una sonrisa y buenas palabras. No te puedo estar más agradecida por estos años en el IAC. Esta Tesis es tanto tuya como mía.

A Fernando Comerón y Anna Pasquali.
Gracias por involucraros tanto en este trabajo, siempre dispuestos a ayudar, aportar conocimientos y buen hacer. Trabajar con gente como vosotros es, sin duda, un privilegio.

A Nick Wright y Fabrice Martins.
Gracias a ambos por recibirme tan cariñosamente en Keele y Montpellier, haciendo que los meses que he pasado con vosotros hayan sido grandes experiencias (además de muy productivos!).

A Sergio, Paco, Ignacio, M. Urbaneja, Danny L., M. Cerviño, Jesús, Emilio A., Pere B., Klaus, Nikolay, Lee, Gonzalo, Ricardo (...) Vosotros representais para mí lo mejor del mundo de las estrellas masivas: buena gente trabajando duro, pero siempre con tiempo para ayudar, aconsejar (y ofrecer un respiro!).

A Miriam, Amparo, Janet D., Mª Fernanda, Melanie, Inés, Carolina, Marisa, Mercedes, Cesca, Cecilia (...) Grandes mujeres haciendo un gran trabajo en un mundo (aún) dificil para nosotras. Muchas gracias por todo! en especial por vuestros consejos, charlas y apoyo en general.

A John E. Beckman, referee interno de esta tesis, por todos sus comentarios para mejorar este trabajo. A los miembros del Tribunal y también *a Gabi y Carlos Allende*, por ayudarme con ese gran (pero sufrido) video.

A Eva, Lourdes e Irene. A Joaquin y Elito. A Juan y Jorge. Personal de cafetería, limpieza y garita. Qué haríamos sin vosotr@s! haceis que todo nos sea mucho más fácil. Mil gracias por vuestra ayuda y (perpetua) sonrisa!.

A mi pequeña pero gran familia en la isla: *Isma, Sergio, Rebe, Victor, Moratecol, Ferra, Awe, Pato, Ernest, Dani, Torni, Parda, Simone, Josafat (...).* Cómo os echo de menos!. Son muchos momentos increibles, pasando por pimientos, cervezas vip, barbacoas gitanas, ballenators, barritos, topas y tocuyos. Habeís sido lo mejor de la isla, sin duda alguna.

A mi familia: *Pili, Fabri, Iria, Eva y Ruth*, por estar siempre ahí :) *A Lala y Lolo. A Juani y Valeria. A Candela y Lucas (+1).* Y a todos los demás abuel@s, ti@s, prim@s y cuñad@s... incluido Droguito!. Sois la mejor familia que una puede tener.

A mis amig@s de siempre. Especialmente *a Loreto* (ya es más de media vida juntas!) Por nada en el mundo cambiaría todos los años de alegrías, penas, mil conciertos y fiestas. Qué bien nos lo hemos pasado!. *A Beíta*, idem, otra 'jefa' indispensable para mí. También *a Dani*, por aguantarnos como un santo, y *a Martín*, por lo que nos aguantará. Y, por supuesto, *a Richar, Chona, Gamo, Chiti, Ali, Amelia* y gente del pueblo (...). Más de lo mismo, que suerte teneros como amig@s!. Gracias a tod@s vosotr@s vuelvo a la realidad, no hay nada como volver a casa. También a esos Roboces y Robotes: *Michi, Lola, Albita, Isaac, Zahonero, Felipe, Esther, Angel L., Uli (...).* Por muchos más reencuentros y cenas de Navidad!.

No me olvido de vosotros, *Nuno y Marta*, ni de tí, Marga, por cuidarnos tanto estos años. Tampoco de vosotros, *Mª Jose y Albertos.* Gracias por toda vuestra ayuda y cariño.

A la Topa, Luz Oscura, Blues, Haring, Pirata, Holandés, Café 7. Al Rock'n rolla, Chigre, Oficina, Errante, Rey Louis (...). Simplemente indispensables en este camino.

A todas y cada una de las personas con las que he reido, pasado buenos ratos, echado una (y mil!) cervezas, y disfrutando de pequeños y grandes momentos juntos.

Y en especial a tí, *Javi*, por ser y estar por y para todo.

Sara Rodríguez Berlanas, La Laguna, Junio de 2019

Summary

This thesis is a compendium of three published articles (plus an additional unpublished work) that represents the fruits of research focused on the massive Cygnus OB2 star-forming region. It is one of the nearest, most massive and youngest Galactic OB association and it provides an excellent target to study massive star properties, formation and evolution in a very active environment. Our main goal is to increase our current knowledge of the Cygnus OB2 association and its massive star population. With this aim, we have carried out four different (but related) studies where the main physical properties of the Cygnus OB2 massive population have been characterized.

Firstly, we present a membership study of Cygnus OB2 and its surroundings for completing the currently known population of early-type stars in the region. From new spectroscopic observations, we have increased the number of OB stars known in the area in spite of the existing limitations for completing the whole census. We also investigated the age and extinction distribution of the region, and whether there exists a correlation between the observed age spread and Galactic longitude.

Since there exist firm indications that many massive stars of Cygnus OB2 have exploded as supernovae during the history of the region, we include a chemical analysis of a sample of OB stars in Cygnus OB2 for checking possible inhomogeneities across the whole association and whether there also exists a correlation of chemical composition with Galactic longitude that could be caused by self-enrichment processes.

A persistent problem for massive star studies has been always the inaccuracy of their distances. Fortunately, the second data release of the *Gaia* satellite has provided high-quality astrometry for a large number of Galactic massive stars, including those in Cygnus OB2. Thus, a study of the spatial substructure of the association is also included in this work, where we have quantified the line-of-sight substructure within the association by using an inference approach and creating a parametrized model that reproduces the observed parallax distribution.

Finally, we present the most complete spectroscopic census of O stars done so far in Cygnus OB2. We have updated the binary fraction currently known in the association, and taking into account the results derived in all previous studies, we performed the quantitative spectroscopic analysis of all the isolated stars. We obtained the distribution of rotational velocities and derived physical and spectroscopic parameters, providing new temperature and gravity scales for O-type stars. To conclude, we interpret the evolutionary status of the region using the Hertzsprung-Russell diagram and its spectroscopic version.

Resumen

Esta tesis es un compendio de tres artículos (más un capítulo adicional) donde se recogen los frutos de un estudio enfocado en Cygnus OB2, una de las asociaciones de formación estelar OB más cercana, masiva y joven de nuestra Galaxia. Esta región supone un excelente lugar donde estudiar las propiedades, formación y evolución de estrellas masivas en un entorno de formación estelar muy activo. Nuestro objetivo principal es aumentar el conocimiento que existe actualmente de esta asociación y su población estelar. Para ello, hemos llevado a cabo cuatro estudios diferentes (aunque relacionados) dónde se han caracterizado las principales propiedades físicas de su población masiva.

En primer lugar presentamos un estudio de membresía en la región de Cygnus OB2 y sus alrededores con el fin de completar la población de estrellas de tipo temprano conocida hasta el momento. Haciendo uso de nuevos datos observacionales, hemos incrementado el número de miembros OB de la asociación, a pesar de las limitaciones encontradas para obtener un censo completo. Además, se ha investigado su distribución de edad y extinción, así como una posible correlación entre edad y longitud Galáctica.

Dado que existen sólidas indicaciones que apuntan a que muchas de las estrellas masivas de Cygnus OB2 ya han explotado como supernova a lo largo de su historia, hemos realizado un estudio químico de la asociación con el propósito de detectar posibles inhomogeneidades y comprobar si también existe una correlación entre composición química y longitud Galáctica que pudiera evidenciar procesos de autoenriquecimiento.

Un problema persistente en estudios de estrellas masivas ha sido la poca precisión en sus distancias. Afortunadamente, el satélite *Gaia* ha proporcionado recientemente astrometría precisa de un gran número de estrellas masivas Galácticas, incluidas aquellas pertenecientes a Cygnus OB2. Por lo tanto, hemos realizado un estudio de su estructura espacial interna, donde se ha cuantificado la subestructura observada a lo largo de la linea de visión mediante el uso de inferencia Bayesiana y la creación de un modelo parametrizado que reproduce la distribución de paralaje observada.

Finalmente, presentamos el censo espectroscópico más completo de estrellas O creado hasta el momento en Cygnus OB2. Se han identificado nuevos sistemas binarios, y teniendo en cuenta los resultados derivados de los trabajos anteriores, hemos realizado el análisis espectroscopico cuantitativo de todas las estrellas aisladas. Se ha obtenido la distribución de velocidad de rotación y derivado sus principales parámetros espectroscópicos y físicos. Para concluir, se ha interpretado el estado evolutivo de la asociación a partir del diagrama Hertzsprung-Russell (HRD) y su análogo espectroscópico (sHRD).

Contents

1

Introduction

1.1 Massive stars

Understanding the physics, formation and evolution of massive stars (those burning carbon in a non-degenerated core) is crucial to understanding the evolution of the Universe. Massive stars are defined as born with masses higher than about 8 $M_{\odot}$ (Maeder & Meynet 2000; Smith 2014). Their violent ends as supernovae (SNe) leave compact remnants (Woosley et al. 2002) and produce a final kinetic energy of the surrounding medium and newly synthesized chemical elements injection that contribute strongly to the chemical and dynamical evolution of galaxies (see, e.g., Langer 2012; Prantzos et al. 2018). Their strong stellar winds and intense ionizing radiation fields have also a direct impact on the dynamics and energetics of the interstellar medium, being the ultimate source of the energy reaching us from intense star-forming regions and starbursts. Therefore, massive stars play a key role in the formation of nearby stars and planetary systems. Furthermore, they have been proposed as main agents of the reionization of the Universe (e.g., Bromm et al. 2009; Robertson et al. 2010).

To asses the role of massive stars for all these processes, we must understand their physics and evolutionary behaviour. However, large uncertainties persist in our understanding of these objects that prevent us from fully understanding how massive stars impact other areas of Astrophysics (Herrero 2016). Metallicity, rotation, binarity, internal mixing and magnetic fields affect their structure, evolution and fate. Large observational multiwavelength databases and the analysis of extensive samples of high quality OB-star spectra in homo-

geneous environments are thus required to understand their physics.

1.1.1 Birth, evolution and final fate

Massive stars are born as O or early-B stars in dense cores of gas and dust, most of them within embedded clusters (Lada & Lada 2003) that collapse gravitationally within large molecular clouds (Zinnecker & Yorke 2007). A gaseous object in quasi-hydrostatic equilibrium (a protostar) forms accumulating mass by accretion of the surrounding gas. When the hydrogen burning starts in its core, it becomes a zero age main sequence (ZAMS) star that may be embedded in its molecular cloud until the latter begins to dissolve.

If this star has a mass above 8 $M_\odot$, we call it a massive OB star, which will spend most of its life burning hydrogen (via CNO-cycle) in the main sequence (MS) phase. When the inner hydrogen is consumed, massive stars can follow different evolutionary paths depending on their mass (see Fig 1.1) that may include red supergiant (RSG), luminous blue variables (LBV) or Wolf-Rayet (WR) stages. When inner He is depleted at the core, the inert carbon core shrinks, its temperature rises again and carbon begins to burn in the interior leaving an evolopping He shell. This cycle is repeated for the different elements synthesized in the stellar interior: after H, He and C, mainly Ne, O, Si and Fe are processed. In Fig. 1.2 we show the 'onion' structure of a massive star close to its end: an iron core surrounded by shells of lighter elements fusing. The cycle finishes with iron, since its fusion is no longer exothermic. At that point, the star becomes unstable and collapses, exploding as a core-collapse SN (CCSN). This violent end produces a final burst of photons, kinetic energy, and newly synthesized chemical elements that pollute the interstellar medium (ISM), contaminating the natal molecular cloud and producing a new generation of massive stars.

Conti (1975) introduced a possible evolutionary scenario where single massive O stars may lose a significant amount of mass though stellar winds, revealing first the H-burning products at its surface, and subsequently the He burning products. Crowther (2007) and Crowther & Smartt (2007) summarized the different evolutionary channels based on the *Conti scenario* as follows

* $8\ M_\odot < M < 25\ M_\odot$
  OB $\rightarrow$ RSG $\rightarrow$ SNIb

* $25\ M_\odot < M < 40\ M_\odot$
  O $\rightarrow$ BSG $\rightarrow$ LBV/RSG $\rightarrow$ WN (H poor) $\rightarrow$ SNIb

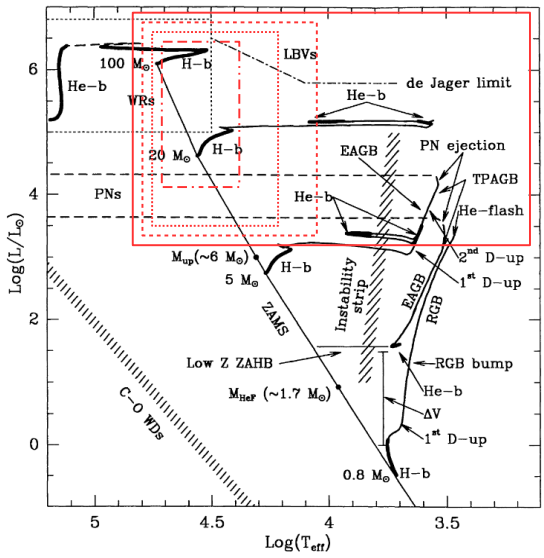

Figure 1.1: Hertzsprung-Russell Diagram from Chiosi (1992). Evolutionary tracks of model stars Y = 0.25 and Z = 0.008 for 0.8 $M_\odot$, 5 $M_\odot$, 20 $M_\odot$, and 100 $M_\odot$. Red lines indicate the location of all massive stars (M > 8 $M_\odot$, solid line), O and B stars (dashed line), O and early-B stars (up to B3, dotted line) and O stars (dash-dotted line) on the diagram.

* 40 $M_\odot$ < M < 75 $M_\odot$
  O → BSG → LBV → WN (H poor) → WC → SNIc

* M > 75 $M_\odot$
  O/Of → WN (H rich) → LBV → WN (H poor) → WC → SNIc

However, the evolution of these stars are highly affected by different factors that play an important role in their evolutionary behaviour and are described as follows.

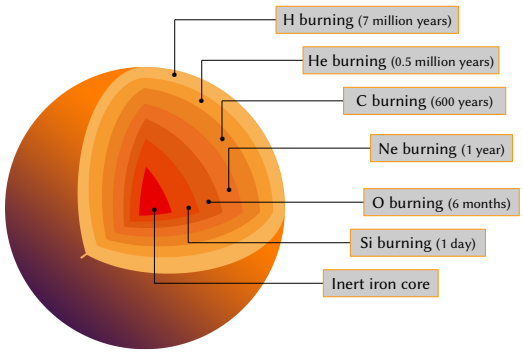

Figure 1.2: The chemical structure of a massive star in its last throes of life. The timescales are calculated for a star of 25 solar masses (based on an image from Phillips 1999).

1.1.2 Factors affecting massive star evolution

It is known that the mass, chemical composition (i.e., metallicity), mass-loss and angular momentum play an important role for massive stars. The combination of all these physical parameters determines the evolution of the star and its position in the Hertzsprung–Russell diagram (HRD). Other factors have been recently recognized to affect the massive star evolution and, therefore, its final fate. Binarity and magnetic fields are key processes that have a direct impact on the evolution of massive stars (Langer 2012). However, not all the processes mentioned are yet totally understood and should be investigated for a valid characterization of massive stars.

Rotation and internal mixing

The study of stellar rotation in massive stars was partly induced by the evidence for mixing processes acting in the stellar interior. Rotation favours the transport of angular momentum from inside the star and produces a circulation of matter from the core to the surface. In some cases, abundance anomalies in the stellar surface may reflect the effects of the nuclear reactions in the CNO cycle (see Maeder & Meynet 2000, and references therein), where helium and nitrogen are enhanced while carbon and to a less extent oxygen are depleted.

Depending on the initial rotational velocity of the star and the mixing

mechanisms working in its interior, the evolution and fate of massive stars may be completely different. Theoretical models have included rotational mixing to explain the observed abundance patterns (e.g., Brott et al. 2011; Ekström et al. 2012). Rotation mixes material from the interior towards the surface though different mechanisms, thus producing the enhancements of He and the CNO patterns observed at the surface. The efficiency of this phenomenon increases with stellar mass and rotational velocity rate, and decreases with time. When rotating stars evolve the rotational velocity at the surface decreases due to expansion, and the angular momentum is reduced by stellar winds (see Ekström et al. 2008; Vink et al. 2010). However, a study of rotational mixing effects on a sample of early B stars in the Large Magellanic Cloud (LMC) found a significant number of slow rotators with enhanced N abundances, as well as fast rotators with no evidence of rotational mixing (Hunter et al. 2008). In recent years, alternative scenarios to the mixing processes have been developed, which involve multiplicity, magnetism or even stellar pulsations and internal gravity waves.

These transport mechanisms are needed not only to explain the behaviour of surface rotation and abundances, but also to explain the rotation rates of young neutron stars and how the initially fast rotating core does not reach critical rotation when it grows (see Langer 2012).

Stellar winds and mass loss

Massive stars, through stellar winds, lose a significant amount of mass during their lives (see Najarro et al. 2006). The stellar wind is driven by the change in momentum through absorption and re-emission of radiation field photons by metal lines in the stellar atmosphere (radiatively driven winds, RDW, see Castor et al. 1975; Pauldrach et al. 1986; Friend & Abbott 1986). The mass-loss rates increase for more luminous stars (Puls et al. 2008), not only dramatically affecting their evolution but also having a significant impact on the environment. Due to mass-loss the star changes its surface chemical composition and luminosity (Langer 2012), and the surrounding ISM gains radiative and kinetic energy, as well as nuclear processed material.

The mass-loss is also related to the evolutionary state of the star, increasing at post-main sequence stages and being favoured by the expansion of the star. LBV stars show irregular eruptions, losing large amount of mass through not well understood mechanisms. In some cases, the strong winds peel the outer envelope of the star, leaving a He core and producing Wolf-Rayet stars.

Kudritzki et al. (1995) established the so-called Wind Momentum – Luminosity Relationship (WLR), which predicts a relation between the wind mo-

mentum gained by the escaping matter and the stellar luminosity. Since this gain of momentum is based on the absorption of photons by metal lines, there exists a dependence of the WRL on metallicity (Kudritzki et al. 1995; Vink et al. 2001). Although this relationship has been confirmed for the range of metallicities between those of the Milky Way (MW) and the Magellanic Clouds (Mokiem et al. 2007), other empirical studies have observed cases where the observed winds are weaker than theoretically expected (Bouret et al. 2003; Martins et al. 2005b; Fullerton et al. 2006). There exist many possible explanations for these observed weak winds, from effects of wind clumping[1], the presence of X-Rays or an early evolutionary stellar stage, to the limitations in a correct determination of the mass loss rate from the Hα profile. Weak winds represent, therefore, another important open question in the field of massive stars.

Multiplicity

An interesting property of massive stars is their high degree of multiplicity. In clusters and associations, using either spectroscopy or imaging techniques, it has been detected that three out of four O-type stars have at least one companion (Mason et al. 2009). New large surveys have resulted in an unprecedented high multiplicity fraction, reaching the 90 percent (Sana et al. 2014). Only a small fraction of massive stars evolve undisturbed toward their final fate (de Mink et al. 2013). Sana et al. (2012) found that 71 percent of the stars born as O-type (including single O stars and O stars in binaries) interact with a companion, over half of which do so before leaving the main sequence and three quarters of all them before exploding as supernovae. The binary scenario has been also proposed as the origin of Wolf-Rayet stars (Clark et al. 2011; Shenar et al. 2019).

Thus, binary interaction could be considered as one of the main processes dominating the evolution of massive stars and their final fate, with important effects on the rotational properties (de Mink et al. 2013). The presence of a nearby companion alters the evolution of these stars, and could lead to phenomena such as stellar mergers, X-ray binaries, hydrogen-deficient CCSNe and gamma-ray bursts (GRB). Multiplicity effects must thus be considered in order to improve our understanding of massive star evolution and to better interpret some processes in which could be involved, such as rotational mixing.

[1] density inhomogeneities in the wind that produce clumps with a higher density than the rest of the wind.

Magnetic fields

The origin and impact of magnetic fields in the evolution of massive stars are poorly understood, although they have recently begun to be investigated. Magnetics fields in massive stars are probably of fossil origin, starting in the collapse of the natal cloud and decaying later, perhaps as a function of mass (see, e.g., Fossati et al. 2015b).

The number of detected magnetic O stars is low. Grunhut et al. (2017), in the framework of the Magnetism in Massive Stars (MiMeS) Survey, derived a magnetic incidence fraction of 7 ± 3 percent among a sample of 108 observed O-type stars, consistent with the findings of other large surveys such as 'B-fields in OB stars' (BOB, Fossati et al. 2015a) who find a global rate of 6 ± 4 percent. Although Grunhut et al. (2017) do not find any evidence of dependence on the physical properties of the star (e.g., temperature, gravity, or age), they notice that the confirmed magnetic stars are rotating much more slowly than non-magnetic stars. Ud-Doula et al. (2009) relate the slower rotation to the loss of enhanced angular momentum due to magnetic coupling with the stellar wind, which is expected to rapidly decrease the angular rotation rate of the star within a few million years. However, Fossati et al. (2015a) do not find a clear variation of the presence of magnetic fields with rotation. The influence of magnetic fields in determining the wind structure (e.g., Babel & Montmerle 1997; ud-Doula & Owocki 2002; Townsend & Owocki 2005), rotation (e.g., Mikulášek et al. 2008; Ud-Doula et al. 2009; Townsend 2010), and evolution of massive stars (e.g., Meynet et al. 2011; Maeder & Meynet 2014) is increasing the current interest in this phenomenon.

It is clear that massive star evolution is complex, being affected by metallicity, mass-loss, binarity, rotation, and possibly magnetic fields (all of them not yet fully understood). Large observational multiwavelength databases and the analysis of extensive samples of high-quality OB star spectra in homogeneous environments can thus help to understand the physics, providing empirical data to constrain the theoretical evolutionary models.

1.2 Galactic star-forming regions

During the last two decades, observations from space and in the near-infrared have revealed that galaxies form a significant fraction of their stars in young, super-massive clusters (YMCs, see, Portegies Zwart et al. 2010). Our knowledge of YMCs is, though, limited by their distances, which allow us to study only their integrated properties. While it is possible to resolve the stellar populations

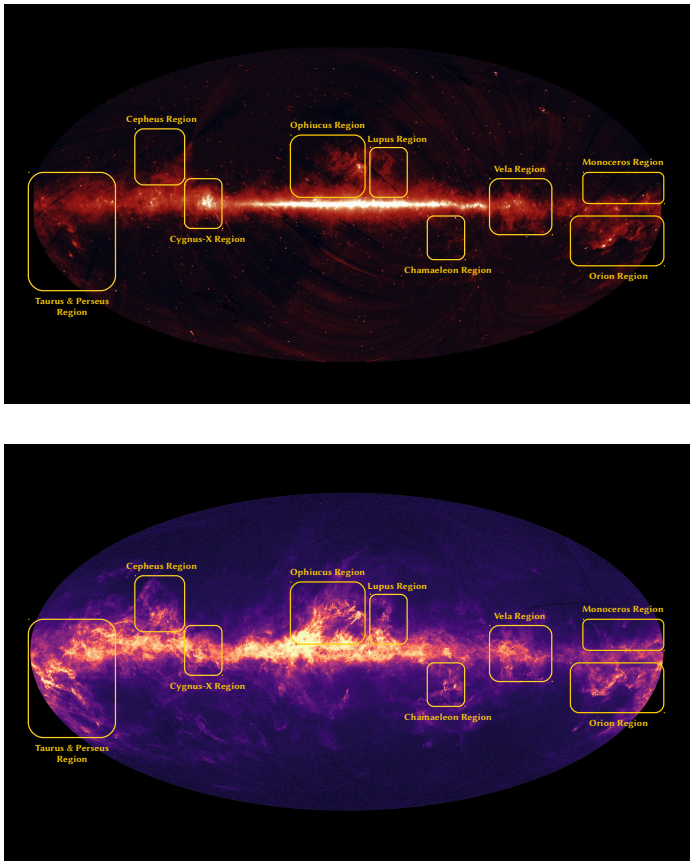

Figure 1.3: *Top*: All-sky map in infrared light at nine micrometres with star-forming regions as seen by the Akari satellite (image credit from ESA). *Bottom*: A two-dimensional projection over the whole sky of the average interstellar extinction using *Gaia* DR2 data (image by ESA/Gaia/DPAC, M. Fouesneau, R. Andrae, C.A.L Bailer-Jones, O. Creevey). In both panels, the most relevant Galactic star-forming regions are marked in yellow.

of the few YMCs known in our Galaxy, such as the Arches (Cotera et al. 1996), Quintuplet (Figer et al. 1999), or Westerlund 1 (Clark et al. 2005), their high dust extinction ($A_V > 10$ mag) and large distances (> 5 kpc) severely hamper such studies, limiting them to the brightest members. However, some closer and less obscured Galactic star-forming regions (SFr) provide an excellent alternative to study star formation in a YMC-like environment. They contain rich OB associations and single and binary stars in all evolutionary stages.

Massive SFr are places where we can observe star formation *in-situ*. They provide a unique laboratory to study both the process of massive star formation and their interaction within the Galaxy. A common way to find these regions is to look for their environmental effects, such as shells and bubble structures (Rahman & Murray 2010; Palmeirim et al. 2017). Most of these bubbles were created by the effects of stellar winds and supernovae, and are associated with H II regions that are generated by massive stars ionizing the surrounding medium, causing it to expand isotropically (Conti & Crowther 2004; Palmeirim et al. 2017). When bubbles expand, they interact with the surrounding cold molecular medium, which may induce triggered star formation (e.g., Zavagno et al. 2007, 2010; Deharveng et al. 2010; Samal et al. 2014; Liu et al. 2016).

These regions are characterized for emitting strong infrared (IR) radiation from the heated interstellar dust, in which their newly born population is embedded. It is common to use the extinction to measure the absorption and scattering of electromagnetic radiation by dust and gas along the line-of-sight. Since blue light is much more strongly attenuated than red light, extinction causes objects to appear redder than expected, producing the associated interstellar reddening. The entire sky in IR light observed with the AKARI[2] satellite at nine micrometres is shown in Fig. 1.3 (top panel). We distinguish several bright regions corresponding to strong IR radiation along the Galactic Plane, that as stated before, shows places of newly born stars. The nearby Cygnus-X complex stands out among the other regions, indicating powerful star-forming activity. In the bottom panel is shown a two-dimensional projection over the whole sky of the average interstellar measured extinction from *Gaia* photometry in the G-band (A_G). This image shows the most detailed all-sky map of dust attenuation based on individual stars yet produced, where brighter regions correspond to higher extinctions. However, we highlight that the extinction actually varies along the line-of-sight, something not evident in this image. In both panels are marked the most-relevant Galactic SFr. All these molecular cloud complexes contain rich OB associations, whose massive star population

[2]Previously known as ASTRO-F or IRIS - InfraRed Imaging Surveyor

Table 1.1: General overview of the main characteristics of Cygnus OB2 compared to the Carina Nebula association and the 30 Doradus SF region.

Parameter	Cygnus OB2	Carina Nebula	30 Doradus
Location	MW	MW	LMC
Known O members	∼70 (1)	∼75 (2)	∼352 (3)
Binary fraction	36% (4)	25% (5)	51% (6)
Age spread	(1 – 6) Myr (1)	(1 – 8) Myr (5)	(1 – 5) Myr (7)
Distance	∼1.4 – 1.7 kpc (8)	∼2.3 kpc (2)	∼50 kpc (9)
Angular/lineal size	∼2 deg / 60 pc (10)	∼1 deg / 40 pc (3)	∼15 arcmin / 200 pc (11)
Extinction	(4 – 7) mag (12)	2 – 3 (13)	(1 – 2) mag (14)

References. (1) Berlanas et al. (2018a) (2) Smith (2006) (3) Walborn et al. (2014) (4) This work, Chapter 6 (5) Berlanas et al. (2019b, in prep) (6) Sana et al. (2013) (7) Sabín-Sanjulián et al. (2017) (8) Berlanas et al. (2019) (9) Gibson (2000) (10) Comerón & Pasquali (2012) (11) Walborn (1991) (12) Wright et al. (2015) (13) Vazquez et al. (1996) (14) De Marchi et al. (2011).

can be investigated. This thesis work is focussed in the Cygnus OB2 association, the central part of the young Cygnus-X complex which represents one of the richest known regions of star formation of our Galaxy, conspicuous at all wavelengths.

1.2.1 Cygnus OB2

The Cygnus-X region is one of the most powerful star-forming complexes of the Galaxy. It is part of a much more complex field that contains several rich OB associations, numerous young open clusters and tens of compact H II regions. The whole region hosts the largest number of nearby massive stars and intense star-forming activity (Reipurth & Schneider 2008), providing a unique testbed for our theories about massive star formation, structure and evolution. Moreover, it is also an ideal place to study the properties of gas and dust in young regions, the interplay between interstellar medium and stars, and the dynamics and kinematics of OB associations and stellar groups.

Its central Cygnus OB2 association represents the most obvious example of recent star formation in the massive Cygnus-X region. It harbours a large homogeneous population of OB stars (Knödlseder 2000; Comerón & Pasquali 2012; Berlanas et al. 2018a) that can be analyzed, providing a template for studies of distant, massive star clusters and OB associations in the MW and in nearby galaxies. Although the optical extinction to Cygnus OB2 is moderately high, is is not sufficient to prevent obtaining spectra of its bright stellar content. Located at less than 2 kpc from the Sun (Knödlseder 2000; Hanson 2003; Rygl et al. 2012; Berlanas et al. 2019), it provides an excellent target for studying

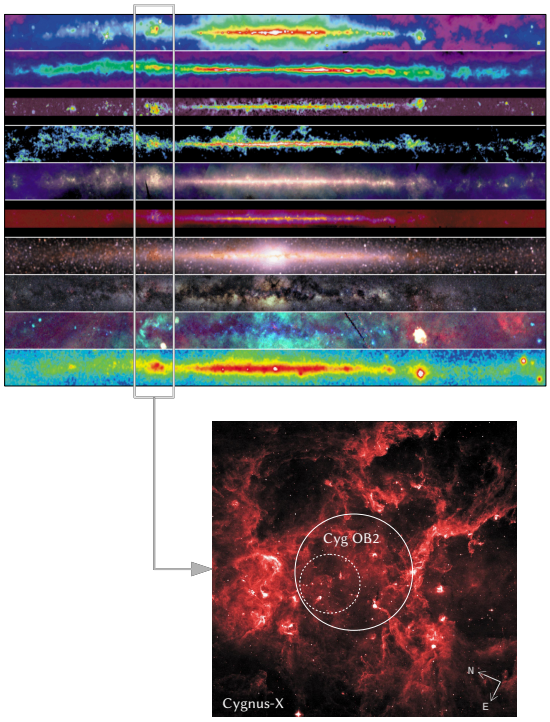

Figure 1.4: Location of the Cygnus-X complex and its central Cygnus OB2 association in the Galaxy. *Top*: Combined maps of the Galaxy at ten wavelengths. From top to bottom: radio continuum (408 MHz), atomic Hydrogen, radio continuum (2.5 GHz), molecular Hydrogen, infrared, mid-infrared, near-infrared, optical, x-ray and gamma-ray. Images from several space and ground-based surveys, available through the National Space Science Data Center at NASA Goddard Space Flight Center. The Cygnus-X star-forming region is marked with gray lines. *Bottom*: Part of the Cygnus-X region observed at 24 μm with MIPS on Spitzer. The solid line circle delimits the $\sim$1 deg area of Cygnus OB2 adopted in this work. For reference, the dotted line circle shows the core of the association.

massive star properties, formation and evolution in a very active environment. For reference, in Table 1.1 we show a general overview of the properties of Cygnus OB2 compared to another relatively close Galactic SF association (the Carina Nebula) and to the most massive SF region known in the LMC (the Tarantula Nebula or 30 Doradus association).

Brief history

Cygnus OB2, along the last decades, has received a lot of attention and has been studied at all wavelengths with different spatial coverage. It was discovered by Münch & Morgan (1953), and further OB stars were identified by Morgan et al. (1954) and Schulte (1956, 1958). The first comprehensive study was developed by Reddish (1968), who obtained UBV photometry of the area. Long time later, Torres-Dodgen et al. (1991) obtained Strömgren and JHKL photometry for a large sample of its stellar content. But it was Massey & Thompson (1991) who performed the first and most complete CCD optical photometry survey of Cygnus OB2 to date, including spectroscopic observations for a large sample of O stars. Ongoing efforts, such as GALANTE (Lorenzo-Gutiérrez et al. 2019), will supersede this work. In a following near-IR study, Knödlseder (2000) used 2MASS photometry to determine statistically the morphology and stellar content of the association. The first optical spectroscopic analyses were carried out by Herrero et al. (1999, 2000, 2002), obtaining the stellar parameters for a limited sample of OB stars. Only a few stars were observed in the UV range by Herrero et al. (2001). At the same time, Comerón et al. (2002) and Hanson (2003) increased the number of known OB members using near-IR and optical spectroscopic surveys, respectively. Some years later, more and deeper surveys were carried out in the region, increasing this number continuously, as well as the number of later-type stars (Kiminki et al. 2007; Negueruela et al. 2008; Drew et al. 2008; Vink et al. 2008). In 2012 an improved census of moderately obscured O and early B stars in the wide area surrounding Cygnus OB2 was presented by Comerón & Pasquali (2012). This work was followed by the quantitative analysis of the star formation history, initial mass function, and total mass by Wright et al. (2015). In recent years, Cygnus OB2 was observed at other wavelengths, such as X-rays (Rauw 2011; Rauw et al. 2015; Guarcello et al. 2012; Wright et al. 2014), radio (Prinja & Fenech 2011; Willis et al. 2011) or Gamma-Ray (Anchordoqui et al. 2009; Araudo et al. 2012). Recently, the census of OB stars has been updated (Berlanas et al. 2018a, see Chaper 3) and the first chemical study (Berlanas et al. 2018b, see Chaper 4) and spatial structure analysis (Berlanas et al. 2019, see Chaper 5) have been performed in the association.

Extension

The extension and limits of Cygnus OB2 are not well defined. The first surveys in the association assumed a smaller area where the most luminous members are located (Münch & Morgan 1953; Massey & Thompson 1991). Then, Knödlseder (2000) and Knödlseder et al. (2002) provided wider limits showing that extinction was a limiting factor in previous studies. The core area was well constrained by Hanson (2003) and Vink et al. (2008), centred on Galactic coordinates $l = 80.22°$, $b = 0.78°$ where the Cyg OB2 #8 trapezium-like system is located. However, this area was then extended with the identification of new early-type members. Comerón et al. (2002, 2008) confirmed new OB members through near-IR spectroscopy in the outskirts of Cygnus OB2, between 1 and 2 degrees from its core. Taking into account their results, more recent studies (such as those presented in this thesis) have considered an extension for Cygnus OB2 slightly beyond the core (i.e., 1 square deg. radius centered on Galactic coordinates $l = 79.80°$, $b = 0.80°$).

OB content

The massive OB content of Cygnus OB2 has been continuously increased with time. Münch & Morgan (1953) identified the first eleven early-type stars of the association. Then, Morgan et al. (1954) increased this number by a further seven new stars. But it was Massey & Thompson (1991) who developed an extensive survey identifying 120 possible massive star members, 70 of which were classified as OB stars (42 O-type stars). However, Knödlseder (2000) based on 2MASS proposed that this number should be much larger, around 100 O-type stars. In the last few decades, many other studies were carried out in the region updating this number continually (Comerón et al. 2002; Hanson 2003; Kiminki et al. 2007; Negueruela et al. 2008; Comerón et al. 2008).

It was not until 2012 that the most complete spectroscopic survey to date was carried out by Comerón & Pasquali (2012). They performed spectral classification of a magnitude limited sample ($B \leq 16$, $K_s < 9$ mag) selected with a homogeneous photometric criterion over a large area that includes Cygnus OB2 and its surroundings. Their study resulted on the largest sample of known OB stars identified in the region, including a list of 61 OB candidates pending spectroscopic confirmation. Assuming the 1 square deg. radius area centered on Galactic coordinates $l = 79.80°$, $b = 0.80°$, they provided a list of (magnitude-limited) 102 OB stars within Cygnus OB2, 63 of which classified as O-type stars. A few years later, a new census of the known OB content of Cygnus OB2 was compiled by Wright et al. (2015) from the available literature. However, in this case only the core of the association was included and no limiting

magnitudes were applied. Thus, they provided a larger list of 169 OB stars within the core of Cygnus OB2, 52 of them identified as O-type stars.

The most recent membership study was carried out by Berlanas et al. (2018a), Chapter 3 of this work, where 42 new O-type stars were confirmed from the Comerón & Pasquali (2012) list of 61 candidates. However, some of them are located in the boundaries assigned to Cygnus OB2. Assuming the extension of Cygnus OB2 as that adopted by Comerón & Pasquali (2012), as well as the non-limited sample provided by Wright et al. (2015), there are 221 currently identified O and B-type stars in Cygnus OB2, 70 of them classified as O-type stars[3].

Distance

The distance to Cygnus OB2 was first estimated by Torres-Dodgen et al. (1991) and Massey & Thompson (1991), who both agree on a value of 1.7 kpc (distance modulus 11.2). This value was widely accepted by the community until the work developed by (Hanson 2003), who estimated a closer distance of ∼1.45 kpc (distance modulus 10.8) from new effective temperature scales for O stars derived by Martins et al. (2002). The distance to the whole Cygnus-X complex was some years later estimated by Rygl et al. (2012), who obtained astrometric data for five massive star-forming regions toward the whole complex and established a common distance of 1.40 ± 0.08 kpc. Since Cygnus OB2 forms part of the complex, the latter value has been adopted for it, being generally used in the last studies performed in the region.

However, the new *Gaia* DR2 data have provided unprecedented high-quality astrometry for more than 1.3 billion objects, including those from the Cygnus OB2 association. A recent study of its spatial structure from *Gaia* astrometry (Berlanas et al. 2019, see Chapter 4 of this work), has led to the identification of two stellar groups spatially separated and superposed in the association. Interestingly, the distance to the main group was found to be ∼1760 pc (in agreement with the distance originally derived by Massey & Thompson (1991)), while the distance to the second foreground group at ∼1350 pc is similar to that determined by Rygl et al. (2012) for the Cygnus-X region as a whole.

Age

The age derived for Cygnus OB2 has followed a converging path with time,

[3]We note that this number includes identified SB2 binaries and does not take into account some stars in multiple systems for which spatially resolved spectroscopy is available (e.g., Cyg OB2 #22). See Chapter 6 for an updated spectroscopic census of the currently known O-population of Cygnus OB2.

evolving with membership studies, estimated distance and improved evolutionary models. Torres-Dodgen et al. (1991), Massey & Thompson (1991) and Knödlseder et al. (2002) established an approximate age of 3 – 4 Myr. Hanson (2003) found a younger age of 2 Myr for the association, with a spread of 1 Myr. The more complete and comprehensive survey conducted by Comerón & Pasquali (2012) found a considerable age spread among the members, many of which turned out to be older than 3 – 4 Myr. Nevertheless, Wright et al. (2015) introduced a comparison with Geneva rotating and non-rotating models (Ekström et al. 2012), deriving a peak stellar age of 2 – 3 Myr from non-rotating stellar evolution models (as suggested by previous authors which, as them, adopted DM = 10.8), but a slightly older peak age at 4 – 5 Myr from the rotating stellar models (in agreement with that found from studies of low- and intermediate-mass, see Drew et al. 2008; Wright et al. 2010). They concluded that the majority of star formation occurred during a period of 1 – 7 Myr ago, with a possible peak in the star formation intensity 4 – 5 Myr ago. The more recent age study in Cygnus OB2 was carried out by Berlanas et al. (2018a), who also introduced a comparison between two different family models (rotating and non rotating Geneva and Bonn stellar models). Again, they adopted a distance modulus 10.8 for the whole sample and found that uncertainties about rotation and adopted models affect only the most massive members, suggesting older ages ($\sim$1 – 2 Myr) when rotation is assumed. Even so, all models supported an observed age spread of 1 – 6 Myr for the OB population of Cygnus OB2, in agreement with previous studies. In Chapter 6 we present an updated HR diagram of the known O population, where the age distribution of the association has been revised.

Extinction

The high extinction towards the stellar content of Cygnus OB2 was claimed from the very first studies of the region (see Johnson & Morgan 1954). Hanson (2003) derived an extinction law for the association (with a ratio of total to selective extinction, R_V, of 3.0) by determining optical and near-IR colour excesses (from MT91 and 2MASS photometry) to the Lejeune & Schaerer (2001) and Fitzgerald (1970) intrinsic colours, respectively. She provided individual visual extinctions (A_V) for a sample of 85 OB-type stars. Then Comerón & Pasquali (2012) used a combination of optical and near-IR photometry (from USNO-B and 2MASS catalogs), updated intrinsic colours from Martins & Plez (2006) and the Cardelli et al. (1989) extinction law (with $R_V = 3.1$) to derive visual extinction values for all the OB stellar content over a wider area across the Cygnus X molecular cloud.

Recently, Wright et al. (2015) derived a new extinction law for Cygnus OB2 with an improved ratio of total to selective extinction $R_V = 2.91 \pm 0.06$. They used a reliable sample of O stars, optical and near-IR photometry (from MT91 and 2MASS catalogs) and Martins & Plez (2006) intrinsic colours. They found that the extinction distribution varies smoothly across the association, from $A_V \sim 4$ – 5 mag in the north-west (where a known *reddening hole* exists, see Reddish 1968) to $A_V \sim 6$ – 7 mag to the south of the association and on the outskirts. Berlanas et al. (2018a) confirm a median value of A_V ∼6.5 mag, although at specific places they also found visual extinctions up to 11 mag in the surrounding area. These results are in relatively good agreement with previous studies of both the high- (Hanson 2003) and low-mass populations (Wright et al. 2010) in Cygnus OB2. However, this statement is only valid for the optical range because of the significant discrepancy found in the near-IR bands, probably due to shifts in the near-IR intrinsic colours of O-type stars between previous studies (e.g., Lejeune & Schaerer 2001; Martins & Plez 2006). A further study of this behaviour is shown in Appendix B.

IMF

Several previous attempts have been made for deriving the initial mass function (IMF) of Cygnus OB2. Massey & Thompson (1991) found a power-law mass function slope of Γ = -1.0 ± 0.1 that was later corrected to Γ = -0.9 ± 0.2 by Massey et al. (1995), both slightly flatter than the Salpeter 'universal' slope of Γ = -1.3 (Salpeter 1955). Then, Knödlseder et al. (2002) obtained a slope of Γ = -1.1 ± 0.3 based on a heterogeneous compilation of data from the youngest parts of the association. In contrast to them, Kiminki et al. (2007) found the function much steeper than the canonical Salpeter IMF by using an expanded stellar sample (Γ = -2.2 ± 0.1), while Wright et al. (2010) derived a flatter slope of Γ = -1.09 ± 0.13 from their sample of X-ray emitting stars.

In more recent years Comerón & Pasquali (2012) attempted to produce a estimate of the IMF slope of massive stars in Cyg OB2 by using an extinction and age-limited stellar sample that resulted in an inaccurate value of Γ = -2.1 ± 1.6. The most recent study was conducted by Wright et al. (2015), who found that the current mass function of the Cygnus OB2 massive stellar content is relatively steep (Γ = -2.1) but the stellar age distribution suggests that it has been steepened by the loss of the most massive stars that have already evolved to their end states. Using both an unbiased sample of stellar masses or by modelling an evolved cumulative mass function, they found that the IMF slope in Cygnus OB2 is consistent with the canonical Salpeter one of Γ = -1.39.

All these studies show the difficulties to derive the initial mass function of

massive stars in regions such as Cygnus OB2, where part of its stellar content remains undetected due to extinction (Berlanas et al. 2018a) and stellar evolution has progressively depopulated the upper main sequence in the older parts of the association. Moreover, masses depend strongly on the distance adopted for the association, and factors such as binarity, rotation and the adopted evolutionary models produce further uncertainties.

Total mass

The total mass of the association has been recently estimated by Wright et al. (2015) on 16500^{+3800}_{-2800} $M_\odot$, smaller than some previous mass estimates of (4 – 10) x 10^4 $M_\odot$ (Knödlseder 2000). They assumed a Kroupa et al. (2001) IMF, taking also into account the loss of the most massive stars. Nevertheless, this mass value is consistent with the studies of lower-mass stars in Cygnus OB2. Wright et al. (2010) estimated (2 – 4) x 10^4 $M_\odot$ from an X-ray study of low mass stars in the region, and Drew et al. (2008) estimated (1 – 4) x 10^4 $M_\odot$ from a photometric study of A-type stars. However, we highlight that in the last decade all the Cygnus OB2 studies were based on a distance of 1.4 kpc. Taking into account the new distance results by Berlanas et al. (2019), the stellar content of the main group of Cygnus OB2 should be actually both more luminous (approximately 1.5 times more luminous compared to the estimates in Wright et al. (2015)) and, consequently, more massive. Therefore, the latter mass estimate represents only a lower limit.

Table 1.2: Summary of the latest published Cygnus OB2 properties.

Parameter	Value	Reference
Centre	$l = 79.80°$, $b = 0.80°$	Comerón et al. (2008); Comerón & Pasquali (2012)
Radius	1 deg^2	Comerón et al. (2008); Comerón & Pasquali (2012)
Core centre	$l = 80.22°$, $b = 0.78°$	Hanson (2003)
Core radius	0.5 deg^2	Hanson (2003)
OB members (< B3)	221	Berlanas et al. (2018a), Chapter 3
O members	70	Berlanas et al. (2018a), Chapter 3
Binary fraction	36%	This work, Chapter 6
Stellar mass	16500^{+3800}_{-2800} $M_\odot$	Wright et al. (2015)
Age spread	(1 – 6) Myr	Berlanas et al. (2018a), Chapter 3
Age peak	(4 – 5) Myr	Wright et al. (2015); Berlanas et al. (2018a)
IMF slope	1.39 ± 0.19	Wright et al. (2015)
Distance	1755 pc^{+23}_{-19} (+ syst.)	Berlanas et al. (2019), Chapter 5
A_V spread	(4 – 7) ± 0.3 mag.	Comerón & Pasquali (2012); Wright et al. (2015)

Note: See text for details about the given values.

1.3 Synergy with *Gaia* and WEAVE

Important uncertainties persist in our understanding of massive stars, even in their early phases, before leaving the Main Sequence. As stated in Sect. 1.1.2, these uncertainties are related to our ability to understand the actual role of mass-loss, rotation, binarity, magnetic fields and internal mixing in their evolution and fate. Nevertheless, these uncertainties are also rooted in the inaccurate distances to OB stars, hindering the precise knowledge of their luminosities and radii. The unprecedented *Gaia* astrometry is thus crucial to disentangle the different evolutionary channels of massive stars, and since the *Gaia* spectral range is not useful for hot stars (early B, O, and WRs stars), ground-based spectra are needed in order to determine their stellar parameters. To improve the situation, the best way is the analysis of extensive samples of OB stars in homogeneous environments, such as the Cygnus OB associations, using new instruments such as WEAVE.

WEAVE is the next multi-object spectrograph at the 4.2 m William Herschel Telescope (WHT), whose first light is planned for 2020. The facility comprises a new two-degree field of view prime focus corrector, a 1000-multiplex fibre positioner (MOS) and a dual-beam spectrograph. A small number of individually deployable integral field units (IFUs) and a large single integral field unit (LIFU) will also be available within the fibre positioner. Both the IFUs and the MOS fibres can be used to feed a dual-beam spectrograph that will provide full coverage of the majority of the visible spectrum in a single exposure at a spectral resolution of ∼5000 or modest wavelength coverage in both arms at a resolution ∼20000. A summary of the main characteristics of WEAVE is shown in Table 1.3. Fortunately, the upcoming WEAVE high-resolution survey of Cygnus will provide high-quality spectra for the whole OB content of several rich Cygnus OB associations over the next years (see Fig. 1.5). Furthermore, a low-resolution disc survey will also cover the Cygnus region, providing spectra suitable for obtaining a first estimation of the main spectroscopic parameters (see Chapter 7.2 for future WEAVE perspectives).

A new era of discovery is coming thanks to unprecedented data releases from the astrometric *Gaia* satellite and forthcoming spectroscopic surveys with WEAVE, with which exist a powerful synergy.

Table 1.3: Main characteristics of the WEAVE instrument.

Parameter	Value
Telescope, diameter	WHT, 4.2 m
Field of view	2°
Number of fibres	1000
Fiber size	1.3 ″
IFUs, size	20.9 ″ x 11 ″ (1.3 ″ spaxels)
LIFU size	2 ′ x 1.5 ′ (2.6 ″ spaxels)
LR mode resolution	4300 – 7200
LR mode λ coverage	3660 – 9840
HR mode resolution	18560 – 21375
HR mode λ coverage	4040 – 4650, 4730 – 5450
	5950 – 6850

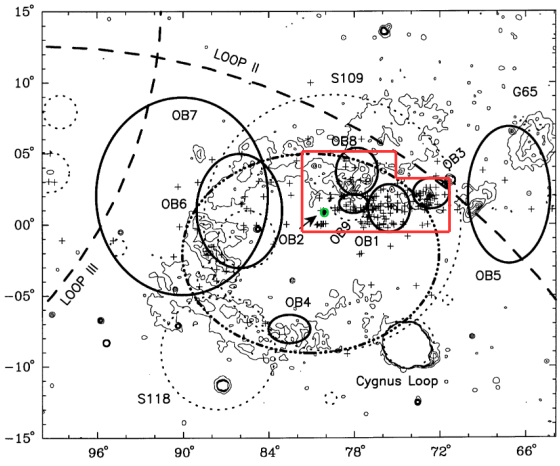

Figure 1.5: Finder chart for the Cygnus region in Galactic coordinates from Uyanıker et al. (2001) showing the regions covered by the upcoming HR WEAVE Cygnus Survey (in red). For reference, the Cygnus OB2 association in indicated in green.

1.4 Objectives and outline

1.4.1 Objectives

The main goal of the work presented in this PhD is to increase our current knowledge of the Cygnus OB2 star-forming region and its massive star population. With this aim, we have carried out four different (but related) studies focused on this association, where the main physical properties of its massive population have been characterized. Adding the formative character of a PhD, the objectives of this thesis can then be summarized in the following points:

- To know, understand and dominate the state-of-the-art techniques for the spectroscopic analysis of massive OB stars. This includes the whole process from obtaining new spectral data and its processing, to the use of modern semi-automatized tools optimized for the quantitative spectroscopic analysis of large samples of OB-type stars.
- To apply these techniques to the massive Cygnus OB2 population in order to perform a comprehensive study of its OB population. As a first step we will use new spectroscopy to search for previously undiscovered massive stars and thus increase the sample of OB members, completing the census up to B = 16 mag.
- To obtain the age and extinction distribution of the whole OB population in Cygnus OB2 to check whether there exist a correlation between age and Galactic longitude in the region, as suggested by other authors.
- To carry out a chemical composition study of the region obtaining precise abundances and checking whether the age spread observed in Cygnus OB2 might be also associated to a composition spread that could demonstrate the presence of self-enrichment processes.
- To use *Gaia* astrometry for estimating distances and include them in our analysis. We aim at exploring the spatial substructure of the Cygnus OB2 association, since the distance spread and substructure found within the association have shown previous concerns over the line-of-sight extent of the region.
- To create the most complete spectroscopic census of O-type stars in Cygnus OB2 done so far. We aim to perform the spectroscopic analysis of the whole known O population, determining the distribution of rotational velocities, updating the currently known binary fraction, and

determining the main spectroscopic parameters for all the isolated stars. Incorporating *Gaia* distances will also allow us to derive radii, luminosities and masses for the sample, providing the ingredients to interpret the results from current theories of atmospheres and evolution of massive stars.

1.4.2 Thesis outline

This thesis is a compendium of three articles, published in Astronomy & Astrophysics[4] and Monthly Notices of the Royal Astronomical Society[5], that are the fruits of research focused on the Cygnus OB2 association.

In Chapter 2 we give a general description of the different methods, tools and techniques used in this work for the analysis of massive OB stars. The next four chapters represent the core of this thesis, and are organized as follows:

- In Chapter 3 we show the published[6] results obtained from a membership study in Cygnus OB2, where we present new spectroscopic observations to confirm new OB members, as well as the limitations on completing the whole census. We also investigated the age and extinction distribution of the region, and whether there exists a correlation between the observed age spread and Galactic longitude.
- In Chapter 4 we present the published[7] results obtained from the chemical analysis of a sample of OB stars in Cygnus OB2, including new spectroscopic observations. Our aim is to check possible inhomogeneities across the whole association and whether there also exists a correlation of chemical composition with Galactic longitude that could be caused by self-enrichment processes. We also investigated the possible explanations for the obtained results.
- In Chapter 5 we present the published[8] study of the spatial substructure of the association from *Gaia* DR2 astrometry. We quantified the line-of-sight substructure within the association by using a probabilistic inference approach and creating a parametrized model that reproduces the observed parallax distribution. We also calculated individual membership probabilities and identified non-members of the association.

[4] `https://www.aanda.org`
[5] `https://academic.oup.com/mnras`
[6] Berlanas et al. 2018a, A&A, 612, A50.
[7] Berlanas et al. 2018b, A&A, 620, A56.
[8] Berlanas et al. 2019, MNRAS, 484, 1838.

- Finally, in an additional chapter (Chapter 6) we present the unpublished spectroscopic census of the whole O population of Cygnus OB2. We have updated the binary fraction currently known in this association, as well as performing the quantitative spectroscopic analysis of all the isolated stars. We obtained the distribution of rotational velocities and derived physical and spectroscopic parameters, providing new temperature and gravity scales for O-type stars. We interpret the evolutionary status of the region using the HRD and its spectroscopic version (sHRD), and compare the results from both diagrams.

To conclude, in Chapter 7 we summarize the results of this thesis work and future research perspectives. The thesis is complemented with four appendices where we describe the implications of considering an alternative line-broadening characterization (App. A) and extinction law (App. B) for the spectroscopic analysis of the O-type Cygnus OB2 population. We also include all the tabulated data (App. C) and spectra (App. D) of our stellar sample.

2

Methodology

In this chapter we introduce the different methods, tools and techniques used in this work for the analysis of massive OB stars. We focus on the methodology followed to perform accurate spectral classification of OB-type stars and the semi-automated tools based on standard techniques for the quantitative analysis of optical spectra of early-type stars. Finally, we introduce the bases of the Bayesian inference approach since it is critical to estimate distances from *Gaia* parallaxes.

2.1 Spectral classification

The accuracy of the spectral classification depends on the spectral resolution as well as on the signal-to-noise ratio (S/N). Differences in these characteristics are one of the main reasons for the discrepant spectral classifications that may be found in the literature for a given star. As an example, a double-lined binary star (SB2) may remain undetected if low resolution spectral data were used for the spectral classification (producing broader lines due to blends of both components). In other cases, a close neighbour could be affecting the observed spectral lines if spatially resolved spectroscopy cannot be obtained. In this thesis work (Chapters 3, 4 and 6) we have increased, in most cases, the quality of the previous data. Thus, we have revised the spectral classification of our OB sample using the following criteria.

The main classification criterion used for O-type stars is the comparison of the He II 4542 and He I 4471 lines, whose ratio is unity for an O7 type star. He I tends to increase in strength with decreasing temperature while He II decreases in strength. Spectral types earlier than O8 can be classified using this criteria (see Gray & Corbally 2009). For later O types the relative strengths of He II 4542/He I 4387 and He II 4200/He I 4144 may be also used, and represent the main diagnostic for types O8 – B0 (Sota et al. 2011). We adopted their criteria, using the list of qualifiers for O spectral types summarized in their work. The presence of metal lines in different ionization stages, such as Si III or O II, indicates early B-type stars, and the relative strength of the He II 4471/Mg II 4481 ratio is a useful indicator for B1 – late B stars. To classify B and later type stars (A, F and G spectral types) we followed the criteria described by Gray & Corbally (2009). Regarding the luminosity class, the classification criteria for early O-type stars were introduced by Walborn (1971, 1973), taking into account the emission effects in the He II 4686 line and N III 4634-4640-4642. Sota et al. (2011) provided an updated classification system for late O-type stars, that we have adopted in this work. For B-type stars we still adopted the system provided by Gray & Corbally (2009), along with the Balmer line widths.

Although in this work the classification for O-type stars was based on He lines as described above, we have confirmed the spectral classification by using the MGB tool (Maíz Apellániz et al. 2012). It compares the observed spectra with a standard library of O stars (in this work the GOSSS library, see Maíz Apellániz et al. (2016)). It is interactive software that allows us to vary the spectral subtype, luminosity class, line broadening and spectral resolving power of the standard spectrum until we obtain the best match. In addition, it also allows us to combine two standard spectra (with different velocities and flux

fractions) to fit SB2 binaries. For our sample of early B-type stars we used templates gathered in the framework of the IACOBsweG spectroscopic survey (Simón-Díaz et al. 2015; Negueruela et al. 2019).

2.2 Spectroscopic analysis

We performed the quantitative spectroscopic analysis of early-type OB stars (excluding detected SB2 binaries) by using semi-automated tools for the determination of the stellar parameters, which are based on large grids of synthetic spectra computed with the FASTWIND non-local thermodynamic equilibrium (NLTE) stellar atmosphere code (Santolaya-Rey et al. 1997; Puls et al. 2005). The whole analysis can be divided in two main steps. We first derive the line-broadening parameters of each star by using the `iacob-broad` tool (Simón-Díaz & Herrero 2014), which allows us to obtain easily the stellar projected rotational velocity ($vsini$) and the amount of non-rotational broadening of unknown origin (known as *macroturbulent* broadening, $vmac$). Then, in a second step, we use the `iacob-gbat` tool (Simón-Díaz et al. 2011) to obtain the main spectroscopic parameters, such as the effective temperature ($T_{\rm eff}$), surface gravity ($\log g$), wind-strength parameter (Q, defined as $\dot{M}/(\mathrm{v}_\infty\ \mathrm{R})^{1.5}$), helium abundance ($Y(He)$, defined as N(He)/N(H)), microturbulence (ξ) and the exponent of the wind velocity-law (β). Although both are automated tools, we highlight the importance of a final revision of their respective outcomes. This is an essential part of the process that is needed to identify cases in which the resulting values are not reliable. Both tools are described in detail in the following subsections.

Our grid of models covers the wide range of stellar and wind parameters considered for standard OB-type stars, from early-O to early-B types and from dwarf to supergiant luminosity classes (see Table 2.1 for grid details).

2.2.1 Line-broadening characterization

The `iacob-broad` tool is a user-friendly IDL procedure for the line-broadening characterization of OB stars developed by Simón-Díaz & Herrero (2007, 2014). It is based on a combined Fourier transform (FT) plus a goodness-of-fit (GOF) methodology that allows a user to determine easily the stellar projected rotational velocity ($vsini$) and the amount of non-rotational broadening ($vmac$) from a specifically selected diagnostic line. The considered rotation profile is approximately semicircular (due to the Doppler effect) while the macroturbulence is represented by a radial-tangential profile (see Gray 2008; Simón-Díaz & Herrero 2014, for further details).

Table 2.1: Parameter ranges of the HHe FASTWIND grid at solar metallicity used in this work.

Parameter	Range or specific values	Step
$T_{\rm eff}$ [K]	22000–55000	1000
log g [dex]	2.6–4.4	0.1
log Q [dex]	-11.7, -11.9, -12.1, -12.3, -12.5, -12.7, -13.0, -13.5, -14.0, -15.0	-
Y(He) [dex]	0.06, 0.10, 0.15, 0.20, 0.25, 0.30	-
ξ [km s^{-1}]	5–20	5
β	0.8–1.2	0.2

Note: Grid calculated using the CONDOR workload management system (http://www.cs.wisc.edu/condor/).

The main advantage of the `iacob-broad` analysis is that we obtain two independent measurements of the *vsini* (resulting from either the FT or GOF analysis) whose comparison is used as a consistency check and to better understand problematic cases. The FT technique is based on the identification of the first zero in the Fourier transform of a given line profile (Gray 2008; Simón-Díaz & Herrero 2014). On the other hand, the GOF technique is based on a simple comparison between the observed and a synthetic line profile. In this case, the latter is convolved with different values of *vsini* and *vmac* to obtain the best-fit by means of a χ^2 optimization. In addition, `iacob-broad` also allows to pre-process the selected spectral line by clipping nebular lines or renormalizing the continuum.

The tool provides a graphical output of the analysis that, at the same time, includes five main graphical results. In Fig. 2.1 we show an example of the output. In the top-left hand panel we plot the profile of the selected line. In the top-right hand panel we show the FT of the line. The two-dimensional χ^2 distribution resulting from the GOF analysis is shown in the bottom-right hand panel, and its projections are plotted on the middle-right and bottom-left panels. Beside this, a summary of the results is provided in the same figure, where the colours are used to identify the resulting profiles:

- Red text: the *vsini* obtained from the first zero of the FT analysis (henceforth, *vsini* (FT)). The profile is purely rotational.
- Blue text: the *vsini* and *vmac* obtained from the GOF analysis (henceforth, GOF$_1$ solution).

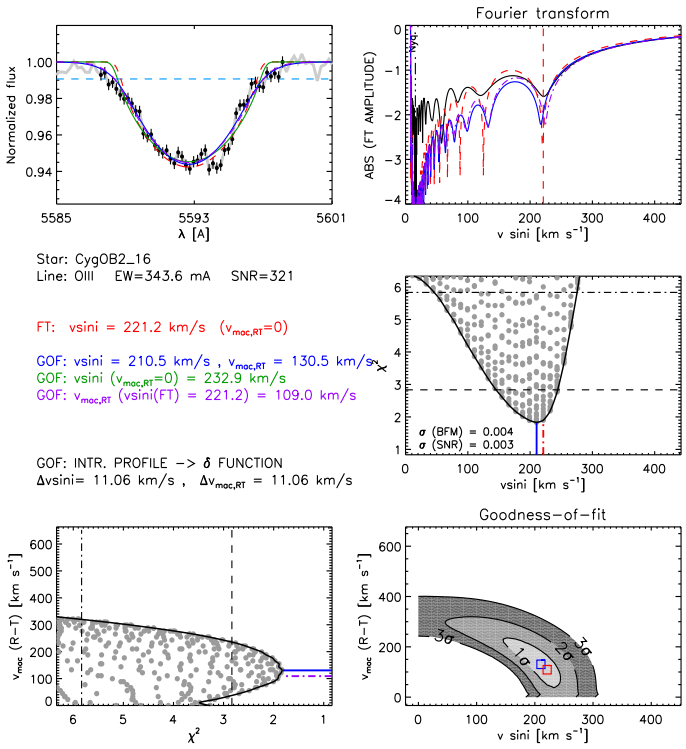

Figure 2.1: Example of the `iacob-broad` output for the CygOB2 #16 star, where the O III 5592 line was used for the analysis. Five graphical results are presented. *Top-left hand panel*: the line profile (black) and the different fits, identified by the colour in text. *Top-right hand panel*: the FT of the different line profiles (again, identified by their colours). *Bottom-right hand panel*: the 2D χ^2 distributions resulting from the GOF analysis with the confidence regions. *Middle-right and bottom-left hand panels*: projections of the 2D χ^2 distributions on *vsini* and macroturbulence planes, respectively. A summary of the FT and GOF results is given by coloured text (see Sect. 2.2.1 for a detailed description).

- Green text: the *vsini* obtained from the GOF analysis, but setting *vmac* to zero (henceforth, GOF_2 solution). It is again a pure rotational profile.
- Violet text: the *vmac* obtained from the GOF analysis when the *vsini*(FT) is adopted (henceforth, (FT+GOF) solution).
- Black text: Identifier of the analyzed star, diagnostic line and uncertainties for *vsini* and *vmac*.

The diagnostic lines used for the line broadening characterization depend on the characteristics of the analyzed spectra (e.g., wavelength coverage, signal-to-noise or the spectral type of the star). Since in this thesis we present different observations where different spectral data have been used, a detailed description of the selected lines is provided in each chapter. Generally, since metallic lines do not suffer from strong Stark broadening nor from nebular contamination, they are best suited for obtaining accurate *vsini* values. Thus, when available, we base the analysis on the Si III 4452 or O III 5592 lines. However, in some cases in which these lines are not present, or are too weak, we have to rely on other lines, e.g., N V or even He I lines.

2.2.2 Determination of the stellar parameters

Both *vsini* and *vmac* parameters along with the normalized observed spectrum are mandatory inputs for the user-friendly `iacob-gbat` tool (Simón-Díaz et al. 2011). From H and He lines[1], it allows us to determine accurately the main six spectroscopic stellar parameters for OB type stars ($T_{\rm eff}$, log g, log Q, $Y(He)$, ξ and β). Basically, once the observed spectrum is processed, the tool compares the observed and the synthetic line profiles (from FASTWIND models, in our case) by applying a χ^2 algorithm. The whole process can be divided in three bocks:

- In addition to the normalized spectra and line-broadening parameters, the user must provide the six parameter ranges that will be considered for the the χ^2 computation. Then, the tool allows the pre-processing of the observed spectra by renormalizing each considered line individually, clipping nebular lines or possible blends or even correcting the whole spectrum for radial velocity, whenever necessary.

[1]The following optical diagnostic lines were considered for the analysis of our stellar samples (whenever present): Hα, Hβ, Hγ, Hδ, Hϵ,He I+II 4026, He I 4387, He I 4471, He I 4713, He I 4922, He I 6678, He II 4200, He II 4541, He II 4686, He II 5411 and He II 6682.

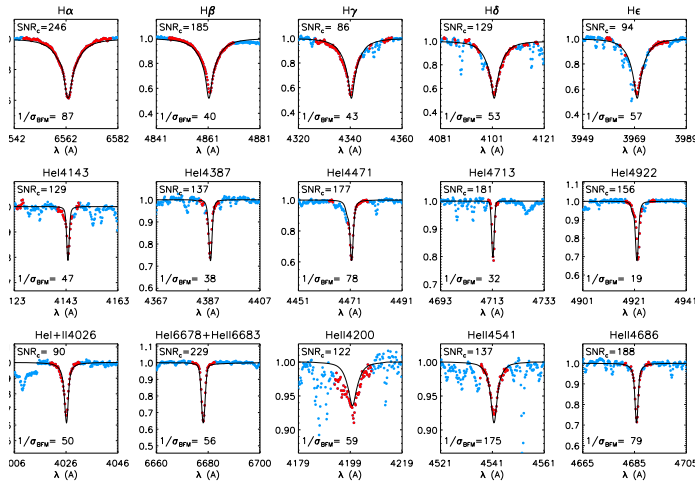

Figure 2.2: Example of the `iacob-gbat` output plots for the [MT91]145 star. The panels show a comparison between the best-fitting model (black solid line) and the observed profiles for the H-He lines considered in the analysis. Red and blue colours indicate the considered and clipped regions of each line, respectively.

- In a second step the tool computes the line-by-line χ^2 distributions, estimating the goodness-of-fit for each model within a subgrid of models selected from the global grid.
- Finally, the tool iteratively computes the global χ^2 distribution, from which the final parameter values and their associated uncertainties are estimated. The given parameters are the mean values computed from the models located within the 1-σ confidence level of the total χ^2 distributions (after each model has been weighed by its corresponding χ^2 value). Then, their uncertainties are given by the standard deviation within the 1-σ level.

If additional stellar information is provided it also computes other physical stellar parameters. When absolute visual magnitude (M_V) is provided, it computes the radius (R), luminosity (L) and spectroscopic mass (M_{sp}) following the same methodology as above. With this aim, the tool uses the equation 2.1

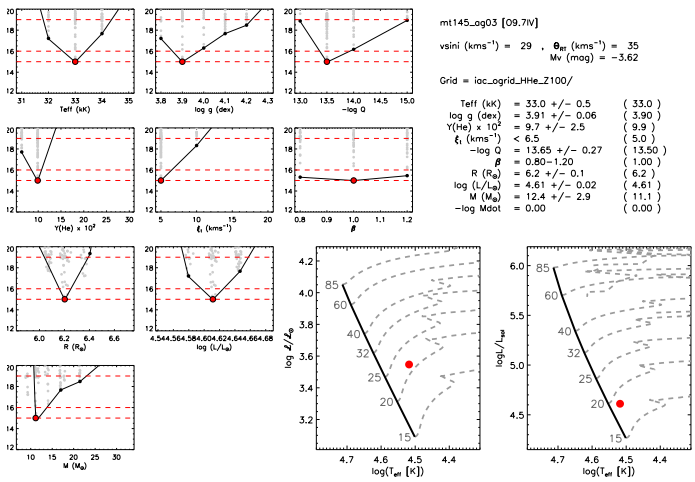

Figure 2.3: Example of the `iacob-gbat` output plots for the [MT91]145 star. The χ^2 distributions of the fitting between models and observed spectrum are shown on the panels, computed for nine of the ten possible stellar parameters that the tool can provide (see text for additional details). Red points represent the value of the best-fitting model that minimizes the global χ^2. The black line gives the lower envelope and the red dashed lines correspond to the minimum χ^2, 1 σ and 2 σ confidence levels. Locations of the star in the sHR and HR diagrams are shown on the bottom right panels.

introduced by Kudritzki (1980), where the V parameter represents the integral in wavelength of the emergent flux of the model (Matthews & Sandage 1963):

$$5\ log(R/R_{\odot}) = 29.57 - M_V + V \tag{2.1}$$

and

$$log(L/L_{\odot}) = 2\ (R/R_{\odot}) + 4\ log(T_{eff}/T_{eff,\odot}) \tag{2.2}$$

$$log(M_{sp}/M_{sp,\odot}) = 2\ (R/R_{\odot}) + log(g/g_{\odot}) \tag{2.3}$$

The tool computes the mass-loss rate ($\dot{M}$) when the terminal velocity (v_{∞}) is given, since $Q = \dot{M}/(v_{\infty}\ R)^{1.5}$. Finally, the numerical results are com-

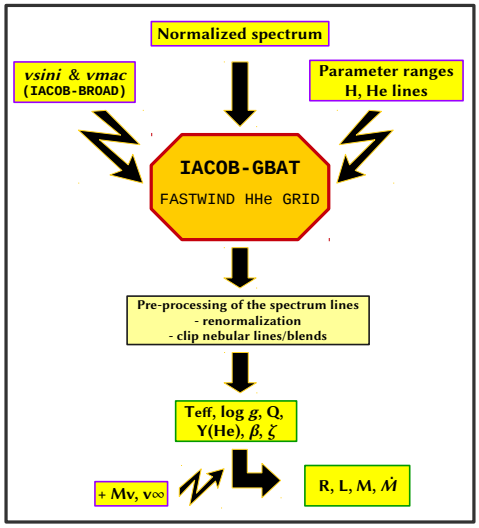

Figure 2.4: Schematic flowchart showing the use of the `iacob-gbat` tool.

plemented with a final graphical output. An example is shown in Figs. 2.2 and 2.3, where a comparison between the observed and the synthetic profiles corresponding to the best fitting model, and the χ^2 distributions for each of the considered free parameters are shown, respectively. A schematic flowchart showing the use of `iacob-gbat` is shown in Fig. 2.4.

2.2.3 Chemical analysis

The chemical analysis carried out in this thesis work (see Chapter 4) was based on equivalent widths (EW) of metal lines, similar to the method used in Orion by Simón-Díaz (2010). We used own IDL routines to identify metal lines in the observed spectra, and to measure the EWs and their uncertainties. For each line, a multi-Gaussian fit of the observed line profile is done in a spectral range of $\lambda_o \pm 2$ max[v sin i λ_o/c, 0.5λ_o/R] around the laboratory wavelength of the

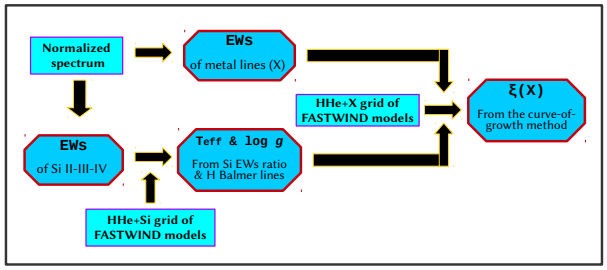

Figure 2.5: Schematic flowchart showing the abundance determination process.

line. The uncertainty is obtained by assuming the continuum at $\pm(\mathrm{S/N})^{-1}$, and comparing the value obtained by means of the Gaussian fitting with the value derived by integrating the line profile.

First, both effective temperature ($T_{\rm eff}$) and surface gravity ($\log g$) are determined by comparing the EW ratio of Si II–III or Si III–IV (depending on the effective temperature of the star) and the wings of the H Balmer lines with FASTWIND stellar atmosphere models. We first used the silicon line ratio to obtain the initial values of $T_{\rm eff}$ for different $\log g$. Then, the models obtained with the different pairs of ($T_{\rm eff}$, $\log g$) were compared with the wings of the observed H Balmer lines to obtain iteratively the final values for both parameters.

Finally, we applied the curve-of-growth method to derive metal abundances (X), considering a grid of HHe+X FASTWIND models for a set of stellar parameters ($T_{\rm eff}$ and $\log g$). For each star, the abundance is obtained for different values of microturbulence and for each line considered. Then, we determined the final abundance value considering the microturbulence that, for all lines, gives a similar value. A schematic flowchart of the abundance determination process is presented in Fig 2.5. More details can be found in Chapter 4 and other articles such as Kilian (1992) or Simón-Díaz (2010).

2.3 Bayesian inference for *Gaia* distances

The recent second data release (DR2) from the *Gaia* satellite (Gaia Collaboration et al. 2016, 2018) has provided unprecedented high-quality astrometry for more than 1.3 billion objects of our Galaxy, all with measured parallaxes. Parallax uncertainties are around 0.04 mas for bright sources ($G < 14$ mag),

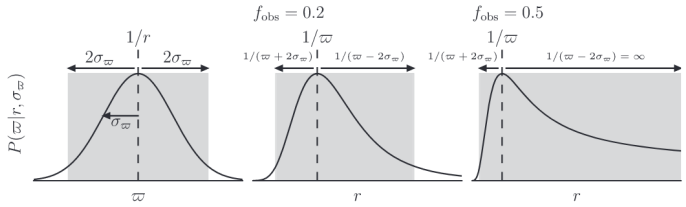

Figure 2.6: (Adopted from Astraatmadja & Bailer-Jones (2016)). Probability $P(\bar{\omega}|r, \sigma_{\bar{\omega}})$ as a function of $\bar{\omega}$ (left), as a function of r for a star with an observed fractional parallax error $f_{obs} = \sigma_{\bar{\omega}}/\bar{\omega} = 0.2$ (middle), and as a function of r but for a star with an observed fractional parallax error $f_{obs} = 0.5$ (right).

around 0.1 mas for sources with a G magnitude ∼17, and around 0.7 mas for the faintest ($G \sim 20$ mag). For Milky Way massive stars (and OB associations) it implies an important revolution. Until now, the large uncertainties in their distances have hindered the comparison with theories of stellar and cluster evolution. Distances are needed to place the stars in the Hertzsprung–Russell diagram (HRD), obtaining a better comparison of stellar masses and radii derived from the spectroscopic analyses and the evolutionary codes (a persistent problem in the field of massive stars, see Herrero et al. 1992; Repolust et al. 2004; Massey et al. 2012; Markova & Puls 2015).

A common practice to estimate distances from parallaxes is to calculate the inverse of the parallax, giving the uncertainty from a first order Taylor expansion. However, this method is only valid when we do not have measurement errors, i.e., in the absence of noise (see Bailer-Jones 2015). This is not the case of *Gaia* astrometry, where parallax uncertainties are derived from the formal errors computed in the astrometric processing (Lindegren et al. 2018). Then, a Bayesian inference process is critical when using parallaxes because of the non-linearity of the transformation between these quantities and the asymmetry of the resulting probability distribution. Assuming a Gaussian noise model for a measure *Gaia* parallax ($\bar{\omega}$), its distribution can be considered to have been drawn from a Gaussian with mean $1/r$ and standard deviation $\sigma_{\bar{\omega}}$:

$$P(\bar{\omega}|r, \sigma_{\bar{\omega}}) = \frac{1}{\sqrt{2\pi}\sigma_{\bar{\omega}}} exp\left(-\frac{1}{2\sigma_{\bar{\omega}}^2}\left(\bar{\omega} - \frac{1}{r}\right)^2\right),\ \sigma_{\bar{\omega}} \geq 0 \tag{2.4}$$

This function is the measurement model (or likelihood), and provides the

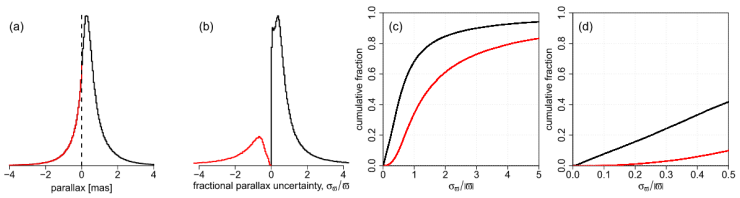

Figure 2.7: (Adopted from Bailer-Jones et al. (2018)). The distribution of parallaxes in *Gaia* DR2 is shown in panel (a). The distribution of fractional parallax uncertainties, f, is shown in panel (b). Linear scales are used on both axes of the histograms. Panel (c) shows the cumulative distribution for the positive parallaxes (black/upper line) and the negative parallaxes (red/lower line). Panel (d) is a zoom of (c).

probability density function for any $\bar{\omega}$, given values of r and $\sigma_{\bar{\omega}}$. Figure 2.6 shows that although the distribution is symmetric in $\bar{\omega}$, it is not in r, being skewed even for small fractional parallax errors (e.g., $f = \sigma_{\bar{\omega}}/\bar{\omega} = 0.2$). If f is even larger, the upper distance limit becomes undefined, losing the probability. Therefore, some finite amount of probability in the likelihood function corresponds to an undefined distance. Because the likelihood does not go to zero even at infinite distance, the confidence intervals could extend to infinity even for finite parallax errors, giving meaningless results. For these skewed distributions it is not obvious that the mode is even a good summary (see below and Bailer-Jones 2015, for further discussion). However, the main problem to use the inverse of the parallax as a distance estimator is that can not be used for negative parallaxes. On the contrary, Equation 2.4 can lead to negative parallaxes, increasing the probability with f and the distance. They are valid measurements that actually provide very useful information, for example, that a star is too distant and/or has a large measurement error. Therefore, they must not be discarded.

The distribution of the *Gaia* DR2 parallaxes and precisions are shown in Fig. 2.7, from Bailer-Jones et al. (2018). We realize that ∼25 % of the sources have negative parallaxes and that only a ∼15% of those with positive parallax have $f < 0.2$. The loss of these negative and/or low S/N parallaxes implies the loss of the relatively distant and faint sources. Therefore, estimating distances from *Gaia* parallaxes must then be treated as an inference problem.

We aim to obtain the probability distribution over the possible distance values, i.e., $P(r|\bar{\omega}, \sigma_{\bar{\omega}})$. The Bayes theorem relates it to the likelihood by

$$P(r|\bar{\omega}, \sigma_{\bar{\omega}}) = \frac{1}{Z} P(\bar{\omega}|r, \sigma_{\bar{\omega}}) P(r) \tag{2.5}$$

where the normalization constant Z is defined as

$$Z = \int_{r=0}^{r=\infty} dr P(\bar{\omega}|r, \sigma_{\bar{\omega}}) P(r) \tag{2.6}$$

and $P(r)$ is the prior, which expresses our knowledge about the distance distribution and is independent of the observed $\bar{\omega}$. Thus, we can only infer the distance if we adopt a prior. It should include any relevant information we have of the expected distance distribution that is not contained in the likelihood. One obvious example is the positivity of distance, but also might be our current knowledge of the Galaxy or even other distance-sensitive measurements. The advantage of the probabilistic approach is that it combines the measurement (likelihood) and assumptions (priors) in a consistent way that makes the former irrelevant when the data are good, but ensures a good transition to dominance by the prior as the quality of the data degrades. We should highlight that we do not have access to the *true* parallax, but to the *observed* parallax. This is actually an important fact, since the mode $(1/\bar{\omega})$ is a very noisy estimator once $f_{true} < 0.22$ and could not coincide with the true value of r (Bailer-Jones 2015). Only a proper prior adoption can resolve this problem (see Bailer-Jones 2015; Astraatmadja & Bailer-Jones 2016, for an exhaustive investigation of using different types of priors). This shows again the possible consequences of using the inverse of the parallax for estimating distances, and points up the importance of a proper prior adoption.

In Chapter 5 an inference approach has been used through the affine-invariant Markov Chain Monte Carlo (MCMC) ensemble sampler (Goodman & Weare 2010) *emcee*, designed for Bayesian parameter estimation and that can be used to estimate the parameters of a straight line model in data with Gaussian noise (Foreman-Mackey et al. 2013). MCMC is a procedure for generating a random walk in the parameter space that, over time, draws a representative set of samples from the distribution. In order to more efficiently sample the parameter space, *emcee* runs in parallel many samplers (called walkers). The walkers 'walk' around the parameter space exploring the posterior distribution, so that the value of the latter in a given region is characterised by the density of walkers in that region. Faster convergence is attained when the walkers are initialised near regions of high likelihood but they will explore the entire space regardless of their initial positions. More information about the code, algorithm and use of *emcee* could be found in its webpage[2].

[2] http://dfm.io/emcee/current/

3

New massive members of Cygnus OB2

In this first paper we conducted a dedicated study, using new intermediate resolution (R $\sim$ 5000) spectra for a sample of OB-type candidates in the Cygnus OB2 region. We performed a spectral classification using He I-II and metal lines rates, as well as the Marxist Ghost Buster (MGB) software for O-type stars and the IACOB standards catalog for B-type stars. The confirmation of 42 new OB massive stars (earlier than B3) in the region allows us to increase the young massive population known in the field, although we concluded that many O and early B stars at $B > 16$ mag are still undiscovered. We placed all of them in a Hertzsprung-Russell Diagram using calibrations for $T_{\rm eff}$ and luminosity confirming the correlation between age and Galactic longitude previously suggested in the region.

A&A 612, A50 (2018)
https://doi.org/10.1051/0004-6361/201731856

Astronomy & Astrophysics

New massive members of Cygnus OB2

S. R. Berlanas[1,2], A. Herrero[1,2], F. Comerón[3], A. Pasquali[4], C. Bertelli Motta[4], and A. Sota[5]

[1] Instituto de Astrofísica de Canarias, 38200 La Laguna, Tenerife, Spain
e-mail: srberlan@iac.es
[2] Departamento de Astrofísica, Universidad de La Laguna, 38205 La Laguna, Tenerife, Spain
[3] ESO, Karl-Schwarzschild-Strasse 2, 85748 Garching bei München, Germany
[4] Astronomisches Rechen-Institut, Zentrum für Astronomie der Universität Heidelberg, Mönchhofstr 12-14, 69120 Heidelberg, Germany
[5] Instituto de Astrofísica de Andalucía-CSIC, 18008 Granada, Spain

Received 29 August 2017 / Accepted 11 November 2017

ABSTRACT

Context. The Cygnus complex is one of the most powerful star forming regions at a close distance from the Sun (~1.4 kpc). Its richest OB association Cygnus OB2 is known to harbor many tens of O-type stars and hundreds of B-type stars, providing a large homogeneous population of OB stars that can be analyzed. Many studies of its massive population have been developed in the last decades, although the total number of OB stars is still incomplete.
Aims. Our aim is to increase the sample of O and B members of Cygnus OB2 and its surroundings by spectroscopically classifying 61 candidates as possible OB-type members of Cygnus OB2, using new intermediate resolution spectroscopy.
Methods. We have obtained intermediate resolution (R ~ 5000) spectra for all of the OB-type candidates between 2013 and 2017. We thus performed a spectral classification of the sample using HeI-II and metal lines rates, as well as the Marxist Ghost Buster (MGB) software for O-type stars and the IACOB standards catalog for B-type stars.
Results. From the whole sample of 61 candidates, we have classified 42 stars as new massive OB-type stars, earlier than B3, in Cygnus OB2 and surroundings, including 11 O-type stars. The other candidates are discarded as they display later spectral types inconsistent with membership in the association. We have also obtained visual extinctions for all the new confirmed massive OB members, placing them in a Hertzsprung-Russell Diagram using calibrations for $T_{\rm eff}$ and luminosity. Finally, we have studied the age and extinction distribution of our sample within the region.
Conclusions. We have obtained new blue intermediate-resolution spectra suitable for spectral classification of 61 OB candidates in Cygnus OB2 and surroundings. The confirmation of 42 new OB massive stars (earlier than B3) in the region allows us to increase the young massive population known in the field. We have also confirmed the correlation between age and Galactic longitude previously found in the region. We conclude that many O and early B stars at $B > 16$ mag are still undiscovered in Cygnus.

Key words. stars: early-type – stars: massive – open clusters and associations: individual: Cygnus OB2 – Hertzsprung-Russell and C-M diagrams – Galaxy: stellar content

1. Introduction

The Cygnus region is the most powerful nearby stellar complex, conspicuous at all wavelengths and very young, with several rich OB associations, numerous young open clusters and tens of compact H II and star formation regions in the field. Hosting the largest number of nearby massive stars and an intense star forming activity (Reipurth & Schneider 2008), it provides an updated view of the high-mass stellar population in one of the largest groups of young stars in our Galaxy. It is an ideal place to study the process of massive star formation and evolution, individually and in stellar groups, and their interaction with the surroundings.

Its association Cygnus OB2 (d ~ 1.4 kpc; Rygl et al. 2012) has received a lot of attention and has been studied at all wavelengths with different spatial coverage since it hosts a high number of early spectral type stars (Walborn et al. 2002). First studies were carried out by Morgan et al. (1954), Schulte (1956, 1958) and Reddish (1968), but it was Massey & Thompson (1991) who developed an extensive survey of the massive population in the association, identifying 120 possible massive star members, 70 of which were classified as OB stars (42 O-type stars). Knödlseder (2000) proposed that this number should be much larger, around 100 O-type stars. In the last few decades, many other studies were carried out in the region updating continually this number (Comerón et al. 2002, 2008; Hanson 2003; Kiminki et al. 2007; Negueruela et al. 2008; Comerón & Pasquali 2012). These surveys have allowed the global study of the massive population in the region, using photometry to place the stars in a Hertzsprung-Russell diagram (HRD) from which the star formation history and mass function of the association were assessed (Wright et al. 2015). In spite of the many photometric and spectroscopic surveys carried out in the region, only a small homogeneous group of early type stars have been spectroscopically analyzed (Herrero et al. 1999, 2002; Negueruela et al. 2008), and few stars have been observed in the UV range (Herrero et al. 2001). There is still a large number of stars that should be explored. The optical extinction of the region is high (A_V = 4.0–7.0 mag; Wright et al. 2015), but not so much as to prevent obtaining spectra of its most massive stars for a rough spectral classification. Therefore, new spectroscopy to search for previously undiscovered massive stars is mandatory to complete the last census of massive O and B-type stars in the association.

A&A 612, A50 (2018)

Table 1. Telescopes, instruments and settings used in this work.

Instrument and grating	Telescope	Resol.	Date	Stars
ISIS – 600B	ORM-WHT	2500	Oct. 2013	1
WYFFOS – H2400B	ORM-WHT	5000	Jul. 2014	7
ISIS – H2400	ORM-WHT	7500	Jul. 2015	2
OSIRIS – R2500U/V	ORM-GTC	2500	May 2016	2
IDS – R1200B	ORM-INT	5000	Jul. 2016	47
ISIS – R1200B	ORM-WHT	5000	Apr. 2017	2

One of the most complete spectroscopic surveys in the Cygnus region was developed by Comerón & Pasquali (2012). They performed spectral classification of a magnitude-limited sample ($B \leq 16$ mag and $Ks < 9$ mag) selected with a homogeneous photometric criterion over a large area that includes Cygnus OB2 and its surroundings, providing a large sample of known and new OB stars, as well as a list of 61 OB candidates for which no spectral data is available and that are pending spectroscopic confirmation.

The main goal of this work is to complete the spectral classification of this latter sample, aiming a later determination of the stellar parameters. Thus, we have obtained intermediate-resolution spectra of all the list candidates, in order to confirm or reject them as true massive OB-type stars. In Sect. 2 we present the observations. In Sect. 3 we describe the spectral classification criteria used in this work, and in Sect. 4 visual extinctions and stellar parameters derived for the new OB-type members. The results are discussed in Sect. 5 where we show the HRD of the region and the age distribution found across Galactic longitude. Finally, we summarize our conclusions in Sect. 6.

2. Observations and data reduction

The study developed by Comerón & Pasquali (2012) produced a sample of O and early B stars (in a $6° \times 4°$ region centered on Galactic coordinates $l = 79.8°$ and $b = +0.8°$ of Cygnus OB2) which were identified using two homogeneous reddening-free criteria

$$Q_{BJK} = 0.196(B-J) - 0.981(J-K) - 0.098 > 0 \quad (1)$$
$$Q_{JHK} = 0.447(J-H) - 0.894(H-K) - 0.089 < 0 \quad (2)$$

which allowed them to classify 60 new OB stars and produce a list of 61 candidates pending spectroscopic data. They used $BJHK$ photometry tabulated in the USNO-B (Zacharias et al. 2010, 2004) and 2MASS all-sky (Skrutskie et al. 2006) catalogs setting limiting magnitudes of $B \leq 16$ mag and $Ks < 9.0$ mag. By combining these two magnitude cuts with the $(B-K)$ colors of OB stars, Comerón & Pasquali (2012) set up a selection method sensitive to main-sequence stars earlier than B1 and obscured by $A_V < 6.7$ mag.

We have obtained new spectra for all the proposed OB candidates, whose location is shown in Fig. 1. The sample has been observed in five different runs between 2013 and 2017. For an accurate spectral classification of OB-type stars we need blue spectra (4000–5000 Å) where the diagnostic He I-II and metal lines are located.

The bulk of stars were observed in July 2016, obtaining spectra of 47 candidates. We have chosen the R1200B grating of IDS (EEV10) on the *Isaac Newton* Telescope (INT) in La Palma, which provides a resolution of ~5000 at 4500 Å. The remaining stars were observed in different runs between 2013 and 2017, at the *William Herschel* Telescope (WHT) using the AF2/WYFFOS and ISIS instruments, and at the Gran Telescopio CANARIAS (GTC) using the OSIRIS instrument. Out of the whole sample, three of the stars (J20301097+4120088, J20315433+4010067, J20345785+4143543) belong to the Galactic O-Star Spectroscopic Survey (GOSSS) catalog (Maíz Apellániz et al. 2016).

The information on the different runs carried out in this work is shown in Table 1. The final spectra were reduced using the IRAF procedures, with standard routines for bias and flat-field subtraction and also for the wavelength calibration.

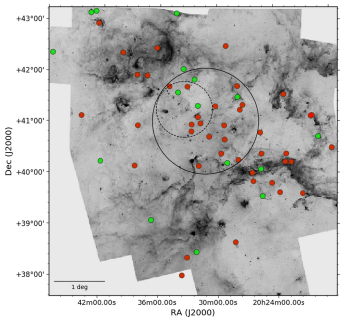

Fig. 1. Inverse *Spitzer* 8 μm image of the Cygnus region showing the location of the 61 OB candidates. The 42 confirmed massive OB-type stars earlier than B3 are indicated with red dots. The remaining stars are late B and foreground A-F-G stars which are indicated with green dots. The solid line circle delimits the 1 deg radius area of Cygnus OB2 adopted by Comerón & Pasquali (2012). For reference, the dash-dotted line circle shows the area considered by Wright et al. (2015).

3. Spectral classification

The accuracy of the spectral classification depends on the effects of spectral resolution as well as the signal-to-noise ratio (S/N). The main diagnostic method for O-type stars is the comparison of He II 4542/He I 4471 ratio (Sota et al. 2011). These lines are similar for a O7 type star. For later O types the relative strengths of He II 4542/He I 4387 and He II 4200/He I 4144 are normally used, and represent the main criteria for types O8-B0. Spectral types earlier than O8 were classified using the criteria described by Gray & Corbally (2009). The presence of metal lines in different ionization stage, such as Si III or Mg II, indicates early B-type stars. The relative strength of HeII 4471/MgII 4481 is a useful indicator for B1-late B stars. As secondary indicators we used the criteria described by Gray & Corbally (2009), which were also used to classify stars of spectral types A, F and G.

Regarding the luminosity class, the criteria used for early O-type stars were introduced by Walborn (1971, 1973), taking into account the emission effects in the He II 4686 line and N III 4634-4640-4642. For late O-type stars, we have used the criteria described by Sota et al. (2011) and for B-type stars the

Table 2. Basic data of the confirmed massive new members (earlier than B3).

Object	RA (hhmmss)	Dec (° ′ ″)	Region	*B*	*Ks*	*J*	SpT	Binary star
J20423509+4256364	20 42 35.08	+42 56 36.43	*c*	14.480	8.304	9.211	O6IIIz	
J20371773+4156316	20 37 17.73	+41 56 31.57	*c*	15.760	8.041	9.071	O7V	
J20345785+4143543	20 34 57.84	+41 43 54.25	*a*	15.430	7.417	8.447	O7:Ib	
J20293563+4024315	20 29 35.63	+40 24 31.45	*b*	12.468	8.268	8.831	O8IIIz	
J20222481+4013426	20 22 24.81	+40 13 42.55	*c*	13.620	8.410	9.034	O8II	
J20261976+3951425	20 26 19.75	+39 51 42.46	*c*	15.600	8.348	9.351	O8.5IV	
J20275292+4144067	20 27 52.92	+41 44 06.65	*b*	13.330	7.277	8.144	O9.5II	
J20262484+4001413	20 26 24.84	+40 01 41.25	*c*	13.290	8.330	9.021	O9.2III	
J20291617+4057372	20 29 16.17	+40 57 37.19	*b*	15.030	7.899	8.855	O9.7III	
J20382173+4157069	20 38 21.72	+41 57 06.89	*c*	15.810	7.682	8.760	O9.7II	
J20181090+4029063	20 18 10.89	+40 29 06.29	*c*	14.940	8.399	9.343	O9.7Ib	yes*
J20273787+4115468	20 27 37.87	+41 15 46.79	*b*	14.570	8.263	9.146	B0II	
J20301097+4120088	20 30 10.97	+41 20 08.82	*b*	15.690	8.882	9.855	B0:II:	
J20323968+4050418	20 32 39.68	+40 50 41.83	*a*	14.410	8.913	9.631	B0II	
J20395358+4222506	20 39 53.58	+42 22 50.62	*c*	15.890	5.822	7.345	B0I	yes*
J20281176+3840227	20 28 11.75	+38 40 22.73	*c*	11.805	7.944	8.349	B0Ib	
J20323882+4058469	20 32 38.82	+40 58 46.85	*a*	15.430	8.821	9.701	B0Ib	
J20225451+4023314	20 22 54.50	+40 23 31.39	*c*	13.107	8.601	9.175	B0Iab	
J20253320+4048444	20 25 33.19	+40 48 44.38	*c*	13.112	7.648	8.340	B0Iab	
J20272099+4121262	20 27 20.99	+41 21 26.15	*b*	13.830	8.730	9.448	B0.5V	yes
HDE229258	20 24 25.51	+39 49 28.30	*c*	10.235	8.689	8.833	B0.7V	
J20330526+4143367	20 33 05.26	+41 43 36.74	*a*	13.940	8.634	9.286	B0.5III	
J20361806+4228483	20 36 18.06	+42 28 48.30	*c*	15.650	8.855	9.814	B0.7III	
J20233816+3938118	20 23 38.16	+39 38 11.84	*c*	11.293	8.731	8.996	B0.7Ib	
HD 228973	20 20 07.35	+41 07 46.72	*c*	10.34	7.684	7.922	B1V	yes
J20201435+4107155	20 20 14.34	+41 07 15.45	*c*	12.412	8.240	8.627	B1V	
J20230290+4133466	20 23 02.90	+41 33 46.59	*c*	14.780	7.809	8.762	B1V	
BD+404193	20 29 13.55	+40 41 03.38	*b*	10.412	8.812	8.945	B1V	
BD+404208	20 30 49.97	+40 44 18.53	*b*	10.654	8.664	8.869	B1V	
J20314341+4100021	20 31 43.40	+41 00 02.07	*a*	15.940	8.957	9.885	B1V	yes*
J20315898+4107314	20 31 58.98	+41 07 31.41	*a*	15.490	8.832	9.773	B1V	yes*
J20330453+3822269	20 33 04.53	+38 22 26.91	*c*	11.383	8.790	9.021	B1V	
J20230183+4014029	20 23 01.83	+40 14 02.90	*c*	13.465	8.060	8.579	B1III	
J20274925+4017004	20 27 49.25	+40 17 00.42	*b*	13.460	8.104	8.713	B1III	
J20315433+4010067	20 31 54.33	+40 10 06.71	*b*	15.990	8.884	9.742	B1III	
J20382889+4009566	20 38 28.88	+40 09 56.63	*c*	9.996	8.816	8.896	B1III	
J20440752+4107342	20 44 07.51	+41 07 34.18	*c*	15.470	8.703	9.562	B1III	
LSII+3797	20 33 35.52	+38 01 36.73	*c*	11.838	5.900	6.691	B1Ia	yes*
J20211924+3936230	20 21 19.24	+39 36 22.98	*c*	12.732	7.886	8.488	B1Ib	yes*
BD+394179	20 25 27.28	+40 24 00.15	*c*	11.066	6.667	7.210	B1Ib	
J20290247+4231159	20 29 02.46	+42 31 15.91	*c*	13.330	8.426	9.090	B1Ib	yes*
J20381289+4057169	20 38 12.88	+40 57 16.86	*c*	12.870	8.675	9.183	B2V	

Notes. *B* magnitudes from the USNO-B catalog. *Ks* and *J* magnitudes from 2MASS catalog. Region *a* indicates the 1 deg. circular area centered on Cyg OB2#8 trapezium adopted by Wright et al. (2015) for the Cygnus OB2 association. Region *b* indicates the 1 deg. radius area adopted by Comerón & Pasquali (2012) for the same Cygnus OB2 association. Region *c* indicates the surrounding area outside the 1 deg. radius adopted by Comerón & Pasquali (2012). For binary stars asterisks indicate possible SB2 stars, whose spectral types are refered to the primary component.

criteria described by Gray & Corbally (2009) and the Balmer lines width.

Although the classification for O-type stars was based on the described He and metal lines diagnostic criteria, we have also used for O-type stars the Marxist Ghost Buster (MGB) code developed by Maíz Apellániz et al. (2012) in order to obtain a more accurate result. This tool compares the observed spectra with a grid of O standards (in this work the GOSSS library), allowing us to vary spectral type, luminosity class, velocity and resolution until obtaining a best match. Furthermore, for B-type stars we have used a sample of IACOB standards (Simón-Díaz et al. 2015) to improve their classification.

4. New confirmed OB type stars

The observed spectra have high enough S/N and resolution for a spectral classification of the stars. All the candidate spectra are plotted in Fig. B.1 where the main diagnostic lines used are also indicated.

A&A 612, A50 (2018)

Table 3. Candidates classified as late B and A-F-G type stars.

Object	RA (hhmmss)	Dec (° ′ ″)
late B-type stars		
CCDMJ20323+4152AB	20 32 20.81	+41 52 00.78
BD+423785a	20 34 15.39	+43 09 35.28
A-type stars		
J20252497+3934030	20 25 24.96	+39 34 03.02
J20285874+4013302	20 28 58.74	+40 13 30.22
J20315984+4120354	20 31 59.84	+41 20 35.41
J20320734+3828586	20 32 07.34	+38 28 58.62
BD+413801	20 33 30.39	+42 04 17.35
J20364336+3906145	20 36 43.36	+39 06 14.53
CCDM J20429+4311AB	20 42 54.24	+43 10 38.71
F-type stars		
J20193232+4042447	20 19 32.32	+40 42 44.72
J20253116+4005508	20 25 31.16	+40 05 50.82
J20275204+4131200	20 27 52.03	+41 31 19.98
CCDM J20420+4015	20 42 01.18	+40 14 42.70
J20500396+4300118	20 50 03.96	+43 00 11.76
J20504551+421012.6	20 50 45.51	+42 10 12.64
G-type stars		
J20300022+4337553	20 30 00.21	+43 37 55.29
J20340430+4136507	20 34 04.29	+41 36 50.67
J20432737+4308525	20 43 27.37	+43 08 52.47
J20472235+4220523	20 47 22.34	+42 20 52.30

Out of the 61 candidates 42 are OB type stars, earlier than B3, including 11 O-type stars. Two more are late B-type stars. The location of these new confirmed OB stars is shown in Fig. 1 while their names, coordinates, magnitudes and the derived spectral classification are listed in Table 2. We have also included the region in which they are located: (a) the Cygnus OB2 area considered by Wright et al. (2015) which is the youngest core of Cyg OB2 at present; (b) the Cygnus OB2 area considered by Comerón & Pasquali (2012) which is the extended Cyg OB2 area containing older stars, on average, and (c) the surrounding area which includes part of the Cygnus OB9 association and field population. The remaining observed stars are late B and foreground A-F-G stars, which are globally listed in Table 3. The selection criteria success rate obtained by Comerón & Pasquali (2012) along with the number of the confirmed OB type obtained in this work (72%), support the success at identifying reddened massive OB stars with this method.

We have also detected nine possible or confirmed SB2 binaries in the sample of new OB stars (see Table 2). In some cases, indicated with asterisks, we can only suggest possible binary nature mainly due to noisy spectra. This number represents a 21% of our massive OB sample. We assign to these stars the spectral classification of their primary component. An example is shown in Fig. 2. Sana & Evans (2011) found that at least 45 – 55% of the O star population in clusters and OB associations is comprized of spectroscopic binaries, which indicates that it is highly likely that more binaries are undetected in our sample.

4.1. Extinction

We used the $(J - Ks)$ colors and the recent extinction law derived by Wright et al. (2015) (R_V = 2.91) to obtain individual extinctions for all the new confirmed massive OB type stars

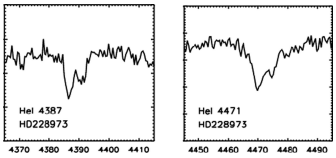

Fig. 2. Example of SB2 detection: HeI lines in star HD 228973.

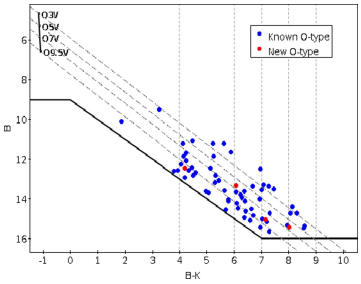

Fig. 3. $(B - K)$, B diagram of the confirmed O-type stars in Cygnus OB2 within the 1 deg. radius area adopted by Comerón & Pasquali (2012). Blue dots indicate stars previously known, and red dots represent the new ones confirmed in this work. The upper left vertical line shows the position of the unreddened main sequence based on intrinsic magnitudes from Martins & Plez (2006) at a distance modulus DM = 10.8 mag. The dash-dotted lines represent the locus expected for different spectral type stars using the reddening law of Wright et al. (2015) with R_V = 2.91. The solid line marks the limits imposed by the selection criteria at magnitudes $B \leq 16$ mag, $Ks < 9$ mag. Vertical dotted lines indicate $(B - K)$ color bins.

(see Table A.1). Most of them have visual extinctions in the range A_V = 4–8 mag, which agrees with previous studies in the region (Comerón & Pasquali 2012; Wright et al. 2015). But, as in Comerón & Pasquali (2012), this is partly consequence of the imposed $B \leq 16$ and $Ks < 9$ magnitude limits.

In Fig. 3 we present the B, $(B - K)$ diagram of the confirmed O-type stars in Cygnus OB2. We observe that some of them are aligned below the O9.5V reddening vector, which could suggest a small shift in the adopted intrinsic color calibration since most of them are already known dwarf late O-type members. In spite of this we can assess the incompleteness of the O population in the region by taking into account the ratios of stars in different spectral (O3-O5, O5-O7 and O7-O9.5) and $(B - K)$ color bins.

All the stars of our sample with $(B - K)$ colors <6 mag should be bright enough to have been detected by our selection criteria. Figure 3 shows that the population is expected to be complete for $(B - K) < 7$ mag. But for $(B - K) > 7$ mag we can not see late O-type stars because they are fainter than B = 16 mag, which is the imposed magnitude limit. Assuming that the ratios of spectral types are independent of extinction, we can conclude we are loosing the fainter or more obscured O-type stars.

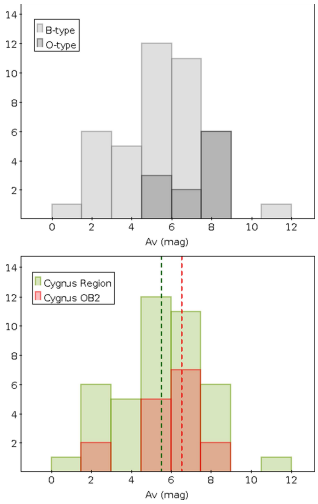

Fig. 4. *Top*: extinction distribution of the new classified OB type stars earlier than B3 in Cygnus OB2 and boundaries. Gray indicates B-type stars while dark gray are O-type stars. *Bottom*: green indicates all the confirmed stars in the Cygnus region, which includes Cyg OB2, Cyg OB9 and field. Red indicates only those new OB stars located in Cygnus OB2. Green and red dashed lines indicate the median values for the stars in the whole Cygnus region and only Cygnus OB2 respectively.

The extinction distribution for the 42 new confirmed OB stars earlier than B3 in Cygnus OB2 and boundaries is shown in Fig. 4 (top). Again, the spectral classification for those stars classified as possible or confirmed SB2 binaries is taken from the primary component. Although O-type stars are clearly more obscured, a median value of $A_V = 5.5$ mag was found for the whole sample. However, this value is also affected by completeness. O-type stars are more obscured on average because we can detect them up to higher foreground extinctions thanks to their intrinsic brightness. In the bottom histogram the same sample is differentiated by location: the whole sample that belongs to Cygnus OB2, Cygnus OB9 and boundaries, and as a sub-sample, those stars located within the Cygnus OB2 area (from Comerón & Pasquali 2012) for which a median value of $A_V = 6.5$ mag is derived.

We see an abrupt cut for $A_V \geq 9$ mag. Stars with such high visual extinctions shall be intrinsically extremely bright to be seen. An O9V star with a visual extinction of $A_V = 9$ mag will have an apparent magnitude $B \simeq 17$ mag, beyond the selection criteria limits and probably this is the reason why we do not find stars beyond this value. However, for the star J20395358+4222506 classified as B0I, we have obtained a visual extinction of 11.0 mag. It has a magnitude in the B band of 15.89 mag but in the Ks band of only 5.82 mag which indicates

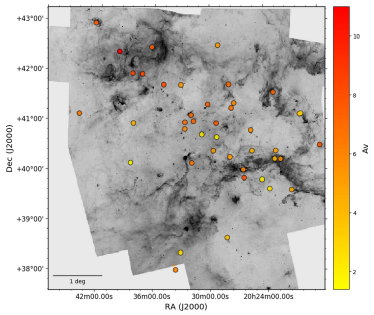

Fig. 5. Location of the new confirmed OB stars in the region colored according to the derived extinction (A_V) and over-plotted on an inverse *Spitzer* 8 μm image.

a very bright star. These cases show again that the sample does not provide a complete census. The magnitude-limited sample of Cygnus OB2 is made incomplete due to extinction.

In Fig. 5 we present the spatial location of the new classified OB stars, where each star is color-coded according to its derived visual extinction A_V. The extinction distribution varies smoothly across the region, increasing from the south-west (Cygnus OB9) to the northeast (Cygnus X-North) where the most extinguished star of our sample, J20395358+4222506, is located.

4.2. Stellar parameters

4.2.1. Effective temperature

For each classified O-type star and luminosity classes V, III and I, we have used the effective temperature ($T_{\rm eff}$) scale developed by Holgado et al. (in prep.) based on a revision of the O-type standards in the IACOB database. We have preferred it over the SpT-$T_{\rm eff}$ calibration suggested by Martins et al. (2005) since the latter gives too low $T_{\rm eff}$ values for late O-type stars (Simón-Díaz et al. 2014).

For early B-type stars and luminosity class V, we decided to use the $T_{\rm eff}$ spectral type compilation of Nieva (2013). An excellent agreement with the calibration of Holgado et al. is found. For late B-type dwarf stars we have used the calibration of Pecaut & Mamajek (2013). Regarding B stars with luminosity class I, we have used the $T_{\rm eff}$ scale of Markova & Puls (2008), and for luminosity class III we have interpolated between classes I and V. In Fig. 6 are represented the different $T_{\rm eff}$ scales adopted in this work, and the derived $T_{\rm eff}$ values for all the new OB type stars are shown in Table A.1. We see that all scales for B-types fit smoothly the Holgado et al. scale. Temperatures were also obtained for those stars classified as SB2 binaries by taking into account the primary component.

Comerón & Pasquali (2012) used the "observational" effective temperature based on the $T_{\rm eff}$ versus spectral type calibration of Martins et al. (2005). For B-type stars, they used the $T_{\rm eff}$ spectral type compilation of Tokunaga (2000) but applying a scaling factor to force the agreement with Martins et al. (2005) temperature scale. In order to be consistent with them we have

A&A 612, A50 (2018)

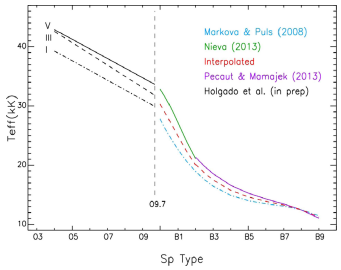

Fig. 6. $T_{\rm eff}$ scales used in this work.

recalculated temperatures for all of their known OB stars sample in the Cygnus Region using our criteria. New values are shown in Table A.2.

4.2.2. Bolometric correction and luminosity

As Comerón & Pasquali (2012), we have adopted a distance modulus of DM = 10.8 mag, and used the intrinsic magnitudes derived by Martins & Plez (2006) for O stars and those compiled by Tokunaga (2000) for B stars. Thus we could derive absolute magnitudes (see Comerón et al. 2008). To derive luminosities we adopted bolometric corrections (BCs) from Lanz & Hubeny (2003, 2007). There is an excellent agreement with Martins et al. (2005) for temperatures higher than ∼32 000 K, and also with the bolometric corrections from Nieva (2013) for cooler stars (see Nieva 2013). The derived luminosity values for the new and already known OB stars are shown in Table A.1 and Table A.2, respectively.

5. Discussion

Some of the new confirmed OB type stars (see Fig. 1) are located at the boundaries assigned to Cygnus OB2. However, the limits of the association are not strongly defined. The first surveys in the association assumed a smaller area where the most luminous members are located (Münch & Morgan 1953; Massey & Thompson 1991). Then, Knödlseder (2000) provided wider limits showing that extinction was a limiting factor in previous studies. This area was thus extended with the identification of new early-type members (Comerón et al. 2002, 2008; Comerón & Pasquali 2012; Wright et al. 2009; Wright et al. 2015). If we assume the extension of Cygnus OB2 as the area adopted by Comerón & Pasquali (2012) (1 deg. radius centered on Galactic coordinates l = 79.8° and b = +0.8°), as well as the most recent census in the area developed by Wright et al. (2015), we can now update the census of O and B-type stars in Cygnus OB2 from 204 to 221, and the number of confirmed O-type members increases from 66 to 70 stars.

5.1. Hertzsprung-Russell diagram

Some studies about the age of Cygnus OB2 have been developed in the last two decades (Massey et al. 2001; Hanson 2003; Drew et al. 2008; Negueruela et al. 2008; Wright et al. 2010; Comerón & Pasquali 2012; Comerón et al. 2016). However, different evolutionary stellar models were used. We decided to explore four different stellar models (two families with two initial rotational velocities) to construct the HRD in order to assess uncertainties on the age distribution.

We have placed the new confirmed OB stars in the HRD to study the evolutionary status of the association. For this aim we have considered the stars within the area adopted by Comerón & Pasquali (2012). We have also added the already known OB stars compiled in their work to complete the sample. Two of them, classified as B0 stars (J20325964+4115146 and J20333700+4116113) were recently reclassified as O9.7III and O9.5IV by Maíz Apellániz et al. (2016). We thus decided to assume this last classification for both. We have used the Geneva evolutionary tracks and isochrones with and without rotation as calculated by Ekström et al. (2012) (Fig. 7, top), and for comparison, the Bonn evolutionary tracks and isochrones with and without rotation as calculated by Brott et al. (2011) (Fig. 7, bottom).

In the Geneva case, we found a difference up to ∼2 Myr in the stellar ages for those most massive members (≥20 $M_{\odot}$) depending on whether we consider rotation or not. Larger stellar lifetimes are derived from rotating stellar models. A similar result was found by Wright et al. (2015) by comparing both non-rotating and rotating Geneva stellar models. They derived an age range of 1–7 Myr for the association, but the results from rotating stellar models suggested an age of 4–5 Myr, while non-rotating models hinted at a younger age (∼2–3 Myr). On the contrary, the Bonn stellar models included on this work do not exhibit a large difference in the estimated age of the stars when they include or not stellar rotation. This different behavior is most likely to be ascribed to their different treatment of rotation. Thus, the positions of the isochrones in both Bonn HR diagrams are very similar. Moreover, in the Bonn case we see an extended terminal age main sequence (TAMS), and therefore, all the OB stars are located on the main sequence (MS). In spite of this, all models suggest that most of the stars are in the age range of 1–6 Myr, indicating a continuous (but not necessarily constant) star formation activity. However, a combination of different scenarios (rotating and non-rotating stellar models) would help to narrow the possible ages. Slow rotators with initial masses of 30 $M_{\odot}$ or less would give similar ages as more massive stars born with larger rotational velocities.

In view of the results, we can conclude that uncertainties due to rotation and adopted models affect mainly the most massive members, suggesting larger ages of about 1–2 Myr for them. This makes the age determination very uncertain and strengthens the need for additional diagnostics, in particular individual rotation velocity measurements, to better constrain them.

5.2. Age distribution across Galactic longitude

Comerón & Pasquali (2012) studied the correlation between ages and Galactic longitudes in Cygnus OB2. They suggest that star formation has proceeded from lower to higher Galactic longitudes, finding most of the old stars located at low Galactic longitudes while the youngest ones lie at higher Galactic longitudes. In order to corroborate it, we have obtained ages by comparing isochrones from the HRDs, and divided the sample of OB stars in three age groups: the young group contains stars in the range of 0–5 Myr, the intermediate group contains stars in the range of 5–10 Myr, and the old one contains stars with ages >10 Myr.

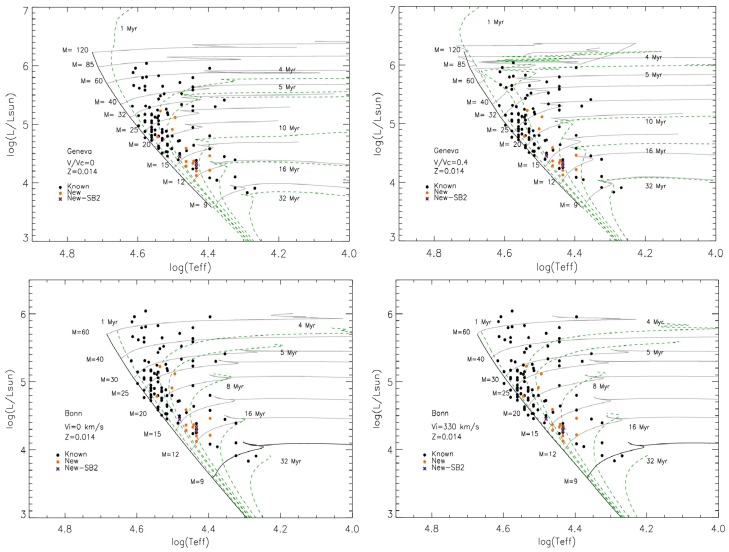

Fig. 7. HR diagrams of OB stars in Cygnus OB2 assuming a DM = 10.8 mag. Known OB stars from Comerón & Pasquali (2012) are also included to complete the sample. Black and orange dots indicate the already known and new OB-type stars respectively. Blue crosses indicate those new stars classified as possible SB2 stars. *Top left hand panel*: isochrones (dotted lines) and evolutionary stellar tracks (solid lines) for non-rotating models from Ekström et al. (2012). *Top right hand panel*: isochrones (dotted lines) and evolutionary stellar tracks (solid lines) for rotating models (V/V_c = 0.4) from Ekström et al. (2012) . *Bottom left hand panel*: isochrones (dotted lines) and evolutionary stellar tracks (solid lines) for non-rotating models from Brott et al. (2011). *Bottom right hand panel*: isochrones (dotted lines) and evolutionary stellar tracks (solid lines) for rotating models (V_i = 330 km s^{-1}) from Brott et al. (2011).

Figures 8 and 9 show the histograms of the relative frequency of our OB type sample located at low (78.5°–79.5°), central (79.5°–80.5°) and high (80.5°–81.5°) Galactic longitudes in each age group and for each model considered (Geneva (Fig. 8) and Bonn (Fig. 9) rotating and non-rotating models). In all cases, most of the stars at high Galactic longitudes belong to the young-intermediate age group, while those stars located at low Galactic longitudes belong to the old age group. We only obtain significant age differences at using the rotating Geneva models since in this case rotation gives older ages for the most massive stars. Thus, we can see a change in the relative frequencies of old and intermediate stars. On the other hand, we do not see these age differences at using rotating Bonn models because of their lower sensitivity to rotation as noted earlier.

This analysis thus supports the correlation between ages and Galactic longitudes in Cygnus OB2 as previously suggested by Comerón & Pasquali (2012). Massive star formation in Cygnus OB2 seems to have proceeded from lower to higher Galactic longitudes, regardless of the details of the models used.

5.3. The whole Cygnus region

In order to obtain a big picture of the age distribution across the Galactic longitude, we have performed the same analysis as in Cygnus OB2 but now in a wider area which includes Cygnus OB2, Cygnus OB9 and boundaries. We have placed the whole sample of OB stars, including late B-type stars, in an HRD (see Fig. 10). Due to the similar results obtained in Cygnus OB2 by using different models, we have now used isochrones and evolutionary stellar tracks for non-rotating models from Ekström et al. (2012). We derived ages by comparison with isochrones and divided again the sample in three age groups: the young group (0–5 Myr), the intermediate group (5–10 Myr), and the old group (>10 Myr). In Fig. 11 we show the spatial distribution of the different age groups, where most of the younger stars (left) are concentrated at higher Galactic longitudes, while the older ones (right) are located at central-lower Galactic longitudes. These results suggest that massive star formation has proceeded from lower to higher Galactic longitudes,

A&A 612, A50 (2018)

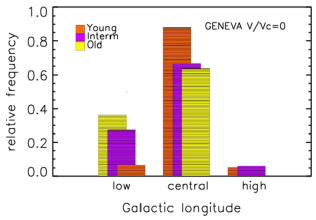

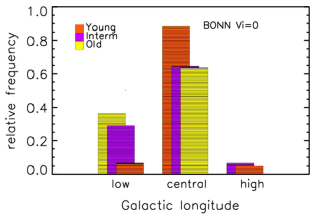

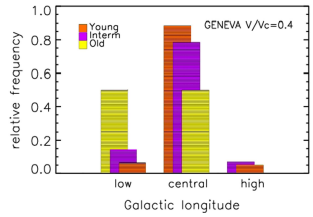

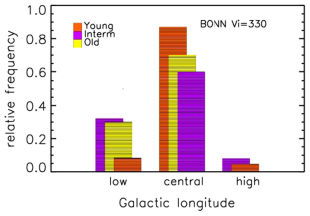

Fig. 8. Relative frequency histograms of the stars located at low (78.5°–79.5°), central (79.5°–80.5°) and high (80.5°–81.5°) Galactic longitudes in Cygnus OB2 using Geneva non-rotating (*top*) and rotating (*bottom*) models. Orange, purple and yellow colors indicate those stars located in the young (0–5 Myr), intermediate (5–10 Myr) and old (>10 Myr) age groups.

Fig. 9. Relative frequency histograms of the stars located at low (78.5°–79.5°), central (79.5°–80.5°) and high (80.5°–81.5°) Galactic longitudes in Cygnus OB2 using Bonn non-rotating (*top*) and rotating (*bottom*) models. Orange, purple and yellow colors indicate those stars located in the young (0–5 Myr), intermediate (5–10 Myr) and old (>10 Myr) age groups.

from Cygnus OB9 to Cygnus OB2, with a strong peak in the northern part of the association.

6. Conclusions

We have carried out several observing runs between 2013 and 2017 to obtain new blue intermediate-resolution spectra suitable for spectral classification for the magnitude-limited ($B \leq 16$ mag, $Ks < 9$ mag) candidate list compiled by Comerón & Pasquali (2012). Out of 61 candidates, we confirm 42 new massive OB-type stars, earlier than B3, including 11 new O-type members. A 21% of this sample results on confirmed or possible SB2 binaries. Two other stars are late-B, seven are A-type, six are F-type, and the remaining four are G-type stars. Therefore, the spectral classification of the homogeneously selected sample is now completed. The selection criteria success rate obtained by Comerón & Pasquali (2012) along with this work is 72%, supporting the success at identifying reddened massive OB stars with the reddening-free parameters based on $BJHK$ photometry (see Sect. 2). However, the magnitude cutoff and dust extinction introduce an incompleteness. We loose the faintest and more obscured late O-type members in Cygnus OB2, and we are still far to obtain a complete census of the early-type population in the association.

We have also estimated individual visual extinctions (A_V) for the new confirmed OB-type stars using the extinction law derived by Wright et al. (2015). We found a median value of ~5.5 mag for the stars in the whole Cygnus region, and as we expect, a large median value of ~6.5 mag for those stars within the Cygnus OB2 association.

We have placed the new sample of OB stars in the HR diagram using both rotating and non-rotating models calculated by Ekström et al. (2012) and Brott et al. (2011) in order to assess uncertainties. We have also placed the already known OB type stars compiled by Comerón & Pasquali (2012) for completeness. To this aim, we derived effective temperatures and luminosities using spectral type calibrations for the whole sample. Although coming from different sources, our adopted calibrations fit very well with each other. Uncertainties about rotation and adopted models affect only the most massive members, suggesting larger ages for them of ~1–2 Myr. Even so, all models support the previous age spread observed in Cygnus OB2 of ~1–6 Myr.

In order to check the correlation between age and Galactic longitude found by Comerón & Pasquali (2012) in Cygnus OB2, we have divided the sample of OB stars in different location and age groups by comparing with isochrones: the young group (0–5 Myr), the intermediate group (5–10 Myr), and the old group (>10 Myr). Despite the differences in physical process treatment (rotation and physics of the stellar interior) done by the Geneva and Bonn groups, the spatial distribution of each age group is globally similar. Therefore, the result obtained by Comerón & Pasquali (2012) can not be an effect of using the Geneva stellar models without rotation when age dating the Cygnus region stars. Most of the stars at high Galactic longitudes belong to the young-intermediate age group, while stars at low Galactic longitudes belong to the old group. Assuming a wider area which includes Cygnus OB2, part of Cygnus OB9 and boundaries, we

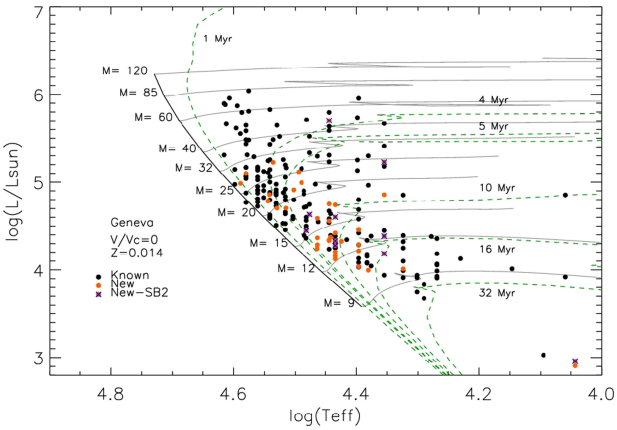

Fig. 10. HR diagram of OB stars in the Cygnus region (Cygnus OB2, Cygnus OB9 and field population) assuming a DM = 10.8 mag. Known OB stars from Comerón & Pasquali (2012) are also included to complete the sample. Black and orange dots indicate the already known and new OB-type stars respectively. Blue crosses indicate those new stars classified as possible or confirmed SB2 stars. Isochrones (dotted lines) and evolutionary stellar tracks (solid lines) for non-rotating models are from Ekström et al. (2012). Late-B stars are also included.

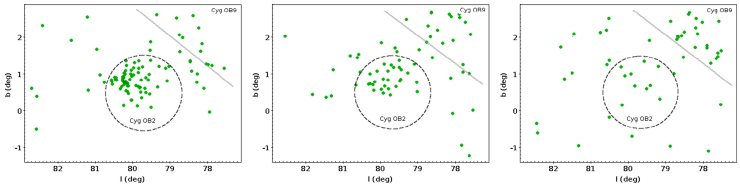

Fig. 11. Spatial distribution of stars of different age in the Cygnus area: the young population (0–5 Myr) on the *left*, the intermediate age one (5–10 Myr) in the *middle*, and the old population (>10 Myr) on the *right*.

obtain similar results suggesting that massive star formation in the region proceeds from Cygnus OB9 to Cygnus OB2, with a strong peak in the northern part of the association. Therefore the correlation between age and Galactic longitude is confirmed, regardless of the details of the models used.

Acknowledgements. We acknowledge financial support from the Spanish Ministry of Economy and Competitiveness (MINECO) under the grants AYA2012-39364-C02-01, AYA 2015-68012-C2-01 and Severo Ochoa SEV-2015-0548. A.S. also acknowledges support from MINECO through grants AYA2013-40 611-P and AYA2016-75 931-C2-2-P. AP and CBM acknowledge support from the Sonderforschungsbereich SFB 881 "The Milky Way System" (subproject B5) of the German Research Foundation (DFG). We also thank the WHT and its service programme (SW2017a04), J. Maíz Apellániz for his useful MGB software, and N. Wright for helpful discussion and comments in this paper.

References

Brott, I., de Mink, S. E., Cantiello, M., et al. 2011, A&A, 530, A115
Comerón, F., & Pasquali, A. 2012, A&A, 543, A101
Comerón, F., Pasquali, A., Rodighiero, G., et al. 2002, A&A, 389, 874
Comerón, F., Pasquali, A., Figueras, F., & Torra, J. 2008, A&A, 486, 453
Comerón, F., Djupvik, A. A., Schneider, N., & Pasquali, A. 2016, A&A, 586, A46
Crowther, P. A., Lennon, D. J., & Walborn, N. R. 2006, A&A, 446, 279
Drew, J. E., Greimel, R., Irwin, M. J., & Sale, S. E. 2008, MNRAS, 386, 1761
Ekström, S., Georgy, C., Eggenberger, P., et al. 2012, A&A, 537, A146
Gray, R. O., & Corbally, C. J. 2009, Stellar Spectral Classification (Princeton University Press)
Hanson, M. M. 2003, ApJ, 597, 957
Herrero, A., Corral, L. J., Villamariz, M. R., & Martín, E. L. 1999, A&A, 348, 542

A&A 612, A50 (2018)

Herrero, A., Puls, J., Corral, L. J., Kudritzki, R. P., & Villamariz, M. R. 2001, A&A, 366, 623
Herrero, A., Puls, J., & Najarro, F. 2002, A&A, 396, 949
Humphreys, R. M., & McElroy, D. B. 1984, ApJ, 284, 565
Kiminki, D. C., Kobulnicky, H. A., Kinemuchi, K., et al. 2007, ApJ, 664, 1102
Knödlseder, J. 2000, A&A, 360, 539
Lanz, T., & Hubeny, I. 2003, ApJS, 146, 417
Lanz, T., & Hubeny, I. 2007, ApJS, 169, 83
Lejeune, T., & Schaerer, D. 2001, A&A, 366, 538
Maíz Apellániz, J., Pellerin, A., Barbá, R. H., et al. 2012, in Proc. Scientific Meeting in Honor of Anthony, ed. F. J. Moffat, 465, 484
Maíz Apellániz, J., Sota, A., Arias, J. I., et al. 2016, ApJS, 224, 4
Markova, N., & Puls, J. 2008, A&A, 478, 823
Martins, F., & Plez, B. 2006, A&A, 457, 637
Martins, F., Schaerer, D., & Hillier, D. J. 2005, A&A, 436, 1049
Massey, P., & Thompson, A. B. 1991, AJ, 101, 1408
Massey, P., Johnson, K. E., & Degioia-Eastwood, K. 1995, ApJ, 454, 151
Massey, P., DeGioia-Eastwood, K., & Waterhouse, E. 2001, AJ, 121, 1050
Morgan, W. W., Johnson, H. L., & Roman, N. G. 1954, PASP, 66, 85
Münch, L., & Morgan, W. W. 1953, ApJ, 118, 161
Negueruela, I., Marco, A., Herrero, A., & Clark, J. S. 2008, A&A, 487, 575
Nieva, M.-F. 2013, A&A, 550, A26
Pecaut, M. J., & Mamajek, E. E. 2013, ApJS, 208, 9
Portegies Zwart, S. F., McMillan, S. L. W., & Gieles, M. 2010, ARA&A, 48, 431
Reddish, V. C. 1968, The Observatory, 88, 139
Reipurth, B., & Schneider, N. 2008, in Handbook of Star Forming Regions (ASP Monograph Publications), 4, 36
Rieke, G. H., & Lebofsky, M. J. 1985, ApJ, 288, 618
Rygl, K. L. J., Brunthaler, A., Sanna, A., et al. 2012, A&A, 539, A79
Sana, H., & Evans, C. J. 2011, Active OB Stars: Structure, Evolution, Mass Loss, and Critical Limits, IAU Symp., 272, 474
Schneider, N., Bontemps, S., Simon, R., et al. 2006, A&A, 458, 855
Schulte, D. H. 1956, ApJ, 124, 530
Schulte, D. H. 1958, ApJ, 128, 41
Simón-Díaz, S., & Herrero, A. 2007, A&A, 468, 1063
Simón-Díaz, S., Herrero, A., Sabín-Sanjulián, C., et al. 2014, A&A, 570, L6
Simón-Díaz, S., Negueruela, I., Maíz Apellániz, J., et al. 2015, Highlights of Spanish Astrophysics VIII, 576
Skrutskie, M. F., Cutri, R. M., Stiening, R., et al. 2006, AJ, 131, 1163
Sota, A., Maíz Apellániz, J., Walborn, N. R., et al. 2011, ApJS, 193, 24
Tokunaga, A. T. 2000, Allen's Astrophysical Quantities, 143
Walborn, N. R. 1971, ApJS, 23, 257
Walborn, N. R. 1973, AJ, 78, 1067
Walborn, N. R., Howarth, I. D., Lennon, D. J., et al. 2002, AJ, 123, 2754
Wright, N. J., Drake, J. J., & Drew, J. E. 2009, AAS Meet. Abstr., 213, 605.10
Wright, N. J., Drake, J. J., Drew, J. E., & Vink, J. S. 2010, ApJ, 713, 871
Wright, N. J., Drew, J. E., & Mohr-Smith, M. 2015, MNRAS, 449, 741
Zacharias, N., Urban, S. E., Zacharias, M. I., et al. 2004, AJ, 127, 3043
Zacharias, N., Finch, C., Girard, T., et al. 2010, AJ, 139, 2184

Appendix A: Table of stellar parameters

Table A.1 shows the derived stellar parameters for the new classified OB stars in a large area which includes Cygnus OB2 and its surroundings. We have also included the derived individual visual extinctions. Table A.2 shows the updated temperatures and luminosities for the already known OB stars from Comerón & Pasquali (2012) assuming the same spectral calibrations used in this work (see Sect. 4.2).

Table A.1. Temperatures, luminosities, and individual visual extinctions derived for the new classified massive OB stars.

Object	SpT	$T_{\rm eff}$ (K)	$\log(L/L_\odot)$	$A_{\rm V}$ (mag)
Cygnus OB2				
J20345785+4143543	O7:Ib	34990	5.25	8.2
J20293563+4024315	O8IIIz	33961	4.75	5.1
J20275292+4144067	O9.5II	30626	5.09	7.1
J20291617+4057372	O9.7III	28518	4.78	7.7
J20273787+4115468	B0II	25932	4.62	6.8
J20301097+4120088	B0:II:	25932	4.39	7.4
J20323968+4050418	B0II	25932	4.32	5.7
J20323882+4058469	B0Ib	27800	4.33	6.7
J20272099+4121262	B0.5V	26308	4.33	5.8
J20330526+4143367	B0.5III	24164	4.27	5.2
BD+404208	B1V	23590	4.14	2.2
J20314341+4100021	B1V	23590	4.21	7.0
J20315898+4107314	B1V	23590	4.26	7.1
BD+404193	B1V	23590	4.06	1.7
J20274925+4017004	B1III	21557	4.27	4.9
J20315433+4010067	B1III	21557	4.02	6.5
CCDMJ20323+4152AB	B9V	10700	2.96	–0.2
Surroundings				
J20423509+4256364	O6IIIz	38192	4.97	7.4
J20371773+4156316	O7V	36872	5.06	8.2
J20222481+4013426	O8II	33570	4.69	5.5
J20261976+3951425	O8.5IV	33391	4.81	8.0
J20262484+4001413	O9.2III	31317	4.65	5.9
J20382173+4157069	O9.7II	30859	4.99	8.5
J20181090+4029063	O9.7Ib	28644	4.58	7.6
J20395358+4222506	B0I	25094	5.57	11.0
J20281176+3840227	B0Ib	25094	4.43	3.6
J20290247+4231159	B1Ib	19979	4.03	5.0
J20225451+4023314	B0Iab	25094	4.21	4.7
J20253320+4048444	B0Iab	25094	4.62	5.5
HDE229258	B0.7V	24949	4.13	1.8
J20361806+4228483	B0.7III	22860	4.14	7.2
J20233816+3938118	B0.7Ib	21514	3.87	2.3
HD 228973	B1V	23590	4.45	2.4
J20201435+4107155	B1V	23590	4.27	3.4
J20230290+4133466	B1V	23590	4.68	7.2
J20330453+3822269	B1V	23590	4.09	2.4
J20230183+4014029	B1III	21557	4.26	4.3
J20382889+4009566	B1III	21557	3.84	1.4
J20440752+4107342	B1III	21557	4.09	6.5
LSII+3797	B1Ia	19979	5.07	5.8
J20211924+3936230	B1Ib	19979	4.23	4.6
BD+394179	B1Ib	19979	4.70	4.2
J20381289+4057169	B2V	20549	3.98	4.2
BD+423785a	B9V	10700	2.90	0.6

A&A 612, A50 (2018)

Table A.2. Temperatures and luminosities derived for the known massive OB stars from Comerón & Pasquali (2012).

Object	RA (hhmmss)	Dec (° ′ ″)	SpT	$T_{\rm eff}$ (K)	log ($L/L_{\odot}$)
Cygnus OB2					
J20331411+4120218	20:33:14.110	+41:20:21.91	O3If	40910	5.66
J20330879+4113179	20:33:08.818	+41:13:17.93	O4III	41070	5.88
J20360451+4056129	20:36:04.500	+40:56:13.01	O5V((f))	41250	5.31
J20331798+4118311	20:33:17.982	+41:18:31.19	O5III	39440	5.62
J20340850+4136592	20:34:08.514	+41:36:59.39	O5I	37630	5.80
J20331074+4115081	20:33:10.735	+41:15:08.22	O5If	37630	6.04
J20332346+4109130	20:33:23.471	+41:09:12.90	O5.5V	40440	5.96
J20331326+4113287	20:33:13.264	+41:13:28.67	O6V	39630	5.14
J20303980+4136506	20:30:39.805	+41:36:50.63	O6V	39630	4.97
J20344410+4051584	20:34:44.146	+40:51:58.67	O6.5III(f)	37845	5.31
J20283203+4049027	20:28:32.027	+40:49:02.88	O7	38010	5.65
J20310019+4049497	20:31:00.204	+40:49:49.70	O7V((f))	38010	5.06
J20341350+4135027	20:34:13.511	+41:35:02.86	O7V	38010	5.04
J20331748+4117093	20:33:17.483	+41:17:09.35	O7V	38010	5.17
J20334086+4130189	20:33:40.863	+41:30:18.95	O7V	38010	4.77
J20342959+4131455	20:34:29.599	+41:31:45.49	O7V	38010	5.58
J20315961+4114505	20:31:59.609	+41:14:50.45	O7V	38010	4.87
J20321383+4127120	20:32:13.822	+41:27:12.01	O7IIIf	36900	5.29
J20313690+4059092	20:31:36.911	+40:59:09.06	O7Ib(f)	34350	5.48
J20323154+4114082	20:32:31.531	+41:14:08.18	O7.5Ib-II(f)	33530	5.52
J20323857+4125137	20:32:38.571	+41:25:13.79	O8V(n)	36390	5.02
J20274361+4035435	20:27:43.616	+40:35:43.51	O8V:	36390	4.72
J20331369+4113057	20:33:13.688	+41:13:05.77	O8V	36390	4.87
J20324545+4125374	20:32:45.450	+41:25:37.57	O8V	36390	5.16
J20331803+4121366	20:33:18.035	+41:21:36.67	O8V	36390	4.90
J20323486+4056174	20:32:34.865	+40:56:17.35	O8V	36390	4.77
J20300788+4123504	20:30:07.877	+41:23:50.44	O8V	36390	4.91
J20330292+4117431	20:33:02.913	+41:17:43.16	O8V	36390	5.06
J20325002+4123446	20:32:50.016	+41:23:44.70	O8V	36390	4.95
J20325919+4124254	20:32:59.057	+41:24:24.79	O8V	36390	4.81
J20333030+4135578	20:33:30.316	+41:35:57.88	O8V	36390	5.17
J20342193+4117016	20:34:21.934	+41:17:01.66	O8III+O8III	35010	5.11
J20323843+4040445	20:32:38.441	+40:40:44.48	O8III	35010	5.24
J20330292+4047254	20:33:02.928	+40:47:25.29	O8II((f))	33860	5.65
J20314540+4118267	20:31:45.403	+41:18:26.73	O8I	32710	5.16
J30332557+4133269	20:33:25.569	+41:33:26.88	O8.5V	35580	5.12
J20331634+4119017	20:33:16.256	+41:19:00.16	O8.5V	35580	4.82
J20332674+4110595	20:33:26.756	+41:10:59.42	O8.5V	35580	4.90
J20313749+4113210	20:31:37.506	+41:13:20.99	O9:	34770	5.83
J20335842+4019411	20:33:58.417	+40:19:41.13	O9:	34770	5.43
J20321656+4125357	20:32:16.563	+41:25:35.67	O9V	34770	4.79
J20311833+4121216	20:31:18.329	+41:21:21.65	O9V	34770	5.06
J20340486+4105129	20:34:04.851	+41:05:11.76	O9V	34770	4.59
J20311055+4131535	20:31:10.543	+41:31:53.53	O9V	34770	5.14
J20332101+4117401	20:33:21.016	+41:17:40.11	O9V	34770	4.63
J20331571+4120172	20:33:15.685	+41:20:18.75	O9V	34770	4.60
J20301839+4053466	20:30:18.391	+40:53:46.56	O9V	34770	4.99
J20314965+4128265	20:31:49.658	+41:28:26.50	O9III	33120	4.53
J20345606+4038179	20:34:56.057	+40:38:17.92	O9.7Iab	29922	5.33
J20305772+4109575	20:30:57.727	+41:09:57.51	O9.5V	33960	4.85
J20340601+4108090	20:34:06.017	+41:08:09.13	O9.5V	33960	4.87
J20335952+4117354	20:33:59.527	+41:17:35.46	O9.5V	33960	4.91
J20341605+4102196	20:34:16.046	+41:02:19.59	O9.5V	33960	4.73
J20272428+4115458	20:27:24.282	+41:15:45.82	O9.5V	33960	4.51
J20293480+4120089	20:29:34.798	+41:20:08.93	O9.5V	33960	4.76
J20323033+4034332	20:32:30.310	+40:34:33.22	O9.5IV	33067	5.25
J20333700+4116113	20:33:36.994	+41:16:11.31	O9.5IV	33067	4.88
J20334610+4133010	20:33:46.112	+41:33:01.00	O9.5Ia	30250	5.71
J20325964+4115146	20:32:59.633	+41:15:14.66	O9.7III	31797	4.80
J20283039+4105290	20:28:30.385	+41:05:29.04	OC9.7Ia	29922	5.52

Table A.2. continued.

Object	RA (hhmmss)	Dec (° ′ ″)	SpT	$T_{\rm eff}$ (K)	log ($L/L_{\odot}$)
J20302730+4113253	20:30:27.300	+41:13:25.13	Ofpe	38612	5.79
J20281547+4038196	20:28:15.471	+40:38:19.81	B0V:	32816	4.79
J20323951+4052475	20:32:39.507	+40:52:47.46	B0:V:	32816	5.19
J20331050+4122224	20:33:10.502	+41:22:22.44	B0V	32816	4.45
J20305552+4109575	20:30:55.516	+40:54:54.03	B0V	32816	4.66
J20295701+4109538	20:29:57.010	+41:09:53.84	B0V	32816	4.64
J20305111+4120218	20:30:51.115	+41:20:21.78	B0V	32816	4.53
J20331130+4042337	20:33:11.300	+40:42:33.73	B0:III:	30308	4.72
J20333821+4041064	20:33:38.213	+40:41:06.35	B0Ia	27800	5.64
J20344471+4051465	20:34:44.716	+40:51:46.73	B0Ia	27800	5.59
J20323904+4100078	20:32:39.057	+41:00:07.78	B0Ia	27800	5.79
J20322774+4128522	20:32:27.738	+41:28:52.26	B0Ib	27800	4.24
J20345878+4136174	20:34:58.781	+41:36:17.35	B0Ib(n)sb	27800	5.31
J20333822+4053412	20:33:38.218	+40:53:41.19	B0Ib	27800	4.94
J20333910+4119258	20:33:39.102	+41:19:25.98	B0Iab	27800	5.23
J20323498+4052390	20:32:34.848	+40:52:39.46	B0.2V	31906	4.58
J20292449+4052599	20:29:24.485	+40:52:59.85	B0.2IV	30588	4.71
J20321568+4046170	20:32:15.679	+40:46:17.00	B0.2IV	30588	4.39
J20294666+4105083	20:29:46.672	+41:05:08.32	B0.5V(n)sb	30288	4.50
J20282772+4104018	20:28:27.723	+41:04:01.80	B0.5V	30288	4.47
J20314605+4043246	20:31:46.053	+40:43:24.61	B0.5IV	28969	4.55
J20331870+4059379	20:33:18.696	+40:59:37.92	B0.5IIIe	27651	4.64
J20303970+4108489	20:30:39.701	+41:08:48.80	B0.7Ib	24014	5.30
J20294060+4109585	20:29:40.601	+41:09:58.54	B1[e]	27173	4.27
J20313338+4122490	20:31:33.378	+41:22:49.02	B1V	27173	4.25
J20340435+4108078	20:34:04.349	+41:08:07.91	B1V	27173	4.27
J20303833+4010538	20:30:38.329	+40:10:53.84	B1V	27173	4.34
J20293473+4020381	20:29:34.728	+40:20:38.09	B1V	27173	4.38
J20273982+4040384	20:27:39.821	+40:40:38.35	B1V	27173	4.28
J20303297+4044024	20:30:32.965	+40:44:02.41	B1V	27173	4.31
J20310464+4030568	20:31:04.659	+40:30:56.93	B1III:e	24903	5.95
J20334783+4120415	20:33:47.831	+41:20:41.37	B1III	24903	4.80
J20281539+4044046	20:28:15.392	+40:44:04.57	B1III	24903	4.58
J20310700+4035537	20:31:07.003	+40:35:53.73	B1III	24903	4.08
J20314885+4038001	20:31:48.848	+40:38:00.05	B1II	23767	4.04
J20333078+4115226	20:33:30.791	+41:15:22.70	B1I	22632	5.41
J20312203+4131284	20:31:22.026	+41:31:28.40	B1Ib:	22632	4.45
J20322734+4055184	20:32:27.339	+40:55:18.25	B2V	21092	4.39
J20312210+4112029	20:31:22.101	+41:12:02.87	B2V	21092	4.10
J20354703+4053012	20:35:47.026	+40:53:01.17	B2V	21092	3.91
J20284657+4107069	20:28:46.566	+41:07:06.86	B2II	19482	3.83
J20320689+4117570	20:32:06.877	+41:17:56.97	B3V	18546	3.91
Cygnus OB9					
HD 229196	20:23:10.784	+40:52:29.85	O5	41250	5.89
J20223777+4140292	20:22:37.766	+41:40:29.23	O5If	37630	5.48
BD+394177	20:25:22.122	+40:13:01.09	O6.5	38820	5.55
HD 229250	20:24:11.733	+39:40:41.54	O7	38010	5.44
BD+394168	20:24:21.475	+39:46:03.90	O7	38010	5.48
HD 229202	20:23:22.840	+40:09:22.53	O8V:	36390	5.14
BD+404159	20:25:06.521	+40:35:49.78	O9V	34770	4.61
BD+404148	20:23:14.549	+40:45:19.07	O9.5:V	33960	4.88
J20194916+4052090	20:19:49.156	+40:52:08.99	O9.5V	33960	4.86
J20190610+4037004	20:19:06.102	+40:37:00.39	O9.7Iab	29922	4.74
HD 193945	20:21:25.823	+41:11:39.56	B0Vnn	32816	4.92
BD+384058	20:23:28.531	+39:20:59.05	B0V	32816	4.83
LSII+4032	20:25:28.893	+40:12:54.13	B0III	30308	4.36
J20243872+3930301	20:24:38.720	+39:30:30.10	B0I:	27800	4.58
J20183413+4025045	20:18:34.130	+40:25:04.47	B0.2IV	30588	4.86
NGC6910-14	20:23:07.575	+40:46:08.87	B0.5V	30288	4.56
J20240515+4046035	20:24:05.154	+40:46:03.51	B0.5V	30288	4.60

A&A 612, A50 (2018)

Table A.2. continued.

Object	RA (hhmmss)	Dec (° ′ ″)	SpT	$T_{\rm eff}$ (K)	log ($L/L_{\odot}$)
HD 194092	20:22:05.443	+40:59:08.17	B0.5III	27651	4.39
HD 228882	20:18:57.784	+40:42:18.52	B0.5Ia	25014	5.25
HD 228929	20:19:36.542	+39:54:41.80	B0.5Ib	25014	5.13
J20234624+3937078	20:23:46.238	+39:37:07.83	B0.7IV	27818	4.54
J20241767+3920326	20:24:17.666	+39:20:32.56	B1V	27173	4.25
J20214868+4043005	20:21:48.682	+40:43:00.45	B1V	27173	4.32
HD 228919	20:19:27.908	+40:27:42.09	B1IV	26038	4.34
J20233375+4045199	20:23:33.752	+40:45:19.93	B1III	24903	4.03
J20223944+3935420	20:22:39.442	+39:35:42.02	B1III	24903	4.42
J20220454+4042487	20:22:04.541	+40:42:48.73	B1III	24903	4.28
J20215593+4110129	20:21:55.930	+41:10:12.92	B1III	24903	4.03
J20220879+3958161	20:22:08.793	+39:58:16.07	B1II	23767	4.38
J20214410+4012529	20:21:44.103	+40:12:52.91	B1Ia	22632	5.18
J20215160+3959496	20:21:51.600	+39:59:49.61	B1Ib	22632	3.94
J20203933+4031176	20:20:39.334	+40:31:17.64	B1.5V	24132	4.08
J20204933+4033027	20:20:49.333	+40:33:02.73	B1.5V	24132	4.15
HD 228911	20:19:21.712	+40:53:16.46	B2	21092	4.25
HD 194194	20:22:44.760	+40:42:52.63	B2III	20019	3.91
J20211677+4023162	20:21:16.773	+40:23:16.19	B2III	20019	3.94
J20250591+4020124	20:25:05.912	+40:20:12.44	B2III	20019	3.75
HD 228928	20:19:32.709	+40:39:13.75	B2Ib:nn	18945	4.38
HD 228941	20:19:40.169	+40:53:19.19	B3	18546	3.98
BD+404146	20:23:10.464	+40:45:52.34	B3	18546	4.35
NGC6910-16	20:23:07.301	+40:46:55.25	B3	18546	4.05
J20215115+3934215	20:21:51.149	+39:37:51.47	B3V	18546	4.18
J20221729+3946035	20:22:17.286	+39:34:21.50	B5Ia	14012	4.01
HD 228821	20:18:04.930	+40:06:06.80	B8	12449	3.03
HD 193426	20:18:39.749	+40:13:36.89	B9Ia	11457	4.85
Boundaries					
BD+433654	20:33:36.079	+43:59:07.38	O4If	39270	5.87
LSII+3953	20:27:17.572	+39:44:32.60	O7V:	38010	5.07
BD+423760	20:28:40.812	+43:08:58.46	O8.5V	35580	4.96
BD+423835	20:42:06.863	+43:11:03.72	O9p...	34770	5.25
J20342894+4156171	20:34:28.941	+41:56:17.09	O9V	34770	4.86
J20462826+4223417	20:46:28.255	+42:23:41.74	O9V	34770	4.88
J20272553+3929246	20:27:25.529	+39:29:24.58	O9.5V	33960	4.88
J20325571+4307583	20:32:55.713	+43:07:58.26	O9.5V	33960	4.97
J20310838+4202422	20:31:08.376	+42:02:42.25	O9.7II	30859	5.15
HD 199021	20:52:53.207	+42:36:27.87	B0V	32816	5.05
J20382040+4156563	20:38:20.413	+41:56:56.51	B0II	29054	5.29
J20385918+4202395	20:38:59.181	+42:02:39.45	B0Ib	27800	4.67
J20294195+3859342	20:29:41.952	+38:59:34.16	B0.2V	31906	4.61
J20352227+4355305	20:35:22.266	+43:55:30.46	B0.2IV	30588	4.90
BD+413794	20:32:02.204	+42:12:26.15	B0.2III	29270	4.97
HD 194839	20:26:21.545	+41:22:45.65	B0.5Iae	25014	5.73
J20313693+4201218	20:31:36.921	+42:01:21.79	B0.7Ib	24014	4.96
J20301273+3904216	20:30:12.732	+39:04:21.59	B1V	27173	4.24
LSIII+4217	20:35:10.623	+42:20:22.83	B1III	24903	4.69
J20374323+4232334	20:37:43.232	+42:32:33.40	B1III	24903	4.13
J20314215+4225532	20:31:42.151	+42:25:53.26	B1Ib	22632	5.67
BD+373976	20:33:49.752	+38:17:00.06	B1.5Vn	24132	4.17
J20313853+4152585	20:31:38.532	+41:52:58.46	B1.5V	24132	4.07
J20312725+4304227	20:31:27.253	+43:04:22.67	B1.5V	24132	4.33
BD+394189	20:26:20.922	+39:40:10.06	B2p?e?	21092	4.85
BD+413762	20:28:15.212	+42:25:39.14	B2V	21092	4.32
J20452110+4223514	20:45:21.103	+42:23:51.37	B2V	21092	3.99
J20264025+4233221	20:26:40.251	+42:33:22.09	B2II	19482	3.67
HD 196489	20:36:24.259	+39:11:40.70	B3V	18546	3.92
J20462289+4212311	20:46:22.892	+42:12:31.07	B3V	18546	4.06
HD 194779	20:25:55.077	+41:20:11.73	B3II	16983	4.12
BD+384098	20:27:33.010	+38:46:19.62	B9Ib	11457	3.92

Appendix B: Candidate spectra

In Fig. B.1 are plotted the normalized spectra of the 61 OB candidates from the list of Comerón & Pasquali (2012). The spectra have been corrected for the stellar radial velocities and diagnostic lines are also indicated.

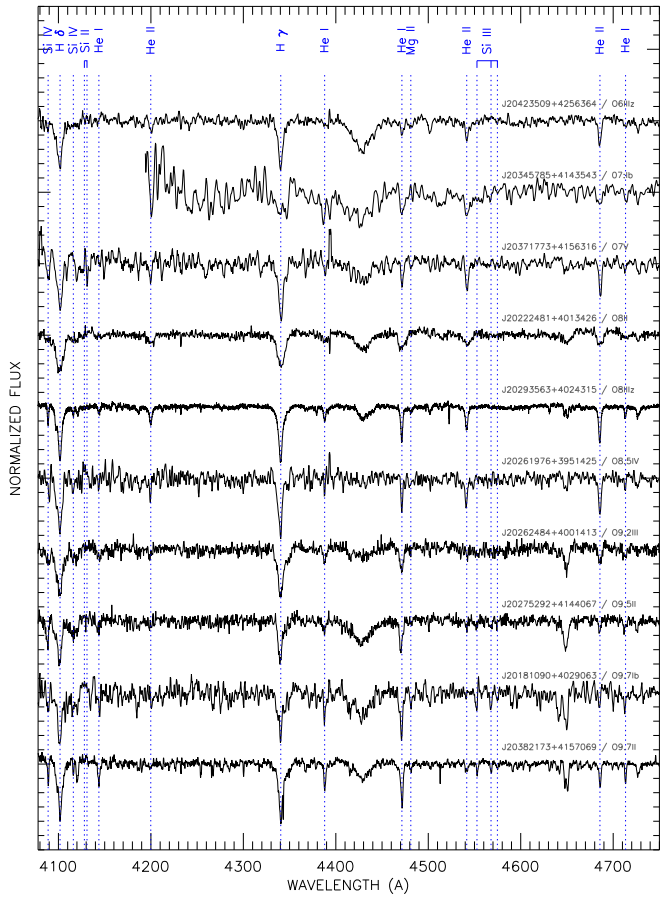

Fig. B.1. Spectra of the 61 OB candidate stars where dotted vertical lines indicate H, He, Si and Mg lines in the wavelength range.

A&A 612, A50 (2018)

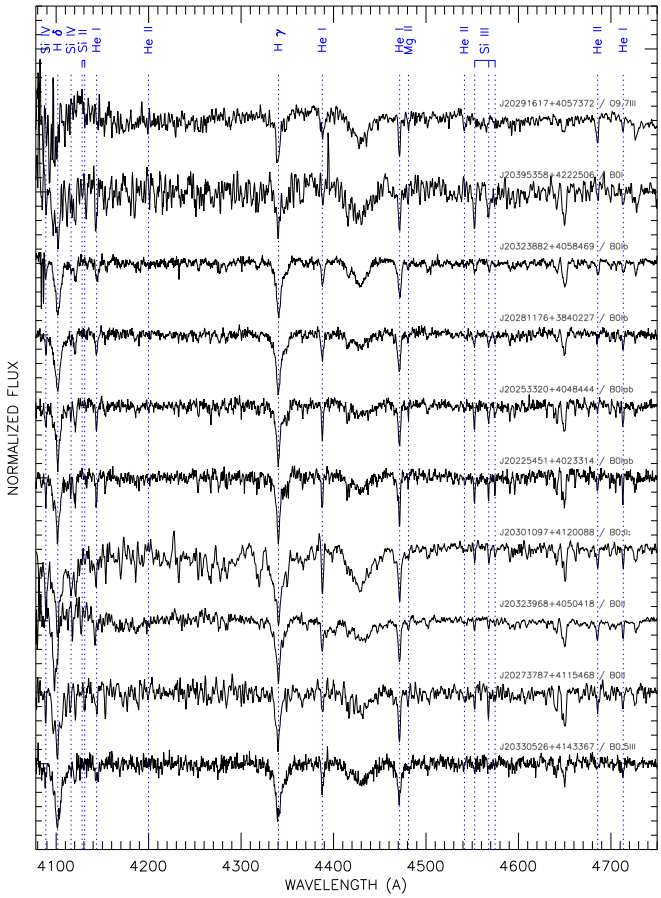

Fig. B.1. continued.

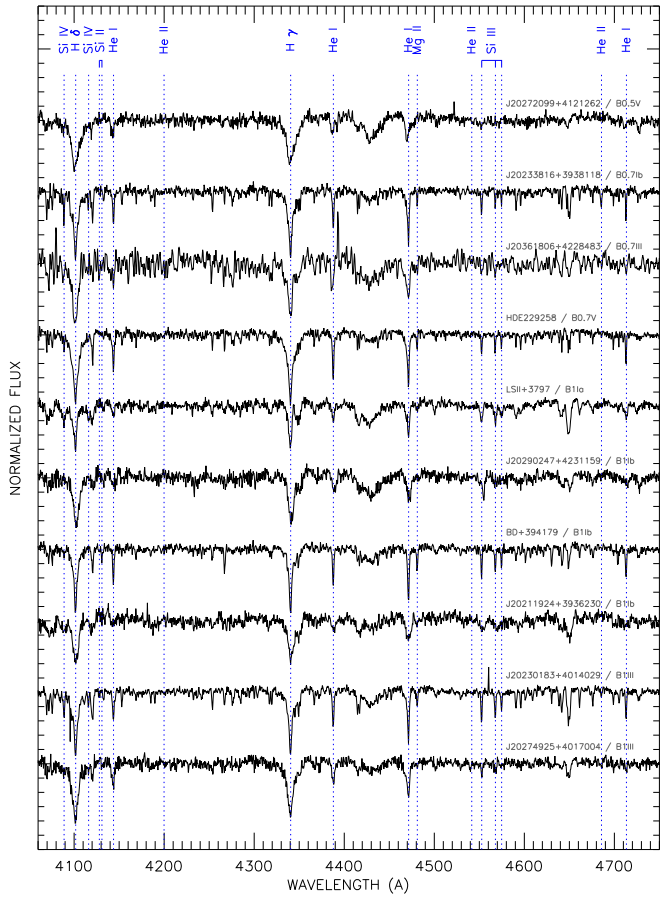

Fig. B.1. continued.

A&A 612, A50 (2018)

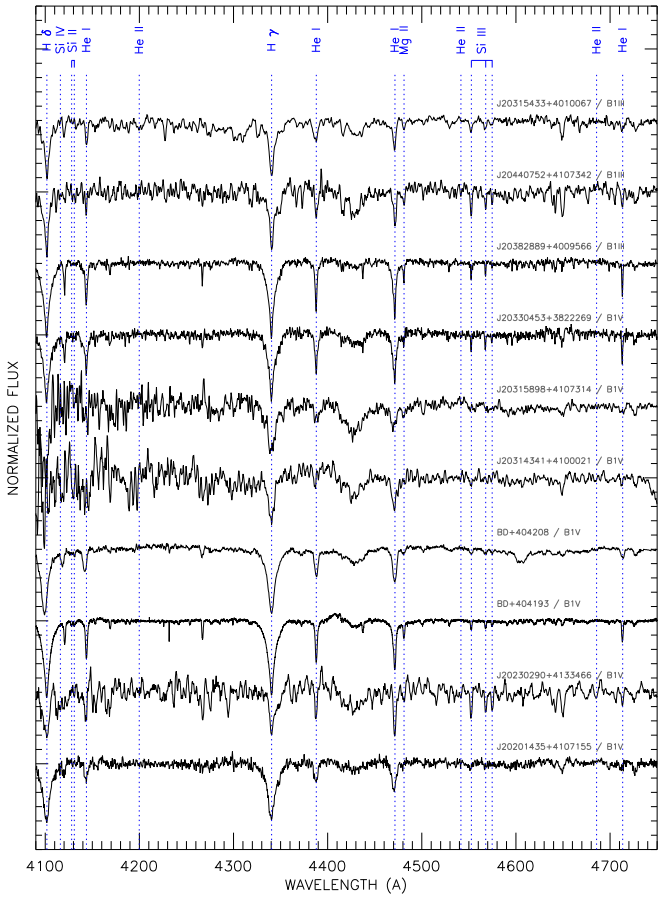

Fig. B.1. continued.

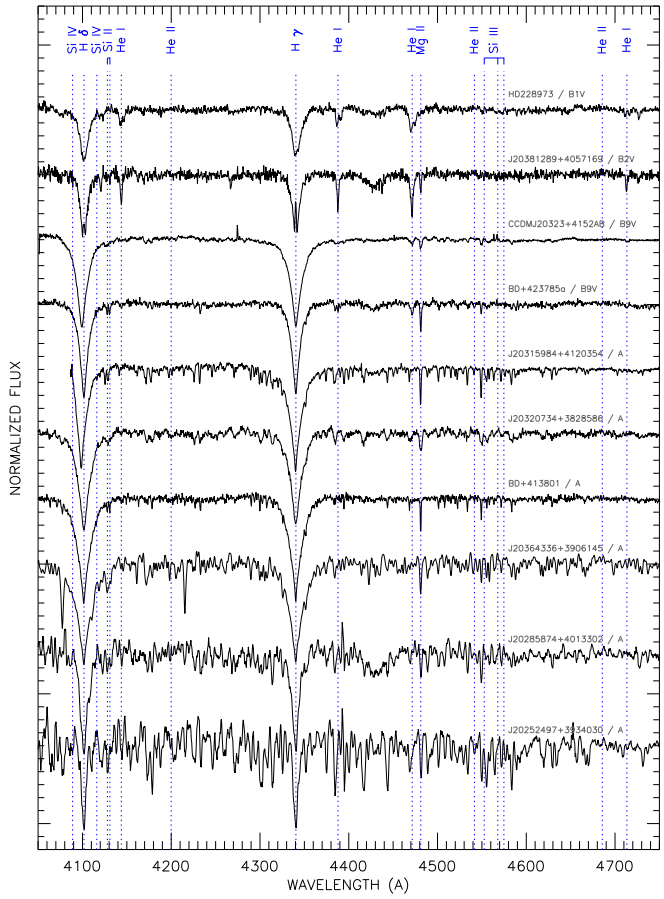

Fig. B.1. continued.

A&A 612, A50 (2018)

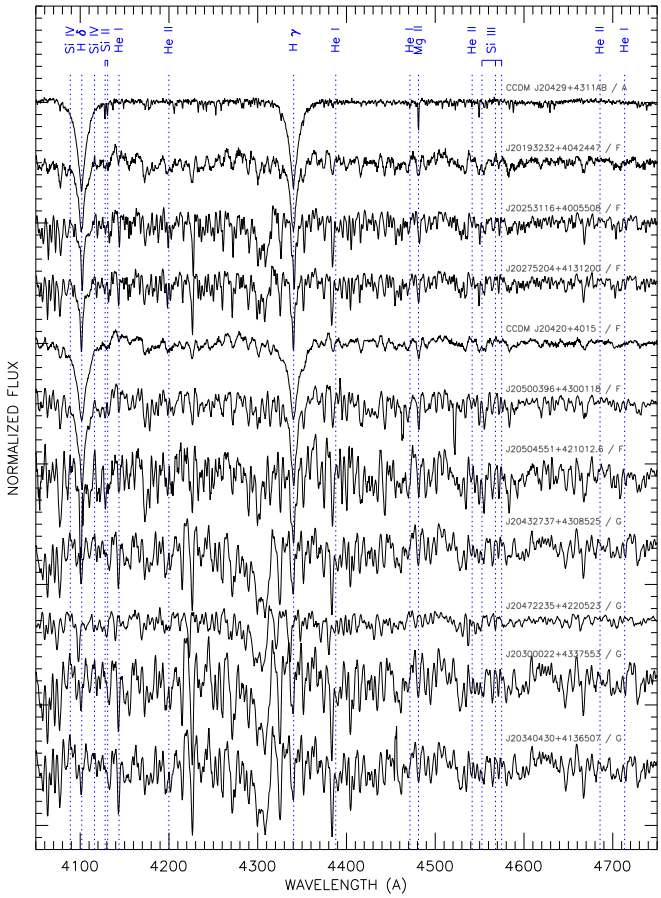

Fig. B.1. continued.

4

Oxygen and silicon abundances in Cygnus OB2: Chemical homogeneity in a sample of OB slow rotators

For this second paper, we carried out the spectroscopic analysis of a sample of late O- and early B-type stars with low rotational velocity in Cygnus OB2. We have carried out an analysis based on equivalent widths of metal lines, the wings of the H Balmer lines and FASTWIND stellar atmosphere models to determine their stellar fundamental parameters (T_{eff} and log g) as well as the silicon and oxygen surface abundances. We derive a rather homogeneous distribution of silicon and oxygen abundances across the region, with average values of $12 + \log(\mathrm{Si/H}) = 7.53 \pm 0.08$ dex and $12 + \log(\mathrm{O/H}) = 8.65 \pm 0.12$ dex, with no clear evidence for significant chemical self-enrichment, despite indications of strong stellar winds and possible supernovae during the history of the region. The degree of homogeneity that we find is consistent with the observed Milky Way oxygen gradient based on HII regions. We also find that the oxygen scatter within Cygnus OB2 is at least of the same order as than among HII regions at similar Galactocentric distance.

A&A 620, A56 (2018)
https://doi.org/10.1051/0004-6361/201833989

Astronomy & Astrophysics

Oxygen and silicon abundances in Cygnus OB2

Chemical homogeneity in a sample of OB slow rotators

S. R. Berlanas[1,2], A. Herrero[1,2], F. Comerón[3], S. Simón-Díaz[1,2], M. Cerviño[4], and A. Pasquali[5]

[1] Instituto de Astrofísica de Canarias, 38200 La Laguna, Tenerife, Spain
e-mail: srberlan@iac.es
[2] Departamento de Astrofísica, Universidad de La Laguna, 38205 La Laguna, Tenerife, Spain
[3] ESO, Karl-Schwarzschild-Strasse 2, 85748 Garching bei München, Germany
[4] Centro de Astrobiología (CSIC/INTA), 28850 Torrejón de Ardoz, Madrid, Spain
[5] Astronomisches Rechen-Institut, Zentrum für Astronomie der Universität Heidelberg, Mönchhofstr 12-14, 69120 Heidelberg, Germany

Received 30 July 2018 / Accepted 17 September 2018

ABSTRACT

Context. Cygnus OB2 is a rich OB association in the Galaxy located at only ~1.4 kpc from us which has experienced intense star formation in the last 20–25 Myr. Its stellar population shows a correlation between age and Galactic longitude. Exploring the chemical composition of its stellar content we will be able to check the degree of homogeneity of the natal molecular cloud and possible effects of self-enrichment processes.
Aims. Our aim is to determine silicon and oxygen abundances for a sample of eight early-type slow rotators (with rotational velocities below 80 km s^{-1}) in Cygnus OB2 in order to check possible inhomogeneities across the whole association and whether there exists a correlation of chemical composition with Galactic longitude.
Methods. We have performed a spectroscopic analysis of a sample of late O and early B stars with low rotational velocity in Cygnus OB2, which have been chosen so as to cover the whole association area. We have carried out an analysis based on equivalent widths of metal lines, the wings of the H Balmer lines and FASTWIND stellar atmosphere models to determine their stellar fundamental parameters (effective temperature and surface gravity) as well as the silicon and oxygen surface abundances.
Results. We derive a rather homogeneous distribution of silicon and oxygen abundances across the region, with average values of $12 + \log(\mathrm{Si/H}) = 7.53 \pm 0.08$ dex and $12 + \log(\mathrm{O/H}) = 8.65 \pm 0.12$ dex.
Conclusions. We find a homogeneous chemical composition in Cygnus OB2 with no clear evidence for significant chemical self-enrichment, despite indications of strong stellar winds and possible supernovae during the history of the region. Comparison with different scenarios of chemical enrichment by stellar winds and supernovae point to star forming efficiencies not significantly above 10%. The degree of homogeneity that we find is consistent with the observed Milky Way oxygen gradient based on H II regions. We also find that the oxygen scatter within Cygnus OB2 is at least of the same order than among H II regions at similar Galactocentric distance.

Key words. stars: abundances – stars: massive – stars: rotation – open clusters and associations: individual: Cygnus OB2 – stars: early-type

1. Introduction

The chemical composition of the natal molecular cloud is one of the fundamental parameters in the process of massive star formation, as it affects the opacity of the infalling matter, the chemical processes that take place during star formation or the upper mass limit, to mention some (e.g., Zinnecker & Yorke 2007; Tan et al. 2014). The previous enrichment history of the interstellar medium (ISM) through stellar evolution and processes like stellar winds, metal-rich yields from supernovae (SNe) or infall of metal-poor gas, directly affects the chemical composition of the natal molecular cloud (e.g., Langer 2012; Prantzos et al. 2018; Barrera-Ballesteros et al. 2018).

Young open clusters and OB associations have been proposed as places to explore the effects of self-enrichment by stellar winds and SNe (e.g., Spina 2017; Palla 2011; Biazzo et al. 2011a; Simón-Díaz 2010; Cunha & Lambert 1994, 1992) as many of them have a star formation history sufficiently long to have experienced the explosion of their oldest massive members as SNe, contaminating the environment through processes driven by the pollution of the ISM by subsequent generations of massive stars. We may thus expect that subsequent stellar generations show chemical differences. Inversely, the presence or absence of these differences allow us to put constrains on the processes involved in the chemical pollution of the protostellar cloud. For example, predictions about the oxygen yields from core-collapse supernovae (CCSN) greatly differ depending on the upper mass limit to become CCSN or on the physics of massive stars included in the models (see e.g., Suzuki & Maeda 2018; Prantzos et al. 2018; and references therein). Unfortunately, the stellar content of many OB associations is difficult to study in detail due to the combined effects of distance and extinction.

A study in Orion (Simón-Díaz 2010) resulted in a chemically homogeneous composition, contrary to previous works claiming evidence of self-enrichment (Cunha & Lambert 1994).

A&A 620, A56 (2018)

The homogeneity has later been confirmed by other independent analysis strategies (see Nieva & Simón-Díaz 2011; Cunha et al. 2012). Moreover, this result was not only found in early-type stars, but also in late-type stars (e.g., Biazzo et al. 2011a,b). But Orion is a modest region in terms of star formation.

Because of its close distance of ∼1.4 kpc (Rygl et al. 2012) and relatively intense star formation, Cygnus OB2 provides an excellent target to study possible chemical composition inhomogeneities through self-enrichment. Massive star formation seems to have peaked around 3 Myr ago (Comerón & Pasquali 2012; Wright et al. 2015; Berlanas et al. 2018) and the distribution of stellar ages extends beyond 20 Myr (Comerón et al. 2016). Although there are no known supernova remnants clearly associated with Cygnus OB2, the current existence of a large number of B-type giants (Berlanas et al. 2018) and seven red supergiants in the region (Comerón et al. 2016) indicates an evolved population whose most massive members have already exploded as SNe. The three Wolf-Rayet stars known in the core of the region and the large number of OB stars (Wright et al. 2015), represent intense stellar wind sources susceptible to produce chemical enrichment across the association. Strong signatures from the decay of ^{26}Al in Cygnus OB2 (Knödlseder et al. 2002), other high-energy detections at γ- and X-rays (Martin et al. 2009, 2010; Bednarek 2003; Butt et al. 2006) or the presence of the young pulsar J2032+4130 in the surroundings (Abdo et al. 2009; Camilo et al. 2009), could have been caused chemical enrichment produced by stellar winds and/or SNe.

In virtue of its rich content in massive stars and an extended star formation history sufficiently long to have included the explosion of its oldest massive members, Cygnus OB2 represents a suitable region to explore possible abundance inhomogeneities. The observed spatial age gradient across its extent (Comerón & Pasquali 2012) might be associated with a chemical composition gradient produced by pollution of the ISM by successive generations of massive stars.

In Sect. 2 we describe the target selection and the observing strategy. In Sect. 3 we present the whole spectroscopic analysis, including the derived equivalent widths, stellar parameters and abundances of a sample of eight early-type slow rotators of Cygnus OB2. In Sect. 4 we discuss our results and their implications. Finally, in Sect. 5, we summarize the main conclusions of this work.

2. Target selection, observations and membership

Late O-type and early B-type stars, with their rich spectrum of silicon and oxygen lines are ideal targets to test possible chemical contamination. These stars should cover the whole association area (1 deg radius centered on Galactic coordinates $l = 79.8°$ and $b = +0.8°$). In addition, to reach an optimal accuracy in the abundance analysis, we need to analyze stars with effective temperature in the range 18 000–34 000 K or, equivalently, spectral types in the range B2–O9.5 (where silicon ionization balance and O II lines are strong enough, see Simón-Díaz 2010) and low projected rotational velocities (in what follows, we call slow rotators those stars with projected rotational velocities below 80 km s^{-1}) at high resolution and signal-to-noise ratio (S/N). The fraction of early-B dwarfs and giants rotating at these velocities depends on the environment and evolutionary stage of the cluster considered, but from the results in the Milky Way (Dufton et al. 2006; Wolff et al. 2007; Huang & Gies 2006) and 30 Dor (Dufton et al. 2013) we may expect it to be 20–30%, which makes mandatory to previously observe a large sample of OB stars to identify early-type slow rotators.

Table 1. Coordinates (J2000.0) of the center of the fields observed in July 2014 using WYFFOS at WHT.

Field	RA (hhmmss)	Dec (° ′ ″)
Cygnus OB2 – field1	20 33 04	41 27 00
Cygnus OB2 – field2	20 31 03	40 36 20
Cygnus OB2 – field3	20 30 03	41 01 20
Cygnus OB2 – field4	20 34 50	40 33 20

In this section we describe the observations and various steps we have performed in order to build an optimal list of stars for the purposes of this paper. Briefly we started with intermediate resolution observations of a large list of OB stars in Cygnus OB2 which helped us identifying the late-O and early-B slow rotators. Then we proceeded to gather new high-resolution observations of this optimized sample. In the last step, we benefit from data about parallaxes and proper motions from the second *Gaia* data release (*Gaia* DR2, Gaia Collaboration 2018) to asses the membership of the final stellar sample.

2.1. Intermediate resolution spectroscopy and early-type slow rotators selection

In July 2014 we obtained intermediate-resolution spectroscopy of 51 stars in Cygnus OB2 classified as late-O and early-B in the large list from Comerón & Pasquali (2012) using the multi-object AF2/WYFFOS spectrograph at the *William Herschel* Telescope (WHT). We selected four fields in the region (see Table 1) in order to maximize the number of suitable candidates. Simulations based on a B1V spectrum broadened by different values of v sin i and different levels of noise indicated that the best trade-off between the required exposure time and enough v sin i accuracy for our target selection can be achieved with a combination of a resolving power of 5000 and $S/N \geq 50$. We thus have chosen the H2400B grating, which provides the required resolution and wavelength coverage, setting the central wavelength to 4500 Å. The spectral region contains the Si III lines at λ4552, λ4568 and λ4575 Å, which are broadened mainly by rotation and are most prominent around the B1V type stars. Finally, in order to improve the statistics of our sample, we added six stars from previous unpublished observations in Cygnus OB2 carried out by A. Herrero in August 2012 at the WHT using the ISIS spectrograph with the R1200B and R1200R gratings (covering all the lines of interest and providing high quality spectra good enough for our purposes).

We determined the projected rotational velocities for the whole stellar sample of 57 stars using `iacob_broad`, an user-friendly tool for OB-type spectra which is based on a combined Fourier transform plus a goodness-of-fit methodology (Simón-Díaz & Herrero 2007, 2014). We have mainly based the analysis on the Si III λ4552 line or the N III λ4510 line in the cases in which the Si III line was weak. When both lines were weak, we have used the He I λ4387, 4471 lines. Typical uncertainties are in the order of 10–20% (Simón-Díaz & Herrero 2014). We found a fraction of OB slow rotators consistent with the expectations, reaching a ∼23% of the targets at v sin $i \lesssim 80$ km s^{-1} (see Fig. 1). For four targets, represented with dark gray color, we suggest possible spectroscopic binarity (two of them are reported as binary candidates by Berlanas et al. 2018). We can only suggest their possible binary nature due to their noisy spectra.

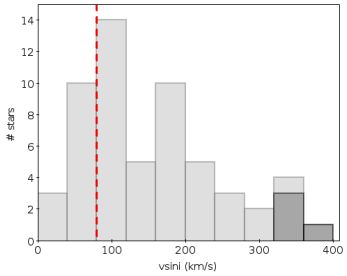

Fig. 1. Rotational velocity distribution of a sample of 57 OB-type stars in Cygnus OB2. Dark gray color indicates possible binary candidates. The red dashed line indicates $v \sin i = 80\,\mathrm{km\,s^{-1}}$.

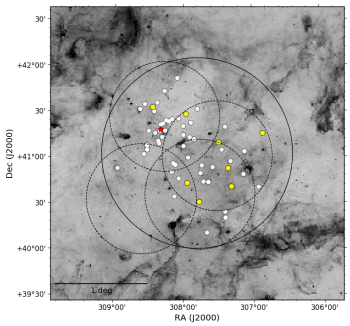

Fig. 2. Inverse *Spitzer* 8 μm image showing the location of the 57 stars (dots) observed in Cygnus OB2, and the selected OB slow rotators (yellow dots) suitable for the abundance analysis. The solid line circle indicates the 1 deg. Cygnus OB2 area adopted in this work, and the four dashed line circles the observed AF2/WYFFOS fields. For reference, the red star indicates the location of the Cyg OB2 #8 Trapezium-like system.

The whole list of 57 stars (we note that some of them are too hot for the abundance analysis) with the derived rotational velocities is given in Appendix A. From this sample, and taking into account the required conditions mentioned above, six stars were suitable for our abundance analysis.

2.2. High resolution and S/N spectroscopy

In July 2015 we obtained high resolution, high S/N spectra of the six selected stars. We obtained ISIS spectra at the WHT using both, the blue and red arms. We chose the H2400B grating for the blue arm, which provides the required resolving power ($R \sim 13\,600$ at 4500 Å). The spectral coverage of the H2400B grating requires the observation of each star in two spectral ranges centered on 4200 and 4600 Å, in order to cover all the lines of interest. But due to bad weather conditions and in order to get high S/N spectra, the H2400B grating was replaced by the R1200B one for the faintest targets (J20292449+4052599 and J20314605+4043246), which provides a lower but still sufficient resolving power ($R \sim 7500$ at 4500 Å by reducing the slit width to 0.7 arcsec) and covers all lines of interest. As the dichroic allows to simultaneously observe the red arm, we used the R1200R grating ($R \sim 9300$ at 6500 Å) centered at 5700 and 6500 Å for all the stars, covering the regions of O III λ5592, C IV λ5811-14 Å and Hα. Additionally we have included two more stars, J20314965+4128265 and J20334610+4133010, both OB slow rotators that meet all the requirements and were observed by A. Herrero in July 2003 using also ISIS at the WHT with the same configuration (H2400B and R1200R gratings). Figure 2 shows the location of the whole sample of 57 OB stars in the region, and the eight stars finally chosen to carry out the abundance analysis.

The spectra were reduced using IRAF[1] with standard routines for bias and flat-field subtraction, and also for the wavelength calibration. A summary of their basic data is presented in Table 2.

[1] IRAF is distributed by the National Optical Astronomy Observatories, which are operated by the Association of Universities for Research in Astronomy, Inc., under cooperative agreement with the National Science Foundation.

2.3. Gaia-DR2 data

We used the recent data (parallaxes and proper motions) from *Gaia* DR2 to check whether all the stars of our sample belong to the same region and present no peculiarities in the data that could indicate a different origin or evolutionary history.

All but one of the stars in our sample with a parallax uncertainty below 0.1 mas (see Table 3) have values consistent with the known Cygnus OB2 distance of 1.4–1.7 kpc (Massey & Thompson 1991; Hanson 2003; Rygl et al. 2012). There is one star (J20272428+4115458) which seems to be at further distance (about 1.8 sigma from the mean parallax value of our sample). However, there is a systematic (but variable) offset up to 0.1 mas that could affect all the reported *Gaia* DR2 parallaxes (Arenou et al. 2018; Lindegren et al. 2018; Stassun & Torres 2018). Nevertheless, the oxygen abundance obtained for this star is consistent with the mean value obtained for the sample. Other two stars have large parallax uncertainties, but still consistent with the average value.

Focusing on proper motions, they are all consistent with membership in Cygnus OB2. Our stellar sample with proper motion uncertainties below 0.1 mas yr^{-1} have mean values of $\mathrm{pm_{RA}} = -2.5 \pm 0.05$ mas yr^{-1} and $\mathrm{pm_{Dec}} = -3.85 \pm 0.06$ mas yr^{-1}.

We therefore conclude that our sample belongs to the normal population of Cygnus OB2 and does not include any runaway star.

3. Spectroscopic analysis

We have followed the same methodology as Simón-Díaz (2010), where the details of the FASTWIND grid used (that includes

A&A 620, A56 (2018)

Table 2. Sample of the selected eight early-type slow rotators observed with ISIS at the WHT.

Object	SpT (this work)	SpT (other works)	B (mag)	Coordinates (°)	$v \sin i$ (km s^{-1})	S/N(b)	S/N(r)	R(b)	R(r)
J20334610+4133010	O9.7 Iab	O9.7 Iab[1]	11.2	308.44 +41.55	55	180	230	13600	9300
J20295701+4109538	O9.7 III	B0V[2]	13.0	307.49 +41.16	70	110	160	13600	9300
J20314965+4128265	O9.7 IV	O9III[3]	12.6	307.96 +41.47	30	180	230	13600	9300
J20272428+4115458	B0 IV	O9.5V[4]	12.6	306.85 +41.26	20	110	220	13600	9300
J20292449+4052599	B0.2 IV	B0.2 IV[4]	13.8	307.35 +40.88	75	100	130	7500	9300
J20314605+4043246	B0.5 IV	B0.5 IV[2]	13.8	307.94 +40.72	60	100	150	7500	9300
BD+40 4210	B2 Ia	B1III:e[4]	12.2	307.77 +40.52	30	130	150	13600	9300
BD+40 4193	B2 V	B1V[5]	10.4	307.31 +40.68	70	150	250	13600	9300

Notes. Columns give their names, spectral types (from this and other works), B magnitudes, coordinates (J2000.0 epoch) and derived rotational velocities. The spectral signal to noise (per pixel) ratio and resolving power (per element) are also indicated. B magnitudes are taken from Comerón & Pasquali (2012). (b) and (r) refer to the blue and red optical range spectra respectively.
References. Spectral type source: (1) Maíz Apellániz et al. (2016), (2) Hanson (2003), (3) Kiminki et al. (2007), (4) Comerón & Pasquali (2012), and (5) Berlanas et al. (2018).

Table 3. *Gaia* sources, parallaxes and proper motions from the second *Gaia* data release.

Target	*Gaia* name	Parallax (mas)	pm$_{RA}$ (mas yr^{-1})	pm$_{Dec}$ (mas yr^{-1})
J20314965+4128265	2067847502568383744	0.595 ± 0.032	−3.09 ± 0.05	−4.18 ± 0.04
J20295701+4109538	2067816681882846464	0.587 ± 0.024	−3.15 ± 0.04	−4.58 ± 0.04
J20272428+4115458	2067642233192106624	0.349 ± 0.027	−2.96 ± 0.04	−3.67 ± 0.05
J20334610+4133010	2067928660269306496	0.590 ± 0.449	1.21 ± 0.85	−1.46 ± 0.77
J20314605+4043246	2067742877164542080	0.377 ± 0.256	−1.26 ± 0.48	−4.38 ± 0.42
J20292449+4052599	2067429168454304896	0.585 ± 0.027	−2.24 ± 0.04	−3.71 ± 0.05
BD+40 4193	2067425461902141056	0.750 ± 0.035	−0.39 ± 0.05	−2.38 ± 0.06
BD+40 4210	2067734012352626816	0.653 ± 0.057	−3.17 ± 0.09	−4.61 ± 0.11

Notes. Parallax errors do not contain the systematic uncertainty discussed by Arenou et al. (2018), Lindegren et al. (2018), and Stassun & Torres (2018).

H I, He I-II, Si II-III-IV and O II) and the considered atomic models are provided. In addition, we have extended the grid to lower gravities for the supergiants analysis.

3.1. Spectral classification

We have reclassified the eight selected stars since the new spectra obtained in this work have, for many of them, a higher quality than in previous studies. We have classified the O-type stars using the MGB tool (Maíz Apellániz et al. 2012). It compares the observed spectra with a grid of O standards (in this work the GOSSS library, see Maíz Apellániz et al. 2016), allowing us to vary spectral type, luminosity class, velocity and resolution until obtaining a best match. For B-type stars we used templates gathered in the framework of the IACOBsweG spectroscopic survey (Simón-Díaz et al. 2015; Negueruela et al., in prep.) to obtain the spectral types. The new classification of the selected stellar sample is presented in Table 2 together with that from other works.

3.2. Equivalent widths

We have carried out an analysis based on equivalent widths (EW) of metal lines, similar to the method used in Orion by Simón-Díaz (2010). We used our own IDL[2] routines to identify metal lines in the observed spectra, and to measure the EWs and their uncertainties. For each line, a multi-Gaussian fit of the observed line profile is done in a spectral range of $\lambda_o \pm 2$ max[$v \sin i\ \lambda_o$/c, 0.5λ_o/R] around the laboratory wavelength of the line. The uncertainty is obtained by assuming the continuum at $\pm(S/N)^{-1}$, and comparing the value obtained by means of the Gaussian fitting with the value derived by integrating the line profile. Measured EWs are given in Appendix B.

[2] Interactive Data Language Proprietary software distributed by Research Systems, Inc. of Boulder, CO now a division of Kodak.

3.3. Stellar parameters

Both parameters, effective temperature ($T_{\rm eff}$) and surface gravity (log g), were obtained by comparing the EW ratio of Si II-III or Si III-IV (depending on the effective temperature of the star) and the wings of the H Balmer lines with FASTWIND stellar atmosphere models (Santolaya-Rey et al. 1997; Puls et al. 2005). We first used the silicon line ratios to obtain the initial values of $T_{\rm eff}$ for different log g values (e.g., Fig. 3, top). Then, the models obtained by setting each set of these parameters were compared with the wings of the observed H Balmer lines (e.g., Fig. 3, bottom) to iteratively obtain the final values for both parameters.

We have used the ratios EW(Si IV λ4116)/EW(Si III λ4552) and EW(Si II λ4130)/EW(Si III λ4552) as $T_{\rm eff}$ indicators, depending on the temperature of the star, because these are the strongest, unblended lines typically present in the stellar spectrum (at the spectral types of our targets and in the range of ∼4000–5000 Å). On the other hand, due to the good agreement between $T_{\rm eff}$ determined using Si III-IV and the He I-II ionization balance found by Simón-Díaz (2010), the He I-II ionization equilibrium has been used for the star J20292449+4052599 because only Si III lines were suitable for the stellar parameter determination in the observed spectrum.

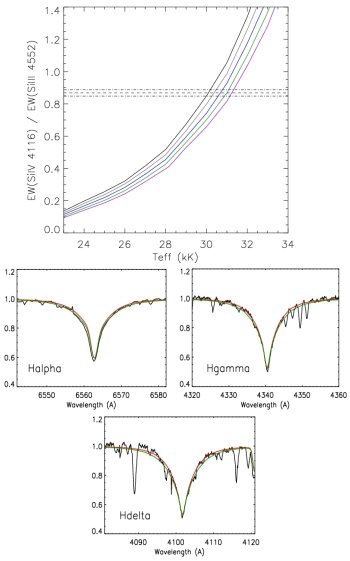

Fig. 3. *Top*: Example of the EW ratio of Si III-IV used as $T_{\rm eff}$ indicator with FASTWIND models for the star J20272428+4115458. Black, gray, blue, green and purple lines correspond to log g values of 3.9, 4.0, 4.1, 4.2 and 4.3 dex respectively. The horizontal dashed line indicates the EW ratio of the star and its associated uncertainty is indicated by the dash-dotted lines. *Bottom*: Example of the H Balmer lines fitting to determine log g for the same star. Only two FASTWIND models are compared with the observed spectrum (black line) for clarity. In red, the $T_{\rm eff}$ = 30 000 K, log g = 3.9 dex model. In green, the $T_{\rm eff}$ = 31 000 K, log g = 4.2 dex model. Final fits can be seen in Figs. C.1–C.8.

Table 4. Stellar parameters derived for the sample of stars by using the Si III-IV or Si II-III ionization equilibrium along with the H Balmer lines.

Target	SpT	$T_{\rm eff}$ (K)	log g (dex)
J20314965+4128265	O9.7 IV	33 000	4.0
J20295701+4109538	O9.7 III	32 000	3.6
J20272428+4115458	B0 IV	30 000	3.9
J20334610+4133010	O9.7 Iab	30 000	3.2
J20314605+4043246	B0.5 IV	30 000	4.0
J20292449+4052599	B0.2 IV	29 000*	3.7
BD+40 4193	B2 V	19 000	3.8
BD+40 4210	B2 Ia	18 300	2.2

Notes. $T_{\rm eff}$ and log g uncertainties are, in all cases, 500 K and 0.1 dex respectively. An asterisk indicates that $T_{\rm eff}$ has been obtained using the He I-II ionization balance.

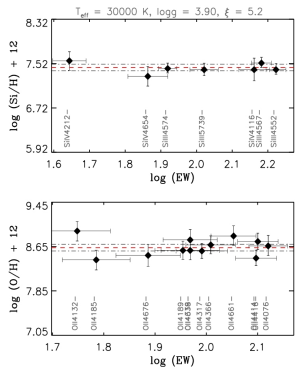

Fig. 4. Example of the silicon (*top*) and oxygen (*bottom*) abundance versus *EW* diagrams for the star J20272428+4115458. All the observed Si III-IV and O II lines are indicated in the plots. The red dashed line indicates the weighed mean abundance (fit to the data), and the gray dash-dotted lines the standard weighed deviation.

Derived $T_{\rm eff}$ uncertainties from *EWs* of Si II-III-IV lines are, for all our stars, lower than 500 K. For the surface gravity we obtain an accuracy better than 0.1 dex. Taking into account the additional uncertainty sources (like continuum normalization) we follow the reasoning by Sabín-Sanjulián et al. (2017) and adopt in all cases errors of ±500 K and ±0.1 dex for $T_{\rm eff}$ and log g, respectively. Derived values are shown in Table 4.

3.4. Silicon and oxygen abundances

We applied the curve-of-growth method to derive silicon and oxygen abundances, considering a grid of HHeSiO FASTWIND models for a set of stellar parameters ($T_{\rm eff}$ and log g). For each star, the abundance is obtained for different values of microturbulence and for each line considered. Then, we determined the final abundance value considering the microturbulence that, for all lines, gives a similar value (see Fig. 4). More details can be found in, for example, Kilian (1992) or Simón-Díaz (2010). We have used all the lines available in our spectra, except those too faint or blended with other lines and that can not be properly separated by our IDL routines (see Sect. 3.2) at the resolving power of the analyzed spectra. This is, for example, the case for the blend of Si IV λ4089 and O II λ4089 lines. Other cases that we have also carefully checked are Si IVλ4631, and Si II λ6347, λ3856 since they could be blended with N II λ4631, Mg II λ6347, and O II λ3856, respectively.

In the FASTWIND oxygen grid, only lines from one ionization state were available (O II), so we could not use the oxygen ionization equilibrium. Therefore, we adopted for the oxygen abundance analysis the same stellar parameters as in the silicon analysis, including microturbulence. Although

A&A 620, A56 (2018)

Table 5. Microturbulences (ξ) and final abundance values (ϵ_x, in units of $12 + \log(X/H)$) derived for our stellar sample.

Target	ξ	ϵ_{Si}	$\Delta\epsilon_{Si}(\sigma)$	$\Delta\epsilon_{Si}(\xi)$	$\Delta\epsilon_{Si}(T_{eff}, \log g)$	ϵ_O	$\Delta\epsilon_O(\sigma)$	$\Delta\epsilon_O(\xi)$	$\Delta\epsilon_O(T_{eff}, \log g)$
J20314965+4128265	3.0	7.67	0.06	0.08	0.07	8.75	0.07	0.02	0.11
J20295701+4109538	7.5	7.61	0.09	0.12	0.07	8.74	0.10	0.07	0.13
J20272428+4115458	5.2	7.45	0.06	0.07	0.05	8.63	0.06	0.12	0.07
J20334610+4133010	17.0	7.54	0.02	0.04	0.08	8.57	0.07	0.10	0.09
J20314605+4043246	5.6	7.54	0.09	0.12	0.05	8.82	0.10	0.12	0.02
J20292449+4052599	6.8	7.47	0.07	0.10	0.12	8.51	0.15	0.02	0.05
BD+40 4193	5.9	7.44	0.11	0.12	0.10	8.70	0.20	0.13	0.10
BD+40 4210	13.3	7.53	0.01	0.09	0.07	8.48	0.06	0.07	0.10

Notes. Abundance uncertainties associated with microturbulence ($\Delta\epsilon(\xi)$), the standard weighted deviation in the line-by-line abundances ($\Delta\epsilon(\sigma)$), and those related to the stellar parameters ($\Delta\epsilon(T_{eff}, \log g)$) are indicated separately.

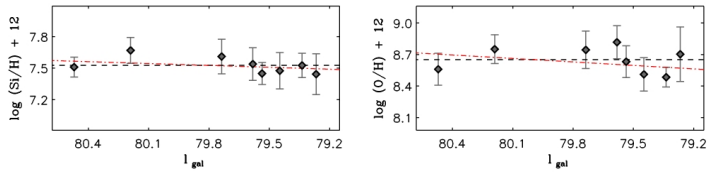

Fig. 5. Derived silicon (*left*) and oxygen (*right*) abundance versus Galactic longitude in degrees. Dashed black line indicates the mean abundance value and dash-dotted red line the best fit to the data. Vertical lines indicate abundance errors, that include uncertainties related to the stellar parameters, microturbulence and the standard weighed deviation in the line-by-line abundances.

Simón-Díaz (2010) used the microturbulence obtained from the O II lines, we are more limited in the number of suitable spectral lines and decided to use the microturbulence derived from the silicon lines to avoid spurious results. In Appendix B the results of the silicon and oxygen abundance analysis obtained for each line are detailed, where the uncertainties related to the errors in EWs ($\Delta\epsilon$), the standard weighted deviation in the line-by-line abundances ($\Delta\epsilon(\sigma)$) and the uncertainties associated with the microturbulence ($\Delta\epsilon(\xi)$) are indicated.

We observed no clear dependence between the derived abundances and T_{eff}. However, due to the strong sensitivity of some line EWs to temperature we check the effect of varying T_{eff} in ±500 K (taking the corresponding gravity variation into account). In the case of silicon, the presence of two ionization stages already restricts the abundance range. In contrast, in the case of oxygen, only lines from one ionization state were available, and therefore the derived abundance is quite sensitive to small changes in temperature. Simón-Díaz (2010) tested this effect in a sample of early dwarf B stars. He showed that the minimum variation in oxygen abundance occurs for $T_{eff} \sim 27\,000$ K, increasing toward higher and lower effective temperatures. We find the same behavior in our study.

4. Results and discussion

4.1. Chemical composition

Table 5 gives the microturbulence (ξ) and final abundance values (where $\epsilon_x = 12 + \log(X/H)$) derived for our stellar sample. It also shows the uncertainties in the derived abundances associated with the uncertainties in microturbulence ($\Delta\epsilon(\xi)$), the standard weighted deviation in the line-by-line abundances ($\Delta\epsilon(\sigma)$) and the impact that a modification of T_{eff} by ±500 K and $\log g$ by ±0.1 dex have on the derived abundances ($\Delta\epsilon(T_{eff}, \log g)$).

Figure 5 represents the derived silicon and oxygen abundances as a function of Galactic longitude for our sample of stars. We find chemical homogeneity for both elements, and derive mean silicon and oxygen values of 7.53 dex and 8.65 dex, respectively, that represent the mean abundance values of Cygnus OB2. The standard deviation for the silicon abundance is 0.08 dex and for the oxygen abundance 0.12 dex. The intrinsic uncertainties (related to the microturbulence, dispersion line-by-line and stellar parameters) are on average on the order of the dispersion in abundances (around 0.1 dex for both silicon and oxygen). The larger dispersion obtained for oxygen, in comparison with silicon, is partially due to the fact that only one ionization state is available for the oxygen analysis, while two ionization states are available for silicon (Si II-III or Si III-IV, depending on the temperature).

Thus our results indicate a homogeneous composition for our stellar sample, without evidence of a dependence on the Galactic longitude (which, according to Comerón & Pasquali (2012) or Berlanas et al. (2018) correlates with stellar age). Appendix C shows the individual spectra with the best fitting FASTWIND model including H I, He I-II, Si II-III-IV and O II.

4.2. Self-enrichment scenario

In order to see whether we can provide some constraints on the metallicity enrichment within star-forming clouds in spite of the small variations obtained for the oxygen and silicon abundances, we estimate in this section the enrichment produced by stellar

winds and SNe that may have polluted the region in the last 30 Myr. This is roughly the time span during which a cluster would contain stars hotter than 20 000 K according the evolutionary tracks with and without rotation by Ekström et al. (2012) and Limongi & Chieffi (2018).

In the following we assume an Initial Mass Function between 0.1 and 120 $M_\odot$ with a slope $\alpha = -2.3$, as in Comerón et al. (2016). We also assume three star formation histories (SFH): (1) An Instantaneous Burst (IB) having taken place 16 Myr ago (corresponding roughly to the age when the number of red supergiants (RSGs) is maximum along the IB evolution for solar metallicity models by Ekström et al. 2012). This scenario shows the enrichment due to stars more massive than 15 $M_\odot$ and it is used as an estimate of the maximum possible enrichment speed (see below). (2) A stair-like SFH with a constant value Φ_1 in the last 6 Myr plus a constant value $\Phi_2 = \frac{1}{6}\Phi_1$ for ages larger than 6 Myr (see again Comerón et al. 2016); in our case we have extended Φ_2 up to 46 Myr which is the maximum age where RSGs (defined as stars with $\log L/L_\odot \gtrsim 4$ and $T_{\rm eff} \lesssim 4000$ K) would be present in a system, hence the lower limit where Comerón et al. (2016) SFH inference is applicable. And (3) a linearly increasing SFH from $\Phi(t_{\rm now}-30\,{\rm Myr}) = \frac{1}{6}\Phi(t_{\rm now})$–$\Phi(t_{\rm now})$, where $t_{\rm now}$ is the present moment and which is a linear approximation of the previous case; this SFH extends down to 35 Myr (larger ages produce negative values). We have used yields and stellar lifetimes from Limongi & Chieffi (2018), solar metallicity evolutionary models[3] (see also Prantzos et al. 2018), which include three initial rotational velocities $v_{\rm rot}$ (0, 150 and 300 km s^{-1}), and two SNe scenarii: a first one where all stars produce SNe explosions, and a second one where stars more massive than 25 $M_\odot$ suffer a direct collapse to black holes. In all cases the enrichment due to stellar winds in the pre-SNe phase (hydrostatic enrichment) has been taken into account, although we have assumed that the hydrostatic enrichment is released to the ISM at the end of the evolution of the star together with the SNe contribution. However, stellar winds produce a minimal effect in the abundance, when defined as a ratio (see below). We note that the variation of the yields with the metallicity has not been considered; this choice is justified a posteriori given the small variation of the total abundance. For all SFHs we have followed the evolution of the total, H, O and Si masses released to the ISM as the stellar populations evolves. As usual in synthesis models computations, the result are normalized to total mass of ever formed stars (i.e., $\int_{\rm SFH\,begins}^{t_{\rm now}} \Phi(t)\,dt = 1\,M_\odot$). Such choice allows to compare the different SFHs self consistently since the total normalized mass of the ejected material is equal in all cases (we would like to point out that normalized mass refers to mean mass values of the underling possible distribution (see Cerviño & Luridiana 2006) because to make choice of an absolute value of the total mass implies to provide an study of the related (sampling) distribution, which is outside the scope of this paper[4]). The only differences among the SFHs are the speed in which such material is released, being the IB case the faster case since all stars have equal ages and the only delay is due to the stellar evolution lifetimes.

In order to obtain the chemical enrichment, we assumed a close system with a global efficiency of 10%, being the efficiency the ratio between total amount of gas ever transformed into stars (the integral over time of the SFH up to present time) and the total mass of the system. We note that efficiency is enough to follow the enrichment evolution of ISM if sampling effects are neglected, since the absolute value of the total mass cancels out when the O/H is computed. As a final note, the initial metallicity assumed in computations and given by the tracks, log(O/H) + 12 = 8.70 dex, is larger than the possible oxygen abundance of Cygnus OB2. As a result, rather than the nominal values of the abundance, we are interested in the abundance variation and how the slope of the chemical enrichment varies with time and, in particular, in the last 20–25 Myr when the present O-type stars were formed.

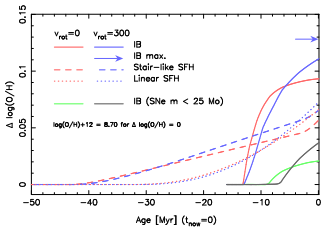

Fig. 6. Time evolution of the log O/H variation obtained from solar metallicity chemical evolution models, using three different SFHs (an IB and two extended SFH, both with a difference of a factor of six between the actual SF value and the value 30 Myr ago, but with different shapes), and two SNe cases: one where all massive stars produce a SNe explosion and another where stars more massive than 25 $M_\odot$ suffer a direct collapse to black holes (where only the IB case is shown). In all cases a star formation efficiency of 10% is assumed. The arrow in the top right shows the maximum enrichment reached by the three SFHs.

The result of the chemical evolution variation is shown in Fig. 6 for the case of O/H (results for Si/H are similar, although with a slightly narrower range of variation). We note that since we are working with the O/H ratio, the enrichment is driven by the populations where (a) the O/H of the ejected material differs significantly from the initial one, and (b) their overall contribution is large in comparison with the other stars which release material to the ISM. Such situation is only meet by the SNe contribution. Actually, there is almost no abundance variation in the IB case where stars more massive than 25 $M_\odot$ collapse to black holes (red and blue solid lines) up to the age when star less massive than 25 $M_\odot$ explode as SNe (green and black solid lines). As a secondary effect, the possible enrichment saturates with time, since the O/H of the ejected material approaches to the initial value when the initial stellar mass decreases. Actually, all models reach a steady state value of the enrichment when extended to larger (future) ages, provided the SFHs stops at $t_{\rm now}$. Such steady state is reached around 25 Myr after the onset of the burst in the IB case, and it is shown in the figure by an horizontal arrow for the extreme case of maximum enrichment. We stress that it does not means that there is no more oxygen released to the ISM, but that such oxygen enrichment is compensated by the hydrogen enrichment. The figure shows that differences between evolutionary models with and without rotation is not larger than 0.02 dex (5%) beyond present-day accuracies in the spectral analysis. On the other hand, the scenario where all stars produce a SNe explosion (red and blue solid lines, with a maximum possible enrichment of 0.14 dex) and that where

[3] Available at http://orfeo.iaps.inaf.it
[4] The current modeling is based on Cerviño et al. (2001) and Cerviño & Mollá (2002) studies, and we refer to these papers the study of sampling distributions in the context of chemical evolution.

A&A 620, A56 (2018)

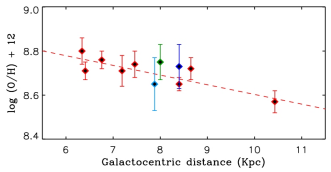

Fig. 7. Spatial distribution of the oxygen abundance as a function of Galactocentric distances for Galactic H II regions (red dots), the mean value obtained for Orion OB1 (dark blue dot), the mean value obtained for the solar vicinity (green dot) and the mean value obtained for Cygnus OB2 (light blue dot). The red dashed line represents the least-squares linear fits to the H II regions. The Sun is assumed at 8 kpc.

only stars less massive than 25 $M_{\odot}$ produce a SNe (green and black solid lines, with a maximum enrichment of 0.05 dex) could be distinguished with techniques like those used in the present work, provided that we extend our sample and/or increase the S/N of the spectra. The only quantity we can constrain is the star forming efficiency. With values significantly larger than the one adopted here (10%) we would see metallicity variations in our sample. Finally, if we would firmly constrain the age of the different stars, it would be much easier to discriminate between different SFHs. *Gaia* DR2 and future DR3 data may be unvaluable to this aim. However, given that the different scenarios produce metallicity variations which are similar to the uncertainties in abundance determination of the current analysis, we conclude that the massive star forming activity during the last 20–25 Myr in Cygnus OB2 has not caused any detectable increase in its O/H and Si/H abundance, within the limitations of the present study, in agreement with the findings in Orion by Simón-Díaz (2010) or Biazzo et al. (2011a).

4.3. The Galactic context

Our abundance results are in agreement with the values obtained in Orion OB1 for a sample of early-B type stars (Simón-Díaz 2010), and also with those obtained for a sample of unevolved early B-type stars in the solar neighborhood (Przybilla et al. 2008). Both studies result in a small dispersion of abundances, indicating a homogeneity of oxygen and silicon among B-type stars.

Regarding oxygen, we find a mean abundance value slightly below the one obtained in both Orion OB1 and the solar vicinity. In order to check whether they are consistent with the oxygen radial abundance gradient of the Milky Way, we have compared these values with the work of Esteban et al. (2005). They presented homogeneous data of eight H II regions with Galactocentric distances (R_G) between 6.3 and 10.4 kpc using recombination lines and assuming the Sun at 8 kpc from the Galactic center. Figure 7 shows the spatial distribution of the oxygen abundance as a function of R_G for the considered Galactic H II regions and the mean values obtained for Orion OB1, the solar vicinity, and Cygnus OB2. All of them are consistent with the observed abundance gradient derived from H II regions in the Milky Way and its dispersion. Although one would expect a large abundance value for Cygnus OB2 due to its shorter Galactocentric distance, the average value is consistent within uncertainties with the Orion OB1, the solar neighborhood and the H II regions. Our conclusion is that the observed scatter associated with individual measurements of Milky Way H II regions at a given Galactocentric distance is at least of the same order than within a cluster or association.

5. Summary and conclusions

We have presented the spectroscopic analysis of eight late O, early B stars in Cygnus OB2 using the curve-of-growth method to derive silicon and oxygen abundances. We have used high S/N, high resolution spectra obtained with ISIS at the WHT, and FASTWIND stellar atmosphere models. Our targets are early-type slow rotators ($v \sin i < 80\,\mathrm{km\,s^{-1}}$) with temperatures below 34 000 K selected from a list of 57 spectroscopically classified OB stars in Cygnus OB2. They have late O or early B spectral type so that we can use their Si II-III-IV lines for our abundance analysis, and are distributed all across the association area. According to *Gaia* data there is no evidence of a peculiar behavior indicating a runaway origin of our stellar sample. Thus, the silicon and oxygen abundances of the targeted stars are considered to reflect those of the cloud out of which the stars formed.

The abundance analysis was based on the EW of silicon and oxygen lines and the Balmer line profiles. We first obtain the fundamental parameters ($T_{\rm eff}$ and $\log g$) by comparing the EW ratio of Si II-III or Si II-IV, depending on the temperature of each star, and the observed wings of H Balmer lines with FASTWIND models. Then, using these parameters, the abundance was computed for different values of microturbulence and for each line considered. Finally, we determined the final abundance value considering the microturbulence that, for all lines, gives the same abundance value.

Both silicon and oxygen analyses suggest a homogeneous stellar chemical composition in Cygnus OB2. We find a mean abundance value of 7.53 dex for silicon and 8.65 dex for oxygen, with a standard deviation of 0.08 dex and 0.12 dex, respectively.

We roughly estimate the contribution to oxygen enrichment of SNe that may have exploded in the region, concluding that the original cloud from which stars formed in the last 20–25 Myr in Cygnus OB2 had a homogeneous metallicity and has not been significantly enriched during its lifetime as a consequence of its star forming activity in agreement with the findings in Orion OB1 and the solar vicinity. All these studies are consistent with the spatial abundance distribution for H II regions in the Milky Way. The oxygen abundance scatter based on H II regions at a given Galactocentric distance is of the same order than within a cluster or association. Therefore, abundance gradients at the local scale, like Cygnus OB2 or Orion OB1, are not expected. We estimate that the effect of self-enrichment by stellar winds and SNe is beyond the accuracy of our analyses, except for the star forming efficiency that cannot be significantly larger than the value of 10% adopted here.

Our computations illustrate the difficulties of making quantitative predictions on the level of enrichment expected in a massive association like Cygnus OB2, and show in any case that such level should be small as compared to the accuracies currently attainable.

Acknowledgements. We thank the referee for useful and valuable comments that helped improve this paper. We also thank F. Najarro, M. A. Urbaneja, and D. J. Lennon for helpful discussions and comments. We thank J. Maíz Apellániz for advice on the use of MGB and L. López-Martín for advice on spectral data reduction. We acknowledge financial support from the Spanish Ministry of Economy and Competitiveness (MINECO) under the grants AYA 2015-68012-C2-01 and Severo Ochoa SEV-2015-0548 and the Gobierno de Canarias under grant

ProID-2017010115. AP acknowledges support from Sonderforschungsbereich SFB 881 "The Milky Way System" (subproject B5) of the German Research Foundation (DFG).

References

Abdo, A. A., Ackermann, M., Ajello, M., et al. 2009, Science, 325, 840
Arenou, F., Luri, X., Babusiaux, C., et al. 2018, A&A, 616, A17
Barrera-Ballesteros, J. K., Heckman, T., Sanchez, S. F., et al. 2018, ApJ, 852, 74
Bednarek, W. 2003, MNRAS, 345, 847
Berlanas, S. R., Herrero, A., Comerón, F., et al. 2018, A&A, 612, A50
Biazzo, K., Randich, S., & Palla, F. 2011a, A&A, 525, A35
Biazzo, K., Randich, S., Palla, F., & Briceño, C. 2011b, A&A, 530, A19
Butt, Y. M., Drake, J., Benaglia, P., et al. 2006, ApJ, 643, 238
Camilo, F., Ray, P. S., Ransom, S. M., et al. 2009, ApJ, 705, 1
Cerviño, M., & Mollá, M. 2002, A&A, 394, 525
Cerviño, M., & Luridiana, V. 2006, A&A, 451, 475
Cerviño, M., Gómez-Flechoso, M. A., Castander, F. J., et al. 2001, A&A, 376, 422
Comerón, F., & Pasquali, A. 2012, A&A, 543, A101
Comerón, F., Djupvik, A. A., Schneider, N., & Pasquali, A. 2016, A&A, 586, A46
Cunha, K., & Lambert, D. L. 1992, ApJ, 399, 586
Cunha, K., & Lambert, D. L. 1994, ApJ, 426, 170
Cunha, K., Hubeny, I., & Lanz, T. 2012, Eur. Phys. J. Web Conf., 19, 08005
Dufton, P. L., Smartt, S. J., Lee, J. K., et al. 2006, A&A, 457, 265
Dufton, P. L., Langer, N., Dunstall, P. R., et al. 2013, A&A, 550, A109
Ekström, S., Georgy, C., Eggenberger, P., et al. 2012, A&A, 537, A146
Esteban, C., García-Rojas, J., Peimbert, M., et al. 2005, ApJ, 618, L95
Gaia Collaboration (Brown, A. G. A., et al.) 2018, A&A, 616, A1
Hanson, M. M. 2003, ApJ, 597, 957
Huang, W., & Gies, D. R. 2006, ApJ, 648, 580
Kilian, J. 1992, A&A, 262, 171
Kiminki, D. C., Kobulnicky, H. A., Kinemuchi, K., et al. 2007, ApJ, 664, 1102
Knödlseder, J., Cerviño, M., Le Duigou, J.-M., et al. 2002, A&A, 390, 945
Langer, N. 2012, ARA&A, 50, 107
Limongi, M., & Chieffi, A. 2018, ApJS, 237, 13
Lindegren, L., Hernandez, J., Bombrun, A., et al. 2018, A&A, 616, A2
Maíz Apellániz, J., Pellerin, A., Barbá, R. H., et al. 2012, Proceedings of a Scientific Meeting in Honor of Anthony, ed. F. J. Moffat, 465, 484
Maíz Apellániz, J., Sota, A., Arias, J. I., et al. 2016, ApJS, 224, 4
Martin, P., Knödlseder, J., Diehl, R., & Meynet, G. 2009, A&A, 506, 703
Martin, P., Knödlseder, J., Meynet, G., & Diehl, R. 2010, A&A, 511, A86
Massey, P., & Thompson, A. B. 1991, A&A, 101, 1408
Morgan, W. W., Code, A. D., & Whitford, A. E. 1955, ApJS, 2, 41
Negueruela, I., Marco, A., Herrero, A., & Clark, J. S. 2008, A&A, 487, 575
Nieva, M.-F., & Simón-Díaz, S. 2011, A&A, 532, A2
Palla, F. 2011, EAS, 51, 245
Prantzos, N., Abia, C., Limongi, M., Chieffi, A., & Cristallo, S. 2018, MNRAS, 476, 3432
Przybilla, N., Nieva, M.-F., & Butler, K. 2008, ApJ, 688, L103
Puls, J., Urbaneja, M. A., Venero, R., et al. 2005, A&A, 435, 669
Rygl, K. L. J., Brunthaler, A., Sanna, A., et al. 2012, A&A, 539, A79
Sabín-Sanjulián, C., Simón-Díaz, S., Herrero, A., et al. 2017, A&A, 601, A79
Santolaya-Rey, A. E., Puls, J., & Herrero, A. 1997, A&A, 323, 488
Simón-Díaz, S. 2010, A&A, 510, A22
Simón-Díaz, S., & Herrero, A. 2007, A&A, 468, 1063
Simón-Díaz, S., & Herrero, A. 2014, A&A, 562, A135
Simón-Díaz, S., Negueruela, I., Maíz Apellániz, J., et al. 2015, Highlights of Spanish Astrophysics VIII, 576
Spina, L., Randich, S., Magrini, R. D., et al. 2017, A&A, 601, A70
Stassun, K. G., & Torres, G. 2018, ApJ, 862, 61
Suzuki, A., & Maeda, K. 2018, ApJ, 852, 101
Tan, J. C., Beltrán, M. T., Caselli, P., et al. 2014, Protostars and Planets VI, eds. H. Beuthler, R. S. Klessen, C. P. Dullemond, & T. Henning (University of Arizona Press), 149
Wolff, S. C., Strom, S. E., Dror, D., & Venn, K. 2007, A&A, 133, 1092
Wright, N. J., Drew, J. E., & Mohr-Smith, M. 2015, MNRAS, 449, 741
Zinnecker, H., & Yorke, H. W. 2007, ARA&A, 45, 481

A&A 620, A56 (2018)

Appendix A: Rotational velocities

Table A.1 shows the whole list of stars observed in July 2014 and August 2012 at the WHT. Names, spectral types and the derived rotational velocities are indicated.

Table A.1. Stars observed in July 2014 and August 2012 at the WHT.

Target	SpT	Ref.	Coordinates (°)	$v \sin i$ (km s^{-1})
J20332346+4109130	O6IV((f))	G16	308.35 +41.15	100
J20331326+4113287	O6V	K07	308.30 +41.22	240
HD195213	O7	M55	307.13 +40.82	90
J20334086+4130189	O7V	K07	308.42 +41.50	55
J20310019+4049497	O7V((f))	H03	307.75 +40.83	95
J20341350+4135027	O7.5(n)((f))z	G16	308.56 +41.58	190
J20323857+4125137	O7.5IV(n)	G16	308.16 +41.42	195
J20315961+4114505	O7.5Vz	G16	307.99 +41.25	185
J20342959+4131455	O7.5V(n)((f))*	G16	308.62 +41.53	325
J20293563+4024315	O8IIIz	B18	307.39 +40.41	60
J20332674+4110595	O8.5Vz	G16	308.36 +41.18	95
J20340486+4105129	O8.5V	C12	308.52 +41.08	45
J20333030+4135578	O8V	M91	308.37 +41.59	120
J20323486+4056174	O8V	N08	308.14 +40.94	130
J20325002+4123446	O8V	K07	308.21 +41.39	85
J20325919+4124254	O8V	K07	308.25 +41.41	155
J20330292+4117431	O8V	K07	308.26 +41.29	175
J20331803+4121366	O8V	K07	308.32 +41.36	110
J20313749+4113210	O9:	M55	307.91 +41.22	115
J20311055+4131535	O9V	M55	307.79 +41.53	235
J20301839+4053466	O9V	C12	307.57 +40.89	55
J20321656+4125357	O9V	K07	308.07 +41.43	215
J20332101+4117401	O9V	K07	308.34 +41.29	130
J20323033+4034332	O9.5IV	H03	308.13 +40.57	120
J20293480+4120089	O9.5V	C12	307.39 +41.33	80
J20341605+4102196	O9.5V	C12	308.57 +41.04	175
J20291617+4057372	O9.7III	B18	307.32 +40.96	100
J20295701+4109538	O9.7III	New	307.49 +41.16	70
J20335952+4117354	O9.7V(n)	G16	308.49 +41.29	335
J20323968+4050418	B0II	B18	308.16 +40.84	75
J20272428+4115458	B0IV	New	306.85 +41.26	20
J20340601+4108090	B0V	C12	308.52 +41.13	145
J20331050+4122224	B0V	K07	308.29 +41.37	110
J20305552+4054541	B0V	N08	307.73 +40.91	180
J20312210+4112029	B0.2III	C12	307.84 +41.20	245
J20292449+4052599	B0.2IV	C12	307.35 +40.88	75
J20321568+4046170	B0.2IV	C12	308.06 +40.77	45
J20330526+4143367	B0.5III	B18	308.27 +41.73	115
J20314605+4043246	B0.5IV	H03	307.94 +40.72	60
J20282772+4104018	B0.5V	C12	307.11 +41.07	305
J20294666+4105083	B0.5V(n)	H03	307.44 +41.08	140
J20340435+4108078	B1III	C12	308.52 +41.13	310
BD+40 4208	B1V	B18	307.71 +40.74	165
J20293473+4020381	B1V*	C12	307.39 +40.34	330
J20303297+4044024	B1V	C12	307.64 +40.73	195
J20303833+4010538	B1V	C12	307.66 +40.18	255
J20313338+4122490	B1V	K07	307.89 +41.38	175
J20314341+4100021	B1V*	B18	307.93 +41.00	370
J20273982+4040384	B1V	C12	306.91 +40.68	175
J20315898+4107314	B1V*	B18	307.99 +41.12	325
J20303297+4044024	B1V	C12	307.64 +40.73	255
BD+40 4210	B2Ia	New	307.77 +40.52	30
BD+40 4193	B2V	New	307.31 +40.68	70
J20322734+4055184	B2V	H03	308.11 +40.92	200
J20354703+4053012	B2V	C12	308.94 +40.88	215
CCDM J20323+4152AB	B9V	B18	308.09 +41.87	110
J20315984+4120354	A	B18	307.99 +41.34	55

Notes. Names, spectral types, coordinates (J2000.0) and the derived projected rotational velocities are indicated. Asterisks indicate possible SB2 stars, whose spectral types are refereed to the primary component.
References. Spectral type source: (B18) Berlanas et al. (2018), (C12) Comerón & Pasquali (2012), (G16) Maíz Apellániz et al. (2016), (H03) Hanson (2003), (K07) Kiminki et al. (2007), (M91) Massey & Thompson (1991), (N08) Negueruela et al. (2008), and (M55) Morgan et al. (1955), (New) This work.

Appendix B: Individual targets

Tables B.1–B.8 show the detailed results of the silicon and oxygen abundance analysis line-by-line for each star of the sample. Abundances ($\xi(x)$) are given in units of $12 + \log(X/H)$. We also indicate the final weighed mean value ($\bar{\epsilon}$) and the uncertainties related to the errors in EW measurements ($\Delta\epsilon$), the standard weighed deviation ($\Delta\epsilon(\sigma)$) and the uncertainties associated with the microturbulence ($\Delta\epsilon(\xi)$).

Table B.1. Detailed results of the silicon and oxygen abundance analysis line-by-line for the star J20314965+4128265 ($T_{\rm eff}$ = 33 000 K, $\log g$ = 4.0 dex and ξ(Si) = ξ(O) = 3.0 km s^{-1}).

Line	EW (mÅ)	$\epsilon_{\rm Si} \pm \Delta\epsilon_{\rm Si}$ (dex)
Si III 4552	129 ± 20	7.83 ± 0.32
Si III 4567	103 ± 13	7.78 ± 0.22
Si III 4574	55 ± 6	7.72 ± 0.13
Si III 5739	70 ± 20	7.60 ± 0.17
Si IV 4116	171 ± 41	7.61 ± 0.36
Si IV 4631	99 ± 9	7.63 ± 0.12
Si IV 6701	68 ± 6	7.63 ± 0.12
		$\bar{\epsilon_{\rm Si}}$ = 7.67
		$\Delta\epsilon_{\rm Si}(\sigma)$ = 0.06, $\Delta\epsilon_{\rm Si}(\xi)$ = 0.08
Line	EW (mÅ)	ϵ(O) ± $\Delta\epsilon_{\rm O}$ (dex)
O II 4317	66 ± 15	8.62 ± 0.24
O II 4319	74 ± 15	8.77 ± 0.26
O II 4366	88 ± 15	8.95 ± 0.26
O II 4414	81 ± 15	8.47 ± 0.24
O II 4416	91 ± 15	8.86 ± 0.24
O II 4638	72 ± 15	8.94 ± 0.31
O II 4661	88 ± 15	9.01 ± 0.28
O II 4676	65 ± 15	8.76 ± 0.32
O II 4072	102 ± 15	8.95 ± 0.31
O II 4076	101 ± 15	8.72 ± 0.13
O II 4189	56 ± 15	8.45 ± 0.30
		$\bar{\epsilon_{\rm O}}$ = 8.75
		$\Delta\epsilon_{\rm O}(\sigma)$ = 0.07, $\Delta\epsilon_{\rm Si}(\xi)$ = 0.02

Table B.2. Detailed results of the silicon and oxygen abundance analysis line-by-line for the star J20295701+4109538 ($T_{\rm eff}$ = 32 000 K, $\log g$ = 3.6 dex and ξ(Si) = ξ(O) = 7.5 km s^{-1}).

Line	EW (mÅ)	$\epsilon_{\rm Si} \pm \Delta\epsilon_{\rm Si}$ (dex)
Si III 4552	138 ± 15	7.58 ± 0.16
Si III 4567	108 ± 15	7.60 ± 0.17
Si IV 4116	241 ± 15	7.63 ± 0.17
Si IV 4212	81 ± 15	7.66 ± 0.22
		$\bar{\epsilon_{\rm Si}}$ = 7.61
		$\Delta\epsilon_{\rm Si}(\sigma)$ = 0.09, $\Delta\epsilon_{\rm Si}(\xi)$ = 0.12
Line	EW (mÅ)	ϵ(O) ± $\Delta\epsilon_{\rm O}(\sigma)$ (dex)
O II 4641	125 ± 15	8.74 ± 0.14
O II 4076	130 ± 15	8.75 ± 0.15
		$\bar{\epsilon_{\rm O}}$ = 8.74
		$\Delta\epsilon_{\rm O}(\sigma)$ = 0.10, $\Delta\epsilon_{\rm Si}(\xi)$ = 0.07

Table B.3. Detailed results of the silicon and oxygen abundance analysis line-by-line for the star J20272428+4115458 ($T_{\rm eff}$ = 30 000 K, $\log g$ = 3.9 dex and ξ(Si) = ξ(O) = 5.2 km s^{-1}).

Line	EW (mÅ)	$\epsilon_{\rm Si} \pm \Delta\epsilon_{\rm Si}$ (dex)
Si III 4552	167 ± 11	7.41 ± 0.14
Si III 4567	152 ± 10	7.53 ± 0.13
Si III 4574	83 ± 8	7.43 ± 0.12
Si III 4539	105 ± 10	7.41 ± 0.16
Si IV 4116	145 ± 20	7.41 ± 0.29
Si IV 4212	44 ± 9	7.57 ± 0.23
Si IV 4654	73 ± 14	7.29 ± 0.25
		$\bar{\epsilon_{\rm Si}}$ = 7.45
		$\Delta\epsilon_{\rm Si}(\sigma)$ = 0.06, $\Delta\epsilon_{\rm Si}(\xi)$ = 0.09
Line	EW (mÅ)	ϵ(O) ± $\Delta\epsilon_{\rm O}$ (dex)
O II 4317	98 ± 15	8.57 ± 0.19
O II 4319	093 ± 16	8.58 ± 0.24
O II 4366	102 ± 15	8.68 ± 0.23
O II 4414	125 ± 15	8.44 ± 0.19
O II 4416	126 ± 15	8.74 ± 0.20
O II 4638	93 ± 15	8.77 ± 0.26
O II 4661	113 ± 15	8.84 ± 0.24
O II 4676	77 ± 15	8.49 ± 0.27
O II 4076	132 ± 15	8.66 ± 0.25
O II 4132	56 ± 12	8.93 ± 0.23
O II 4185	61 ± 13	8.41 ± 0.23
O II 4189	90 ± 15	8.58 ± 0.21
		$\bar{\epsilon_{\rm O}}$ = 8.63
		$\Delta\epsilon_{\rm O}(\sigma)$ = 0.06, $\Delta\epsilon_{\rm O}(\xi)$ = 0.12

Table B.4. Detailed results of the silicon and oxygen abundance analysis line-by-line for the star J20334610+4133010 ($T_{\rm eff}$ = 30 000 K, $\log g$ = 3.2 dex and ξ(Si) = ξ(O) = 17.0 km s^{-1}).

Line	EW (mÅ)	$\epsilon_{\rm Si} \pm \Delta\epsilon_{\rm Si}$ (dex)
Si III 4552	188 ± 21	7.42 ± 0.12
Si III 4567	148 ± 16	7.49 ± 0.09
Si III 4574	72 ± 15	7.57 ± 0.15
Si IV 4116	445 ± 30	7.70 ± 0.06
Si IV 4631	100 ± 20	7.37 ± 0.23
		$\bar{\epsilon_{\rm Si}}$ = 7.54
		$\Delta\epsilon_{\rm Si}(\sigma)$ = 0.02, $\Delta\epsilon_{\rm Si}(\xi)$ = 0.04
Line	EW (mÅ)	ϵ(O) ± $\Delta\epsilon_{\rm O}$ (dex)
O II 4317	98 ± 15	8.76 ± 0.15
O II 4366	97 ± 20	8.69 ± 0.20
O II 4069	110 ± 20	8.45 ± 0.18
O II 4076	126 ± 20	8.43 ± 0.17
O II 4132	34 ± 10	8.49 ± 0.15
		$\bar{\epsilon_{\rm O}}$ = 8.57
		$\Delta\epsilon_{\rm O}(\sigma)$ = 0.07, $\Delta\epsilon_{\rm O}(\xi)$ = 0.10

A&A 620, A56 (2018)

Table B.5. Detailed results of the silicon and oxygen abundance analysis line-by-line for the star J20314605+4043246 ($T_{\rm eff}$ = 30 000 K, $\log g$ = 4.0 dex and ξ(O) = ξ(Si) = 5.6 km s^{-1}).

Line	EW (mÅ)	$\epsilon_{\rm Si} \pm \Delta\epsilon_{\rm Si}$ (dex)
Si III 4552	185 ± 15	7.49 ± 0.17
Si III 4567	156 ± 20	7.50 ± 0.24
Si III 4574	97 ± 10	7.52 ± 0.14
Si III 5739	150 ± 20	7.77 ± 0.23
Si IV 4116	140 ± 20	7.42 ± 0.29
		$\bar{\epsilon_{\rm Si}}$ = 7.54
		$\Delta\epsilon_{\rm Si}(\sigma)$ = 0.09, $\Delta\epsilon_{\rm Si}(\xi)$ = 0.12
Line	EW (mÅ)	ϵ(O) ± $\Delta\epsilon_{\rm O}$ (dex)
O II 4366	111 ± 20	8.74 ± 0.29
O II 4452	83 ± 15	9.04 ± 0.24
O II 4661	91 ± 20	8.55 ± 0.34
O II 4676	104 ± 20	8.79 ± 0.33
O II 6641	63 ± 15	9.14 ± 0.28
O II 6721	48 ± 15	8.54 ± 0.29
O II 4076	137 ± 20	8.67 ± 0.33
O II 4132	56 ± 15	8.90 ± 0.30
O II 4189	104 ± 20	8.71 ± 0.29
	Final value	$\bar{\epsilon_{\rm O}}$ = 8.82
		$\Delta\epsilon_{\rm O}(\sigma)$ = 0.10, $\Delta\epsilon_{\rm O}(\xi)$ = 0.12

Table B.6. Detailed results of the silicon and oxygen abundance analysis line-by-line for the star J20292449+4052599 ($T_{\rm eff}$ = 29 000 K, $\log g$ = 3.7 dex and ξ(O) = ξ(Si) = 6.8 km s^{-1}).

Line	EW (mÅ)	$\epsilon_{\rm Si} \pm \Delta\epsilon_{\rm Si}$ (dex)
Si III 4552	222 ± 15	7.49 ± 0.25
Si III 4567	185 ± 15	7.47 ± 0.08
Si III 4574	112 ± 15	7.48 ± 0.19
		$\bar{\epsilon_{\rm Si}}$ = 7.47
		$\Delta\epsilon_{\rm Si}(\sigma)$ = 0.07, $\Delta\epsilon_{\rm Si}(\xi)$ = 0.10
Line	EW (mÅ)	ϵ(O) ± $\Delta\epsilon_{\rm O}$ (dex)
O II 4366	89 ± 20	8.37 ± 0.29
O II 4076	145 ± 20	8.59 ± 0.30
O II 4661	115 ± 20	8.65 ± 0.29
O II 4676	88 ± 20	8.44 ± 0.31
		$\bar{\epsilon_{\rm O}}$ = 8.51
		$\Delta\epsilon_{\rm O}(\sigma)$ = 0.15, $\Delta\epsilon_{\rm O}(\xi)$ = 0.02

Table B.7. Detailed results of the silicon and oxygen abundance analysis line-by-line for the star BD+40 4193 ($T_{\rm eff}$ = 19 000 K, $\log g$ = 3.8 dex and ξ(O) = ξ(Si) = 5.9 km s^{-1}).

Line	EW (mÅ)	$\epsilon_{\rm Si} \pm \Delta\epsilon_{\rm Si}$ (dex)
Si II 6347	107 ± 20	7.45 ± 0.27
Si III 4552	113 ± 15	7.47 ± 0.22
Si III 4567	86 ± 11	7.40 ± 0.19
Si III 4574	57 ± 15	7.54 ± 0.34
Si III 5739	43 ± 15	7.40 ± 0.39
		$\bar{\epsilon_{\rm Si}}$ = 7.44
		$\Delta\epsilon_{\rm Si}(\sigma)$ = 0.11, $\Delta\epsilon_{\rm Si}(\xi)$ = 0.12
Line	EW (mÅ)	ϵ(O) ± $\Delta\epsilon_{\rm O}$ (dex)
O II 4366	37 ± 15	8.84 ± 0.40
O II 4650	52 ± 15	8.63 ± 0.31
O II 4661	34 ± 15	8.86 ± 0.41
O II 4072	25 ± 15	8.38 ± 0.42
		$\bar{\epsilon_{\rm O}}$ = 8.70
		$\Delta\epsilon_{\rm O}(\sigma)$ = 0.20, $\Delta\epsilon_{\rm O}(\xi)$ = 0.13

Table B.8. Detailed results of the silicon and oxygen abundance analysis line-by-line for the star BD+40 4210 ($T_{\rm eff}$ = 18 300 K, $\log g$ = 2.2 and ξ(O) = ξ(Si) = 13.3 km s^{-1}).

Line	EW (mÅ)	$\epsilon_{\rm Si} \pm \Delta\epsilon_{\rm Si}$ (dex)
Si II 6347	89 ± 20	7.52 ± 0.14
Si III 4552	397 ± 16	7.50 ± 0.08
Si III 4567	340 ± 20	7.51 ± 0.16
Si III 4574	212 ± 15	7.46 ± 0.14
Si III 5739	370 ± 20	7.53 ± 0.01
		$\bar{\epsilon_{\rm Si}}$ = 7.53
		$\Delta\epsilon_{\rm Si}(\sigma)$ = 0.01, $\Delta\epsilon_{\rm Si}(\xi)$ = 0.09
Line	EW (mÅ)	ϵ(O) ± $\Delta\epsilon_{\rm O}$ (dex)
O II 4317	111 ± 15	8.43 ± 0.20
O II 4366	120 ± 15	8.43 ± 0.19
O II 4414	146 ± 20	8.37 ± 0.20
O II 4416	124 ± 20	8.47 ± 0.21
O II 4438	133 ± 15	8.66 ± 0.20
O II 4650	251 ± 15	8.63 ± 0.15
O II 4661	134 ± 15	8.55 ± 0.20
O II 4676	100 ± 15	8.37 ± 0.22
O II 6721	47 ± 15	8.30 ± 0.22
O II 4189	53 ± 15	8.47 ± 0.22
		$\bar{\epsilon_{\rm O}}$ = 8.48
		$\Delta\epsilon_{\rm O}(\sigma)$ = 0.06, $\Delta\epsilon_{\rm O}(\xi)$ = 0.07

Appendix C: Fitting line models

Figures C.1–C.8 show, for each selected sample star, several H, He, Si and O spectral lines and the best fitting model derived from our abundance analysis.

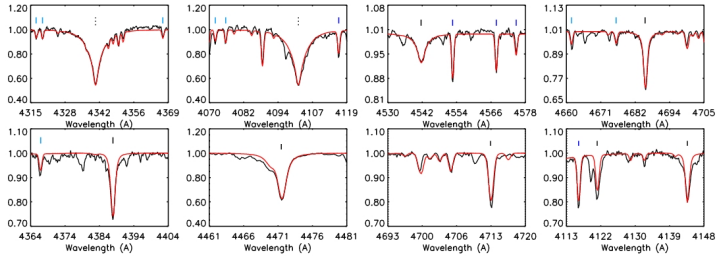

Fig. C.1. Best-fit HHeSiO model ($T_{\rm eff}$ = 33 000 K, log g = 4.0 dex, ξ(Si) = ξ(O) = 3.0 km s^{-1}, log(Si/H) = −4.20 dex, log(O/H) = −3.30 dex) to the observed spectrum of J20314965+4128265. Si and O lines used in the analysis are indicated with dark and light blue vertical lines, respectively. H and He lines are indicated with dotted and solid black vertical lines for reference.

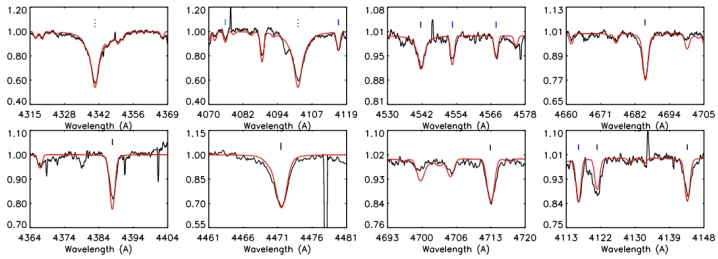

Fig. C.2. Best-fit HHeSiO model ($T_{\rm eff}$ = 32 000 K, log g = 3.6 dex, ξ(Si) = ξ(O) = 7.5 km s^{-1}, log(Si/H) = −4.50 dex, log(O/H) = −3.30 dex) to the observed spectrum of J20295701+4109538. Sort lines mark the positions of Si, O, H and He lines, as in Fig C.1.

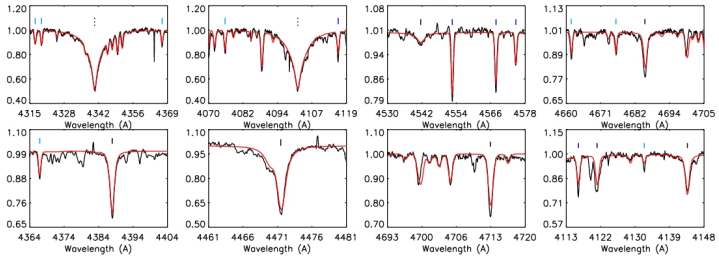

Fig. C.3. Best-fit HHeSiO model ($T_{\rm eff}$ = 30 000 K, log g = 3.9 dex, ξ(Si) = ξ(O) = 5.2 km s^{-1}, log(Si/H) = −4.50 dex, log(O/H) = −3.30 dex) to the observed spectrum of J20272428+4115458. Sort lines mark the positions of Si, O, H and He lines, as in Fig C.1.

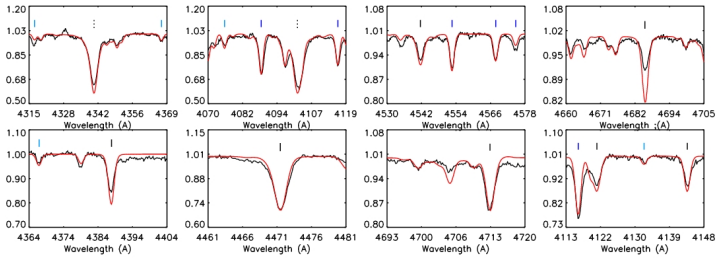

Fig. C.4. Best-fit HHeSiO model ($T_{\rm eff}$ = 30 000 K, log g = 3.2 dex, ξ(Si) = ξ(O) = 17.0 km s^{-1}, log(Si/H) = −4.50 dex, log(O/H) = −3.40 dex) to the observed spectrum of J20334610+4133010. Sort lines mark the positions of Si, O, H and He lines, as in Fig C.1.

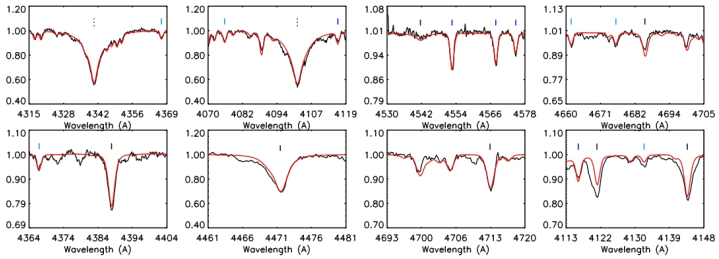

Fig. C.5. Best-fit HHeSiO model ($T_{\rm eff}$ = 30 000 K, log g = 4.0 dex, ξ(Si) = ξ(O) = 5.6 km s^{-1}, log(Si/H) = −4.50 dex, log(O/H) = −3.30 dex) to the observed spectrum of J20314605+4043246. Sort lines mark the positions of Si, O, H and He lines, as in Fig C.1.

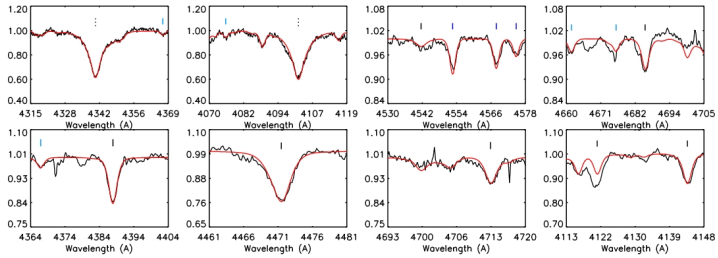

Fig. C.6. Best-fit HHeSiO model ($T_{\rm eff}$ = 29 000 K, log g = 3.7 dex, ξ(Si) = ξ(O) = 6.8 km s^{-1}, log(Si/H) = −4.50 dex, log(O/H) = −3.30 dex) to the observed spectrum of J20292449+4052599. Sort lines mark the positions of Si, O, H and He lines, as in Fig C.1.

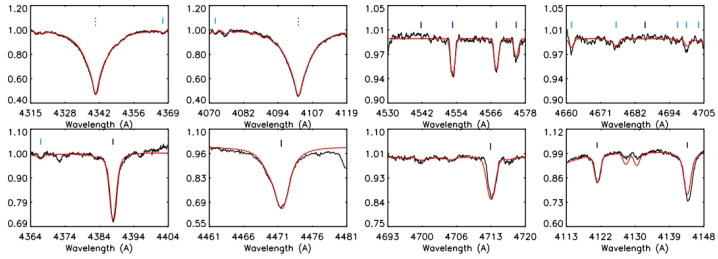

Fig. C.7. Best-fit HHeSiO model ($T_{\rm eff}$ = 19 000 K, log g = 3.8 dex, ξ(Si) = ξ(O) = 5.9 km s^{-1}, log(Si/H) = −4.50 dex, log(O/H) = −3.30 dex) to the observed spectrum of BD+40 4193. Sort lines mark the positions of Si, O, H and He lines, as in Fig C.1.

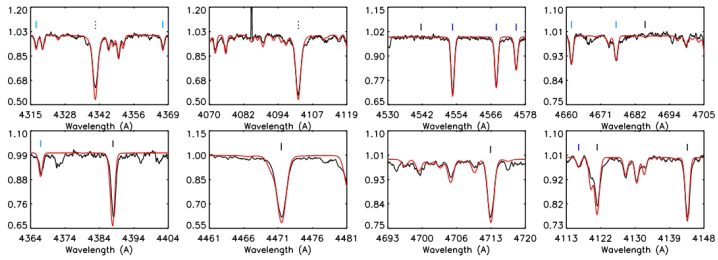

Fig. C.8. Best-fit HHeSiO model ($T_{\rm eff}$ = 18 300 K, log g = 2.20 dex, ξ(Si) = ξ(O) = 13.3 km s^{-1}, log(Si/H) = −4.50 dex, log(O/H) = −3.40 dex) to the observed spectrum of BD+40 4210. Sort lines mark the positions of Si, O, H and He lines, as in Fig C.1.

5

Disentangling the spatial substructure of Cygnus OB2 from *Gaia* DR2

In the third paper of this thesis, and for the first time ever, we have explored the spatial substructure of the Cygnus OB2 association using parallaxes from the recent second *Gaia* data release. We have created a parameterised model to reproduce the observed parallax distribution since an inference procedure is needed due to the non-linearity of the parallax-distance transformation and the asymmetry of the resulting probability distribution. By using the MCMC ensemble sampler *emcee* and an unbinned maximum likelihood test we have been able to unveil two different stellar populations within the association. We find the main Cygnus OB2 group at ∼1760 pc, further away than previously thought, and a foreground group separated from it by several hundred parsecs, at ∼1370 pc. We have finally calculated individual membership probabilities and discussed outliers as possible non-members of the association.

Monthly Notices of the ROYAL ASTRONOMICAL SOCIETY
MNRAS **484,** 1838–1842 (2019) doi:10.1093/mnras/stz117
Advance Access publication 2019 January 16

Disentangling the spatial substructure of Cygnus OB2 from *Gaia* DR2

S. R. Berlanas,[1,2]★ N. J. Wright,[3] A. Herrero,[1,2] J. E. Drew [4] and D. J. Lennon[1,5]
[1]*Instituto de Astrofísica de Canarias, E-38200 La Laguna, Tenerife, Spain*
[2]*Departamento de Astrofísica, Universidad de La Laguna, E-38205 La Laguna, Tenerife, Spain*
[3]*Astrophysics Group, Keele University, Keele ST5 5BG, UK*
[4]*School of Physics, Astronomy & Mathematics, University of Hertfordshire, Hatfield AL10 9AB, UK*
[5]*ESA, European Space Astronomy Centre, Apdo. de Correos 78, E-28691 Villanueva de la Cañada, Madrid, Spain*

Accepted 2019 January 9. Received 2019 January 8; in original form 2018 November 28

ABSTRACT

For the first time, we have explored the spatial substructure of the Cygnus OB2 association using parallaxes from the recent second *Gaia* data release. We find significant line-of-sight substructure within the association, which we quantify using a parametrized model that reproduces the observed parallax distribution. This inference approach is necessary due to the non-linearity of the parallax distance transformation and the asymmetry of the resulting probability distribution. Using a Markov Chain Monte Carlo ensemble sampler and an unbinned maximum likelihood test, we identify two different stellar groups superposed on the association. We find the main Cygnus OB2 group at ∼1760 pc, further away than recent estimates have envisaged, and a foreground group at ∼1350 pc. We also calculate individual membership probabilities and identify outliers as possible non-members of the association.

Key words: astrometry – parallaxes – stars: distances – stars: early-type – stars: massive – open clusters and associations: individual: Cygnus OB2.

1 INTRODUCTION

A key difficulty in the study of Milky Way massive stars and OB associations has been the large uncertainty in their distances, hindering the comparison with theories of stellar and cluster evolution. They are needed to place the stars in the Hertzsprung–Russell diagram (HRD), obtaining a better comparison of stellar masses and radii derived from the spectroscopic analyses and the evolutionary codes (a persistent problem in the field of massive stars, see Herrero et al. (1992); Repolust, Puls & Herrero 2004; Massey et al. 2012; Markova & Puls 2015).

The recent second data release (DR2) from the *Gaia* satellite (Gaia Collaboration 2016, 2018) has provided unprecedented high-quality astrometry for more than 1.3 billion objects, all with measured parallaxes. Parallax uncertainties (excluding a conservative systematic error up to 0.1 mas, see Luri et al. 2018) are around 0.04 mas for bright sources ($G < 14$ mag), around 0.1 mas for sources with a G magnitude ∼17, and around 0.7 mas for the faintest ($G \sim 20$ mag). This scenario provides a unique opportunity to inspect the internal structure of Galactic young open clusters and relatively nearby massive OB associations.

The Cygnus OB2 association is one of the most massive OB associations at less than 2 kpc from the Sun (Knödlseder 2003; Rygl et al. 2012). Hosting hundreds of OB stars, it is the most obvious example of recent star formation in the massive Cygnus-X complex. Its massive star population has been widely studied, including membership (Massey & Thompson 1991; Knödlseder 2000; Comerón et al. 2002; Hanson 2003; Negueruela et al. 2008; Comerón & Pasquali 2012; Berlanas et al. 2018a), mass function (Kiminki et al. 2007; Wright et al. 2015), extinction (Hanson 2003; Comerón & Pasquali 2012; Guarcello et al. 2012; Wright et al. 2015), and chemical composition (Berlanas et al. 2018b) studies. The distribution of stellar ages extends beyond 20 Myr (Comerón et al. 2016) and a correlation between age and Galactic longitude exists, suggesting that massive star formation has proceeded from lower to higher Galactic longitudes (Comerón & Pasquali 2012; Berlanas et al. 2018a). The significant spatial (Wright et al. 2014) and kinematic substructure found by Wright et al. (2016) could indicate that Cygnus OB2 is made up of different individual subgroups. However, an uncertainty over whether all its OB stellar content is at the same distance persists. The high-precision *Gaia* DR2 parallaxes could therefore be used to properly study and unravel the spatial substructure of this association. Differentiating internal subgroups will help to understand the star formation process, origin, and evolution of the association, as well as better characterize the stellar content in the region.

This paper is organized as follows. In Section 2, we present the data and selection criteria. In Section 3, the modelling approach used in this work is detailed. In Section 4, we show the results of the best-fitting model and membership probabilities. A discussion of these results is provided in Section 5. Finally, we summarize the work in Section 6.

★ E-mail: srberlan@iac.es

2 DATA

2.1 Stellar sample

The sample of stars used for this study is comprised of known OB members of Cygnus OB2 within a radius of 1° of the coordinates $l = 79.8°$ and $b = +0.8°$. We gathered stars from the samples of Wright et al. (2015) and Berlanas et al. (2018a), the former of which is a census of spectroscopic members gathered from the literature (e.g. Massey & Thompson 1991; Comerón et al. 2002; Hanson 2003; Kiminki et al. 2007), while the latter expands this work to include more stars over a wider area. This produced a sample of 229 members of Cygnus OB2, 167 of which are located in the core of the region (see Fig. 1).

2.2 *Gaia* DR2 parallaxes

Astrometry for this work was taken from *Gaia* DR2 (Gaia Collaboration 2018). We included stars that have astrometry that passed the selection criteria recommended by L. Lindegren based on the renormalized unit weight error (or RUWE), defined as $u_{\rm norm} = u/u_0(G, C)$ where $u = (\texttt{astrometric\_chi2\_al}/\texttt{astrometic\_n\_good\_obs\_al} - 5)^{1/2}$, and $u_0(G, C)$ is a smooth function in magnitude (G) and colour ($C = G_{BP} - G_{RP}$).[1] We adopted RUWE $\leq$ 1.4 as the selection criterion for good astrometric solutions, as recommended in the above cited technical note. This cut caused us to discard 29 stars, resulting in a sample of 200 targets with reliable *Gaia* astrometry. We also note that all the targets of our sample meet with the $\texttt{visibility\_periods\_used} > 8$ criterion, which is a key recommendation from the data release papers (Arenou et al. 2018; Lindegren et al. 2018). The final stellar sample used for this work and those stars discarded by the selection criteria are available in electronic form at the CDS and at MNRAS online.

Gaia DR2 parallax uncertainties are derived from the formal errors computed in the astrometric processing. Additional systematic uncertainties of up to 0.1 mas exist and depend on factors such as the position on the sky, magnitude, and colour of the targets (Lindegren et al. 2018). Since our goal is not to obtain absolute distances for individual sources but to resolve internal substructure of the association, we only consider the relative parallaxes of sources in the association. We do not expect the systematic error to vary across our sample since our field of view is relatively small (1°), and our sample has similar magnitudes and colours. Therefore, systematic parallax uncertainties are not included in our analysis, but are added when absolute distances are calculated (as will the parallax zero-point offset of −0.03 mas, Lindegren et al. 2018).

3 MODELLING METHOD

The observed parallax distribution of our sample (see Fig. 2, in black) peaks at about 0.6 mas, but is wider than would be expected if it's width was entirely due to parallax uncertainties. The distribution also shows evidence for multiple groups along the line of sight. Therefore, instead of estimating the distance to the association based on the average parallax we model the parallax distribution as a series of groups, each with an inherent width and different distance.

To infer the distance to the Cygnus OB2 association, we use a parametrized model of the distance to the association to reproduce the observed parallax distribution of the massive stars. The model predicts a distribution of parallaxes that is then compared to the observed distribution in parallax space. This Bayesian inference process is critical when using parallaxes because of the non-linearity of the transformation between these quantities and the asymmetry of the resulting probability distribution (Bailer-Jones 2015).

We model the stellar population assuming it is composed of N components, each of which contains a fraction of the total stellar content, f_N, and have distances that follow a Gaussian distribution. Each component therefore has free parameters for the centre, d_N, and standard deviation, σ_N, of each Gaussian, as well as an additional $N - 1$ parameters to represent the fraction of stars in each component. Thus, the model has a total of $3N - 1$ parameters. We use wide and linear priors, allowing the central distances for each component of the association to vary in the range of 1–2 kpc and the standard deviations to vary from 0 to 1 kpc.

The posterior distribution was sampled using the Markov Chain Monte Carlo affine-invariant ensemble sampler *emcee* (Foreman-Mackey et al. 2013) with 500 walkers and 10 000 iterations. The model was compared to the observations using an unbinned maximum likelihood test. The posterior distributions were found to follow a normal distribution, and thus the median value of each parameter was used as the best fit, with the 16th and 84th percentiles used for the 1σ uncertainties.

4 RESULTS

We applied the Shapiro–Wilk test (Shapiro & Wilk 1965) to the observed parallax distribution, which evidences that it does not follow a single normal distribution. The p-value returned (10^{-27}) rejects the null hypothesis that the data come from a single normally distributed population. We then fit the observed distribution with both 2- and 3-component models (see Fig. 2 and Table 1) and determine which provides the best fit using the Bayesian information criterion (BIC, see Schwarz 1978), which applies a penalty to the likelihood of more complex models so that models with different numbers of parameters can be compared.

We find that the 2-component model provides the lowest BIC and therefore the best fit to the data. Fig. 2 corroborates that the observed parallax distribution does not fit well with a single component, and the 3-component one does not offer enough improvement. Hence, we do not investigate more complex models and choose the 2-component model as representative of the observed distribution. Two different groups can be clearly distinguished, with approximate central distances of 1350^{+45}_{-60} (rand) $^{+210}_{-160}$ (syst.) pc and 1755^{+25}_{-19} (rand) $^{+373}_{-261}$ (syst.) pc (systematic uncertainties take into account the 0.1 mas systematic parallax uncertainty in *Gaia* DR2), showing a significant distance separation between the two groups.

Based on our 2-component model fit we calculated, for each star, membership probabilities for each of the populations: the foreground group (at ∼1350 pc, henceforth Group 1), the main group (at ∼1760 pc, henceforth Group 2), and whether they are foreground or background contaminants (Group 3). We then assign stars to each of these classes based upon their membership probabilities. If a star has a >75 per cent probability of belonging to group 1 or 2, then it is assigned to that group. For a star to be flagged as a foreground or background contaminant, we require a higher probability (or effectively a lower probability that it is not a member of the other groups) of >99 per cent. And finally, there is a group of objects that we cannot reliably place in any group (Group 0). Fig. 3 shows the parallax distribution of the sources in

[1] See technical note GAIA-C3-TN-LU-LL-124-01 available at https://www.cosmos.esa.int/web/gaia/public-dpac-documents

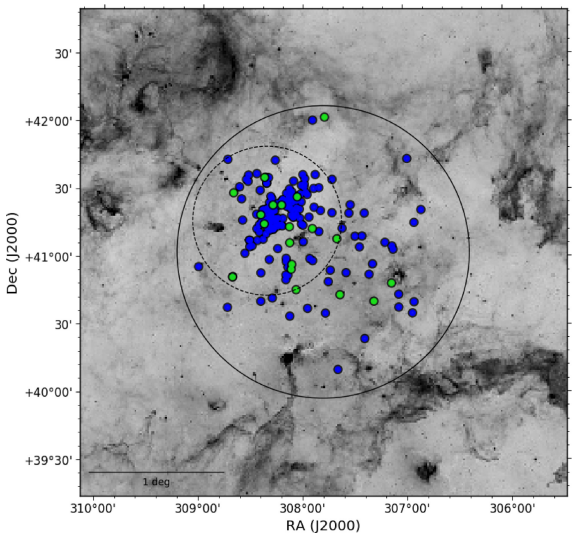

Figure 1. Inverse Spitzer 8 μm image showing the location of the two main stellar groups found in the region (see Section 4 for further details). The blue colour represents stars from the main Cygnus OB2 population, and the green colour represents those stars found to be in a foreground group. The solid line circle delimits the 1° radius area adopted in this work. For reference, the dash-dotted line circle shows the area considered by Wright, Drew & Mohr-Smith (2015) indicating the core of the association.

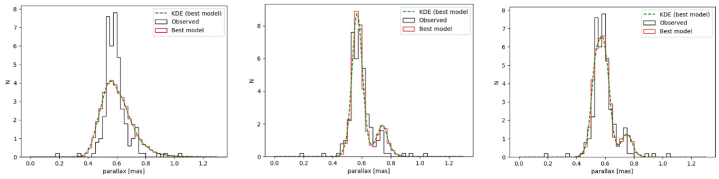

Figure 2. Normalized parallax distribution of the Cygnus OB2 sources (in black) and the derived best-fitting models (in red). The green colour represents a kernel density estimation using Gaussian kernels. The left-hand, middle, and right-hand panels show the 1-, 2- and 3-component distributions, respectively.

each group, coloured green (Group 1), blue (Group 2), grey (Group 3), or red (Group 0). Membership groups of the final stellar sample are available in electronic form at the CDS and at MNRAS online.

While *Gaia* DR2 data are not as well characterized in the Galactic Plane as out of it, for the observed substructure to originate from errors or biases in the data would require systematic offsets of at least 0.2 mas in parallax, significantly larger than any quoted uncertainties or systematics in the data (Gaia Collaboration 2018). We can also find no difference in the distributions of RUWE values or parallax uncertainties between the stars in the two main groups.

Table 1. Statistical data of the obtained Gaussian distributions based on 1-, 2-, and 3-component best-fitting models.

	Model 1	Model 2		Model 3		
N	1	1	2	1	2	3
d_N (pc)	1706 $^{+33}_{-32}$	1350 $^{+45}_{-59}$	1755 $^{+23}_{-19}$	1328 $^{+42}_{-42}$	1676 $^{+34}_{-39}$	1872 $^{+36}_{-40}$
σ_N (pc)	268 $^{+41}_{-39}$	33 $^{+23}_{-16}$	31 $^{+26}_{-17}$	32 $^{+18}_{-16}$	34 $^{+13}_{-13}$	24 $^{+11}_{-11}$
Fraction (per cent)	100	19	81	11	50	39

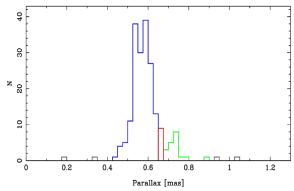

Figure 3. Stellar sample subdivided and colour-coded by membership group. Groups 1 and 2 are represented with the green and blue colour, respectively, while the red colour indicates sources with parallaxes between those of Groups 1 and 2 that cannot be placed in confidently assigned to either group (Group 0). The grey colour represents foreground and background contaminants (Group 3).

5 DISCUSSION

5.1 Spatial structure

We have modelled the parallax distribution of Cygnus OB2, resolving for the first time its spatial structure along the line of sight. Although our analysis is restricted to the OB population, Wright et al. (2014) showed that low- and high-mass stars are distributed in the same way, without evidence of mass segregation. We have distinguished between two clusterings, distributed on the sky as shown in Fig. 1. The centres of the two groups projected on the sky are not very different. Given the low density and extended nature of the foreground population, it is possible that it extends beyond our field of view. The statistical parameters obtained for each group distribution (d_N and σ_N of Model 2, see Table 1) suggest that the two groups are spatially separate. We consider the larger population to be the main Cygnus OB2 association (Group 2) and consider the foreground population to be a separate group approximately ∼400 pc in the foreground (Group 1).

The distance of the foreground group of ∼1350 pc puts it at a similar distance to Cygnus-X as a whole (see Rygl et al. 2012) suggesting that the main part of Cygnus OB2 is actually behind Cygnus-X by several hundred parsecs (though the line-of-sight depth of Cygnus-X is not well constrained). Consequently, the main group is more distant than previously thought, and therefore its stellar content will both be more luminous (approximately 1.5 times more luminous compared to the estimates in Wright et al. 2015) and more massive. Interestingly, this puts the distance to the main part of Cygnus OB2 closer to that originally derived by Massey & Thompson (1991).

5.2 The foreground group

We have identified 19 stars in the foreground group (∼10 per cent of the sample), seven of them classified as O-type stars. The bright BD + 40 4212 double system ($G = 9.39$ mag) is included in this group, as well as the star HD 195213 ($G = 8.38$ mag). This group includes approximately 10 per cent of the total population of O-type stars in Cygnus OB2, and thus its total mass can be estimated as a similar fraction of the total mass of 16 500 $M_\odot$ estimated by Wright et al. (2015), i.e. 1650 $M_\odot$, similar to that of the Orion Nebula Cluster (although according to our results, the estimation by Wright et al. 2015 will have to be corrected upwards). We note that the foreground group is appreciably more dispersed on the sky than the main group. The proper motions also suggest it to be more diffuse and less likely to be a bound group. This could suggest that it is a part of older foreground population that extends further outside our field of view. However, a detailed study of the physical properties of its stellar content is needed to establish the most probable scenario.

5.3 Potential contaminants

Here, we discuss the sources identified as probable foreground or background contaminants (Group 3) and not part of either the main Cyg OB2 population or the foreground group.

(i) *Foreground contaminants*: HD 196305 is a very luminous star and has a parallax that places it at a distance of 333^{+5}_{-5} pc, in agreement with previous studies that suggest it to be a foreground contaminant (Chentsov et al. 2013). CCDMJ20323 + 4152AB has been reported as a visual double star by Gili & Bonneau (2001) and therefore its binary nature could be affecting the parallax. MT91-426 and MT-170 also appear as foreground sources, despite the fact that Wright et al. (2015) proposed them as background sources based on their position in the HRD. This could suggest either erroneous photometry of spectral classification, particularly in the luminosity class (e.g. a subdwarf nature).

(ii) *Background contaminants*: J20272428 + 4115458 was classified as a B0IV star by Berlanas et al. (2018b) for which *Gaia* DR2 provides a parallax value of 0.35 ± 0.03 mas. It has a G magnitude of 11.4 mag, so the parallax uncertainty could be underestimated by up to 30 per cent. If we also add in possible systematic errors, this star is compatible with the main Cygnus OB2 population, but tentatively we suggest it as a background contaminant. For MT91-459 (J20331433 + 4119331), *Gaia* DR2 provides a parallax of 0.19 ± 0.04 mas, clearly indicating a background contaminant.

Although the highly massive, reddened, and luminous Cyg OB2 #12 hypergiant has been discarded by the astrometric selection criteria (RUWE = 1.56 for this star), we highlight that *Gaia* DR2 places it significantly in the foreground at a distance of 840^{+105}_{-85} pc (Bailer-Jones et al. 2018). There are good reasons to doubt such a small inferred distance: The star has a peculiar spectrum suggesting very high luminosity and a large extinction (e.g. Clark et al. 2012); the astrometry could reflect light centre variations in what is potentially a large angular diameter object (see Salas, Maíz Apellániz & Barbá 2015). Given these issues, it is appropriate that it has been excluded here.

6 CONCLUSIONS

The structure of young star clusters and associations is fundamental to our understanding of their formation and dynamical evolution, as well as of their stellar content. In this work, we have used *Gaia* DR2 parallaxes to study the 3D structure of the Cygnus OB2 association, finding significant spatial substructure along the line of sight.

We fitted the observed parallax distribution with both 1-, 2-, and 3- component Gaussian models and find that the best fit to the data was provided by the 2-component model, obtaining median distances to the two components of 1350^{+45}_{-50} (rand) $^{+210}_{-160}$ (syst.) pc and 1755^{+23}_{-19} (rand) $^{+373}_{-261}$ (syst.) pc. The main Cygnus OB2 group appears to be at a greater distance than has recently been thought (implying its stellar content is therefore brighter and more massive). Furthermore, the parallax distribution observed suggests there may be further substructure within the association, though this is not well resolved by the available parallaxes. The foreground group, constituting approximately 10 per cent of the stellar content, is several hundred parsecs in the foreground and appears more extended than the main group. A further six stars have also been found as possible background or foreground contaminants, unrelated to either group.

Gaia DR2 has provided a new view of the Cygnus OB2 association. The distance spread and substructure found within the association have shown previous concerns over the line-of-sight extent of the region were warranted. The better vision we now have moves us closer to a complete understanding of the origin and evolution of Cygnus OB2, Cygnus-X, and OB associations.

ACKNOWLEDGEMENTS

We thank J.H.J. de Bruijne, X. Luri, and J. Maíz-Apellaniz for helpful discussions and comments that helped improve this work. SRB and AH acknowledge financial support from the Spanish Ministry of Science, Innovation and Universities (MCIU) under the grants AYA2015-68012-C2-01 and SEV-2015-0548, and the Gobierno de Canarias under the grant ProID-2017010115. NJW acknowledges an STFC Ernest Rutherford Fellowship (grant number ST/M005569/1). JED's research is supported via STFC grant ST/M001008/1.

REFERENCES

Arenou F. et al., 2018, A&A, 616, A17
Bailer-Jones C. A. L., 2015, PASP, 127, 994
Bailer-Jones C. A. L., Rybizki J., Fouesneau M., Mantelet G., Andrae R., 2018, AJ, 156, 58
Berlanas S. R., Herrero A., Comerón F., Pasquali A., Bertelli Motta C., Sota A., 2018, A&A, 612, A50
Berlanas S. R., Herrero A., Comerón F., Simón-Díaz S., Cerviño M., Pasquali A., 2018, A&A, 620, A56
Chentsov E. L., Klochkova V. G., Panchuk V. E., Yushkin M. V., Nasonov D. S., 2013, Astron. Rep., 57, 527
Clark J. S., Najarro F., Negueruela I., Ritchie B. W., Urbaneja M. A., Howarth I. D., 2012, A&A, 541, A145
Comerón F., Pasquali A., 2012, A&A, 543, A101
Comerón F. et al., 2002, A&A, 389, 874
Comerón F., Djupvik A. A., Schneider N., Pasquali A., 2016, A&A, 586, A46
Foreman-Mackey D. et al., 2013, Astrophysics Source Code Library, record ascl:1303.002
Gaia Collaboration, 2016, A&A, 595, A1
Gaia Collaboration, 2018, A&A, 616, A1
Gili R., Bonneau D., 2001, A&A, 378, 954
Guarcello M. G., Wright N. J., Drake J. J., García-Alvarez D., Drew J. E., Aldcroft T., Kashyap V. L., 2012, ApJS, 202, 19
Hanson M. M., 2003, ApJ, 597, 957
Herrero A., Kudritzki R. P., Vilchez J. M., Kunze D., Butler K., Haser S., 1992, Lecture Notes in Physics, Vol. 401, The Atmospheres of Early-Type Stars. Springer-Verlag, Berlin, p. 21
Kiminki D. C. et al., 2007, ApJ, 664, 1102
Knödlseder J., 2003, in van der Hucht K., Herrero A., César E., eds, Proc. IAU Symp. 212, A Massive Star Odyssey: From Main Sequence to Supernova. Astron. Soc. Pac., San Francisco, p. 505
Knödlseder J., 2000, A&A, 360, 539
Lindegren L. et al., 2018, A&A, 616, A2
Luri X. et al., 2018, A&A, 616, A9
Markova N., Puls J., 2015, in Proc. IAU Symp. 307, New windows on massive stars: asteroseismology, interferometry, and spectropolarimetry, Cambridge Univ. Press, Cambridge, p. 117
Massey P., Thompson A. B., 1991, AJ, 101, 1408
Massey P., Morrell N. I., Neugent K. F., Penny L. R., DeGioia-Eastwood K., Gies D. R., 2012, ApJ, 748, 96
Negueruela I., Marco A., Herrero A., Clark J. S., 2008, A&A, 487, 575
Repolust T., Puls J., Herrero A., 2004, A&A, 415, 349
Rygl K. L. J. et al., 2012, A&A, 539, A79
Salas J., Maíz Apellániz J., Barbá R. H., 2015, in Cenarro A. J., Figueras F., Hernández-Monteagudo C., Trujillo Bueno J., Valdivielso L., eds, Proc. XI Scientific Meeting of the Spanish Astronomical Society, Highlights of Spanish Astrophysics VIII. p. 615
Schwarz G., 1978, Ann. Stat., 6, 461
Shapiro S. S., Wilk M. B., 1965, Biometrika, 52, 591
Wright N. J., Parker R. J., Goodwin S. P., Drake J. J., 2014, MNRAS, 438, 639
Wright N. J., Drew J. E., Mohr-Smith M., 2015, MNRAS, 449, 741
Wright N. J., Bouy H., Drew J. E., Sarro L. M., Bertin E., Cuillandre J.-C., Barrado D., 2016, MNRAS, 460, 2593

SUPPORTING INFORMATION

Supplementary data are available at *MNRAS* online.

Appendix A. List of Sources.

The list of Cygnus OB2 sources used for this work, derived membership, and those stars that have not passed the selection criteria are available in electronic form at the CDS and at MNRAS online.

Please note: Oxford University Press is not responsible for the content or functionality of any supporting materials supplied by the authors. Any queries (other than missing material) should be directed to the corresponding author for the article.

This paper has been typeset from a TEX/LATEX file prepared by the author.

APPENDIX A: LIST OF SOURCES

The list of Cygnus OB2 sources that have passed the selection criteria for reliable *Gaia* astrometry is shown in Table A1. Names, *Gaia* DR2 sources, parallaxes, G magnitudes and group probabilities (based on the 2-component best-fitting model, see text) are indicated. Table A2 shows those stars that have not passed the selection criteria and, therefore, have not been included in our analysis. We note that in both tables systematic uncertainties are not included in parallax values.

Table A1. List of suitable Cygnus OB2 sources used in this work. Names, *Gaia* DR2 sources, parallaxes, G magnitudes and group probabilities (based on the 2-component best-fitting model) are shown.

NAME	*Gaia* source	parallax (mas)	G (mag)	Group
Cyg #7	2067785070923663104	0.625 ± 0.029	9.74	2
Cyg #22AB	2067781905528395264	0.623 ± 0.067	10.83	2
Cyg #8C	2067784246289931776	0.554 ± 0.030	9.48	2
Cyg #9	2067783623515353728	0.601 ± 0.033	9.61	2
Cyg #11	2067888218857234304	0.581 ± 0.027	9.24	2
A37	2064838375463800448	0.557 ± 0.040	11.65	2
ALS 15148	2067781939888133248	0.569 ± 0.044	12.25	2
Cyg #5AB	2067830941174418048	0.638 ± 0.056	8.24	2
A24	2064757698797394688	0.568 ± 0.036	11.71	2
V1827 Cyg	2067818533010251776	0.572 ± 0.054	11.44	2
Cyg #8A	2067784624247057920	0.618 ± 0.038	8.42	2
Cyg #8B	2067784619950644480	0.624 ± 0.041	9.66	2
HD 195213	2067430718942052224	0.727 ± 0.040	8.38	1
Cyg #B18	2067913164027256960	0.515 ± 0.045	11.96	2
Cyg #29	2067887840900094848	0.597 ± 0.033	11.13	2
Cyg #16	2067833204620693632	0.631 ± 0.034	10.29	2
ALS 15114	2067883820810670336	0.613 ± 0.036	10.79	2
A11	2067829596846026880	0.736 ± 0.058	11.42	1
J20315961+4114504	2067827466541470080	0.539 ± 0.024	12.05	2
ALS 15128	2067781871173898624	0.585 ± 0.031	11.89	2
A15	2067796787591714048	0.560 ± 0.065	11.53	2
Cyg #4A	2067835682818357376	0.670 ± 0.036	9.67	0
J20334086+4130189	2067881548771533312	0.547 ± 0.029	11.93	2
A46	2067788713055642880	0.611 ± 0.025	10.73	2
BD +404212	2067826062091598976	0.683 ± 0.036	9.39	1
Cyg #8D	2067785002204178688	0.630 ± 0.032	11.27	2
Cyg #6	2067833243277076864	0.644 ± 0.035	10.12	0
ALS 15134	2067780054401820544	0.548 ± 0.029	11.95	2
Cyg #25A	2067928110513529216	0.463 ± 0.043	11.23	2
Cyg #15	2067834926904094848	0.629 ± 0.030	10.57	2
A38	2067769609040987648	0.551 ± 0.031	12.35	2
A18	2068008164405551104	0.538 ± 0.062	12.89	2
Cyg #17	2067832968398974208	0.690 ± 0.037	10.93	1
ALS 15111	2067832624801783040	0.586 ± 0.036	11.24	2
J20330292+4117431	2067784516868550016	0.607 ± 0.041	11.77	2
ALS 15115	2067785208362826112	0.607 ± 0.042	11.27	2
J20333030+4135578	2067929794140714752	0.875 ± 0.054	11.40	1
Cyg #24	2067783799613328128	0.541 ± 0.041	10.99	2
Schulte 73	2067862414694092544	0.606 ± 0.059	11.38	2
BD +404179	2067398416488472704	0.576 ± 0.027	9.47	2
J20291617+4057371	2067807885789820160	0.533 ± 0.038	12.12	2
J20275292+4144067	2068074620437883520	0.644 ± 0.049	11.16	2
Cyg #22C	2067781905528395776	0.649 ± 0.036	11.91	2
A32	2067726006532873728	0.637 ± 0.047	11.04	2
Cyg #14	2067835614098871040	0.579 ± 0.029	10.91	2
ALS 15119	2067781016474500864	0.619 ± 0.031	11.46	2
ALS 15125	2067887802243913216	0.617 ± 0.027	11.97	2
Cyg #23	2067785070923661440	0.593 ± 0.026	11.79	2
J20272428+4115458	2067642233192106624	0.349 ± 0.027	11.44	3
J20293480+4120089	2068007034832335104	0.541 ± 0.035	12.72	2
A28	2067763080691028736	0.573 ± 0.031	12.59	2
ALS 15123	2067784173274044928	0.591 ± 0.028	11.88	2
Cyg #22D	2067781909827710720	0.530 ± 0.037	12.52	2
ALS 15146	2067766787246422400	0.469 ± 0.042	12.19	2
Cyg #22E	2067781909827930624	0.674 ± 0.050	13.69	0
A29	2064739041458261120	0.638 ± 0.036	10.72	2
A41	2068155125305302144	0.744 ± 0.054	10.72	1
ALS 15144	2067782936320586240	0.544 ± 0.039	12.18	2
Cyg #20	2067847502568383744	0.595 ± 0.032	11.05	2
ALS 15133	2067840149584105344	0.598 ± 0.037	11.75	2
ALS 15145	2067766379225921152	0.613 ± 0.028	12.48	2
J20301838+4053466	2067793351620401024	0.559 ± 0.031	12.23	2

3

Table A1 – *continued*

NAME	*Gaia* source	parallax (mas)	G (mag)	Group
Tyc 3156-998-1	2067625637438421248	0.540 ± 0.037	10.30	2
WR 144	2067824545964503168	0.535 ± 0.051	12.87	2
WR 145	2067745076187793024	0.655 ± 0.041	10.63	0
J20322615+4057194	2067769574681275904	0.705 ± 0.054	16.57	1
J20324719+4117500	2067830185260341504	0.522 ± 0.041	14.57	2
J20324863+4114298	2067782700101719808	0.538 ± 0.047	14.09	2
J20325904+4117589	2067784723027769728	0.641 ± 0.037	14.98	0
J20325976+4114196	2067782837540661248	0.542 ± 0.038	13.95	2
J20332563+4115247	2067783524735406336	0.564 ± 0.033	14.26	2
ALS 15180	2067879354045188992	0.513 ± 0.025	13.98	2
A22	2067751604537938688	0.513 ± 0.037	12.51	2
ALS 15169	2067780397999213952	0.541 ± 0.043	13.29	2
ALS 15147	2067766276146708608	0.569 ± 0.031	12.72	2
Cyg #4B	2067835682818358400	0.693 ± 0.034	11.36	1
J20323951+4052475	2067768195993175936	0.586 ± 0.041	12.09	2
A30	2067826332670106112	0.615 ± 0.025	12.32	2
J20321568+4046170	2067743976676134784	0.721 ± 0.026	12.61	1
J20292449+4052599	2067429168454304896	0.585 ± 0.027	11.87	2
A33	2067768372090380800	0.559 ± 0.037	12.52	2
Cyg #2	2067845887660714880	0.553 ± 0.030	10.09	2
J20330526+4143367	2067934394049131520	0.592 ± 0.034	12.00	2
J20331870+4059379	2067759056302388992	0.586 ± 0.028	12.44	2
J20272099+4121262	2067691195819277056	0.472 ± 0.026	12.08	2
Cyg #25B	2067928110510738432	0.635 ± 0.041	11.83	2
J20282772+4104018	2067625195062093312	0.547 ± 0.027	12.14	2
J20330661+4121131	2067784967844456192	0.546 ± 0.027	13.24	2
A45	2067810183593068160	0.592 ± 0.031	11.50	2
BD +404223	2067771533186357888	0.555 ± 0.028	9.09	2
Cyg #18	2067780947755025920	0.703 ± 0.038	9.67	1
A23	2067813005390784896	0.749 ± 0.039	10.09	1
A34	2068142755799441536	0.585 ± 0.035	10.09	2
A12	2064748559105788160	0.536 ± 0.054	10.74	2
A27	2064757703093913984	0.700 ± 0.043	10.00	1
Cyg #19	2067877910936163968	0.792 ± 0.037	10.08	1
J20323882+4058467	2067769845260237568	0.564 ± 0.036	12.84	2
J20333822+4053412	2067754731274151424	0.627 ± 0.029	10.98	2
J20273787+4115468	2067642920388313600	0.544 ± 0.036	12.21	2
J20301097+4120088	2068007687667323904	0.557 ± 0.047	13.13	2
J20323968+4050418	2067768097212457344	0.489 ± 0.029	12.41	2
J20332099+4135518	2067929862860202752	0.617 ± 0.036	13.31	2
Cyg #21	2067837263366481536	0.616 ± 0.031	10.98	2
J20305552+4054541	2067795752502969472	0.528 ± 0.028	12.03	2
A42	2067816681882846464	0.587 ± 0.023	11.69	2
J20305111+4120218	2067842756625081856	0.482 ± 0.040	13.07	2
MT91-426	2067781944187448704	1.039 ± 0.046	15.84	3
ALS 15181	2067778783091509888	0.665 ± 0.032	13.43	0
ALS 15160	2067779779523905792	0.614 ± 0.032	12.85	2
BD +404185	2067421304373639552	0.563 ± 0.029	9.51	2
ALS 15191	2067772048582426240	0.544 ± 0.034	13.71	2
J20294060+4109585	2067811768440282880	0.532 ± 0.025	11.88	2
MT91-187	2067835438000806016	0.585 ± 0.027	12.45	2
J20322651+4119138	2067830833796676352	0.526 ± 0.022	13.28	2
J20334884+4119406	2067875024718082816	0.612 ± 0.034	12.60	2
J20321381+4127414	2067835781598188160	0.536 ± 0.033	12.49	2
J20314885+4038001	2067735760399789568	0.596 ± 0.025	12.24	2
Cyg #26	2067875127797303040	0.653 ± 0.038	10.83	0
J20281539+4044046	2067424053152797568	0.492 ± 0.034	10.61	2
J20310700+4035537	2067734901406331776	0.535 ± 0.027	12.39	2
ALS 15151	2067766684167207424	0.594 ± 0.030	12.63	2
J20331548+4127331	2067926598685455744	0.562 ± 0.032	12.85	2
ALS 15158	2067767337001802496	0.539 ± 0.037	12.93	2
BD +404210	2067734012352626816	0.653 ± 0.057	8.96	0
J20303833+4010538	2067342448773511680	0.608 ± 0.028	12.58	2

4

Table A1 – *continued*

NAME	*Gaia* source	parallax (mas)	G (mag)	Group
J20273982+4040384	2067610042417228416	0.524 ± 0.033	10.85	2
J20303297+4044024	2067786475373617280	0.725 ± 0.043	11.48	1
J20331046+4120574	2067785272785269888	0.622 ± 0.038	13.06	2
J20321460+4122330	2067834342788541056	0.557 ± 0.023	13.55	2
J20322135+4118354	2067830941174419968	0.521 ± 0.030	14.12	2
J20323886+4125208	2067833204623425280	0.534 ± 0.038	12.81	2
J20325075+4115022	2067783078058841600	0.573 ± 0.031	13.29	2
J20325667+4123408	2067832246844656768	0.575 ± 0.025	13.12	2
J20330441+4117089	2067784521167847424	0.524 ± 0.043	13.14	2
J20330519+4117512	2067784555527587072	0.532 ± 0.022	13.28	2
J20331914+4117449	2067783799613328768	0.560 ± 0.021	13.97	2
Cyg #66	2067780432358951296	0.578 ± 0.039	13.39	2
J20332334+4120171	2067784383729101696	0.534 ± 0.039	12.96	2
J20342462+4126250	2067877498618793856	0.578 ± 0.029	13.73	2
J20313338+4122490	2067840974218090112	0.574 ± 0.039	12.75	2
J20334254+4114566	2067780741596586752	0.564 ± 0.028	13.83	2
V*V2188 Cyg	2067783559095152768	0.485 ± 0.043	13.54	2
J20324645+4124223	2067833037118456576	0.513 ± 0.021	14.24	2
J20323141+4130516	2067837400805452032	0.609 ± 0.028	13.52	2
J20284657+4107069	2067998101300361984	0.613 ± 0.026	12.76	2
J20305074+4135066	2068034488263553792	0.586 ± 0.017	13.16	2
J20322608+4129393	2067837263366486144	0.524 ± 0.040	12.37	2
J20334835+4113138	2067779916962859136	0.597 ± 0.030	13.58	2
J20322724+4121566	2067831525289977856	0.583 ± 0.025	14.01	2
MT91-264	2067775823854708096	0.741 ± 0.023	12.28	1
J20331137+4117585	2067784589887320576	0.551 ± 0.028	13.60	2
Schulte 30	2067882755658754432	0.747 ± 0.028	11.56	1
J20315694+4131478	2067848048024783360	0.605 ± 0.035	11.99	2
A39	2067769265443613568	0.711 ± 0.034	11.42	1
J20354703+4053012	2064836554397669376	0.662 ± 0.029	12.17	0
J20320797+4121598	2067834308428808832	0.592 ± 0.024	13.66	2
J20313055+4137159	2067853171925419392	0.590 ± 0.023	14.02	2
J20322212+4127420	2067835751537826560	0.579 ± 0.030	12.84	2
J20315637+4133050	2067848911317810176	0.574 ± 0.019	13.33	2
J20321352+4127299	2067835678524562944	0.515 ± 0.039	12.65	2
J20321965+4120389	2067834067910619904	0.598 ± 0.029	12.69	2
J20322549+4124520	2067834682086562048	0.614 ± 0.027	12.76	2
J20323266+4127046	2067836232574322048	0.584 ± 0.022	13.00	2
J20323702+4123052	2067831624070707840	0.547 ± 0.027	12.31	2
J20323776+4126154	2067836159558192896	0.661 ± 0.019	13.19	0
J20332245+4122169	2067785242722566784	0.582 ± 0.024	13.49	2
J20333164+4121459	2067878254533644288	0.578 ± 0.022	13.08	2
J20333433+4118113	2067784035835091072	0.582 ± 0.029	12.19	2
J20334879+4137400	2067929450543312640	0.537 ± 0.025	13.91	2
V*V2190 Cyg	2067785174003089664	0.476 ± 0.021	13.38	2
J20320311+4132302	2067848189763302400	0.514 ± 0.023	13.51	2
J20333393+4119382	2067784143210932352	0.430 ± 0.029	13.47	2
J20324968+4125364	2067833071478386048	0.570 ± 0.023	13.59	2
J20320480+4128441	2067847708726800896	0.531 ± 0.019	13.32	2
J20313415+4131082	2067848567720295424	0.539 ± 0.028	14.67	2
J20333334+4108364	2067779229768091136	0.614 ± 0.032	13.47	2
J20320689+4117570	2067828020596671104	0.576 ± 0.038	12.79	2
J20315322+4129246	2067847640007337088	0.553 ± 0.038	15.47	2
J20315540+4135276	2067849220555468928	0.559 ± 0.027	14.43	2
J20321504+4119303	2067833930471667200	0.527 ± 0.025	14.06	2
J20323835+4128567	2067836576171717120	0.576 ± 0.024	13.79	2
J20331029+4123446	2067832418643351424	0.739 ± 0.028	14.55	1
J20331433+4119331	2067785070923660416	0.187 ± 0.036	13.52	3
J20323254+4126468	2067836232574148864	0.540 ± 0.024	14.31	2
ALS 15172	2067929686763411584	0.585 ± 0.043	13.29	2
J20331927+4124448	2067879354045188864	0.642 ± 0.032	14.03	0
J20333456+4121372	2067878220173813376	0.609 ± 0.026	14.03	2
HD 196305	2067889696326278272	2.976 ± 0.045	7.56	3

5

Table A1 – *continued*

NAME	*Gaia* source	parallax (mas)	G (mag)	Group
BD +404193	2067425461902141056	0.750 ± 0.035	9.86	1
BD +404208	2067787746683936640	0.653 ± 0.033	9.91	0
J20314341+4100021	2067797195612486656	0.543 ± 0.041	13.19	2
GSC13157-01377	2067821664044745984	0.575 ± 0.038	12.99	2
CCDMJ20323+4152AB	2067950096449560320	1.547 ± 0.066	9.15	3
MT91-325	2067833277636820608	0.549 ± 0.022	13.52	2
MT91-179	2067850732383966976	0.540 ± 0.022	13.23	2
MT91-239	2067849873390497024	0.573 ± 0.024	13.84	2
MT91-271	2067831662728930304	0.569 ± 0.020	13.77	2
MT91-170	2067849220555467264	0.932 ± 0.045	15.69	3
MT91-444	2067832418643353344	0.586 ± 0.026	13.24	2
MT91-453	2067926564325711872	0.602 ± 0.021	13.77	2

Table A2. List of stars that have not passed the selection criteria. Names, *Gaia* DR2 sources, parallaxes and G magnitudes are shown.

NAME	*Gaia* source	parallax (mas)	G (mag)
ALS 15108AB	2067778538274037504	0.278 ± 0.839	10.79
J20303980/1+4136506/7	2068035342958597760	2.094 ± 0.371	11.95
J20293563+4024315	2067401375725290496	0.525 ± 0.044	11.07
J20314540+4118267	2067828639068547200	0.453 ± 0.073	11.15
A20	2067755379810392320	2.051 ± 0.365	10.83
A25	2067730816896271488	0.131 ± 0.110	11.85
Cyg #1	2067846574853004672	0.549 ± 0.065	10.44
J20335842+4019411	2064705991687575424	0.658 ± 0.092	11.75
A26	2067814306761678336	4.815 ± 0.813	12.22
Cyg #10	2067928660269306496	0.590 ± 0.449	9.06
Cyg #27	2067874028285659520	0.693 ± 0.059	11.37
WR 146AB	2067867358199590400	0.834 ± 0.367	11.05
A44	2067742877164542080	0.377 ± 0.256	11.67
J20253320+4048444	2067600799643251072	2.696 ± 0.817	10.91
A36	2067885779315742592	1.058 ± 0.066	10.37
V2186 Cyg	2067785375864885888	0.942 ± 0.293	12.15
J20274925+4017004	2067390277529622144	0.656 ± 0.073	11.32
J20315433+4010067	2064337036816956032	0.771 ± 0.087	12.95
J20293473+4020381	2067353851907821568	0.363 ± 0.084	12.11
J20331531+4129567	2067926804843893504	0.342 ± 0.104	12.68
J20333979+4122523	2067878357612771200	0.223 ± 0.413	11.13
J20321470+4127396	2067835785897573120	0.885 ± 0.147	12.98
ALS 21109	2067830563217283968	0.584 ± 0.035	13.18
J20305938+4135599	2068034694421980416	0.555 ± 0.029	13.59
J20334758+4109064	2067767375658346624	0.742 ± 0.085	13.41
J20325440+4115219	2067783112418577536	-0.455 ± 0.445	13.65
MT91-129	2067848219824399616	1.278 ± 0.225	13.77
J20313364+4136046	2067852416011174016	0.663 ± 0.209	13.98
Cyg #12	2067782734461462912	1.175 ± 0.128	8.89

6

Spectroscopic analysis of the known O-type population in Cygnus OB2

In this chapter we present the most complete spectroscopic census of the currently known O-type stars in Cygnus OB2 so far, using previous and new spectroscopy. We have discovered new binary systems, obtained the distribution of rotational velocities, determined the spectroscopic stellar parameters as well as luminosities, masses and radii for those stars that pass the criterion for reliable *Gaia* DR2 astrometry. These results have been used to place the sample in the Hertzsprung-Russell Diagram (HRD) and compare it with its spectroscopic version (sHRD) in order to study the stellar evolution of the whole population. This work will contribute significantly to our understanding of the physics of massive stars and the structure and evolution of young regions, forming a solid background to interpret the results from other studies such as the forthcoming WEAVE Cygnus survey.

6.1 New spectroscopic observations and data reduction

We have compiled new intermediate-high resolution and high signal-to-noise ratio (S/N) spectra to build up the most complete spectroscopic census of the currently known O-type stars in Cygnus OB2 (including the recently newly classified O-type members in the association by Berlanas et al. (2018a), see Chapter 3). These new data have been complemented with already available spectra from previous observations: our own observations and others from our collaborators (see Sect. 6.2 for details). We included in this sample all the stars identified as O-type stars within 1 deg radius centred on Galactic coordinates $l = 79.8°$ and $b = +0.8°$ (see Fig. 1 in Chapter 5). Since our goal is to perform an accurate spectroscopic analysis of the whole sample, we need spectral data in the 4000 – 5000 Å wavelength range to cover all the main diagnostic lines. Besides this, we also need to cover the Hα line in order to obtain an accurate analysis of the stellar wind.

To complete the database we have performed five different campaigns (see Table 6.1 for specific dates) at the Isaac Newton Telescope (INT) on La Palma. We used the first two days to complete the observations of 61 OB candidates in the region, that resulted in four new O stars within the considered area (see Chapter 3). We included them in the final list of confirmed O members and obtained intermediate-high resolution, high S/N (100 to 200) spectra for a total of 66 O-type stars of Cygnus OB2. Since we already had blue spectra for some of them from previous observations (see Sect. 6.2), we observed fewer stars in the blue than in the red, i.e., 27 in the blue (3900 – 5100 Å) and 66 in the red (6100 – 6800 Å) wavelength regions.

We used the Intermediate Dispersion Spectrograph (IDS) and the EEV10 detector, and chose the H1800V grating for the red wavelength region and the R1200B grating for the blue wavelength region. In the first case, the instrument configuration provides a resolving power of R ∼10000 at 6500 Å, which allows us to perform an accurate analysis of the Hα profiles. From the INT Exposure Time Calculator (ETC) and setting the slit width at one arcsec, we find that ∼7000 seconds are required to reach S/N > 100 per pixel for a star of magnitude $B = 14.0$. However, due to the high extinction of Cygnus OB2 (we assume $A_0 = 5$ and $A_B = 7$ from Sale et al. 2014) we estimate a magnitude $\mathcal{R} = B - 1.5$ for this wavelength range, so an exposure time of ∼1750 seconds would be sufficient to reach S/N > 100 per pixel for the same star. Nevertheless, due to bad weather conditions during the observing runs (dust in the air) the exposure times were increased by a factor of 2, resulting in times of around one hour to reach S/N > 100 per pixel for a star of magnitude $B = 14.0$ in the red.

Table 6.1: Summary of the observational schedule at the INT.

	Semester	Dates	λ coverage	B (mag.)	# Stars
Phase 1	16A	14-15 July 2016	Blue	$B < 16.0$	47 OB candidates
	16A	16-19 July 2016	Blue	$B < 14.5$	13 O-type
	16B	18-23 August 2016	Red	$B < 14.5$	52 O-type
Phase 2	17A	30 June - 5 July 2017	Blue	$14.5 < B < 16.0$	12 O-type
	17B	9-14 August 2017	Blue+Red	$14.5 < B < 16.0$	2+14 O-type

Note: Blue and Red indicate the (3900 – 5100 Å) and (6100 – 6800 Å) wavelength regions.

In the second case, the instrument configuration provides a resolving power of R ∼5000 at 4500Å, adequate for an accurate determination of the spectroscopic stellar parameters (and similar to what we expect from WEAVE). From the ETC we estimate that ∼2200 seconds are needed to reach S/N > 100 per pixel for a star of magnitude $B = 14.0$. But in the blue wavelength region the dust has a higher impact on the exposure times and, consequently, the times were increased by a factor of 3. Therefore, in the blue we needed ∼7000 seconds to reach S/N > 100 per pixel for a star of magnitude $B = 14.0$. In all cases, exposure times above 30 minutes were divided into ranges of 20 minutes to avoid cosmic rays.

The observational plan was divided into two phases, extending over four semesters, where two spectra were obtained for each star on different days (belonging to the same semester or not) to detect possible spectral or radial velocity variations. The four observing runs were held throughout the summer of 2016 and 2017, in a total of 24 nights distributed as follows:

1. Phase one:

   We observed 47 OB candidates, all of them with B magnitudes below 16 mag, in the first two days. We obtained S/N ∼60 spectra in the blue, which covers the wavelength region required for an accurate spectral classification (see Sect 2.1). We used the rest of the days to observe the bulk of confirmed O stars, covering the magnitude range up to $B = 14.5$. This allowed us to observe 70% of the sample, in both red and blue wavelength regions for most of the stars. This phase covered the first and second semesters (16A and 16B).

Table 6.2: Telescopes, instruments and settings used in this work.

Source	Instrument	Grating	Telescope	Resolving power	S/N	λ range (Å)	# Stars
1	ISIS	600B	WHT	3000	∼300	3900 – 5500	20
2	TWIN	1200	CAHA-3.5m	3000	∼300	3900 – 5100	15
3	Albireo	1800	OSN-1.5m	2500	∼300	3900 – 5100	2
4a	HRS	600g4739	HET	30000	≥100	3800 – 4700	12
4b	HRS	600g4739	HET	30000	≥100	4700 – 5700	12
4c	HRS	600g6302	HET	30000	≥100	5300 – 6300	12
4d	HRS	600g6302	HET	30000	≥100	6400 – 7400	12
5a	ISIS	H2400B	WHT	13600	>100	3900 – 5100	15
5b	ISIS	R1200R	WHT	9300	>150	5500 – 6800	15
6a	IDS	R1200B	INT	5000	>100	3900 – 5100	27
6b	IDS	H1800V	INT	7200	>150	6100 – 6800	66
Total number of individual spectra → 208							
Total number of full spectra → 157							
Total number of stars (not repeated) → 77							

Notes: Spectra for the detected binary stars (Sect. 6.2.1) are included in the table. Spectral data from sources 1, 2 and 3 belong to the GOSSS catalog, see Sota et al. (2011); Maíz Apellániz et al. (2016) for further observing details.

2. Phase two:

   We observed the rest of confirmed O stars in the third and fourth semesters (17A and 17B). Again, two spectra per object were obtained (in both red and blue wavelengths regions).

The spectra were reduced using IRAF[1] with standard routines for bias, flat-field subtraction and wavelength calibration. No significant problems were found during the process. We also proceed with the radial velocity correction of the spectra from the Doppler shift of metal and He I spectral lines. A summary of the observing runs is presented in Table 6.1.

6.2 The sample

As stated in Sect. 6.1, we have built up a complete spectral sample of the already known O-type population of Cygnus OB2. With this aim we have complemented new observations with already available spectra (own and from collaborators) whose observational details are described as follows.

The major part of the available optical–blue data (see Table C.1) belongs to the Galactic O-Star Spectroscopic Survey (GOSSS) (Sota et al. 2011, 2014;

[1]IRAF is distributed by the National Optical Astronomy Observatories, which are operated by the Association of Universities for Research in Astronomy, Inc., under cooperative agreement with the National Science Foundation

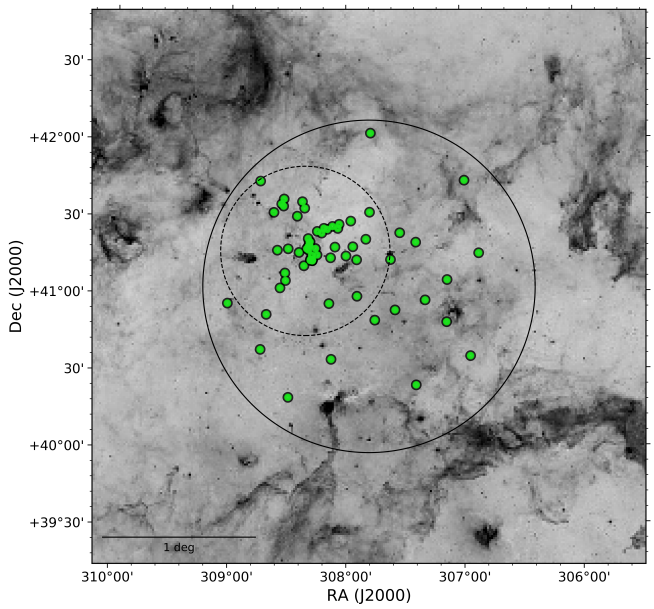

Figure 6.1: Inverse Spitzer 8 μm image showing the location of the known O-type population in Cygnus OB2 (77 stars represented by green dots). The solid line circle delimits the 1 degree radius area adopted for the association. For reference, the dash-dotted line circle shows the area considered by Wright et al. (2015) indicating the core of the association.

Maíz Apellániz et al. 2016), which obtained a large number of homogeneous Galactic O-type high S/N (∼300) blue-violet spectra at R ∼2500. The GOSSS data used in this work were observed between 2007 and 2014 using three different instruments: the Albireo spectrograph at the 1.5 m telescope of the Observatorio de Sierra Nevada (OSN), the TWIN spectrograph at the 3.5 m telescope of Calar Alto Observatory (CAHA, Centro Astronomico Hispano-Aleman), and the ISIS instrument (blue arm) at the William Herschel Telescope (WHT) of the Observatorio del Roque de los Muchachos (ORM).

We also have spectra from The Hobby-Eberly Telescope (HET) kindly provided by A. Pellerin. These data were observed throughout 2012 in four different spectral ranges (3800 – 4700, 4700 – 5700, 5300 – 6300 and 6400 –

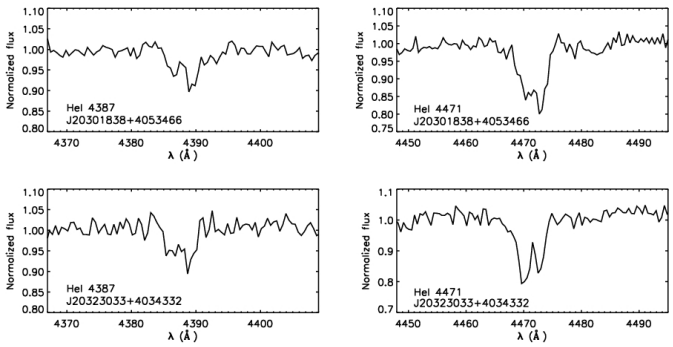

Figure 6.2: Example of the new SB2 detections: HeI lines in stars J20301838+4053466 (top) and J20323033+4034332 (bottom).

7400 Å) using the High-Resolution Spectrograph (HRS) at R ∼30000 and the 600g4739/6302 gratings. We have a total of 48 spectra for 12 stars (one in each spectral range). The signal-to-noise of these spectra is variable, from 100 to 300.

Finally, we also compiled our own spectra observed in different runs at the William Herschel Telescope (WHT) using the ISIS spectrograph (a total of 30 spectra, 15 in each blue and red arms). These data were observed in two different observing runs. In 2015 we chose the H2400B grating for the blue arm, which provides a resolving power of ∼13600 at 4500 Å. As the dichroic allows us to observe simultaneously with the red arm, we used the R1200R grating (R ∼9300 at 6500 Å). Additionally we have included stars observed by A. Herrero in 2003 using also ISIS at the WHT with the same configuration (H2400B and R1200R gratings). All ISIS spectra have S/N >100 (from 100 to 200, depending on the stellar magnitude).

A brief summary of the data used in this work is shown in Table 6.2. The final spectral sample is composed by 77 O-type stars (nine of them already known SB2) whose location is shown in Fig. 6.1. Main data and photometric information is presented in Table C.1.

6.2.1 Binary systems

A large number of multiplicity studies among massive stars have been developed during the last years (see Sana 2017, for a brief overview) where the

Table 6.3: Binary systems identified in Cygnus OB2 and containing at least one O-type star.

Star	Binary type	Components	SpT	SpT ref.	Bin. ref.
CygOB2 #1	SB1	A, B	O8V(n)((f)) + B	1	13
J20311833+4121216	SB1	A, B	O9.5IV + B	1	6
[MT91] 145	SB1	A, B	O9IV + mid-B	1	12
CygOB2 #15	SB1	A, B	O8III + B	1	12
ALS 21079	SB1	A, B	O7.5Ib(f) + O/B	2	6
CygOB2 #17	SB1	A, B	O8V + O-G	4	4
ALS 15144	SB1	A, B	O9.7III(n) + B:	2	4
J20330292+4117431	SB1	A, B	O7.5V((f)) + G-O	1	4
CygOB2 #22B	SB1	B1, B2	O6V((f)) + A-O	9	10
CygOB2 #22C	SB1	C1, C2	O9.5IIIn + B9V-A0V	9	7
CygOB2 #9	SB2	A, B	O4If + O5.5III(f)	1	8
ALS 15148	SB1	A, B	O6.5:V + early A-O	1	4
CygOB2 #8A	SB2	A1, A2	O6Ib(fc) + O4.5III(fc)	1	14
CygOB2 #8D	SB1	D1,D2,D3	O8.5V + O9V + A2V-O	4	4
ALS 15115	SB1	A, B	O8V + early B-O	2	4
J20333030+4135578	SB1	A, B	O8V + B2-O	4	4
ALS 15119	SB1	A, B	O9.5IV(n) + early A-B	1	4
CygOB2 #27	SB2	A, B	O9.7V(n) + O9.7V:(n)	2	3
ALS 15146	SB2	A, B	O9.5V + B1-2V	4	6
CygOB2 #11	SB1	A, B	O5.5Ifc + O/early B	9	6
CygOB2 #29	SB1	A, B	O7V(n)((f))z + B-O	2	4
ALS 15114	SB2	A, B	O7V((f)) + O7IV((f))	1	7
CygOB2 #3A	SB2	A, B	O8.5Ib(f) + O6III:	1	13
CygOB2 #5A	SB2	A1,A2	O6.5Iafe + O7Iafe	1	15
Shulte 73	SB2	A, B	O8Vz + O8Vz	2	12
CygOB2 #B17	SB2	A, B	O6Iaf + O9:Ia:	2	11
J20301838+4053466	SB2	A, B	O9V + OB	0	0
J20323033+4034332	SB2	A, B	O9.5IV + OB	0	0

Refs. (0) This work, (1)Maíz Apellániz et al. (2019), (2) Maíz Apellániz et al. (2016), (3) Salas et al. (2015), (4) Kobulnicky et al. (2014), (5) Sota et al. (2014), (6)Kobulnicky et al. (2012), (7) Kiminki et al. (2012), (8) Nazé et al. (2012), (9) Sota et al. (2011), (10) Maíz Apellániz (2010) , (11) Stroud et al. (2010), (12) Kiminki et al. (2009), (13) Kiminki et al. (2008), (14) De Becker et al. (2004), (15) Rauw et al. (1999).

number of detected massive O-type binaries has been continuously revised and updated. The Cygnus OB2 Radial Velocity Survey is one of the most relevant multiplicity studies carried out in this association (Kiminki et al. 2007, 2008, 2009, 2012; Kobulnicky et al. 2012) where the binary properties of its massive star population have been statistically studied. Kobulnicky et al. (2014) list 48 massive OB multiple binaries known in Cygnus OB2, 26 of them containing at least one O-type star. In recent years, Maíz Apellániz et al. (2016, 2019) have provided spectral classification for most of the detected companions.

In this work we have found two new SB2 systems within our sample of known O-type members of Cygnus OB2: J20301838+4053466 and J20323033+4034332 (see Fig. 6.2 for an example of the binary detection). A list of the currently known binary (or multiple) systems in the association is presented in Table 6.3 where we also show the binary type (single-lined SB1 or double-lined SB2), the components, spectral types and bibliographic references. Taking into account the results of this work, 28 of 77 O-type stars in the region are part of binary/multiple systems (representing a fraction of 36%). Sana & Evans (2011) found that at least 45 – 55% of the O star population in clusters and OB associations is comprised of spectroscopic binaries, which indicates that it is highly likely that more binaries are undetected in our sample.

We highlight some individual remarks for three of the most relevant multiple systems known in Cygnus OB2: CygOB2 #5, CygOB2 #22 and CygOB2 #8. CygOB2 #5 is a multiple system for which Maíz Apellániz (2010) lists up to four components. #5A is the star giving name to the system, and is an eclipsing, contact binary formed by an O6.5 – O7 and a WN9/Ofp stars (Rauw et al. 1999), that is overluminous for its mass. The #5B component, separated 0.9″ from #5A, has been classified as O6.5Iabfp by Maíz Apellániz et al. (2016). The GOSSS catalogue gives separated spectra for #5A and #5B. On the other hand, Maíz Apellániz (2010) has identified a total of 10 components for the trapezium-like system CygOB2 #22 and the GOSSS Survey has provided spectral data for the first five O components (A,B,C,D and E). Finally, at least four O-type visual components have been detected in the CygOB2 #8 trapezium-like system (Maíz Apellániz et al. 2012). The first component, #8A, has been identified as an SB2 star composed by two early O-type stars (De Becker et al. 2004; Maíz Apellániz et al. 2019).

6.2.2 Selecting the final spectral sample

The detected SB2 stars (see Table. 6.3) have been excluded from our final sample for the spectroscopic analysis. Beside this, we have also excluded the Cyg#5B and Cyg#22E components since they are not suitable targets for an accurate determination of the stellar parameters. Tentatively, we also exclude the Cyg#22D component. For this star we have spatially resolved spectroscopy from sources 1 and 6 of Table 6.2, but a detailed inspection of the spectra reveals peculiar line profiles in the red spectrum not compatible with those from the blue one. Since they were obtained in different observing campaigns and separated in time by a few years, new data are required to evaluate stellar variability or even a possible target confusion.

We therefore have a final sample of 63 O-type stars (of a total of 77 present

in our census) suitable for the quantitative spectroscopic analysis. Since we have compiled spectral data from different sources, in many cases we have different spectra for the same star. In these cases we have selected the data by taking into account the following criteria:

- To determine the distribution of rotational velocities (henceforth, sample A), we first chose those spectra that cover the Si III 4552 or O III 5592 lines (see Sect. 2.2.1). Then, we looked for the data with the higher resolving power since the higher resolution of the spectra allows us to better identify spectroscopic binaries and to disentangle the macroturbulence broadening component, obtaining more accurate *vsini* determinations (see Simón-Díaz & Herrero 2007, 2014, and references therein).
- However, in order to determine the fundamental parameters we have used the spectra with the best quality in terms of S/N (henceforth, sample B) and, whenever possible, the best resolution for the H and He lines.

As an example, for the Cyg#6 star we had data from three different instruments: sources 2, 4 and 6 of Table 6.2. In order to determine the rotational velocity and macroturbulence broadening component, we have use the source number 4 because of the higher spectral resolution (R ∼30000) and the fact that the line of O III 5592 is covered. On the other hand, to determine the fundamental parameters we used sources number 2 (for the optical-blue range) and 6b (for the optical-red range) because of the higher quality of the spectra (in terms of S/N). We note that we are assuming no significant variations between individual blue and red spectral data (e.g. no strong variations in Hα), although in the cases where only one spectrum is available for each wavelength range this assumption can not be confirmed.

A final list of the whole O-type population of our sample, along with the new spectral classification (see Sect. 2.1 for methodology details) and the spectral data selected for each case (A or B) is shown in Table C.2.

6.2.3 Implications of using an inhomogeneous spectral sample

Since our final sample is spectrally inhomogeneous in terms of R, S/N and wavelength coverage, we have evaluated the implications of using data with different spectral characteristics for the spectroscopic analysis.

In the case of the wavelength coverage, we know that a limited set of lines affects the parameter determination (mainly for gravities and, therefore, masses) and the errors decrease as we increase the number of diagnostic lines (Berlanas et al. 2017). Nevertheless, all our spectral data cover the whole range where

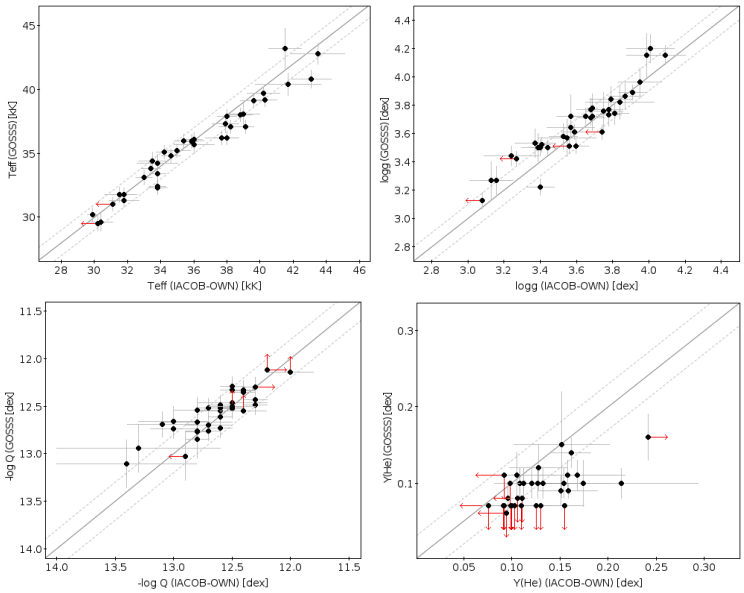

Figure 6.3: Comparison between the stellar parameters obtained using spectral data from the IACOB-OWN (R $\geq$ 25000) and the GOSSS surveys (R $\sim$2500) for the same stellar sample of 37 standard O-type stars. The same *vsini* values and set of diagnostic lines were used for the spectroscopic analysis.

the main diagnostic lines for O-type stars are located (4000 – 5000 Å) and we have supplied the lack of the Hα and He I+II 6678 lines that existed in some spectra by carrying out new spectroscopic observations (see Sect. 6.1).

Although all the data used for the spectroscopic analysis have high S/N (exceeding 100 in all cases), the resolving power varies in a wide range (from 2500 to 30000, see Table 6.2). We therefore decided to evaluate the possible effect that resolution could have in the derivation of the stellar parameters using spectral data from the IACOB-OWN (R $\geq$ 25000) and GOSSS (R $\sim$2500) surveys. For the test, we have selected the same 37 standard O-type stars (at least one for each type and luminosity class) from both surveys. In order to avoid possible additional uncertainties we performed the spectroscopic analysis considering only the common set of lines and the same values of *vsini* and

Table 6.4: Mean and standard deviation of the difference in the derived spectroscopic parameters obtained from high resolution IACOB-OWN (R $\geq$ 25000) and low resolution GOSSS (R $\sim$2500) spectra.

$< \Delta T_{eff} > \pm \sigma_{\Delta T}$ [kK]	$< \Delta$log g $> \pm \sigma_{\Delta log g}$ [dex]	$< \Delta$log Q $> \pm \sigma_{\Delta log Q}$ [dex]	$< \Delta$Y(He) $> \pm \sigma_{\Delta Y(He)}$ [dex]
0.39 $\pm$ 0.87	-0.05 $\pm$ 0.08	0.08 $\pm$ 0.15	0.03 $\pm$ 0.03

vmac (see Sect.2.2.1 and Sect.2.2.2 for methodology details).

In Fig. 6.3 we present a comparison between the derived stellar parameters and Table 6.4 shows the mean and standard deviation of the difference in the spectroscopic parameters. We can see that $T_{\rm eff}$, log g and log Q are only slightly affected by the spectral resolution and most of the stars are located within the usual uncertainties without a global impact (see Table 6.4). However, we find a different behaviour for the He abundance: there are many more stars with Y(He) < 0.1 when the resolution is low. In addition to this, the number of stars for which we can obtain only abundance limits increases when the resolution decreases. We should highlight that the pair (*vsini*, *vmac*) used in this test was obtained from the high resolution IACOB-OWN spectra, since the line of O III 5592 is covered and it is one of the best lines for an accurate line-broadening characterization (see Sect.2.2.1).

We also know that resolution affects the *vsini* determination: Simón-Díaz & Herrero (2014) (henceforth, SDH14) show that low resolution could lead to an overestimate of the derived *vsini* of $\sim$25 ($\pm$ 20) km s^{-1} in stars rotating more slowly than 120 km s^{-1}. And consequently, it could lead to errors in the gravity determination of up to 0.1 dex (see Sabín-Sanjulián, 2014, PhD). Adopting lower values makes the model profiles narrower and therefore they are widened by increasing log g. Instead, higher *vsini* values make the model profiles broader and they will be weakened by decreasing the gravity. Since gravity and effective temperature are related, the $T_{\rm eff}$ would be also affected.

Taking into account these results, when only low resolution is available it may be sufficient for an appropriate parameter determination (at least for temperature, Q parameter and gravity) if accurate *vsini* values are used. If we use low resolution spectra for the line-broadening characterization we can lead to errors in gravity of up to 0.1 dex (although in most cases the errors are smaller) and the consequent change in temperature. But the main implication is that, in any case, we should be cautious with the derived helium abundances, since lower values are obtained when the resolution decreases.

Table 6.5: Diagnostic lines used for the line-broadening characterization of our final sample.

Line	O III 5592	Si III 4552	He I[a]	N V 4603	He II 4541
# Stars	8	9	43	2	2
% Sample	12%	14%	67%	3%	3%

a) unweighed average of nebular free or weakly contaminated He 4713, 4922, 4387 and/or 4471 lines (whenever present).

6.3 Distribution of rotational velocities

6.3.1 Diagnostic lines

Since metallic lines do not suffer from strong Stark broadening nor from nebular contamination, they are best suited for obtaining accurate *vsini* values. Unfortunately, they are not present in all our spectra. In consequence we have assumed the following criteria based on the works by Herrero et al. (1992), Simón-Díaz et al. (2014) and Ramírez-Agudelo et al. (2013):

i) We based the analysis mainly on the O III 5592 or Si III 4552 diagnostic lines, when either of them is available. If both are present, we prioritize the O III 5592 line since it is usually stronger and more isolated than Si III 4552 for O-type stars.

ii) If any of them is present, we use nebular free or weakly contaminated He I lines (an unweighed average of the He I 4387, He I 4471, He I 4713 and He I 4922 lines).

iii) If any star suffers strong nebular contamination or the He I lines are weak or too noisy, we then relied on He II 4542.

iv) Finally, if the wind is weak and the line is of photospheric origin, we can also use N V 4603.

A summary of the diagnostic lines used for the line-broadening characterization of our final sample of 66 O-type stars is shown in Table 6.5.

6.3.2 Line-broadening parameters

We have obtained the projected rotational velocities (*vsini*) and the macroturbulent broadening component (*vmac*) for the whole O-type sample of Cygnus

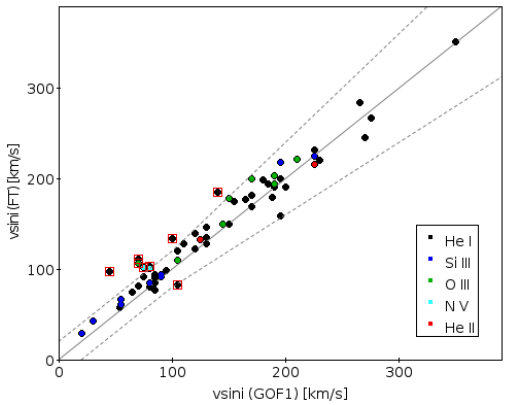

Figure 6.4: Comparison of projected rotational velocities resulting from the Fourier Transform (FT) and the Goodness-of-fit (GOF_1) techniques obtained using the `iacob-broad` tool. Dashed lines represent a difference of 20 km s^{-1} or 20% from the 1:1 relation, whichever is the largest. Red squares indicate those stars out of these limits. Different colors indicate the diagnostic lines used for the line-broadening characterization.

OB2 (excluding detected SB2 and problematic stars). As mentioned in Sect. 6.2.2, whenever possible we used the spectra with the higher spectral resolution (Sample A). The analysis was carried out using the `iacob-broad` tool, whose description and handling are detailed in Sect. 2.2.1.

We first compared the *vsini* values derived from the Fourier Transform technique (FT) and those derived from the goodness-of-fit technique (GOF) as an assessment of the reliability of the results from the line-broadening analysis (see Fig.6.4). We see that only a few stars have discrepancies beyond 20 km s^{-1} (or 20%, whichever is the largest) with no clear systematic trends due to the lines used for the analysis after the choice presented in the previous section. For those stars for which we find good agreement (below the mentioned limit) we assumed the pair *vsini* and *vmac* provided by the GOF technique (henceforth, GOF_1) since it is less affected by the subjectivity in the selection of the first zero of the FT (see SHD14). For those few cases in which we find larger discrepancies (red squares) we identified clear signatures of asymmetry in the line, probably due to a broad-line secondary component. In these cases, the GOF solution tries to fit the line by increasing *vmac*, hence resulting in a lower *vsini*. We then used the *vsini* provided by the FT technique (which is not

very much affected) and the associated *vmac* (obtained from the fit of the line assuming a fixed *vsini* value derived from the FT). However, we remark that nearly all discrepancies are close to the limit and, therefore, our choice will have little impact on the final distribution. The adopted values for the distribution of rotational velocities (and the subsequent parameter determination) are listed in Table C.3. Typical uncertainties for all sources are in the order of 10 – 20%, as seen in Fig.6.4.

One final point to keep in mind is the importance of understanding the macroturbulent broadening in massive O-type stars (Simón-Díaz et al. 2017). In some cases the obtained *vmac* could be considered an upper limit if the value associated with the best-fitting solution is higher than zero, but *vmac* = 0 km s^{-1} is still an acceptable solution (within the 1σ confidence level). Since the adoption of a wrong rotational velocity could affect the parameter determination (see Sect. 6.2.3), we performed a brief study of the implications of considering the solution provided by the goodness-of-fit technique that sets *vmac* = 0 km s^{-1}(henceforth, GOF$_2$) for those cases in which *vmac* could be considered an upper limit (see Appendix A).

6.3.3 The vsini histogram

The distribution of rotational velocities of the O population in Cygnus OB2 is shown in Fig. 6.5. A representative bin size of 40 km s^{-1} is used for the whole sample (*top left hand panel*). We find an absence of stars at lower rotational velocities (*vsini* $\leq$ 20 – 30 km s^{-1}), a feature also observed in previous studies (e.g, Conti & Ebbets 1977, SHD14). There is a main peak of slow rotators at $\sim$80 – 100 km s^{-1}, although a secondary peak of intermediate velocity rotators is present at $\sim$160 – 180 km s^{-1}. We also distinguish a soft tail of fast rotators reaching 360 km s^{-1}. Recently, binary interaction has been proposed as the origin of the high rotational velocities (e.g, de Mink et al. 2013), where an estimated fraction of around 20% of the stars should have been accelerated in binary systems during their evolution. In our case we find 23% of the stars rotating with projected rotational velocities above 200 km s^{-1}, which agrees with the predictions of de Mink et al. (2013).

However, since the projected rotational velocities have been derived from data with different spectral characteristics (mainly in terms of R, see Table 6.2) we should take into account the lower limits that can be detected at each of the spectral resolutions used in this work. Using a rough approximation (v_{lim} $\sim$ c/R) values of $\sim$100, $\sim$60, $\sim$30 and $\sim$10 km s^{-1} are the lower limits that can be detected at R $\sim$3000, R $\sim$5000, R $\sim$10000 and R $\sim$30000, respectively. We therefore have adjusted the bin size to be consistent with these limits and

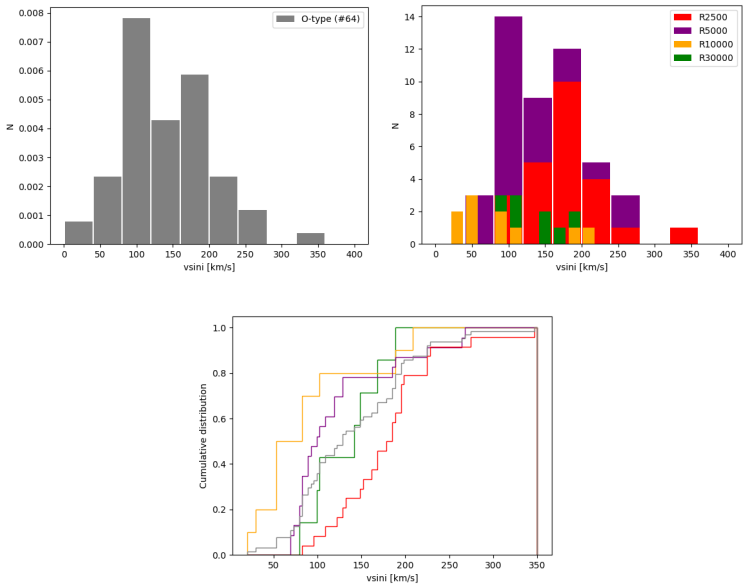

Figure 6.5: Distribution of rotational velocities of our final sample of 66 O-type stars in Cygnus OB2. *Top, left*: Normalized histogram where a representative bin size of 40 km s^{-1} is used for the whole sample. *Top, right*: Histogram where the bin size has been adjusted to be consistent with the resolving power of the spectra used for each target. *Bottom*: A cumulative velocity distribution subdivided by the resolving power of the spectra used for each target. Colors as in top, right panel. Gray color represents the total cumulative function.

represented each group of stars separately (*top right hand panel*).

Since the largest part of our spectral sample is composed by spectra with R $\leq$ 5000, the main peak of slow rotators is found above 70 km s^{-1}. As mentioned before, low resolution could lead to an overestimation of the derived *vsini* for stars rotating slower than 120 km s^{-1}. Thus, this peak is probably overestimated by $\sim$25 km s^{-1}, which is consistent with previous studies of O-type stars (see next subsection). We also see that the stars with R = 10000 are dominated by slow rotators. This is in part due to the fact that some of them were selected for a chemical study (see Chapter 4). On the other hand, we can also see that the secondary peak at $\sim$180 km s^{-1} is mainly composed by the

values obtained from the lower resolution spectra (R = 2500). Although SDH14 found that low resolution could affect the *vsini* for stars rotating slower than 120 km s^{-1}, they considered a resolving power of R ∼8000 as low resolution. We therefore suspect that a resolution of 2500 could increase this limit, and then the secondary peak could be also slightly 'pushed' to higher rotational velocities.

6.3.4 Comparison with similar studies

Since there are no previous studies focused on the distribution of rotational velocities for O-type stars in Cygnus OB2, we have compared our results to other similar works such as the study of SDH14 for a general sample of O-type stars in the Milky Way (MW), the study performed by Berlanas et al. 2019b (*in prep.*) in the Carina Nebula, or the study done by Ramírez-Agudelo et al. (2013) in 30 Doradus in the Large Magellanic Cloud (LMC).

In Fig.6.6 we compare our results with those obtained by these studies. In the top left hand panel we compare our results in Cygnus OB2 and the distribution obtained for a general sample of Galactic O stars in the MW. In this case both are Galactic samples, the first one composed by O stars belonging to the same young star-forming region and the latter composed by O bright stars belonging to many regions within the Galaxy. For the latter, the sample consists of 116 O-type stars[2] from the IACOB database that have been homogeneously observed at R = 46000. Both studies have followed the same methodology for the line-broadening characterization although the wavelength coverage of the IACOB spectra allows them to use the Si III 4552 and O III 5592 lines for all their sources. The sample of Galactic O stars presents a clear bimodal distribution, with a main peak of slow rotators at ∼40 km s^{-1} and a tail of fast rotators reaching 450 km s^{-1}. In Cygnus OB2 we find the peak of slow rotators at higher velocities (80 – 100 km s^{-1}) but, as stated before, it is probably a consequence of the spectral resolution: the lower limit that can be detected for most of the targets in Cygnus OB2 is higher than 60 km s^{-1}, reaching 100 km s^{-1} in many cases.

In the top right hand panel we compare the *vsini* distribution resulting from our study in Cygnus OB2 and the distribution for a sample of 216 O-type stars in 30 Doradus (Ramírez-Agudelo et al. 2013). Both are samples of stars belonging to young star-forming regions and the overall shape of both distributions is similar. The main differences between the two studies are the number of targets (66 versus 216), the metallicity environment (Z_{LMC} = 0.5

[2] earlier than B0

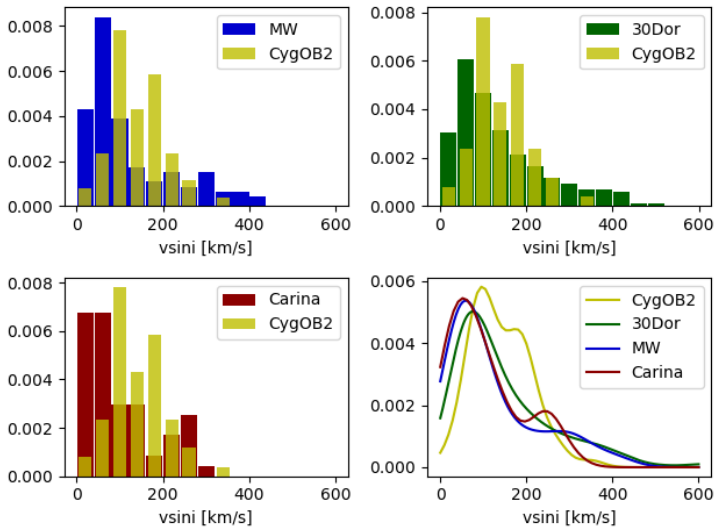

Figure 6.6: Normalized *vsini* histograms showing the comparison between the distribution of rotational velocities found for our sample of O-type stars in Cygnus OB2 and the distribution of O-type stars found in the MW (*top, left*), 30 Dor (*top, right*) and Carina (*bottom, left*). Kernel density estimations using Gaussian kernels are represented in the (*bottom, right*) hand panel for a better comparison of all samples.

$Z_{\odot}$) and the resolving power of the spectral data (R ∼8000 for all targets in 30 Dor). Again, the same methodology was used for the line-broadening characterization, and due to similar wavelength restrictions both had to rely in many cases on He I instead of metallic lines. Comparing the distributions, we find the same behaviour as before. The lower spectral resolution pushes the Cygnus OB2 distribution to higher velocities for those stars rotating at *vsini* below 200 km s^{-1}. The peak of slow rotators in 30 Dor is found at 40 – 80 km s^{-1} since ∼40 km s^{-1} is the lower limit that could be detected at R ∼8000. There is also a more evident tail of fast rotators reaching 600 km s^{-1}, but this is something expected for O stars located in lower metallicity regions as they lose less angular momentum through stellar winds (see, e.g., Langer 2012).

In the bottom left hand panel we compare our results in Cygnus OB2 and the distribution for the sample of O stars in another Galactic star-forming re-

gion, the Carina Nebula. Both studies have a similar number of targets (66 versus 60) and the line-broadening characterization has been done using the same methodology. The main difference is that for Carina we have a homogeneous spectral sample from the *Gaia*-ESO Survey (GES) at R ∼20000. Again, the lower spectral resolution of the Cygnus OB2 sample is affecting the distribution, detecting the peak of slow rotators at higher velocities. On the contrary both distributions have similar short tails of fast rotators not exceeding 400 km s^{-1} and, interestingly, in Carina we also find a secondary peak of intermediate velocity rotators at ∼220 km s^{-1}. We note that both distributions fall rapidly after this secondary peak without the extended tail of fast rotators. Among the possible explanations we highlight an age effect or even a statistical or an observational bias (fast rotators tend to be underluminous for their spectral type). A more detailed study is required to evaluate whether the lack of very fast rotators in Cygnus OB2 and Carina is significant. In the bottom right hand panel we represent Kernel density estimations using Gaussian kernels for a more clear comparison of all distributions where the secondary peak in Cygnus OB2 and Carina could be clearly distinguished.

In conclusion, we find the distribution of rotational velocities for O stars in Cygnus OB2 similar to those obtained from analogous studies of early-type stars in other Galactic (and extragalactic) regions (Conti & Ebbets 1977; Ramírez-Agudelo et al. 2013; Simón-Díaz & Herrero 2014; Holgado et al. 2018; Berlanas et al. 2019). In spite of the differences in the main peak of slow rotators (that we find at higher rotational velocities due to our restrictions on spectral resolution) the overall shape is similar in all cases, suggesting a general trend for massive O stars that is independent of the considered region. However, for Carina and Cygnus OB2 we find a shorter tail of fast rotators just after a secondary peak of intermediate velocity rotators. Although in Cygnus OB2 it may be consequence of the low resolution, as suggested in the previous subsection, the fact that we find a similar peak in Carina (R ∼20000) makes us consider other possible explanations such as a statistical bias. Therefore, a more detailed study is necessary to clarify the most probable scenario.

6.4 Stellar parameters: $T_{\rm eff}$, log g, log Q and Y(He)

We have determined the fundamental stellar parameters ($T_{\rm eff}$, log g, log Q and Y(He)) for the final sample of 66 O-type stars in Cygnus OB2 performing a quantitative spectroscopic analysis using synthetic FASTWIND models and the `iacob-gbat` tool (see Section 2.2.2). The H and He lines used for each spectral source are summarized in Table 6.6. As explained in Sect. 6.2.2, when different

Table 6.6: Diagnostic lines used for the parameter determination of our sample of O-type stars in Cygnus OB2 subdivided by spectral source (see Table 6.2 for setting details).

	Sources										
Line	1	2	3	4a	4b	4c	4d	5a	5b	6a	6b
Hα							X		X		X
Hβ	X	X	X		X			X		X	
Hγ	X	X	X	X				X		X	
Hδ	X	X	X	X				X		X	
Hϵ	X	X	X	X				X			
He I 4387	X	X	X	X				X		X	
He I 4471	X	X	X	X				X		X	
He I 4713	X	X	X		X			X		X	
He I 4922	X	X	X		X			X		X	
He I 5875						X			X		
He II 4200	X	X	X	X				X		X	
He II 4541	X	X	X	X				X		X	
He II 4686	X	X	X	X	X			X		X	
He II 5411	X					X					
He I+II 4026	X	X	X	X				X		X	
He I+II 6678							X		X		X

spectral data are available for the same target we chose the spectra with the best quality in terms of S/N (and highest resolving power if possible). Derived stellar parameters are shown in Table C.3. We complemented these results with a series of figures (Appendix D) in which the best-fitting model resulting from the analysis of each star is overplotted on the observed spectrum.

6.4.1 Temperature and gravity scales

We have established new effective temperature and gravity scales for O stars in Cygnus OB2 based on the analysis of our sample of O stars. With this aim we first have reclassified all stars in our sample using the MGB software, as described in Sect. 2.1.

In Fig. 6.7 we show the derived $T_{\rm eff}$ and log g values resulting from the

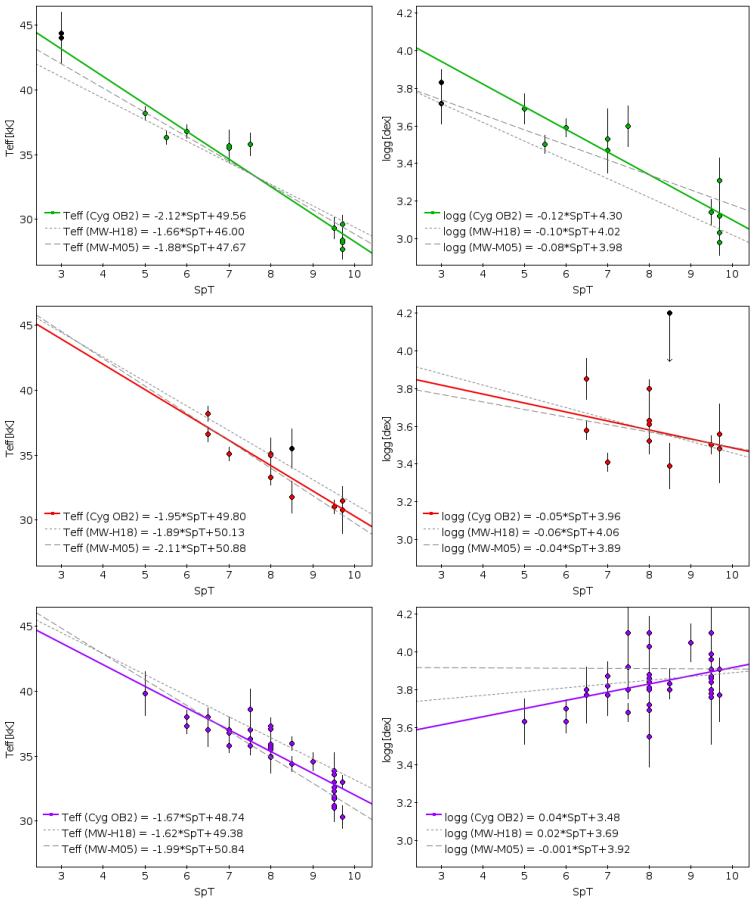

Figure 6.7: Temperature (left) and gravity (right) scales for the Cygnus OB2 O-type sample. *Top*: I-II luminosity classes. *Middle*: III luminosity class. *Bottom*: IV-V luminosity classes. Solid lines indicate the results obtained from our work. Dashed and dotted lines indicates the M05 and H18 scales obtained for a general sample of O-type stars in the MW. Black dots are stars not considered for the fits (see text).

quantitative spectroscopic analysis as a function of the revised spectral type and separated in three blocks by luminosity class (green, orange and purple colours represent I-II, III and IV-V luminosity classes, respectively). The detected SB2 binaries are excluded from the sample. We compare our distributions with two previous scales for O stars in the Milky Way. We first compare with the calibrations presented by Martins et al. (2005a) (dashed lines and henceforth, M05) that have been widely used in many studies of O-type stars. However, we should remark that they are based on a limited stellar sample of 45 stars whose parameters have been compiled from the literature, and therefore, there is a mixture of spectral characteristics, stellar atmosphere codes (FASTWIND and CMFGEN) and subjective criteria that could affect their results. We have also included the recent calibrations presented by Holgado et al. (2018) (dotted lines and henceforth, H18) for a sample of 114 standard O-type stars in our Galaxy, although only 65 were used for the calibrations. In this case, they exclude the detected SB2 stars and those stars with too low He I signal which could lead to a wrong temperature determination. Beside this, they also exclude those O-type supergiants approaching the Eddington limit, i.e., with values of log ${g_{true}}^3 \leq 2.9$ dex and effective temperatures lower than 28500 K. Contrary to M05, they used an homogeneous sample in terms of spectral resolution, analysis methodology (`iacob-gbat`) and stellar atmosphere code (FASTWIND).

We find a general good agreement with both calibrations presented by M05 and H18. For the supergiant sample (luminosity classes I and II, *top* panel) we follow the selection criteria given by H18 and exclude the two hottest stars from our sample with low He I signal (indicated with black dots). This produces a lack of stars earlier than O4.5 that affects more critically the log g scale. In the giant scale (luminosity class III, *middle* panel) we find a much better agreement of our results with both works despite of having a lack of stars earlier than O6. But we should highlight that both H18 and M05 supergiant scales have also a lack of early-type giants. Finally, for the dwarf scale (luminosity classes IV and V, *bottom* panel) we do not find significant differences. Again our sample is not complete in stars earlier than O5, which probably causes the offset found with respect to H18 that increases towards early-type stars. We also find a broad scatter in the gravities associated with a given SpT, as found by H18. However, this is a natural consequence of the wide range of gravities observed in Galactic O-type dwarfs (Simón-Díaz et al. 2014). We also note that in this case log g decreases towards earlier spectral types (higher masses) as it does along the theoretical Zero Age Main Sequence (ZAMS).

Globally the agreement with both studies is good, although we should take

[3] gravity corrected from centrifugal acceleration

into account some relevant points. Firstly, our work is focused on O stars belonging to the same young star-forming region while the studies presented by H18 and M05 are composed by brighter and, in most cases, field O Galactic stars and limited to the standard O-type sample. We have followed the same analysis methodology as H18, but as stated in Sect.6.2.3, our sample is not homogeneous in terms of R, which in some cases could slightly affect the derived scales. Even so, we find minor discrepancies with their results, that we mainly attribute to a statistical bias due to the lack of stars in the earliest O-type regime (see Simón-Díaz et al. 2014).

6.5 Radii, luminosities and masses from *Gaia* DR2

As stated in Sect. 2.2.2, the `iacob-gbat` tool allows to obtain directly radii, luminosities and spectroscopic masses when the absolute magnitude M_v is provided. By using the unprecedented parallaxes delivered by *Gaia* DR2 we have derived M_v values for all our stellar sample with reliable astrometry (RUWE $\leq$ 1.4, see Chapter 5 for details on this criterion). However, we should take into account that these parallax values could be affected by systematic uncertainties of up to 0.1 mas that are not well understood (Luri et al. 2018) and, therefore, should be taken with caution.

Since V-band photometry is not available for all stars of our sample (see Table C.1) we followed the same procedure used by Comerón et al. (2008) to derive M_V values. The absolute magnitude is defined as

$$M_V = 5 - 5 * log(d) + V - A_V = -DM + V - A_V \tag{6.1}$$

where DM is the distance modulus. A_V can be defined in terms of $(V - K_s)$ color excess as

$$A_V = E(V - K_s) + A_{K_s} \tag{6.2}$$

then

$$M_V = K_s - DM - A_{K_s} + (V - K_s)_o \tag{6.3}$$

We used BJ18 distances to estimate individual values of the DM and adopted optical and near-IR photometry (from the USNO-B and 2MASS catalogs) and unreddened intrinsic colours from Martins & Plez (2006). Here, $A_{Ks} = 0.092 * E(B - K_s)$, where the factor 0.092 is derived from the RL85 extinction

law ($1/((A_B/A_{K_s}) - 1) = 0.092$). For five stars of our sample only B- and J-band photometry (from Tycho-2 and 2MASS catalogs) is available, so we adapted Eq. 6.3 to these magnitudes. In these cases, $A_J = 0.271 * E(B-J)$, where ($1/((A_B/A_J) - 1) = 0.271$). For all the sample we find good agreement between the derived M_V values and those obtained from the Martins & Plez (2006) calibration. M_V uncertainties were obtained from the distance errors provided by BJ18. Uncertainties related to the apparent magnitudes are negligible compared with those obtained from distances, that are of the order of $\pm$ 0.13 magnitudes.

However, we should highlight the dependence of A_{K_s} on the assumed extinction law. In order to quantify this effect, in Appendix B we present a study of the implications of considering two different extinction laws for deriving absolute magnitudes. The final list of targets with reliable astrometry for the O-type population in Cygnus OB2 is composed of 53 stars, whose *Gaia* DR2 sources, estimated distances by BJ18 and derived M_V values are presented in Table C.4.

We have also calculated individual visual extinctions (A_V) for all our stellar sample. To achieve this, we used $(B - K_s)$ colors, the unreddened intrinsic colours for O-type stars from Martins & Plez (2006) (the 'observational' T_{eff} scale) and the $R_V = 3.1$ extinction law derived by Rieke & Lebofsky (1985) (henceforth, RL85). For the five stars for which only B- and J-band photometry is available we used $(B-J)$ colours. In Appendix B we also evaluate the impact of the extinction law on the derived visual extinctions.

In Table C.4 we also include the membership group of each star from results of Chapter 5. Luminosities, radii and spectroscopic masses from the `iacob-gbat` tool (Eqs. 2.1, 2.2 and 2.3, see Chapter 2.2.2) are given as well. Uncertainties include (by quadrature) the `iacob-gbat` formal uncertainties and those related to M_V. The latter are calculated from the following equations (and are indicated with an M_V subscript):

$$\Delta log\ R_{M_V} = 0.2 * \Delta M_V \rightarrow \Delta R_{M_V} = 0.46 * R * \Delta M_V \tag{6.4}$$

$$\Delta log\ (L_{M_V}) = 2 * \Delta log\ (R_{M_V}) \tag{6.5}$$

$$\Delta log\ M_{(sp,M_V)} = 2 * \Delta log\ (R_{M_V}) \rightarrow \Delta M_{(sp,M_V)} = 2 * M_{sp}/R * \Delta log\ (R_{M_V}) \tag{6.6}$$

6.5.1 HRD versus sHRD: the evolutionary status

Using the luminosities derived from M_V and the `iacob-gbat` tool, we placed the sample of stars that have passed the criteria for reliable astrometry (RUWE < 1.4, see Chapter 5) in the Hertzsprung-Russell Diagram (HRD). Mean uncertainties are small, $\sim$0.01 dex in log T_{eff} and $\sim$0.05 dex in log($L/L_\odot$). For comparison, we have also placed this sample in the so-called spectroscopic Hertzsprung-Russell Diagram (sHRD), a distance independent diagram presented by Langer & Kudritzki (2014) based on the effective temperature and surface gravity where a spectroscopic luminosity is defined as $\log(\mathcal{L}) = 4 * \log(T_{eff})$ - $\log g$. In both cases, we decided to explore four different stellar models (two families with two initial rotational velocities) in order to assess possible uncertainties in the obtained distribution. We used rotating and non-rotating Geneva (Ekström et al. 2012) and Bonn (Brott et al. 2011) stellar evolutionary tracks and isochrones. In addition, we also divided the sample into the different stellar groups found by Berlanas et al. (2019) (henceforth, B19).

In Fig. 6.8 (top left hand panel) we show the HR diagram using Geneva non-rotating evolutionary models. The age of the O population is well constrained between 1 – 6 Myr, as estimated by other authors (Hanson 2003; Comerón & Pasquali 2012; Wright et al. 2015; Berlanas et al. 2018a). We find the most massive star at around 85 $M_\odot$ and the least massive one at 18 $M_\odot$, as expected for O-type stars. However, four different stellar age groups can be clearly distinguished within the whole population:

(i) We find the older group following the $\sim$6 Myr isochrone with initial masses between 18 – 40 $M_\odot$. The group is well separated in luminosity class, with the two supergiants ALS19627 and J20283038+4105290 close to (but before) the Terminal Age Main Sequence (TAMS) and the dwarfs located along the Main Sequence (MS).

(ii) A more numerous and younger group is found following the $\sim$3 Myr isochrone with initial masses between 20 – 60 $M_\odot$. It is more compact than the others, containing most of the population. Interestingly, all the stars but one belonging to the foreground group at $\sim$1350 pc and those from Group 0 (located between the latter and the main group) seem to follow the same isochrone.

(iii) A third smaller group containing the youngest stars of the sample seems to follow the $\sim$1.5 Myr isochrone with masses between 20 – 85 $M_\odot$. The hottest stars of our sample, Cyg#22A and Cyg#7, are included in this

group. We highlight an apparent lack of stars close to the ZAMS between 40 – 60 $M_{\odot}$.

The same HR diagram is shown in the bottom left hand panel of Fig. 6.8 but now considering rotation ($v/v_{crit} = 0.4$). As stated in Chapter 3, Geneva rotating stellar models provide larger main sequence stellar lifetimes than their non-rotating models. The most massive members are more affected, and in average we find all the age groups ∼2 Myr older than in the non-rotating case.

On the contrary, the Bonn stellar models do not exhibit a large difference in the estimated age of the stars when they include values of initial rotational velocities (v_{ini}) as high as 330 km s^{-1} or no stellar rotation (see Fig 6.9, top and bottom left hand panels). This different behaviour is most likely to be ascribed to their different treatment of angular momentum transport in the stellar interior. In these cases the picture is similar to the non-rotating Geneva case. The most relevant difference is that Bonn models provide a more extended TAMS, and when the models include rotation the ZAMS seems to be slighted displaced to higher luminosities and lower temperatures. In consequence, we find more stars close (or on) the ZAMS.[4]

Finally, comparing the HR diagrams to their respective sHR diagrams (right panels of both Figs. 6.8 and Fig. 6.9) we find some notable differences. On the one hand, the whole population seems to be displaced to higher masses in the sHRD. The most massive star is found at around 120 $M_{\odot}$ and the less massive one at 18 $M_{\odot}$. The age groups seem to be more dispersed although still present: the older group follows the 4 – 5 Myr isochrones (+2 for Geneva rotating models) reaching masses up to 60 $M_{\odot}$, and we find a more concentrated young group at ∼3 Myr (+2) with masses up to 85 $M_{\odot}$. Besides this, we now find an evident gap between the predicted ZAMS and the observed stars above 32 $M_{\odot}$, similar to that found in other studies of O stars (e.g, Herrero et al. 2007; Castro et al. 2014; Sabín-Sanjulián et al. 2017; Holgado et al. 2018). From the HRD we only find a small lack of stars close to the ZAMS, between 40 – 60 $M_{\odot}$. Therefore, we highlight the need for a detailed study on the nature of this gap in order to clarify its origin.

In view of the above results we conclude that although the sHRD is useful to interpret the stellar ages and a general evolutionary status of massive stars when no reliable distances (RUWE > 1.4) are available for them, due to the significant difference in mass found here between the two types of diagrams we

[4]We note that if the canonical distance modulus of 10.8 (Rygl et al. 2012) is used to derive M_V values for all stars of our sample, some of them would appear located close or even slightly below the ZAMS, depending on the considered stellar models. At face, they could constitute the result of a very recent star-forming burst.

should be aware of a possible mass overestimation with respect to the HRD. To reconcile the masses from the two diagrams we would need to increase the stellar luminosity by ∼0.3 – 0.5 dex or decrease the spectroscopic luminosity by a similar amount. But that could imply increasing log g by an amount incompatible with present day atmosphere models (which would also have an impact on the spectroscopic masses). Alternatively (or complementarily) T_{eff} should also decrease beyond present uncertainties.

The sample of the ten O stars that have not passed the selection criteria for reliable astrometry (RUWE > 1.4) have been placed in the sHRD. As before, in Fig. 6.10 we show the four different stellar models discussed above. The only significant point we see is that this small sample increases the number of stars with 3 – 5 Myr, including the evolved star CygOB2 #10.

The points that we can emphasize after placing the stars in the HRD and sHRD are:

- There seems to be on-going star formation in Cygnus OB2 in the last 1 – 6 Myr (+2 Myr if we use the Geneva rotating models). The bursts seem centred roughly at 1.5, 3 and 5 Myr.
- All three bursts could have the same upper mass (∼60 – 85 $M_{\odot}$) although these stars would have already evolved beyond the O-star domain in the case of the 5 Myr burst.
- There is a lack of stars close to the ZAMS, between 40 and 60 $M_{\odot}$ in the HRD and between 32 and 85 $M_{\odot}$ in the sHRD. The gap is more evident in the sHRD.
- We obtain similar results when using the HRD and the sHRD, except that we derive higher stellar masses from the sHRD than from the HRD. If confirmed, this would be a cautionary remark for the use of the sHRD, although it would still be possible to use it to study the evolutionary status of a stellar population.

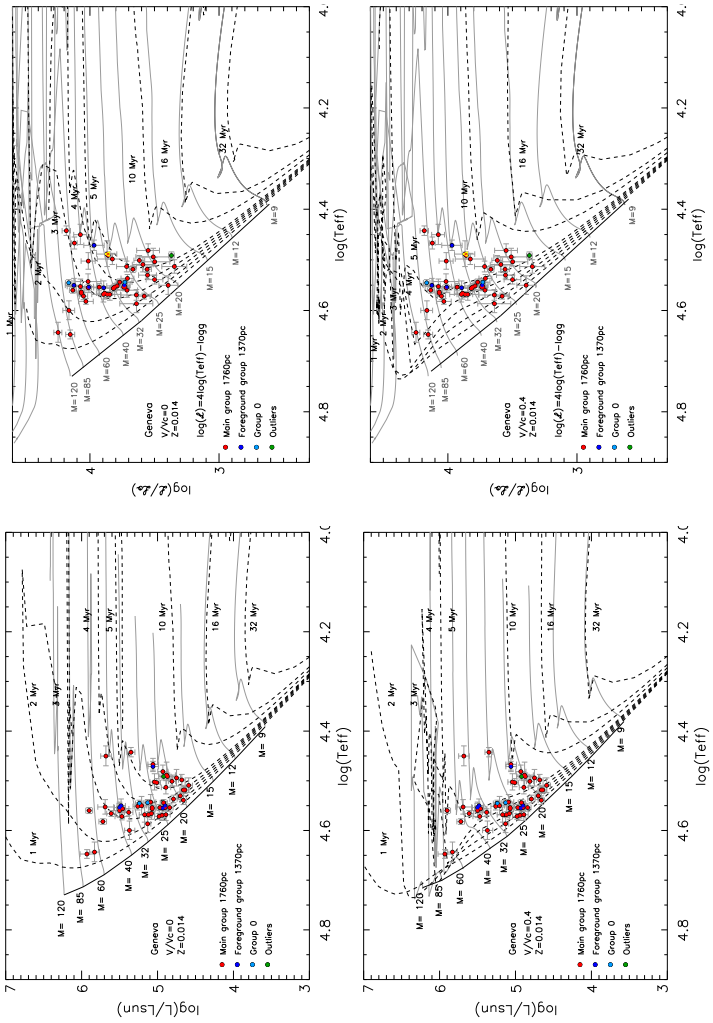

Figure 6.8: HR and sHR diagrams for the sample of O stars in Cygnus OB2 with reliable astrometry using Geneva evolutionary stellar tracks and isochrones from Ekström et al. (2012) and subdivided into the stellar groups found by Berlanas et al. (2018b). *Top left hand panel:* HR diagram considering non-rotating models. *Top right hand panel:* sHR diagram considering non-rotating models. *Bottom left hand panel:* HR diagram considering rotating models ($V/V_c = 0.4$). *Bottom right hand panel:* sHR diagram considering rotating models ($V/V_c = 0.4$). The yellow triangle in the right plots indicates an upper limit for $\log g$.

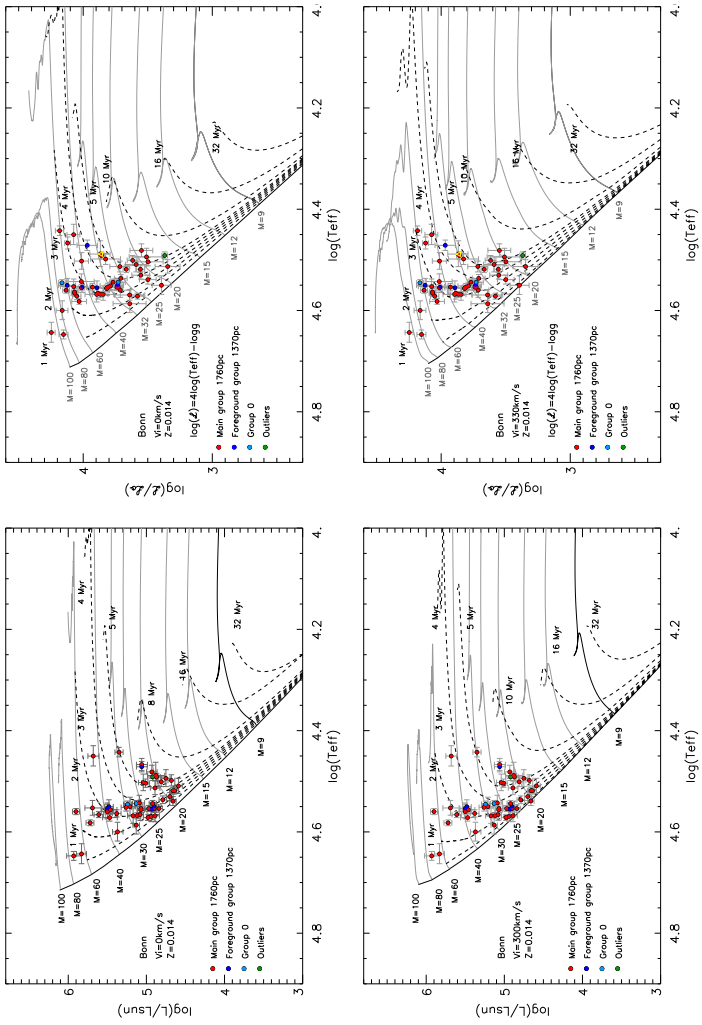

Figure 6.9: HR and sHR diagrams for the sample of O stars in Cygnus OB2 with reliable astrometry using Bonn evolutionary stellar tracks and isochrones from Brott et al. (2011) and subdivided into the stellar groups found by Berlanas et al. (2018b). *Top left hand panel:* HR diagram considering non-rotating models. *Top right hand panel:* sHR diagram considering non-rotating models. *Bottom left hand panel:* HR diagram considering rotating models ($V_i = 330$ km s^{-1}). *Bottom right hand panel:* sHR diagram considering rotating models ($V_i = 330$ km s^{-1}). The yellow triangle in the right plots indicates an upper limit for log g.

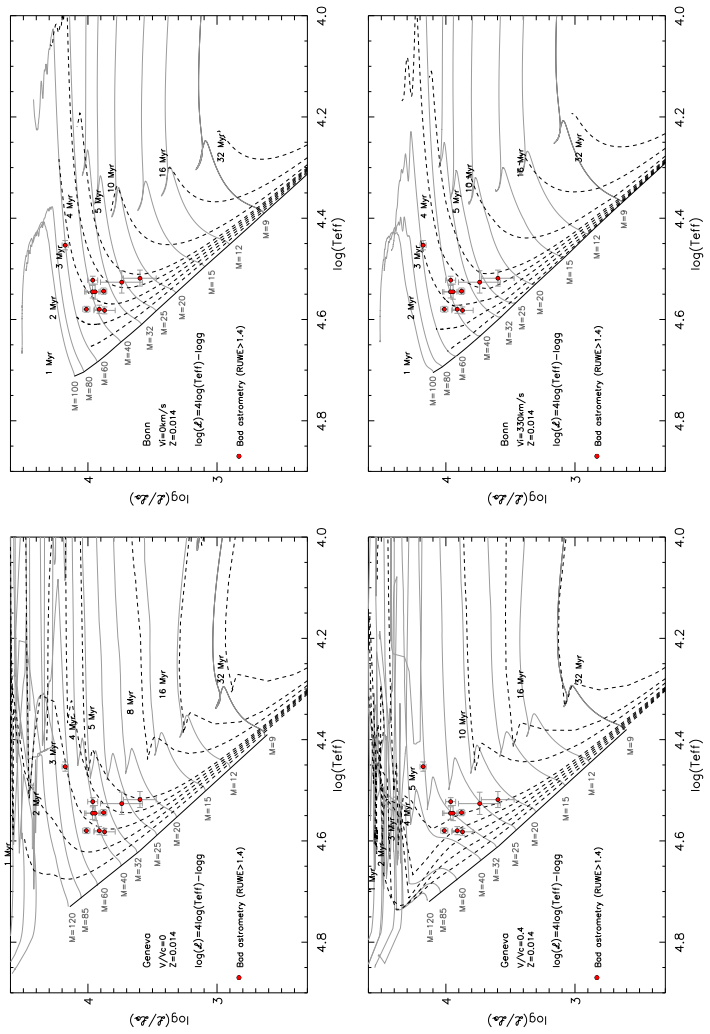

Figure 6.10: sHR diagrams for the sample of O stars in Cygnus OB2 that have not passed the criterion for reliable astrometry. *Top left hand panel*: sHR diagram considering Geneva non-rotating models. *Top right hand panel*: sHR diagram considering Bonn non-rotating models. *Bottom left hand panel*: sHR diagram considering Geneva rotating models ($V/V_c = 0.4$). *Bottom right hand panel*: sHR diagram considering Bonn rotating models ($V_i = 330$ km s^{-1}).

6.5.2 Mass discrepancy

The discrepancy between evolutionary and spectroscopic masses in O-type stars (known as the 'mass discrepancy problem') has been widely discussed in previous studies of O-type stars (e.g., Herrero et al. 1992, 2002; Massey et al. 2005; Mokiem et al. 2007; Sabín-Sanjulián et al. 2017). The spectroscopic mass (M_{sp}) is derived by comparison with stellar atmosphere models (see Sect.2.2.2), while the evolutionary mass (M_{ev}) is obtained by comparing the position of a star in the HR or log g – T_{eff} diagrams with theoretical evolutionary tracks. Some authors find the inferred evolutionary masses significantly higher than the derived spectroscopcic ones. However, others find a relatively good agreement or no compelling evidence for a systematic mass discrepancy. Inaccurate distances, the treatment of mass-loss by stellar atmosphere models, or the treatment of overshooting, rotation, and/or binary evolution in the evolutionary models have been proposed as possible explanations. Nonetheless, there is not a firm consensus about this problem.

We have compared the spectroscopic masses derived from the quantitative spectroscopic analysis (see Table C.4) with evolutionary masses derived by interpolation between Bonn evolutionary tracks (at solar metallicity and v_{ini} = 0 km s^{-1}). For the latter, we used an automatic tool developed by Dr. Miriam García that allows us to obtain initial masses by interpolating the location of a star with the closest tracks. For this first exploration, we used the log g – T_{eff} (Kiel) diagram for the M_{ev} determination since it depends only on spectroscopic parameters and additional uncertainties related to distance, photometry or extinction can be avoided (see Appendix B). Figure 6.11 shows the position of our stars in the Kiel diagram, with Bonn tracks as indicated above.

A preliminary comparison between evolutionary and spectroscopic masses for our sample of O stars with reliable astrometry is shown in Fig. 6.5.2. We find a clear trend to obtain $M_{ev} > M_{sp}$ for stars with $M_{sp} \leq 20$ M$\odot$, in agreement with results from Herrero et al. (1992) for Galactic O stars or Sabín-Sanjulián et al. (2017) in the LMC. However, Sabín-Sanjulián et al. (2017) argued that it could be due to an observational bias, since O-type stars have systematically masses above 15 M$\odot$ and, consequently, any star having a negative mass discrepancy below this value is missed by the stellar sample. In fact, for stars with $M_{sp} \geq 20$ M$\odot$ we find both positive and negative discrepancies between evolutionary and spectroscopic masses. We find no systematic trends with rotational velocity, although there is a trend towards higher M_{ev} for the luminosity class I-II. However, we cannot conclude any obvious systematic pattern when uncertainties are considered. A detailed further quantitative study of a more

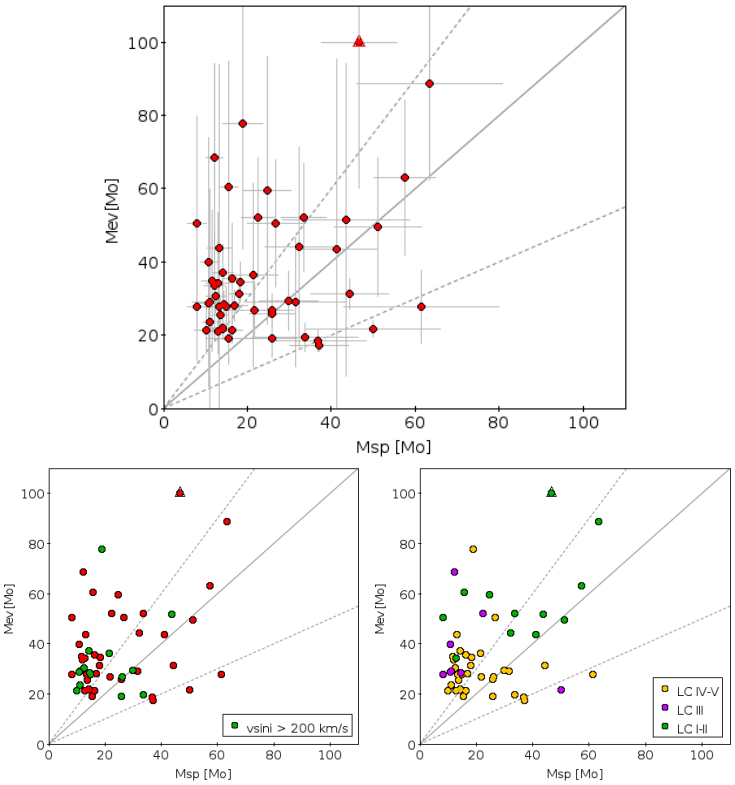

Figure 6.11: *Top*: Comparison between the derived evolutionary and spectroscopic masses for our sample of O-stars in Cygnus OB2. The triangle indicates a M_{ev} lower limit. Evolutionary masses have been obtained from interpolation in the log $g - T_{eff}$ diagram with Bonn evolutionary tracks (at solar metallicity and $v_{ini} = 0$ km s^{-1}). Solid line indicates the 1:1 relation, with $\pm$ 50% shown by dashed lines. *Bottom*: As the top panel, but divided for rotational velocities (left) and luminosity class (right).

extensive sample including B-type stars is thus required to investigate the observed behaviour. The next WEAVE survey in Cygnus will provide the data needed to achieve this purpose (see Chapter 7.2).

7

Conclusions & future work

In this final chapter we summarize the main results obtained in the present thesis, as well as future research perspectives to continue this work.

7.1 Conclusions

In the three published articles that comprise the main part of this thesis work we have carried out different (but related) studies in the Cygnus OB2 star-forming association, where the main physical properties of its massive population have been characterized.

In the first article of this thesis (Chapter 3: *New massive members of Cygnus OB2*) we present a membership study of Cygnus OB2 and its surroundings. We carried out new spectroscopic observations for a magnitude-limited list of 61 OB candidates in the region. Here, we list the main results obtained from this study.

1) The confirmation of 42 new OB massive stars (including 11 new O-type stars), which allowed us to increase the young massive population known in the region and provided new data on the extinction distribution of the area.

2) The realization that many OB stars are still undiscovered in the Cygnus region, since the magnitude cut-off of the photometric selected candidates ($B < 16$ mag) and the strong dust extinction introduce an incompleteness.

3) The confirmation of an age spread of 1 – 6 Myr in Cygnus OB2, as well as a correlation between age and Galactic longitude. This suggests that massive star formation has proceeded from lower to higher Galactic longitudes, from Cygnus OB9 to Cygnus OB2, with a strong peak in the northern part of the latter.

In the second article (Chapter 4: *Oxygen and silicon abundances in Cygnus OB2. Chemical homogeneity in a sample of OB slow rotators*) a chemical study of the region is presented in order to check possible inhomogeneities across the whole association and whether there also exists a correlation of chemical composition with Galactic longitude that could show evidence for effects of self-enrichment processes. With this aim, we derived silicon and oxygen abundances in a sample of OB stars that was carefully selected to obtain accurate abundance values: it is a sample of late O- and early B-type stars covering the whole association area and with projected rotational velocities below 80 km s^{-1}. The abundance analysis was based on the EW of silicon and oxygen lines and the Balmer line profiles. The main results obtained from this study are listed below.

1) A homogeneous chemical composition across Galactic longitude has been found in the association, with no evidence for significant self-enrichment

processes despite indications that many massive stars have exploded as supernovae during the history of the region. We derive average silicon and oxygen abundance values of 12 + log(Si/H) = 7.53 ± 0.08 dex and 12 + log(O/H) = 8.65 ± 0.12 dex, respectively.

2) The estimate of the contribution to oxygen enrichment of SNe that may have exploded in the region shows that the original cloud from which stars formed in Cygnus OB2 had a homogeneous metallicity and has not been significantly enriched during its lifetime as a consequence of its star-forming activity. This result is in agreement with the findings in Orion OB1 and the solar vicinity.

3) The effect of self-enrichment is currently beyond the accuracy of our analyses. Our computations illustrate the difficulties of making quantitative predictions of the level of enrichment expected in a massive association like Cygnus OB2, and show in any case that this level should be small compared to the accuracies currently attainable.

In the third article (Chapter 5: *Disentangling the spatial substructure of Cygnus OB2 from Gaia DR2*) the internal substructure of Cygnus OB2 has been explored using parallaxes (that passed the criterion for reliable astrometry) from the recent second *Gaia* data release (DR2). We used a Bayesian inference procedure to derive distances from parallaxes due to the non-linearity of the transformation and the asymmetry of the resulting probability distribution. Thus we created a parametrized model to reproduce the observed parallax distribution and then we sampled fully the posterior distribution to compare it finally to the observations using an unbinned likelihood test. The main results obtained from this study are

1) We fitted the observed parallax distribution with both 1-, 2-, and 3-component Gaussian models and found that the best fit to the data was provided by the 2-component model. We identified two superposed but spatially separated stellar groups within Cygnus OB2.

2) We found the main Cygnus OB2 group is at ∼1760 pc, further away than recent estimates have envisaged, implying that all its stellar content is in fact more massive and brighter. Furthermore, the observed parallax distribution suggests there may be further substructure within the association, though this is not well resolved by the available parallaxes.

3) The second group is several hundred parsecs in the foreground, at ∼1350 pc, and appears more extended than the main group. It represents 10 % of the whole OB population.

4) We have calculated individual membership probabilities and identified outliers as possible foreground or background contaminants, unrelated to either group.

In addition to these articles, we have added an extra chapter where the stellar parameters of the current known O-type population of Cygnus OB2 have been derived using semi-automated tools for the quantitative spectroscopic analysis of OB stars. With this aim, we complemented new intermediate-high resolution and high S/N spectra with already available spectra from previous observations. The main results from this study are listed as follows.

1) The creation of the most complete spectroscopic census of O stars so far in the association, consisting of a sample of 77 O-type stars that includes the new O stars identified in the first article of this thesis. We have identified new binary systems and performed quantitative spectroscopic analysis of the sample (excluding detected SB2 stars) to obtain the distribution of rotational velocities and main stellar parameters.

2) We find the distribution of rotational velocities similar to those obtained from analogous studies of early-type stars in other Galactic (and extra-galactic) regions, with a main peak of slow rotators at $\sim$80 – 100 km s^{-1} that is probably overestimated by 25 km s^{-1} due to low resolution. However, a short tail of fast rotators just after a secondary peak of intermediate velocity rotators is also present in the distribution. Interestingly, a similar behaviour has been found in Carina (from the *Gaia*-ESO Survey), but not in the other samples studied here.

3) New O spectral type scales for temperature and gravity have been created. We find a general good agreement with previous calibrations of Galactic O-type stars.

4) In addition to this, using distances from *Gaia* DR2 we have estimated radii, luminosities and spectroscopic masses for the stars in our sample with reliable astrometry (RUWE $\leq$ 1.4). We also derived evolutionary masses by interpolation with theoretical evolutionary tracks. We find that the less massive stars of our sample show $M_{ev} > M_{sp}$. However, we cannot conclude any obvious systematic pattern when uncertainties are considered.

5) The global evolutionary status of the association using the Hertzsprung-Russell diagram, has been discussed. We find star formation during the

last 1 – 6 Myr, with three bursts centred roughly at 1.5, 3 and 5 Myr. All of them have the same upper mass ($\sim$60 – 85 $M_{\odot}$) although these stars would have already evolved beyond the O-star domain in the case of the 5 Myr burst. We obtain similar results when using the HRD and its spectroscopic version (sHRD), except that we derive higher stellar masses from the sHRD than from the HRD. If confirmed, this would be a cautionary remark for the use of the sHRD, although it would still be possible to use it to study the evolutionary status of a stellar population.

6) The implications of not considering the macroturbulent broadening when it could be considered an upper limit have been evaluated. Although in the cases analyzed here the distribution of rotational velocities is not strongly affected due to the possible overestimation of *vmac*, some individual *vsini* values suffer an important variation. Therefore, this effect could be significant for the spectral characterization of individual stars.

7) The importance of the adopted photometry and extinction law for obtaining visual extinctions has been confirmed. They can be additional sources of uncertainty and have a significant impact in the characterization of the interstellar extinction of obscured regions, especially when near-IR colours are used.

The results presented in this thesis have increased the current knowledge on Cygnus OB2 and its massive star population. The better vision we now have moves us a bit closer to a complete understanding of the origin and evolution of Cygnus OB2, Cygnus-X, and OB associations in general.

7.2 Future work

The work presented in this thesis has provided further data to form a much more complete view of the OB population in Cygnus OB2. Nevertheless, large uncertainties persist in our understanding of massive stars. This study has left open questions that need to be addressed in the near future and that are summarized as follows.

Distances and proper motions

We will use data from current and further *Gaia* data releases to increase the accuracy in the derived physical parameters for all our stellar sample in Cygnus OB2. As stated in Sect. 2.3, parallaxes may be affected by systematic errors up to 0.1 mas that are complicated to handle and must be taken into account for deriving accurate individual stellar distances. Unfortunately, Bailer-Jones et al. (2018) do not include them in their analysis and there is no simple recipe to account for them. To deal with systematics, an extension of the classical Bayesian inference method is recommended, where complementary information can be added to the model (see, e.g., Luri et al. 2018). It is obvious that parallax has a direct relation to the distance of a star. However, it is not the unique measurement containing information about it. As an example, the colour of a star includes significant information on the plausible stellar distance since it is related to the absolute magnitude of the star (see, e.g., Anderson et al. 2018). Proper motions also contain distance information that can be used to derive more precise distances for cluster members (e.g., de Bruijne et al. 2001).

Thus, the methodology used in Chapter 5 can be extended to include parallax systematics and known correlation terms in the modelling, that will help to constrain systematic uncertainties and derive more accurate distance values for individual massive stars. A better comparison of stellar masses and radii derived from the spectroscopic analyses and the evolutionary codes (the 'mass discrepancy' problem, see Chapter 6.5.1) will be then carefully studied. Furthermore, we will have a unique opportunity for a detailed 3D kinematic study of young star-forming regions (Wright et al. 2016; Armstrong et al. 2018; Drew et al. 2018). A detailed dynamical study of the Cygnus OB2 region along with the spatial structure found in Chapter 5, could help to obtain a much fuller view of its OB population. The high-quality of proper motions provided by *Gaia* DR2, that will be improved in future releases, has enabled detailed studies of the spatial and kinematic substructure of close stellar associations (see, e.g. Cantat-Gaudin et al. 2018, 2019) that can be reproduced in the Cygnus region.

Carbon and Nitrogen abundances

We will determine accurate abundances of C and N for all O-type stars in Cygnus OB2 using state-of-the-art model atmospheres and tools (see Chapter 2.2.3 and the recent work by Carneiro et al. (2019)). As pointed out in Sect. 1.1.2, He and N overabundances and C underabundances are evidence of the mixing mechanisms that take place in the stellar interior. Combined with other stellar parameters (mass, age, luminosity, rotational velocity) we will establish whether they are the result of rotational mixing, of binary interaction (including merger processes) or a combination of the effects discussed in Chapter 1.

Extension to other wavelengths and stellar evolutionary stages

The incorporation of near-IR spectroscopic data to state-of-the-art analysis of massive stars in Galactic star-forming regions will help to create large observational multi-wavelength databases of extensive samples of high-quality OB star spectra in homogeneous environments. This will allow us to observe objects inaccessible at optical wavelengths due to absorption, and to study highly extinguished objects. The extension of FASTWIND to near-IR wavelengths (see Rübke 2017, PhD) along with the tools presented in Chapter 2.2.2 for the spectroscopic analysis of OB-type stars, will allow us to analyze very extinguished stars in Cygnus OB2, combining and expanding our research at optical wavelength to wider ranges.

We will also extend our stellar sample to stars in other evolutionary stages, such as red supergiants and Wolf-Rayets, in order to understand the implications of rotation, multiplicity, internal mixing and large scale motions in their structure and evolution. FASTWIND is not well suited to analyze these objects, so for the former, MARCS stellar models (Gustafsson et al. 2008) can be used to perform the spectroscopic analysis, while for the latter, we will use models calculated with the CMFGEN code (Hillier & Miller 1998).

WEAVE Cygnus Survey

As a finishing remark to this thesis work, the results presented here will be used to optimize the sample for the future high-resolution WEAVE Cygnus survey at R = 20000 (henceforth, WCYGS).

As stated in Sect. 1.3, the upcoming WEAVE survey of the Cygnus region will provide high-quality spectra for the whole OB content of several rich Cygnus OB associations over the coming years, including Cygnus OB2. This survey will be built on top of the results from the low-resolution WEAVE sur-

vey on the disc plane at R = 5000 (which will also cover the Cygnus region) to confirm spectral types and obtain a first estimate of the basic stellar parameters. The results of Chapter 6 will help to optimize the final WCYGS sample of Cygnus OB2, representing a statistical template for the other Cygnus associations. Moreover, our spectral sample will add an additional epoch, which is particularly important to identify multiplicity.

The WCYGS is the natural follow-up of this thesis, representing a unique opportunity to improve the work presented here. As pointed out in Sect. 6.2.3, the spectroscopic study of the known O population of Cygnus OB2 comprises an inhomogeneous spectral sample, mainly in terms of spectral resolution. The difference between a resolution of 2500 and 20000 is important because of the rotational velocities of OB stars, that could lead to significant errors in gravity (and the consequent change in temperature). WCYGS will provide homogeneous high-resolution spectra of the whole OB sample for a better determination of the rotational parameters (*vsini* and *vmac*, especially at velocities below 100 km s^{-1}) and the stellar parameters (particularly gravity and, therefore, mass). Moreover, the 'mass discrepancy' problem (see Chapter 6.5.2) will be carefully investigated, using a more extensive sample of OB-type stars.

In addition to this, one of the main goals of the WCYGS is the determination of accurate stellar abundances for a large sample of OB stars in the region. We show in Chapter 4 that the quality of the spectra is essential for determining accurate abundances. WEAVE will allow us to increase significantly the suitable stellar sample for the chemical analysis. Furthermore, the difference between a resolution of 10000 and 20000 will lead to smaller abundance errors, improving the accuracy of our results to study spatial abundance patterns and test processes such as self-enrichment. Moreover, we will also be able to extend all the studies carried out in Cygnus OB2 to other Cygnus associations covered by the survey.

Combining the findings of this thesis, WEAVE data and *Gaia* astrometry we will be in the best position to improve our knowledge of star formation and evolution of star-forming regions and clusters, including our understanding of the dynamics and kinematics of OB associations and stellar groups.

Bibliography

Anchordoqui, L. A., Goldberg, H., Moore, R. D., et al. 2009, Phys. Rev. D, 80, 103004

Anderson, L., Hogg, D. W., Leistedt, B., Price-Whelan, A. M., & Bovy, J. 2018, AJ, 156, 145

Araudo, A. T., Ortiz-León, G. N., & Rodríguez, L. F. 2012, in American Institute of Physics Conference Series, Vol. 1505, American Institute of Physics Conference Series, ed. F. A. Aharonian, W. Hofmann, & F. M. Rieger, 422–425

Arenou, F., Luri, X., Babusiaux, C., et al. 2018, A&A, 616, A17

Armstrong, J. J., Wright, N. J., & Jeffries, R. D. 2018, MNRAS, 480, L121

Astraatmadja, T. L., & Bailer-Jones, C. A. L. 2016, ApJ, 832, 137

Babel, J., & Montmerle, T. 1997, A&A, 323, 121

Bailer-Jones, C. A. L. 2015, PASP, 127, 994

Bailer-Jones, C. A. L., Rybizki, J., Fouesneau, M., Mantelet, G., & Andrae, R. 2018, AJ, 156, 58

Berlanas, S. R., Herrero, A., Comerón, F., et al. 2018a, A&A, 612, A50

—. 2018b, A&A, 620, A56

Berlanas, S. R., Herrero, A., Martins, F., et al. 2017, in Highlights on Spanish Astrophysics IX, ed. S. Arribas, A. Alonso-Herrero, F. Figueras, C. Hernández-Monteagudo, A. Sánchez-Lavega, & S. Pérez-Hoyos, 453–456

Berlanas, S. R., Wright, N. J., Herrero, A., Drew, J. E., & Lennon, D. J. 2019, MNRAS, 484, 1838

Bouret, J. C., Lanz, T., Hillier, D. J., et al. 2003, ApJ, 595, 1182

Bromm, V., Yoshida, N., Hernquist, L., & McKee, C. F. 2009, Nature, 459, 49

Brott, I., de Mink, S. E., Cantiello, M., et al. 2011, A&A, 530, A115

Cantat-Gaudin, T., Mapelli, M., Balaguer-Núñez, L., et al. 2019, A&A, 621, A115

Cantat-Gaudin, T., Jordi, C., Wright, N. J., et al. 2018, arXiv e-prints, arXiv:1812.08114

Cardelli, J. A., Clayton, G. C., & Mathis, J. S. 1989, ApJ, 345, 245

Carneiro, L. P., Puls, J., Hoffmann, T. L., Holgado, G., & Simón-Díaz, S. 2019, A&A, 623, A3

Castor, J. I., Abbott, D. C., & Klein, R. I. 1975, ApJ, 195, 157

Castro, N., Fossati, L., Langer, N., et al. 2014, A&A, 570, L13

Chentsov, E. L., Klochkova, V. G., Panchuk, V. E., Yushkin, M. V., & Nasonov, D. S. 2013, Astronomy Reports, 57, 527

Chlebowski, T., & Garmany, C. D. 1991, ApJ, 368, 241

Clark, J. S., Najarro, F., Negueruela, I., et al. 2012, A&A, 541, A145

Clark, J. S., Negueruela, I., Crowther, P. A., & Goodwin, S. P. 2005, A&A, 434, 949

Clark, J. S., Ritchie, B. W., Negueruela, I., et al. 2011, A&A, 531, A28

Comerón, F., Djupvik, A. A., Schneider, N., & Pasquali, A. 2016, A&A, 586, A46

Comerón, F., & Pasquali, A. 2012, A&A, 543, A101

Comerón, F., Pasquali, A., Figueras, F., & Torra, J. 2008, A&A, 486, 453

Comerón, F., Pasquali, A., Rodighiero, G., et al. 2002, A&A, 389, 874

Conti, P. S. 1975, Memoires of the Societe Royale des Sciences de Liege, 9, 193

Conti, P. S., & Crowther, P. A. 2004, MNRAS, 355, 899

Conti, P. S., & Ebbets, D. 1977, ApJ, 213, 438

Cotera, A. S., Erickson, E. F., Colgan, S. W. J., et al. 1996, ApJ, 461, 750

Crowther, P., & Smartt, S. 2007, Astronomy and Geophysics, 48, 1.35

Crowther, P. A. 2007, ARA&A, 45, 177

Crowther, P. A., Lennon, D. J., & Walborn, N. R. 2006, A&A, 446, 279

Cunha, K., & Lambert, D. L. 1992, ApJ, 399, 586

—. 1994, ApJ, 426, 170

De Becker, M., Rauw, G., & Manfroid, J. 2004, A&A, 424, L39

de Bruijne, J. H. J., Hoogerwerf, R., & de Zeeuw, P. T. 2001, A&A, 367, 111

De Marchi, G., Paresce, F., Panagia, N., et al. 2011, ApJ, 739, 27

de Mink, S. E., Langer, N., Izzard, R. G., Sana, H., & de Koter, A. 2013, ApJ, 764, 166

Deharveng, L., Schuller, F., Anderson, L. D., et al. 2010, A&A, 523, A6

Drew, J. E., Greimel, R., Irwin, M. J., & Sale, S. E. 2008, MNRAS, 386, 1761

Drew, J. E., Herrero, A., Mohr-Smith, M., et al. 2018, MNRAS, 480, 2109

Drew, J. E., Greimel, R., Irwin, M. J., et al. 2005, MNRAS, 362, 753

Ekström, S., Meynet, G., Chiappini, C., Hirschi, R., & Maeder, A. 2008, A&A, 489, 685

Ekström, S., Georgy, C., Eggenberger, P., et al. 2012, A&A, 537, A146

Esteban, C., García-Rojas, J., Peimbert, M., et al. 2005, ApJ, 618, L95

Figer, D. F., McLean, I. S., & Morris, M. 1999, ApJ, 514, 202

Fitzgerald, M. P. 1970, A&A, 4, 234

Fitzpatrick, E. L., & Massa, D. 2007, ApJ, 663, 320

Foreman-Mackey, D., Conley, A., Meierjurgen Farr, W., et al. 2013, emcee: The MCMC Hammer, Astrophysics Source Code Library, ascl:1303.002

Fossati, L., Castro, N., Schöller, M., et al. 2015a, A&A, 582, A45

Fossati, L., Castro, N., Morel, T., et al. 2015b, A&A, 574, A20

Friend, D. B., & Abbott, D. C. 1986, ApJ, 311, 701

Fullerton, A. W., Massa, D. L., & Prinja, R. K. 2006, ApJ, 637, 1025

Gaia Collaboration, Prusti, T., de Bruijne, J. H. J., et al. 2016, A&A, 595, A1

Gaia Collaboration, Brown, A. G. A., Vallenari, A., et al. 2018, A&A, 616, A1

Garcia, M., Najarro, F., & Herrero, A. 2011, Bulletin de la Societe Royale des Sciences de Liege, 80, 144

Gibson, B. K. 2000, Mem. Soc. Astron. Italiana, 71, 693

Gili, R., & Bonneau, D. 2001, A&A, 378, 954

Goodman, J., & Weare, J. 2010, Communications in Applied Mathematics and Computational Science, 5, 65

Gray, D. F. 2008, The Observation and Analysis of Stellar Photospheres

Gray, R. O., & Corbally, J., C. 2009, Stellar Spectral Classification

Grunhut, J. H., Wade, G. A., Neiner, C., et al. 2017, MNRAS, 465, 2432

Guarcello, M. G., Wright, N. J., Drake, J. J., et al. 2012, ApJS, 202, 19

Gustafsson, B., Edvardsson, B., Eriksson, K., et al. 2008, A&A, 486, 951

Hanson, M. M. 2003, ApJ, 597, 957

Heger, A. 2012, in Astrophysics and Space Science Library, Vol. 384, Eta Carinae and the Supernova Impostors, ed. K. Davidson & R. M. Humphreys, 299

Herrero, A. 2016, in Astronomical Society of the Pacific Conference Series, Vol. 507, Multi-Object Spectroscopy in the Next Decade: Big Questions, Large Surveys, and Wide Fields, ed. I. Skillen, M. Balcells, & S. Trager, 135

Herrero, A., Corral, L. J., Villamariz, M. R., & Martín, E. L. 1999, A&A, 348, 542

Herrero, A., Kudritzki, R. P., Vilchez, J. M., et al. 1992, in Lecture Notes in Physics, Berlin Springer Verlag, Vol. 401, The Atmospheres of Early-Type Stars, ed. U. Heber & C. S. Jeffery, 21

Herrero, A., Puls, J., Corral, L. J., Kudritzki, R. P., & Villamariz, M. R. 2001, A&A, 366, 623

Herrero, A., Puls, J., & Najarro, F. 2002, A&A, 396, 949

Herrero, A., Puls, J., & Villamariz, M. R. 2000, A&A, 354, 193

Herrero, A., Simon-Diaz, S., Najarro, F., & Ribas, I. 2007, in Astronomical Society of the Pacific Conference Series, Vol. 367, Massive Stars in Interactive Binaries, ed. N. St.-Louis & A. F. J. Moffat, 67

Hillier, D. J., & Miller, D. L. 1998, ApJ, 496, 407

Holgado, G., Simón-Díaz, S., Barbá, R. H., et al. 2018, A&A, 613, A65

Humphreys, R. M., & McElroy, D. B. 1984, ApJ, 284, 565

Hunter, I., Brott, I., Lennon, D. J., et al. 2008, ApJ, 676, L29

Johnson, H. L. 1966, ARA&A, 4, 193

Johnson, H. L., & Morgan, W. W. 1954, ApJ, 119, 344

Kennedy, M., Dougherty, S. M., Fink, A., & Williams, P. M. 2010, ApJ, 709, 632

Kilian, J. 1992, A&A, 262, 171

Kiminki, D. C., & Kobulnicky, H. A. 2012, ApJ, 751, 4

Kiminki, D. C., Kobulnicky, H. A., Gilbert, I., Bird, S., & Chunev, G. 2009, AJ, 137, 4608

Kiminki, D. C., McSwain, M. V., & Kobulnicky, H. A. 2008, ApJ, 679, 1478

Kiminki, D. C., Kobulnicky, H. A., Kinemuchi, K., et al. 2007, ApJ, 664, 1102

Kiminki, D. C., Kobulnicky, H. A., Ewing, I., et al. 2012, ApJ, 747, 41

Knödlseder, J. 2000, A&A, 360, 539

Knödlseder, J. 2003, in IAU Symposium, Vol. 212, A Massive Star Odyssey: From Main Sequence to Supernova, ed. K. van der Hucht, A. Herrero, & C. Esteban, 505

Knödlseder, J., Cerviño, M., Le Duigou, J.-M., et al. 2002, A&A, 390, 945

Kobulnicky, H. A., Smullen, R. A., Kiminki, D. C., et al. 2012, ApJ, 756, 50

Kobulnicky, H. A., Kiminki, D. C., Lundquist, M. J., et al. 2014, ApJS, 213, 34

Kroupa, P., Aarseth, S., & Hurley, J. 2001, MNRAS, 321, 699

Kudritzki, R. P. 1980, A&A, 85, 174

Kudritzki, R. P., Lennon, D. J., & Puls, J. 1995, in Science with the VLT, ed. J. R. Walsh & I. J. Danziger, 246

Lada, C. J., & Lada, E. A. 2003, ARA&A, 41, 57

Langer, N. 2012, ARA&A, 50, 107

Langer, N., & Kudritzki, R. P. 2014, A&A, 564, A52

Lanz, T., & Hubeny, I. 2003, ApJS, 146, 417

—. 2007, ApJS, 169, 83

Laur, J., Kolka, I., Eenmäe, T., Tuvikene, T., & Leedjärv, L. 2017, A&A, 598, A108

Lejeune, T., & Schaerer, D. 2001, A&A, 366, 538

Lindegren, L., Hernández, J., Bombrun, A., et al. 2018, A&A, 616, A2

Linder, N., Rauw, G., Manfroid, J., et al. 2009, A&A, 495, 231

Liu, H.-L., Li, J.-Z., Wu, Y., et al. 2016, ApJ, 818, 95

Lorenzo-Gutiérrez, A., Alfaro, E. J., Maíz Apellániz, J., et al. 2019, MNRAS, 486, 966

Luri, X., Brown, A. G. A., Sarro, L. M., et al. 2018, A&A, 616, A9

Maeder, A., & Meynet, G. 2000, ARA&A, 38, 143

—. 2014, ApJ, 793, 123

Maíz Apellániz, J. 2010, A&A, 518, A1

Maíz Apellániz, J., Pellerin, A., Barbá, R. H., et al. 2012, in Astronomical Society of the Pacific Conference Series, Vol. 465, Proceedings of a Scientific Meeting in Honor of Anthony F. J. Moffat, ed. L. Drissen, C. Robert, N. St-Louis, & A. F. J. Moffat, 484

Maíz Apellániz, J., Alfaro, E. J., Arias, J. I., et al. 2015, in Highlights of Spanish Astrophysics VIII, ed. A. J. Cenarro, F. Figueras, C. Hernández-Monteagudo, J. Trujillo Bueno, & L. Valdivielso, 603–603

Maíz Apellániz, J., Sota, A., Arias, J. I., et al. 2016, ApJS, 224, 4

Maíz Apellániz, J., Trigueros Páez, E., Negueruela, I., et al. 2019, arXiv e-prints, arXiv:1904.11385

Markova, N., & Puls, J. 2008, A&A, 478, 823

Markova, N., & Puls, J. 2015, in IAU Symposium, Vol. 307, New Windows on Massive Stars, ed. G. Meynet, C. Georgy, J. Groh, & P. Stee, 117–118

Martins, F., & Plez, B. 2006, A&A, 457, 637

Martins, F., Schaerer, D., & Hillier, D. J. 2002, A&A, 382, 999

—. 2005a, A&A, 436, 1049

Martins, F., Schaerer, D., Hillier, D. J., et al. 2005b, A&A, 441, 735

Mason, B. D., Hartkopf, W. I., Gies, D. R., Henry, T. J., & Helsel, J. W. 2009, AJ, 137, 3358

Massey, P., DeGioia-Eastwood, K., & Waterhouse, E. 2001, AJ, 121, 1050

Massey, P., Johnson, K. E., & Degioia-Eastwood, K. 1995, ApJ, 454, 151

Massey, P., Morrell, N. I., Neugent, K. F., et al. 2012, ApJ, 748, 96

Massey, P., Puls, J., Pauldrach, A. W. A., et al. 2005, ApJ, 627, 477

Massey, P., & Thompson, A. B. 1991, AJ, 101, 1408

Matthews, T. A., & Sandage, A. R. 1963, ApJ, 138, 30

Meynet, G., Eggenberger, P., & Maeder, A. 2011, A&A, 525, L11

Mikulášek, Z., Krtička, J., Henry, G. W., et al. 2008, A&A, 485, 585

Mokiem, M. R., de Koter, A., Vink, J. S., et al. 2007, A&A, 473, 603

Morgan, W. W., Johnson, H. L., & Roman, N. G. 1954, PASP, 66, 85

Münch, L., & Morgan, W. W. 1953, ApJ, 118, 161

Najarro, F., Herrero, A., & Verdugo, E. 2006, Ap&SS, 303, 153

Nazé, Y., Mahy, L., Damerdji, Y., et al. 2012, A&A, 546, A37

Negueruela, I., Marco, A., Herrero, A., & Clark, J. S. 2008, A&A, 487, 575

Negueruela, I., Simón, S., Dorda, R., et al. 2019, in Highlights on Spanish Astrophysics X, Proceedings of the XIII Scientific Meeting of the Spanish Astronomical Society held on July 16-20, 2018, in Salamanca, Spain, ISBN 978-84-09-09331-1. B. Montesinos, A. Asensio Ramos, F. Buitrago, R. Schödel, E. Villaver, S. Pérez-Hoyos, I. Ordóñez-Etxeberria (eds.) p. 425-425, ed. B. Montesinos, A. Asensio Ramos, F. Buitrago, R. Schödel, E. Villaver, S. Pérez-Hoyos, & I. Ordóñez-Etxeberria, 425–425

Nieva, M.-F. 2013, A&A, 550, A26

Palmeirim, P., Zavagno, A., Elia, D., et al. 2017, A&A, 605, A35

Pauldrach, A., Puls, J., & Kudritzki, R. P. 1986, A&A, 164, 86

Pecaut, M. J., & Mamajek, E. E. 2013, ApJS, 208, 9

Phillips, A. C. 1999, The Physics of Stars, 2nd Edition

Portegies Zwart, S. F., McMillan, S. L. W., & Gieles, M. 2010, ARA&A, 48, 431

Prantzos, N., Abia, C., Limongi, M., Chieffi, A., & Cristallo, S. 2018, MNRAS, 476, 3432

Prinja, R. K., & Fenech, D. 2011, in IAU Symposium, Vol. 272, Active OB Stars: Structure, Evolution, Mass Loss, and Critical Limits, ed. C. Neiner, G. Wade, G. Meynet, & G. Peters, 306–307

Przybilla, N., Nieva, M.-F., & Butler, K. 2008, ApJ, 688, L103

Puls, J., Urbaneja, M. A., Venero, R., et al. 2005, A&A, 435, 669

Puls, J., Vink, J. S., & Najarro, F. 2008, A&A Rev., 16, 209

Puls, J., Kudritzki, R. P., Herrero, A., et al. 1996, A&A, 305, 171

Rahman, M., & Murray, N. 2010, ApJ, 719, 1104

Ramírez-Agudelo, O. H., Simón-Díaz, S., Sana, H., et al. 2013, A&A, 560, A29

Rauw, G. 2011, A&A, 536, A31

Rauw, G., Vreux, J. M., & Bohannan, B. 1999, ApJ, 517, 416

Rauw, G., Nazé, Y., Wright, N. J., et al. 2015, ApJS, 221, 1

Reddish, V. C. 1968, The Observatory, 88, 139

Reed, B. C. 2003, AJ, 125, 2531

Reipurth, B., & Schneider, N. 2008, Star Formation and Young Clusters in Cygnus, ed. B. Reipurth, 36

Repolust, T., Puls, J., & Herrero, A. 2004, A&A, 415, 349

Rieke, G. H., & Lebofsky, M. J. 1985, ApJ, 288, 618

Robertson, B. E., Ellis, R. S., Dunlop, J. S., McLure, R. J., & Stark, D. P. 2010, Nature, 468, 49

Roman-Lopes, A., & Roman-Lopes, G. F. 2019, MNRAS, 484, 5578

Rygl, K. L. J., Brunthaler, A., Sanna, A., et al. 2012, A&A, 539, A79

Sabín-Sanjulián, C., Simón-Díaz, S., Herrero, A., et al. 2017, A&A, 601, A79

Salas, J., Maíz Apellániz, J., & Barbá, R. H. 2015, in Highlights of Spanish Astrophysics VIII, ed. A. J. Cenarro, F. Figueras, C. Hernández-Monteagudo, J. Trujillo Bueno, & L. Valdivielso, 615–615

Sale, S. E., Drew, J. E., Barentsen, G., et al. 2014, MNRAS, 443, 2907

Salpeter, E. E. 1955, ApJ, 121, 161

Samal, M. R., Zavagno, A., Deharveng, L., et al. 2014, A&A, 566, A122

Sana, H. 2017, in IAU Symposium, Vol. 329, The Lives and Death-Throes of Massive Stars, ed. J. J. Eldridge, J. C. Bray, L. A. S. McClelland, & L. Xiao, 110–117

Sana, H., & Evans, C. J. 2011, in IAU Symposium, Vol. 272, Active OB Stars: Structure, Evolution, Mass Loss, and Critical Limits, ed. C. Neiner, G. Wade, G. Meynet, & G. Peters, 474–485

Sana, H., de Mink, S. E., de Koter, A., et al. 2012, Science, 337, 444

Sana, H., de Koter, A., de Mink, S. E., et al. 2013, A&A, 550, A107

Sana, H., Le Bouquin, J. B., Lacour, S., et al. 2014, ApJS, 215, 15

Santolaya-Rey, A. E., Puls, J., & Herrero, A. 1997, A&A, 323, 488

Schneider, N., Bontemps, S., Simon, R., et al. 2006, A&A, 458, 855

Schulte, D. H. 1956, ApJ, 124, 530

—. 1958, ApJ, 128, 41

Shenar, T., Sablowski, D. P., Hainich, R., et al. 2019, arXiv e-prints, arXiv:1905.09296

Simón-Díaz, S. 2010, A&A, 510, A22

Simón-Díaz, S., Castro, N., Herrero, A., et al. 2011, in Journal of Physics Conference Series, Vol. 328, Journal of Physics Conference Series, 012021

Simón-Díaz, S., Godart, M., Castro, N., et al. 2017, A&A, 597, A22

Simón-Díaz, S., & Herrero, A. 2007, A&A, 468, 1063

—. 2014, A&A, 562, A135

Simón-Díaz, S., Herrero, A., Sabín-Sanjulián, C., et al. 2014, A&A, 570, L6

Simón-Díaz, S., Negueruela, I., Maíz Apellániz, J., et al. 2015, in Highlights of Spanish Astrophysics VIII, ed. A. J. Cenarro, F. Figueras, C. Hernández-Monteagudo, J. Trujillo Bueno, & L. Valdivielso, 576–581

Skrutskie, M. F., Cutri, R. M., Stiening, R., et al. 2006, AJ, 131, 1163

Smith, M. D. 2014, MNRAS, 438, 1051

Smith, N. 2006, MNRAS, 367, 763

Sota, A., Maíz Apellániz, J., Morrell, N. I., et al. 2014, ApJS, 211, 10

Sota, A., Maíz Apellániz, J., Walborn, N. R., et al. 2011, ApJS, 193, 24

Stroud, V. E., Clark, J. S., Negueruela, I., et al. 2010, A&A, 511, A84

Tokunaga, A. T. 2000, Infrared Astronomy, ed. A. N. Cox, 143

Torres-Dodgen, A. V., Tapia, M., & Carroll, M. 1991, MNRAS, 249, 1

Townsend, R. H. D. 2010, ApJS, 191, 247

Townsend, R. H. D., & Owocki, S. P. 2005, MNRAS, 357, 251

ud-Doula, A., & Owocki, S. P. 2002, ApJ, 576, 413

Ud-Doula, A., Owocki, S. P., & Townsend, R. H. D. 2009, MNRAS, 392, 1022

Uyanıker, B., Fürst, E., Reich, W., Aschenbach, B., & Wielebinski, R. 2001, A&A, 371, 675

Vazquez, R. A., Baume, G., Feinstein, A., & Prado, P. 1996, A&AS, 116, 75

Vink, J. S., Brott, I., Gräfener, G., et al. 2010, A&A, 512, L7

Vink, J. S., de Koter, A., & Lamers, H. J. G. L. M. 2001, A&A, 369, 574

Vink, J. S., Drew, J. E., Steeghs, D., et al. 2008, MNRAS, 387, 308

Walborn, N. R. 1971, ApJS, 23, 257

—. 1973, AJ, 78, 1067

Walborn, N. R. 1991, in IAU Symposium, Vol. 148, The Magellanic Clouds, ed. R. Haynes & D. Milne, 145

Walborn, N. R., Howarth, I. D., Lennon, D. J., et al. 2002, AJ, 123, 2754

Walborn, N. R., Sana, H., Simón-Díaz, S., et al. 2014, A&A, 564, A40

Wesselius, P. R., van Duinen, R. J., de Jonge, A. R. W., et al. 1982, A&AS, 49, 427

Willis, A., Prinja, R., & Fenech, D. 2011, Bulletin de la Societe Royale des Sciences de Liege, 80, 524

Woosley, S. E., Heger, A., & Weaver, T. A. 2002, Reviews of Modern Physics, 74, 1015

Wright, N. J., Bouy, H., Drew, J. E., et al. 2016, MNRAS, 460, 2593

Wright, N. J., Drake, J. J., Drew, J. E., & Vink, J. S. 2010, ApJ, 713, 871

Wright, N. J., Drew, J. E., & Mohr-Smith, M. 2015, MNRAS, 449, 741

Wright, N. J., Parker, R. J., Goodwin, S. P., & Drake, J. J. 2014, MNRAS, 438, 639

Zacharias, N., Finch, C. T., Girard, T. M., et al. 2012, VizieR Online Data Catalog, I/322A

—. 2013, AJ, 145, 44

Zacharias, N., Urban, S. E., Zacharias, M. I., et al. 2004, AJ, 127, 3043

Zacharias, N., Finch, C., Girard, T., et al. 2010, AJ, 139, 2184

Zavagno, A., Pomarès, M., Deharveng, L., et al. 2007, A&A, 472, 835

Zavagno, A., Russeil, D., Motte, F., et al. 2010, A&A, 518, L81

Zinnecker, H., & Yorke, H. W. 2007, ARA&A, 45, 481

A

The macroturbulent broadening effect

In this appendix we have evaluated the implications of considering the goodness-of-fit (GOF) solution when setting $vmac = 0$ km s^{-1} in those cases in which the $vmac$ associated with the best-fitting solution could be considered an upper limit, i.e., it is higher than zero, but zero is still an acceptable solution. We have carried out a brief study focused on the possible effects that, in such cases, setting $vmac = 0$ km s^{-1} could have on the distribution of rotational velocities and derived stellar parameters.

As stated in Sect. 6.3, in some cases the macroturbulent broadening *vmac* associated with the best-fitting solution obtained from the line-broadening characterization is higher than zero, but $vmac = 0$ km s^{-1} is still an acceptable solution (within the 1σ confidence level). In these cases, the *vmac* value could be considered an upper limit. Figure A.1 shows an example of the final output obtained from the `iacob-broad` tool for one of such case (see Sect 2.2.1 for a detailed description of the output contents). The χ^2 distributions resulting from the GOF analysis are represented in the bottom right plot. We note that $vmac = 0$ km s^{-1} is located within the 1σ confidence level and, therefore, the associated *vsini* (green text) is also an acceptable solution that, if used for the spectroscopic analysis, could lead to possible additional uncertainties that should be quantified.

In order to assess the possible effect of the macroturbulent broadening on the distribution of rotational velocities and parameter determination, we decided to perform a brief study of the implications of considering the pair (*vsini*, $vmac = 0$) provided by the goodness-of-fit technique for all cases in which the *vmac* initially obtained could be considered as an upper limit (GOF_2 solution). We will compare these results to those obtained considering the pair (*vsini*, *vmac*) associated with the best-fitting solution, i.e. the minimum χ^2 (GOF_1 solution). However, we highlight the need for a more detailed future study of the line-broadening effects on the spectroscopic analysis of OB stars.

A.1 Effect on the distribution of rotational velocities

The line-broadening characterization of our stellar sample is shown in the top left hand panel of Fig. A.2. Stars for which the analysis results in possible upper limits for *vmac* ($\sim 60\%$ of the total sample) are marked with blue crosses. We do not find any systematic trend related to the spectral type or luminosity class. We have also divided the diagram into two groups by using the 1:2 relation as reference. Stars dominated by the macroturbulent broadening are represented in green while those dominated by rotational broadening are represented in red. Most of the stars with possible upper limits for *vmac* belong to this latter group, something expected if remember that the extra broadening only affects slightly the wings of the line profiles when the rotational broadening dominates (Simón-Díaz et al. 2017).

The relative difference between the *vsini* values obtained when considering the GOF_1 solution and the values obtained from the GOF_2 solution is shown in the top right hand panel. The stars dominated by the macroturbulent broadening suffer a significant change in the *vsini* value when we set $vmac = 0$ km

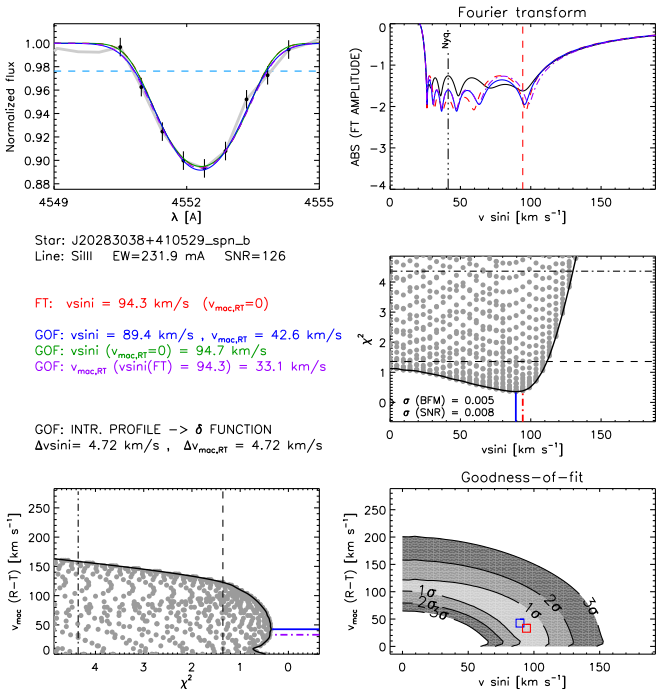

Figure A.1: Example of `iacob-broad` output for the star J20283038+410529. From left to right, top to bottom the plots show: the line profile, the FT of the line, the projections of the 2D-χ^2 distributions resulting from the GOF analysis, and the own 2D-χ^2 distributions.

s^{-1}. That is also expected since the loss of a large amount of extra broadening implies increasing the *vsini* to compensate it.

Finally, in the bottom panel we compare the distribution of rotational velocities obtained when assuming the *vsini* values from the GOF_1 solution with that from the GOF_2 solution. Both distributions are globally similar, although for GOF_2 the tail of very fast rotators extends to higher values and the peak of rotators at $vsini = 100$ km s^{-1} has increased because some stars have been

shifted from lower to higher velocities (the $40 - 80$ km s^{-1} bin). The same effect is seen at $\sim$200 km s^{-1}, where some stars are shifted from the bins between 120 and 200 km s^{-1}, decreasing the peak centred at 180 km s^{-1}. Thus, in our case the distribution of rotational velocities is not strongly affected and is globally similar in both cases. However, in cases where a large part of the stellar sample is dominated by the macroturbulent broadening and the resolving power of the

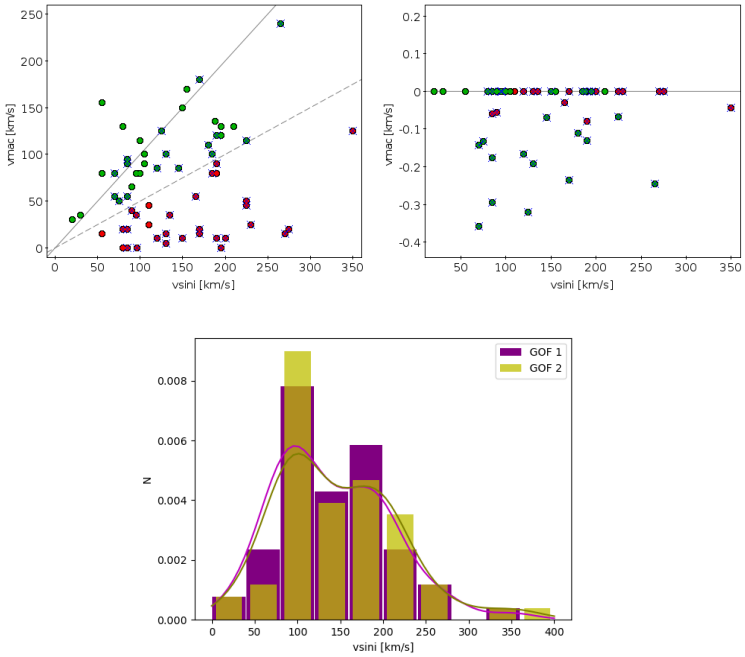

Figure A.2: *Top, left hand panel*: Line-broadening characterization of our sample of 66 O-type stars where those stars for which the derived *vmac* could be considered an upper limit are marked with blue crosses. Stars dominated by the macroturbulent broadening are represented in green while those dominated by rotational broadening are represented in red. *Top, right hand panel*: Relative difference between the *vsini* values obtained considering the GOF_1 and GOF_2 solutions. *Bottom panel*: Comparison of the distribution of rotational velocities assuming the *vsini* values obtained from the GOF_1 solution (in purple) and from the GOF_2 solution (in brown). Solid lines indicate Kernel density estimates from Gaussian kernels.

spectral data is higher, the distribution could be critically affected, extending to larger rotational velocities.

A.2 Effect on the derived stellar parameters

We have re-derived the stellar parameters for our stellar sample but assuming the GOF_2 solution for those stars for which *vmac* could be an upper limit. Compared to the case in which the GOF_1 solution is adopted we find insignificant differences for the wind Q parameter and He abundance (mean values of -0.002 ± 0.06 and -0.003 ± 0.006 dex for -log Q and Y(He), respectively). However, we find more relevant systematic differences for temperature and gravity. Figure A.3 shows the difference between the derived temperatures and surface gravities when considering the GOF_1 and GOF_2 solutions for those stars for which *vmac* could be an upper limit (blue crosses). In the previous section it was shown that the *vsini* values provided by the GOF_2 solution are larger to compensate for the loss of the extra-broadening represented by *vmac*. Thus, we would expect that this compensation makes the derived stellar parameters invariable. However, in Fig. A.3 we find a clear systematic effect on both the temperature and gravity: both parameters increase when assuming the GOF_2 solution, although the offset is within the uncertainties. We find a mean offset of -0.18 ± 0.22 kK for T_{eff} and -0.04 ± 0.04 dex for log g. The larger value of log g (GOF_2) is probably due to the fact that the increase in *vsini* does not completely compensate the loss of *vmac*. The increase in T_{eff} is then an effect of the increased gravity.

In order to evaluate if these offsets on the individual stellar parameters influence the scales obtained from the GOF_1 solution (see Sect. 6.4.1), we have recalculated them but adopting the GOF_2 solution for the stars with possible *vmac* upper limits. Table A.1 shows the fit obtained in both cases (divided by I-II, III and IV-V luminosity classes). We see that the individual differences on the stellar parameters are not affecting the different scales, resulting on a negligible impact for the whole stellar sample.

Finally, we have also evaluated the possible effects on the HR and sHR diagrams (see Fig. A.4). We have chosen non-rotating Geneva isochrones and evolutionary tracks from Ekström et al. (2012). We placed on the diagrams our stellar sample of O-type stars in Cygnus OB2 that have passed the criterion for good astrometry but, for clarity, we represented in orange the stars with upper limits for *vmac*. In the left hand panels we show the case in which we assume the GOF_1 solution for the parameter determination while in the right hand panels the GOF_2 solution has been adopted. On the HRD (top panels) we find

Table A.1: Linear fits of the temperature and gravity scales obtained from the GOF_1 and GOF_2 solutions. We present the data separated by luminosity class, as in Fig 6.7. SPT indicates the spectral type.

	GOF_1		GOF_2	
Lumin. Class	T_{eff}	log g	T_{eff}	log g
I-II	-2.12*SpT+49.56	-0.12*SpT+4.30	-2.11*SpT+49.56	-0.12*SpT+4.33
III	-1.95*SpT+49.80	-0.05*SpT+3.96	-1.96*SpT+49.93	-0.04*SpT+3.91
IV-V	-1.67*SpT+48.74	0.04*SpT+3.48	-1.68*SpT+48.95	0.04*SpT+3.51

minor differences between both cases. When assuming the GOF_2 solution the derived luminosity values increase, but very slightly. As mentioned before, the increase of the temperature is also small, so the global picture of the diagram is the same in both cases. Hence, we do not expect significant differences between individual ages and evolutionary masses derived from the HRD.

On the sHRD (bottom panels) we find larger (although not critical) differences. In this case, and as we show before, when assuming the GOF_2 solution for the parameter determination we obtain larger values for both temperature and gravity, and the spectroscopic luminosity decreases for most of the stars. In spite of this, the inferred evolutionary status of the sample from the sHRD is similar when assuming either the GOF_1 or GOF_2 solution on the line-broadening characterization.

We conclude that, globally, no additional uncertainty is introduced in our results by the possible overestimation of *vmac* in the cases analyzed here. However, some individual *vsini* values suffer a significant variation that can affect the spectral characterization of individual stars. A more comprehensive study of these effects, including a possible underestimation of *vmac*, is proposed for the near future.

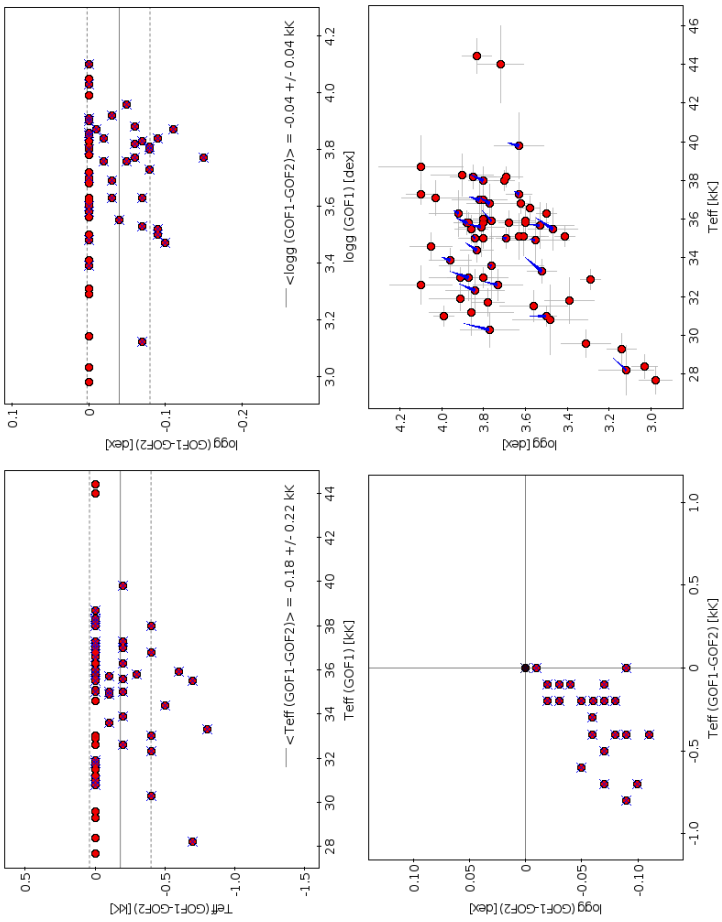

Figure A.3: Comparison of temperatures and surface gravities derived at considering the GOF_1 and GOF_2 solution for the parameter determination. Crosses indicate those stars for which we obtain an upper limit for *vmac*. On the top panels, solid and dotted horizontal grey lines indicate mean differences and standard deviations, respectively. On the bottom right panel, solid blue arrows indicate the change in T_{eff} and log g from GOF_1 and GOF_2.

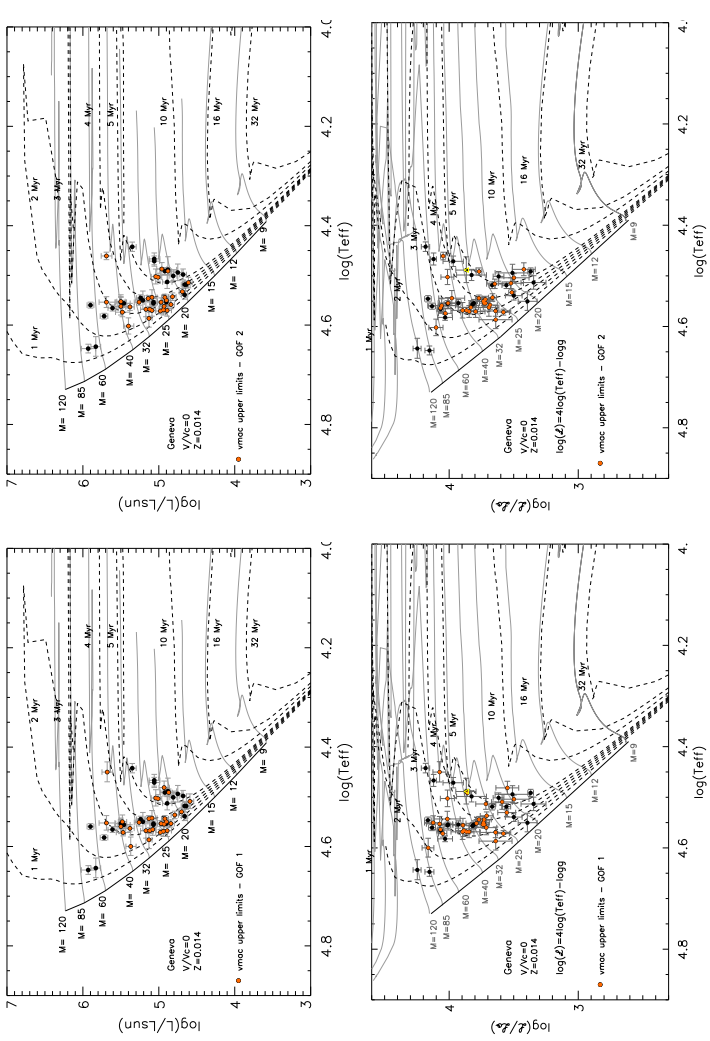

Figure A.4: HR diagrams (*top*) and sHR diagrams (*bottom*) for our sample of O stars in Cygnus OB2 that have passed the criterion for reliable astrometry. Non-rotating evolutionary tracks and isochrones are from Ekström et al. (2012). Orange dots represents the stars for which the derived *vmac* value provided by the `iacob-broad` tool can be considered an upper limit. On the left panel we show the case of assuming the GOF_1 solution for the parameter determination. On the right we show the same but when assuming the GOF_2 solution.

B

Impact of the extinction law on A_V and M_V

In this appendix we study the impact of the adopted photometry and extinction law on the derived individual visual extinctions, absolute visual magnitudes and fundamental stellar parameters. We also include their impact on the HR diagram and the evolutionary status of the whole stellar sample.

The extinction law is a key ingredient for the estimation of individual extinctions (A_λ), absolute magnitudes (M_λ) and, therefore, the derived stellar luminosities and the interpretation of the HRD. In order to evaluate whether this additional source of uncertainty could modify our conclusions, we have adopted two different extinction laws for our analysis.

We first used the interstellar law derived by Rieke & Lebofsky (1985) (RL85, $R_V = 3.09 \pm 0.03$) from measurements beyond 1 mμ toward o Sco and the Galactic center. We note that this law was used in Chapter 6 for the spectroscopic analysis. For comparison, we have also used the law derived by Wright et al. (2015) (W15, $R_V = 2.91 \pm 0.06$) from a more recent study focused in Cygnus OB2. A summary of both extinction laws is presented in Table B.1. As stated in Sect. 6.5, we estimated individual visual extinctions (A_V) for all our stellar sample by using the colour $(B - K_s)$ from the USNO-B and 2MASS catalogs, the unreddened intrinsic colours for O-type stars from Martins & Plez (2006) (the 'observational' T_{eff} scale) and both selected extinction laws (RL85 and W15). We note that for the five stars for which only B- and J-band photometry is available we used $(B - J)$ colours.

To derive M_V we followed the same methodology as in Sect. 6.5. Thus, we used the Eq. 6.3, where A_{K_s} was calculated from both extinction laws. The comparison of the visual extinctions and absolute magnitudes derived from both selected laws when using $(B - K_s)$ colors (and $(B - J)$ colours when no other photometry is available) is shown in Figure B.1. There is good agreement between the two laws although we find slightly higher A_V (and brighter M_V) values when we use the RL85 law than when the W15 law is used. The difference is within the usual uncertainties and does not produce significant effects on the

Table B.1: Summary of the RL85 and W15 extinction laws.

	A_V/A_λ	
	RL85	W15
Band (λ)	($R_V = 3.09$)	($R_V = 2.91$)
B (0.44 μm)	1.324	1.318
V (0.55 μm)	1.000	1.000
J (1.27 μm)	0.282	0.234
H (1.67 μm)	0.175	0.139
K_s (2.16 μm)	0.112	0.0845

Note: RL85 centered the K_s band at 2.22 μm.

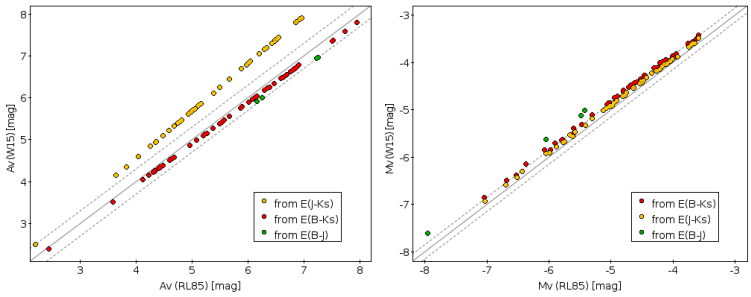

Figure B.1: Comparison between the derived visual extinctions (*left*) and absolute magnitudes (*right*) obtained from the Rieke & Lebofsky (1985) and Wright et al. (2015) extinction laws. Red, green and yellow dots indicate that $(B-K_s)$, $(B-J)$ and $(J-K_s)$ colors that have been used for the analysis, respectively. Solid lines indicate the 1:1 relation.

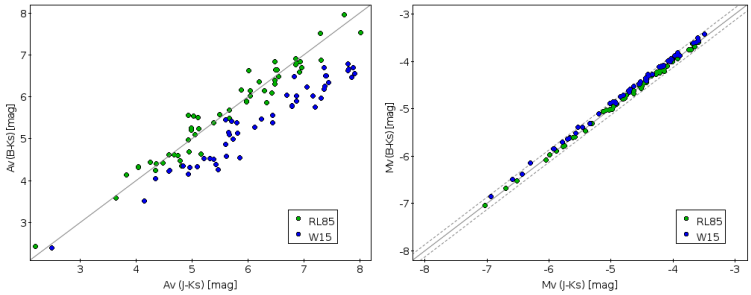

Figure B.2: Comparison between the derived visual extinctions (*left*) and absolute magnitudes (*right*) obtained from $(B-K_s)$ and $(J-K_s)$ colors. Green and blue dots indicate the Rieke & Lebofsky (1985) and Wright et al. (2015) extinction law used for the analysis, respectively. Solid lines indicate the 1:1 relation.

luminosity nor the HR diagram.

The picture changes when the infrared $(J-K_s)$ colour is used for the same analysis (yellow dots in Fig. B.1). Now we can see a different scenario: significantly lower A_V values are derived when the RL85 law is used. We find a mean difference of 0.73 ± 0.24 mag between the two extinction laws. However, the impact in the derived M_V values is negligible since they are derived from Eq. 6.3, where A_{K_s} is used instead of A_V. This supports our choice of Eq. 6.3 in Sect. 6.5, but also indicates that something is not consistent.

Table B.2: Visual extinctions derived from $(B - K_s)$ and $(J - K_s)$ colours when using RL85 and W15 extinction laws.

Extinction law	$[(A_B/\ A_{Ks})$-1]	$A_{V,(B-Ks)}$	$[(A_J/\ A_{Ks})$-1]	$A_{V,(J-Ks)}$
RL85	10.82	$0.825 * E(B - K_s)$	1.52	$5.875 * E(J - K_s)$
W15	14.60	$0.810 * E(B - K_s)$	1.77	$6.687 * E(J - K_s)$

As the colour excess does not depend on the adopted extinction law, we calculated A_V in terms of both $E(B - K_s)$ and $E(J - K_s)$ (see Table B.2). A comparison of the visual extinctions obtained when both colours are used to derive this quantity is shown in Fig. B.2. Green and blue dots indicate the assumed RL85 and W15 extinction laws, respectively. It is obvious that optical extinctions derived from $(B - K_s)$ and from $(J - K_s)$ are consistent when using RL85, but not when using W15. There is a difference of less than 2% in $(B - K_s)$ (towards higher extinction with RL85) but more than 12% in $(J - K_s)$ (towards higher extinction with W15). Thus, the RL85 extinction law is more consistent than the W15 one, at least in terms of the colours used for estimating A_V.

Although both laws would have given the same results in our case due to the chosen method, we highlight the importance of the adopted photometry and extinction law for characterizing the stellar visual extinction, since they can be additional sources of uncertainty. Moreover, depending on the method used to derived M_V (e.g., directly using Eq. 6.1) they can cause a significant change in luminosity and, therefore, in the inferred evolutionary status of a given population. The consistency found for the RL85 extinction law (in terms of the adopted photometry) justifies its choice for the final analysis of our stellar sample in Chapter 6.

C

Tables

In this appendix we include all the tabulated data of the whole O-type population up to $B = 16$ mag. in Cygnus OB2 and the results obtained from the spectroscopic analysis.

Table C.1: Basic photometric data of the currently known O-type population of Cygnus OB2. Columns give their names, coordinates (J2000.0 epoch), V, B, J and K_s magnitudes. B magnitudes are from the USNO-B and Tycho-2 catalogs (the latter indicated with an asterisk). K_s and J magnitudes are from the 2MASS catalog. V magnitudes gathered from the literature (see table footnote).

ID	Name	2MASS Name	RA(hhmmss)	Dec(° ′ ″)	V [mag]	B [mag]	J [mag]	K_s [mag]
1	-	J20272428+4115458	20 27 24.28	+41 15 45.82	11.76[5]	12.62	9.36	8.83
2	BD+404179	J20274361+4035435	20 27 43.62	+40 35 43.53	9.71[2]	10.11	8.42	8.26
3	-	J20275293+4144067	20 27 52.92	+41 44 06.65	-	13.33	8.14	7.28
4	-	J20283038+4105290	20 28 30.38	+41 05 29.04	12.16[5]	13.36	7.09	6.12
5	HD195213	J20283203+4049027	20 28 32.03	+40 49 02.88	8.83[6]	9.50	6.67	6.26
6	-	J20291617+4057371	20 29 16.17	+40 57 37.19	-	15.03	8.85	7.89
7	-	J20293480+4120089	20 29 34.79	+41 20 08.93	-	15.43	9.45	8.48
8	-	J20293563+4024315	20 29 35.63	+40 24 31.45	11.64[5]	12.47	8.83	8.27
9	A42	J20295701+4109538	20 29 57.01	+41 09 53.84	12.21[5]	13.01	9.12	8.45
10	A18	J20300788+4123504	20 30 07.88	+41 23 50.50	-	15.64	9.39	8.36
11	-	J20301838+4053466	20 30 18.39	+40 53 46.56	-	15.15	8.92	7.96
12	Cyg#B17	J20302730+4113253	20 30 27.30	+41 13 25.31	-	14.74	7.63	6.44
13	ALS15129	J20303981+4136507	20 30 39.82	+41 36 50.72	12.93[2]	14.57	9.10	8.31
14	A26	J20305772+4109575	20 30 57.73	+41 09 57.60	-	14.61	9.09	8.19
15	A46	J20310019+4049497	20 31 00.20	+40 49 49.70	11.22[5]	12.07	8.38	7.83
16	A41	J20310838+4202422	20 31 08.30	+42 02 42.00	12.29[5]	13.10	7.82	7.02
17	Cyg#1	J20311055+4131535	20 31 10.55	+41 31 53.54	11.18[4]	12.48	7.96	7.36
18	ALS15133	J20311833+4121216	20 31 18.33	+41 21 21.66	12.99[2]	14.13	8.61	7.75
19	A15	J20313690+4059092	20 31 36.91	+40 59 09.06	-	15.38	7.91	6.81
20	Cyg#3A	J20313749+4113210	20 31 37.50	+41 13 21.05	10.35[4]	11.63	6.49	5.75
21	ALS15116	J20314540+4118267	20 31 45.40	+41 18 26.75	12.26[2]	13.62	8.06	7.26

Table C.1: continued.

ID	Name	2MASS Name	RA(hhmmss)	Dec(° ′ ″)	V [mag]	B [mag]	J [mag]	K_s [mag]
22	[MT91]145	J20314965+4128265	20 31 49.65	+41 28 26.52	11.52[1]	12.57	9.07	8.63
23	-	J20315961+4114504	20 31 59.61	+41 14 50.45	-	14.46	9.12	8.33
24	Cyg#4A	J20321383+4127120	20 32 13.82	+41 27 12.01	10.23[1]	11.23	7.58	7.10
25	Cyg#14	J20321656+4125357	20 32 16.56	+41 25 35.71	11.47[1]	12.25	8.71	8.18
26	Cyg#5A	J20322242+4118190	20 32 22.42	+41 18 19.00	-	10.80*	5.30	-
27	Cyg#5B	J20322248+4118190	20 32 22.49	+41 18 19.00	-	13.40*	7.80	-
28	Cyg#15	J20322766+4126220	20 32 27.66	+41 26 22.11	11.10[1]	12.30	8.54	8.02
29	A32	J20323033+4034332	20 32 30.33	+40 34 33.30	-	14.0	7.89	7.07
30	ALS21079	J20323154+4114082	20 32 31.53	+41 14 08.18	-	14.72	7.82	6.66
31	A38	J20323486+4056174	20 32 34.87	+40 56 17.40	-	14.93	9.38	8.56
32	A25	J20323843+4040445	20 32 38.44	+40 40 44.5	-	15.33	8.35	7.38
33	Cyg#16	J20323857+4125137	20 32 38.58	+41 25 13.66	10.84[1]	11.86	8.19	7.72
34	Cyg#6	J20324545+4125374	20 32 45.44	+41 25 37.51	10.68[1]	11.67	7.95	7.42
35	Cyg#17	J20325002+4123446	20 32 50.02	+41 23 44.68	11.60[1]	12.43	8.58	7.98
36	ALS15111	J20325919+4124254	20 32 59.19	+41 24 25.47	11.91[1]	12.82	8.88	8.31
37	ALS15144	J20325964+4115146	20 32 59.64	+41 15 14.67	13.49[1]	14.94	9.05	8.14
38	A20	J20330292+4047254	20 33 02.92	+40 47 25.40	-	14.40	7.25	6.27
39	ALS15131	J20330292+4117431	20 33 02.92	+41 17 43.13	12.95[1]	14.50	8.72	7.87
40	Cyg#22A	J20330879+4113182	20 33 08.77	+41 13 18.74	-	14.20*	7.60	-
41	Cyg#22B	J20330883+4113174	20 33 08.84	+41 13 17.48	-	14.80*	8.20	-
42	Cyg#22E	J20330944+4112583	20 33 09.44	+41 12 58.30	-	16.80*	10.60	-
43	Cyg#22C	J20330960+4113005	20 33 09.60	+41 13 00.60	12.84[2]	15.00	8.65	7.76
44	Cyg#22D	J20331011+4113101	20 33 10.11	+41 13 10.10	13.62[3]	15.60	9.44	8.62
45	Cyg#9	J20331074+4115081	20 33 10.73	+41 15 08.22	10.96[1]	12.77	6.47	5.57

Table C.1: continued.

ID	Name	2MASS Name	RA(hhmmss)	Dec(° ′ ″)	V [mag]	B [mag]	J [mag]	K_s [mag]
46	ALS15148	J20331326+4113287	20 33 13.26	+41 13 28.67	13.61[1]	15.02	8.98	8.01
47	ALS15128	J20331369+4113057	20 33 13.69	+41 13 05.78	12.92[1]	14.06	9.03	8.28
48	Cyg#7	J20331411+4120218	20 33 14.11	+41 20 21.91	10.55[1]	11.86	7.25	6.61
49	Cyg#8B	J20331476+4118416	20 33 14.76	+41 18 41.63	10.33[1]	11.77	7.21	6.57
50	Cyg#8A	J20331508+4118504	20 33 15.08	+41 18 50.48	9.06[1]	10.36	6.12	5.50
51	Cyg#23	J20331571+4120172	20 33 15.71	+41 20 17.20	12.50[1]	12.92	9.33	8.72
52	Cyg#8D	J20331634+4119017	20 33 16.26	+41 19 00.16	12.02[1]	12.58	8.84	8.24
53	Cyg#24	J20331748+4117093	20 33 17.48	+41 17 09.35	11.88[1]	13.09	8.35	7.65
54	Cyg#8C	J20331798+4118311	20 33 17.98	+41 18 31.19	10.19[1]	11.06	7.16	6.58
55	ALS15115	J20331803+4121366	20 33 18.03	+41 21 36.65	12.06[1]	12.69	8.74	8.11
56	ALS15123	J20332101+4117401	20 33 21.02	+41 17 40.14	12.70[1]	13.63	9.30	8.67
57	[MT91]516	J20332346+4109130	20 33 23.47	+41 09 12.90	11.84[1]	13.50	7.02	6.05
58	Cyg#25A	J20332556+4133269	20 33 25.56	+41 33 27.00	11.58[1]	13.15	8.17	7.52
59	ALS15134	J20332674+4110595	20 33 26.75	+41 10 59.51	13.00[1]	14.24	8.97	8.16
60	ALS15121	J20333030+4135578	20 33 30.31	+41 35 57.90	12.51[1]	13.79	8.38	7.57
61	ALS15119	J20333700+4116113	20 33 37.00	+41 16 11.30	12.40[1]	13.53	8.68	7.93
62	ALS15124	J20334086+4130189	20 33 40.87	+41 30 18.98	12.77[2]	13.68	9.26	8.61
63	Cyg#10	J20334610+4133010	20 33 46.11	+41 33 01.05	9.88[1]	11.19	6.29	5.58
64	-	J20335842+4019411	20 33 58.42	+40 19 41.13	-	15.48	7.96	6.93
65	Cyg#27	J20335952+4117354	20 33 59.53	+41 17 35.48	12.32[1]	13.18	8.53	7.89
66	ALS15145	J20340486+4105129	20 34 04.86	+41 05 12.90	13.50[1]	14.53	9.56	8.84
67	ALS15146	J20340601+4108090	20 34 06.02	+41 08 09.00	13.59[1]	14.84	9.05	8.15
68	Cyg#11	J20340850+4136592	20 34 08.51	+41 36 59.39	10.03[1]	11.22	6.65	5.99
69	ALS15125	J20340951+4134136	20 34 09.52	+41 34 13.69	12.79[1]	14.25	9.30	8.65

Table C.1: continued.

ID	Name	2MASS Name	RA(hhmmss)	Dec(° ′ ″)	V [mag]	B [mag]	J [mag]	K_s [mag]
70	Cyg#29	J20341350+4135027	20 34 13.51	+41 35 02.86	11.91[1]	13.56	8.55	7.92
71	A28	J20341604+4102196	20 34 16.05	+41 02 19.59	13.89[7]	15.10	9.41	8.52
72	S73	J20342193+4117016	20 34 21.93	+41 17 01.60	12.40[1]	13.66	8.39	7.60
73	ALS15114	J20342959+4131455	20 34 29.60	+41 31 45.49	12.06[1]	13.37	7.56	6.71
74	A24	J20344410+4051584	20 34 44.15	+40 51 58.67	-	14.74	8.40	7.45
75	ALS19627	J20345606+4038180	20 34 56.06	+40 38 17.92	-	13.54	7.44	6.54
76	Cyg#B18	J20345785+4143543	20 34 57.85	+41 43 54.25	-	15.43	8.45	7.42
77	A37	J20360451+4056129	20 36 04.50	+40 56 13.01	-	13.95	8.57	7.68

Refs: (1) Massey & Thompson (1991), (2)Reed (2003), (3)Wright et al. (2015), (4)Laur et al. (2017), (5) Tycho-2 catalog.
(6) Wesselius et al. (1982), (7) Zacharias et al. (2012)

Table C.2: List of the whole O-type population used in this work along with previous (see table footnote for references) and new spectral classification as well as the spectral data used to characterize the broadening (case A) and determine the spectroscopic parameters (case B). See Sect. 6.2.2 for further details.

ID	Name	2MASS Name	SpT(prev)	SpT(new)	Comments	Data (A)	Data (B)
1	-	J20272428+4115458	O9.5V[5]	B0IV	Group3	5a	5a & 5b
2	BD+404179	J20274361+4035435	O8Vz[4]	O8Vz	-	3	3 & 6b
3	-	J20275293+4144067	O9.5II[2]	O9.5II	-	6a	6a & 6b
4	-	J20283038+4105290	OC9.7Ia[5]	OC9.7Iab	-	6a	6a & 6b
5	HD195213	J20283203+4049027	O7[11]	O7Ib(f)	-	3	3 & 6b
6	-	J20291617+4057371	O9.7III[2]	O8.5III	-	6a	6a & 6b
7	-	J20293480+4120089	O9.5V[5]	O9.5IV	-	6a	6a & 6b
8	-	J20293563+4024315	O8IIIz[2]	O8IIIz	-	5a	5a & 5b
9	A42	J20295701+4109538	O9.7III[3]	O9.7III	-	5a	5a & 5b
10	A18	J20300788+4123504	O8V[11]	O9.7III(n)	-	6a	6a & 6b
11	-	J20301838+4053466	O9V[5]	SB2	SB2	-	-
12	Cyg#B17	J20302730+4113253	O6Iaf+O9:Ia:[4]	-	SB2	-	-
13	ALS15129	J20303981+4136507	O6V[7]	O6.5V((f))z	-	6a	6a & 6b
14	A26	J20305772+4109575	O9.5V [9]	O9.5IV	-	6a	6a & 6b
15	A46	J20310019+4049497	O7V((f))[8]	O7V((f))	-	6a	6a & 6b
16	A41	J20310838+4202422	O9.7II[8]	O9.7II(n)	-	6a	6a & 6b
17	Cyg#1	J20311055+4131535	O8IV((f))(n)[1]	O8IV((f))(n)	SB1	2	2 & 6b
18	ALS15133	J20311833+4121216	O9IV [1]	O8.5III	SB1	6a	6a & 6b
19	A15	J20313690+4059092	O7Ibf[9]	O7Ibf	-	6a	6a & 6b
20	Cyg#3A	J20313749+4113210	O8.5Iab(f)+O6III:[1]	O8.5Iab(f)	SB2	-	-
21	ALS15116	J20314540+4118267	O8I[7]	O8III	-	6a	6a & 6b
22	[MT91]145	J20314965+4128265	O9.7IV[3]	O9.7IV	SB1	5a	5a & 5b

Table C.2: continued.

ID	Name	2MASS Name	SpT(prev)	SpT(new)	Comments	Data (A)	Data (B)
23	-	J20315961+4114504	O7V[5]	O7.5Vz	-	6a	6a & 6b
24	Cyg#4A	J20321383+4127120	O7IIIf[7]	O7IIIf	-	4b	5a & 5b
25	Cyg#14	J20321656+4125357	O9V[7]	O9.5IV	-	2	2 & 6b
26	Cyg#5A	J20322242+4118190	O6.5:Iafe+O7Iafe[1]	O7Iafpe+O	SB2	-	-
27	Cyg#5B	J20322248+4118190	O6.5Iabfp[4]	O6.5Iabfp	-	-	-
28	Cyg#15	J20322766+4126220	O8III[1]	O8III	SB1	2	2 & 6b
29	A32	J20323033+4034332	O9.5IV[8]	SB2	SB2	-	-
30	ALS21079	J20323154+4114082	O7Ib(f)[4]	O7.5Ib(f)	SB1	1	1 & 6b
31	A38	J20323486+4056174	O8V[9]	O8Vz(n)	-	6a	6a & 6b
32	A25	J20323843+4040445	O8III[9]	O8III((f))	-	6a	6a & 6b
33	Cyg#16	J20323857+4125137	O7.5IV(n)[4]	O7.5:IV(n)	-	5b	5a & 5b
34	Cyg#6	J20324545+4125374	O8.5V(n)[4]	O8V(n)	-	4b	2 & 6b
35	Cyg#17	J20325002+4123446	O8V[7]	O8:V:	SB1	2	2 & 6b
36	ALS15111	J20325919+4124254	O8V[7]	O8V	-	2	2 & 6b
37	ALS15144	J20325964+4115146	O9.7III(n)[4]	O9.7IV:(n)	SB1	1	1 & 6b
38	A20	J20330292+4047254	O8II(f)[5]	O6.5III((f))	-	6a	6a & 6b
39	ALS15131	J20330292+4117431	O7.5V((f))[1]	O8:V(n)	SB1	6a	6a & 6b
40	Cyg#22A	J20330776+4113186	O3If*[6]	O3If*	-	4a	1 & 4cd
41	Cyg#22B	J20330883+4113174	O6V((f))[6]	O6IV((f))	SB1	4b	1 & 4cd
42	Cyg#22E	J20330944+4112583	O9.7:V:[12]	O9.7V:	-	-	-
43	Cyg#22C	J20330960+4113005	O9.5IIIn[6]	O9.5IV:n	SB1	2	2 & 6b
44	Cyg#22D	J20331011+4113101	O9.5Vn[4]	O9.5Vn	-	2	-
45	Cyg#9	J20331074+4115081	O4If+O5.5III(f)[1]	-	SB2	-	-
46	ALS15148	J20331326+4113287	O6.5:V[1]	O6.5V((f))	SB1	2	2 & 6b

Table C.2: continued.

ID	Name	2MASS Name	SpT(prev)	SpT(new)	Comments	Data (A)	Data (B)
47	ALS15128	J20331369+4113057	O8V[5]	O7Vz((f))	-	2	2 & 6b
48	Cyg#7	J20331411+4120218	O3If*[7]	O3If*	-	4b	4a,b,c,d
49	Cyg#8B	J20331476+4118416	O6II(f)[6]	O6II(f)	-	1	1 & 6b
50	Cyg#8A	J20331508+4118504	O6Ib(fc)+O4.5III(fc)[1]	-	SB2	-	-
51	Cyg#23	J20331571+4120172	O9.5V[7]	O9.5V	-	5a	5a & 5b
52	Cyg#8D	J20331634+4119017	O8.5V(n)[13]	O8.5V(n)	SB1	4b	1 & 6b
53	Cyg#24	J20331748+4117093	O8V(n)[6]	O8V(n)	-	1	1 & 6b
54	Cyg#8C	J20331798+4118311	O4.5(fc)pvar[13]	O5I(fc)	-	4b	5a & 5b
55	ALS15115	J20331803+4121366	O8V[4]	O8V	SB1	2	2 & 6b
56	ALS15123	J20332101+4117401	O9Vn[5]	O9.5V(n)	-	1	1 & 6b
57	[MT91]516	J20332346+4109130	O6IVf[4]	O6IVf	-	5a	5a & 5b
58	Cyg#25A	J20332556+4133269	O8.5Vz[4]	O8.5V	-	1	1 & 6b
59	ALS15134	J20332674+4110595	O8.5Vz[4]	O8.5V	-	1	1 & 6b
60	ALS15121	J20333030+4135578	O8V[10]	O8V((f))	SB1	6a	6a & 6b
61	ALS15119	J20333700+4116113	O9.5IVn[1]	O9.5IV:n	SB1	1	1 & 6b
62	ALS15124	J20334086+4130189	O7V[7]	O7V((f))	-	6a	6a & 6b
63	Cyg#10	J20334610+4133010	O9.7Iab[3]	O9.7Iab	-	5a	5a & 5b
64	-	J20335842+4019411	O9:[5]	O9.5Vn	-	6a	6a & 6b
65	Cyg#27	J20335952+4117354	O9.7V(n)+O9.7:V[4]	-	SB2	-	-
66	ALS15145	J20340486+4105129	O9V [7]	O9V	-	5a	5a & 5b
67	ALS15146	J20340601+4108090	O9.5V + B1-2V[12]	-	SB2	-	-
68	Cyg#11	J20340850+4136592	O5.5If[6]	O5.5Ifc	SB1	5a	5a & 5b
69	ALS15125	J20340951+4134136	O9.5IV:[4]	O9.5IV	-	2	2 & 6b
70	Cyg#29	J20341350+4135027	O7.5V((f))(n)z[4]	O7.5V((f))(n)z	SB1	2	2 & 6b

Table C.2: continued.

ID	Name	2MASS Name	SpT(prev)	SpT(new)	Comments	Data (A)	Data (B)
71	A28	J20341604+4102196	O9.5V(n)[5]	O9.5V(n)	-	6a	6a & 6b
72	S73	J20342193+4117016	O8Vz + O8Vz[4]	-	SB2	-	-
73	ALS15114	J20342959+4131455	O7V((f))+O7IV((f))[1]	O7.5IV((f))(n)	SB2	-	-
74	A24	J20344410+4051584	O6.5III(f)[9]	O6.5III(f)	-	1	1 & 6b
75	ALS19627	J20345606+4038180	O9.7Iab[8]	O9.7Iab	-	6a	6a & 6b
76	Cyg#B18	J20345785+4143543	O7:Ib[2]	O7.5IV:(f)	*a*	6a	6a & 6b
77	A37	J20360451+4056129	O5V((f))[8]	O5V((f))	-	6a	6a & 6b

SpT sources from previous works: (1) Maíz Apellániz et al. (2019), (2) Berlanas et al. (2018a), (3) Berlanas et al. (2018b), (4) Maíz Apellániz et al. (2016), (5) Comerón & Pasquali (2012), (6)Sota et al. (2011), (7) Kiminki et al. (2007), (8) Hanson (2003). (9) Negueruela et al. (2008), (10)Massey & Thompson (1991), (11) Morgan et al. (1954), (12) Maíz-Apellániz, private comment. (13) Sota et al. (2014). Other notes: (a) Recently classified as O8III by Roman-Lopes & Roman-Lopes (2019)

Table C.3: Spectroscopic stellar parameters, rotational velocities and macroturbulent broadening (from the GOF_1 solution) of the final O-type sample obtained using the `iacob-gbat` and `iacob-broad` tools (see Sects. 2.2.2 and 2.2.1 for methodology details). Uncertainties for *vsini* and *vmac* are in the order of 10 – 20% (see Sect.6.3.2).

ID	SpT	$T_{\rm eff}$ [kK]	log g [dex]	-log Q [dex]	Y(He) [10^{-2}dex]	*vsini* [km s^{-1}]	*vmac* [km s^{-1}]
1	B0IV	31.0 ± 0.5	3.99 ± 0.05	> 13.5	10.1 ± 2.5	20.	30.
2	O8Vz	35.8 ± 0.6	3.88 ± 0.06	> 13.0	10.0 ± 2.5	125.	125.
3	O9.5II	29.3 ± 0.8	3.14 ± 0.07	12.8 ± 0.2	11.3 ± 2.8	190.	80.
4	OC9.7Iab	28.2 ± 1.3	3.12 ± 0.13	12.5 ± 0.1	< 8.3	90.	40.
5	O7Ib(f)	35.5 ± 1.1	3.47 ± 0.12	12.5 ± 0.2	14.3 ± 4.3	180.	110.
6	O8.5III	35.5 ± 1.5	< 4.20	13.4 ± 0.5	< 6.9	110.	25.
7	O9.5IV	32.6 ± 1.0	4.10 ± 0.15	13.5 ± 0.5	9.9 ± 3.3	105.	90.
8	O8IIIz	35.1 ± 1.0	3.61 ± 0.10	> 13.1	10.4 ± 2.5	55.	155.
9	O9.7III	31.5 ± 0.8	3.56 ± 0.16	> 13.3	11.4 ± 2.7	85.	90.
10	O9.7III(n)	30.8 ± 1.8	3.48 ± 0.18	> 13.0	< 15.5	185.	100.
13	O6.5V((f))z	38.0 ± 0.7	3.80 ± 0.07	13.3 ± 0.5	11.0 ± 2.5	70.	80.
14	O9.5IV	33.0 ± 1.2	3.87 ± 0.19	> 13.3	10.0 ± 2.5	85.	95.
15	O7V((f))	36.8 ± 1.0	3.77 ± 0.11	13.6 ± 0.7	< 8.0	75.	50.
16	O9.7II(n)	29.6 ± 0.7	3.31 ± 0.12	12.9 ± 0.2	< 8.7	80.	0.
17	O8IV((f))(n)	35.0 ± 0.5	3.69 ± 0.05	13.0 ± 0.2	< 6.6	185.	80.
18	O8.5III	31.8 ± 1.2	3.39 ± 0.12	13.5 ± 0.5	10.0 ± 2.5	85.	0.
19	O7Ibf	35.7 ± 1.2	3.53 ± 0.16	12.3 ± 0.2	10.6 ± 2.6	270.	15.
21	O8III	33.3 ± 0.6	3.52 ± 0.07	12.9 ± 0.2	< 6.6	85.	55.
22	O9.7IV	33.0 ± 0.5	3.91 ± 0.06	13.6 ± 0.3	9.7 ± 2.5	30.	35.
23	O7.5Vz	38.6 ± 1.6	4.10 ± 0.20	> 12.9	< 11.8	130.	5.
24	O7IIIf	35.1 ± 0.5	3.41 ± 0.05	12.9 ± 0.2	9.9 ± 2.5	105.	100.

Table C.3: continued.

ID	SpT	$T_{\rm eff}$ [kK]	$\log g$ [dex]	-$\log Q$ [dex]	Y(He) [10^{-2}dex]	$vsini$ [km s^{-1}]	$vmac$ [km s^{-1}]
25	O9.5IV	31.7 ± 0.7	3.78 ± 0.08	> 13.4	9.8 ± 2.5	190.	135.
28	O8III	35.0 ± 0.5	3.80 ± 0.05	13.5 ± 0.4	< 6.9	200.	10.
30	O7.5Ib(f)	35.8 ± 0.9	3.60 ± 0.11	12.7 ± 0.1	< 6.9	135.	35.
31	O8Vz(n)	37.1 ± 0.9	4.03 ± 0.16	> 13.2	10.5 ± 2.5	120.	10.
32	O8III(f))	35.1 ± 1.2	3.63 ± 0.14	13.1 ± 0.3	< 7.3	100.	115.
33	O7.5:IV(n)	35.8 ± 0.6	3.68 ± 0.05	13.5 ± 0.5	10.1 ± 2.5	210.	130.
34	O8V(n)	35.0 ± 0.5	3.84 ± 0.08	13.5 ± 0.3	< 6.6	190.	120.
35	O8V:	35.5 ± 0.7	3.86 ± 0.08	13.5 ± 0.5	< 7.3	190.	10.
36	O8V	35.8 ± 0.6	3.80 ± 0.05	13.1 ± 0.2	9.7 ± 2.5	195.	130.
37	O9.7IV:(n)	30.3 ± 0.9	3.77 ± 0.14	13.3 ± 0.3	10.5 ± 2.5	225.	50.
38	O6.5III((f))	38.2 ± 0.6	3.85 ± 0.11	12.7 ± 0.1	< 7.1	80.	20.
39	O8V(n)	34.9 ± 1.2	3.55 ± 0.16	13.8 ± 0.9	< 12.3	130.	100.
40	O3If*	44.4 ± 0.9	3.83 ± 0.07	12.5 ± 0.1	9.9 ± 2.5	100.	80.
41	O6IV((f))	37.3 ± 0.6	3.63 ± 0.06	13.0 ± 0.2	< 6.6	145.	85.
43	O9.5IV:n	31.9 ± 0.6	3.91 ± 0.15	13.5 ± 0.3	< 6.6	275.	20.
46	O6.5V((f))	37.0 ± 1.3	3.77 ± 0.15	13.2 ± 0.5	13.5 ± 4.1	195.	0.
47	O7Vz((f))	35.8 ± 0.5	3.87 ± 0.07	13.3 ± 0.4	< 6.9	170.	20.
48	O3If*	44.0 ± 2.0	3.72 ± 0.11	12.1 ± 0.1	16.0 ± 4.0	80.	130.
49	O6II(f)	36.8 ± 0.5	3.59 ± 0.05	12.6 ± 0.1	< 6.6	110.	45.
51	O9.5V	32.3 ± 1.1	3.84 ± 0.14	> 13.4	13.3 ± 3.4	190.	90.
52	O8.5V(n)	34.4 ± 0.6	3.83 ± 0.08	> 13.5	10.0 ± 2.5	170.	180.
53	O8V(n)	35.6 ± 0.6	3.81 ± 0.11	13.0 ± 0.2	< 6.4	230.	25.
54	O5I(fc)	38.2 ± 0.5	3.69 ± 0.08	12.5 ± 0.1	< 7.1	150.	150.

Table C.3: continued.

ID	SpT	$T_{\rm eff}$ [kK]	$\log g$ [dex]	-$\log Q$ [dex]	Y(He) [10^{-2}dex]	$vsini$ [km s^{-1}]	$vmac$ [km s^{-1}]
55	O8V	37.3 ± 0.5	4.10 ± 0.07	13.5 ± 0.4	9.9 ± 2.5	130.	15.
56	O9.5V(n)	33.0 ± 0.5	3.80 ± 0.05	> 13.7	14.3 ± 2.5	195.	120.
57	O6IVf	38.0 ± 0.5	3.70 ± 0.05	12.7 ± 0.1	< 6.6	85.	90.
58	O8.5V	36.0 ± 0.5	3.80 ± 0.05	13.0 ± 0.2	< 7.1	85.	20.
59	O8.5V	36.0 ± 0.5	3.80 ± 0.05	13.5 ± 0.5	9.9 ± 2.5	96.	0.
60	O8V((f))	35.9 ± 1.1	3.72 ± 0.13	12.9 ± 0.2	< 6.6	120.	85.
61	O9.5IV:n	31.0 ± 0.5	3.50 ± 0.05	> 13.0	< 11.1	225.	115.
62	O7V((f))	37.0 ± 1.0	3.82 ± 0.13	> 13.0	11.3 ± 2.5	70.	55.
63	O9.7Iab	28.4 ± 0.6	3.03 ± 0.06	12.7 ± 0.1	9.4 ± 2.6	55.	80.
64	O9.5Vn	33.6 ± 1.7	3.76 ± 0.25	13.4 ± 0.4	< 18.4	265.	240.
66	O9V	34.6 ± 0.7	4.05 ± 0.10	13.8 ± 0.8	9.9 ± 2.5	55.	15.
68	O5.5Ifc	36.3 ± 0.5	3.50 ± 0.05	12.3 ± 0.1	10.1 ± 2.5	95.	80.
69	O9.5IV	33.9 ± 0.6	3.96 ± 0.10	> 13.0	9.2 ± 2.5	165.	55.
70	O7.5V((f))(n)z	37.0 ± 0.5	3.80 ± 0.05	13.5 ± 0.3	9.7 ± 2.5	170.	15.
71	O9.5V(n)	31.2 ± 1.2	3.86 ± 0.20	> 13.0	15.7 ± 6.0	155.	170.
74	O6.5III(f)	36.6 ± 0.6	3.58 ± 0.05	12.9 ± 0.2	12.0 ± 2.6	150.	10.
75	O9.7Iab	27.7 ± 0.6	2.98 ± 0.07	13.0 ± 0.2	9.8 ± 2.5	90.	65.
76	O7.5IV:(f)	36.3 ± 1.2	3.92 ± 0.14	12.8 ± 0.3	10.3 ± 2.5	95.	35.
77	O5V((f))	39.8 ± 1.7	3.63 ± 0.12	12.6 ± 0.2	10.5 ± 2.7	225.	45.

Table C.4: O-type sample with reliable astrometry (RUWE ≤ 1.4, see Sect. 6.5.1 and Chapter 5). Visual extinctions and absolute visual magnitudes have been calculated using the extinction law derived by Rieke & Lebofsky (1985), distances derived by Bailer-Jones et al. (2018) and photometry from Table C.1. Membership groups are from results obtained in Chapter 5. Radii, luminosities and masses derived using the `iacob-gbat` tool (see Sect. 2.2.2 for methodology details). We include the `iacob-gbat` formal uncertainties and errors related to M_V.

ID	Gaia source	Distance [pc]	A_V [mag]	M_V [mag]	Group	R [$R_\odot$]	log $L/L_\odot$ [dex]	M_{sp} [$M_\odot$]
1	2067642233192106624	2634^{+208}_{-181}	4.01	$-4.55^{-0.17}_{+0.15}$	3	$10.10^{+0.70}_{-0.79}$	$4.92^{+0.06}_{-0.07}$	$37.0^{+6.5}_{-7.0}$
2	2067398416488472704	1652^{+77}_{-71}	2.43	$-3.95^{-0.10}_{+0.10}$	2	$6.80^{+0.33}_{-0.33}$	$4.84^{+0.04}_{-0.04}$	$13.4^{+2.4}_{-2.4}$
3	2068074620437883520	1489^{+118}_{-103}	5.87	$-5.06^{-0.17}_{+0.15}$	2	$13.20^{+0.96}_{-1.07}$	$5.06^{+0.07}_{-0.07}$	$8.1^{+2.3}_{-2.4}$
4	2067625637438421248	1757^{+126}_{-111}	6.84	$-6.68^{-0.15}_{+0.14}$	2	$28.70^{+2.01}_{-2.13}$	$5.68^{+0.07}_{-0.07}$	$41.2^{+9.6}_{-9.8}$
5	2067430718942052224	1324^{+76}_{-69}	3.59	$-5.61^{-0.12}_{+0.11}$	1	$14.80^{+0.81}_{-0.87}$	$5.48^{+0.05}_{-0.06}$	$24.7^{+5.6}_{-5.7}$
6	2067807885789820160	1777^{+130}_{-114}	6.76	$-4.95^{-0.15}_{+0.15}$	2	$10.90^{+0.78}_{-0.78}$	$5.21^{+0.06}_{-0.07}$	$40.0^{+15.9}_{-15.9}$
7	2068007034832335104	1755^{+118}_{-104}	6.60	$-4.30^{-0.14}_{+0.13}$	2	$8.60^{+0.55}_{-0.59}$	$4.89^{+0.06}_{-0.06}$	$36.8^{+11.3}_{-11.5}$
9	2067816681882846464	1623^{+65}_{-60}	4.64	$-3.95^{-0.08}_{+0.08}$	2	$7.50^{+0.29}_{-0.29}$	$4.68^{+0.04}_{-0.04}$	$8.1^{+2.3}_{-2.3}$
10	2068008164405551104	1763^{+220}_{-177}	6.87	$-4.46^{-0.26}_{+0.23}$	2	$9.60^{+1.09}_{-1.21}$	$4.88^{+0.10}_{-0.11}$	$11.1^{+4.0}_{-4.2}$
15	2067788713055642880	1561^{+65}_{-60}	4.42	$-4.50^{-0.08}_{+0.09}$	2	$8.60^{+0.37}_{-0.33}$	$5.08^{+0.05}_{-0.04}$	$16.3^{+2.4}_{-2.3}$
16	2068155125305302144	1297^{+100}_{-87}	5.88	$-5.02^{-0.16}_{+0.15}$	1	$12.80^{+0.89}_{-0.95}$	$5.06^{+0.07}_{-0.07}$	$12.9^{+2.7}_{-2.7}$
18	2067840149584105344	1595^{+101}_{-89}	6.15	$-4.80^{-0.13}_{+0.13}$	2	$10.90^{+0.66}_{-0.66}$	$5.04^{+0.06}_{-0.06}$	$10.9^{+1.9}_{-1.9}$
19	2067796787591714048	1694^{+216}_{-174}	7.96	$-6.07^{-0.27}_{+0.23}$	2	$18.30^{+1.98}_{-2.31}$	$5.69^{+0.09}_{-0.11}$	$43.6^{+14.1}_{-15.2}$
22	2067847502568383744	16023^{+88}_{-79}	4.13	$-3.68^{-0.12}_{+0.11}$	2	$6.40^{+0.34}_{-0.37}$	$4.64^{+0.05}_{-0.05}$	$12.9^{+1.9}_{-2.1}$
23	2067827466541470080	1760^{+78}_{-71}	6.16	$-4.45^{-0.09}_{+0.09}$	2	$8.10^{+0.39}_{-0.39}$	$5.13^{+0.04}_{-0.04}$	$31.6^{+12.0}_{-12.0}$
24	2067835682818357376	1431^{+80}_{-72}	4.31	$-5.01^{-0.11}_{+0.12}$	0	$11.30^{+0.63}_{-0.58}$	$5.24^{+0.05}_{-0.05}$	$12.2^{+2.0}_{-1.9}$
25	2067835614098871040	1645^{+83}_{-75}	4.23	$-4.20^{-0.11}_{+0.10}$	2	$8.30^{+0.39}_{-0.43}$	$4.81^{+0.04}_{-0.05}$	$16.3^{+2.5}_{-2.6}$
28	2067834926904094848	1519^{+73}_{-67}	4.43	$-4.23^{-0.11}_{+0.10}$	2	$7.90^{+0.38}_{-0.41}$	$4.92^{+0.04}_{-0.05}$	$14.5^{+2.1}_{-2.2}$
30	2067829596846026880	1309^{+110}_{-95}	7.53	$-5.60^{-0.18}_{+0.16}$	1	$14.70^{+1.12}_{-1.25}$	$5.50^{+0.06}_{-0.07}$	$32.3^{+7.7}_{-8.1}$
31	2067769609040987648	1723^{+99}_{-89}	6.14	$-4.14^{-0.13}_{+0.11}$	2	$7.20^{+0.38}_{-0.44}$	$4.94^{+0.05}_{-0.06}$	$21.7^{+5.9}_{-6.1}$

Table C.4: continued.

ID	Gaia source	Distance [pc]	A_V [mag]	M_V [mag]	Group	R [$R_\odot$]	log $L/L_\odot$ [dex]	M_{sp} [$M_\odot$]
33	2067833204620693632	1514^{+85}_{-77}	4.33	$-4.53^{-0.12}_{+0.11}$	2	$8.80^{+0.46}_{-0.49}$	$5.07^{+0.05}_{-0.05}$	$14.2^{+2.5}_{-2.5}$
34	2067833243277076864	1487^{+83}_{-75}	4.40	$-4.77^{-0.12}_{+0.11}$	0	$10.00^{+0.51}_{-0.56}$	$5.13^{+0.05}_{-0.05}$	$26.0^{+4.8}_{-4.9}$
35	2067832968398974208	1391^{+78}_{-70}	4.61	$-4.09^{-0.12}_{+0.11}$	1	$7.20^{+0.38}_{-0.41}$	$4.90^{+0.05}_{-0.05}$	$14.9^{+2.4}_{-2.5}$
36	2067832624801783040	1625^{+104}_{-93}	4.61	$-4.10^{-0.13}_{+0.13}$	2	$7.30^{+0.45}_{-0.45}$	$4.90^{+0.06}_{-0.05}$	$12.5^{+2.1}_{-2.1}$
37	2067782936320586240	1742^{+128}_{-112}	6.48	$-4.62^{-0.15}_{+0.15}$	2	$10.60^{+0.76}_{-0.76}$	$4.93^{+0.07}_{-0.07}$	$25.9^{+5.7}_{-5.7}$
39	2067784516868550016	1573^{+110}_{-97}	6.35	$-4.66^{-0.15}_{+0.14}$	2	$9.70^{+0.65}_{-0.69}$	$5.09^{+0.06}_{-0.07}$	$13.2^{+2.6}_{-2.7}$
40	2067781905528395264	1534^{+180}_{-147}	7.25	$-6.05^{-0.24}_{+0.22}$	2	$15.90^{+1.62}_{-1.77}$	$5.93^{+0.09}_{-0.09}$	$63.5^{+16.2}_{-17.2}$
41	2067781905528395264	1534^{+180}_{-147}	7.24	$-5.42^{-0.24}_{+0.22}$	2	$13.10^{+1.33}_{-1.45}$	$5.47^{+0.09}_{-0.09}$	$26.6^{+6.2}_{-6.6}$
43	2067781905528395776	1475^{+84}_{-75}	6.84	$-4.68^{-0.11}_{+0.12}$	2	$10.40^{+0.58}_{-0.53}$	$5.01^{+0.05}_{-0.05}$	$33.6^{+12.5}_{-12.4}$
46	2067781939888133248	1670^{+136}_{-117}	6.69	$-4.71^{-0.17}_{+0.16}$	2	$9.40^{+0.67}_{-0.74}$	$5.17^{+0.07}_{-0.07}$	$21.4^{+5.9}_{-6.0}$
47	2067781871173898624	1627^{+87}_{-79}	5.68	$-4.27^{-0.12}_{+0.11}$	2	$7.90^{+0.41}_{-0.45}$	$4.97^{+0.05}_{-0.05}$	$16.9^{+3.1}_{-3.2}$
48	2067785070923663104	1530^{+73}_{-67}	5.26	$-5.78^{-0.10}_{+0.10}$	2	$13.90^{+0.81}_{-0.81}$	$5.83^{+0.06}_{-0.06}$	$46.5^{+9.1}_{-9.1}$
49	2067784619950644480	1531^{+104}_{-91}	5.20	$-5.80^{-0.14}_{+0.14}$	2	$15.80^{+1.04}_{-1.04}$	$5.61^{+0.06}_{-0.06}$	$33.5^{+5.2}_{-5.2}$
51	2067785070923661440	1607^{+66}_{-72}	4.34	$-3.62^{-0.10}_{+0.09}$	2	$6.30^{+0.28}_{+0.31}$	$4.59^{+0.05}_{-0.05}$	$10.1^{+2.6}_{-2.7}$
52	2067785002204178688	1517^{+78}_{-71}	4.48	$-4.01^{-0.11}_{+0.11}$	2	$7.20^{+0.38}_{-0.38}$	$4.79^{+0.05}_{-0.05}$	$13.6^{+1.7}_{-1.7}$
53	2067783799613328128	1751^{+137}_{-119}	5.38	$-5.01^{-0.16}_{+0.15}$	2	$11.10^{+0.77}_{-0.82}$	$5.26^{+0.06}_{-0.07}$	$29.9^{+6.8}_{-6.9}$
54	2067784246289931776	1713^{+97}_{-87}	4.62	$-5.98^{-0.11}_{+0.12}$	2	$16.90^{+0.95}_{-0.88}$	$5.72^{+0.05}_{-0.05}$	$51.2^{+10.6}_{-10.3}$
55	2067785208362826112	1571^{+115}_{-100}	4.68	$-4.23^{-0.15}_{+0.14}$	2	$7.50^{+0.49}_{-0.53}$	$4.98^{+0.06}_{-0.06}$	$25.9^{+5.2}_{-5.3}$
56	2067784173274044928	1611^{+76}_{-70}	4.97	$-3.75^{-0.10}_{+0.10}$	2	$6.50^{+0.31}_{-0.31}$	$4.66^{+0.04}_{-0.04}$	$11.1^{+1.8}_{-1.8}$
58	2067928110513529216	2025^{+195}_{-165}	5.53	$-5.47^{-0.20}_{+0.19}$	2	$13.80^{+1.21}_{-1.27}$	$5.46^{+0.08}_{-0.08}$	$44.4^{+8.8}_{-9.2}$
59	2067780054401820544	1731^{+96}_{-86}	5.90	$-4.53^{-0.11}_{+0.11}$	2	$8.80^{+0.46}_{-0.46}$	$5.07^{+0.04}_{-0.04}$	$18.0^{+2.6}_{-2.5}$
60	2067929794140714752	1108^{+72}_{-63}	6.02	$-4.17^{-0.14}_{+0.13}$	1	$7.50^{+0.46}_{-0.49}$	$4.93^{+0.06}_{-0.06}$	$11.7^{+2.4}_{-2.5}$
61	2067781016474500864	1542^{+80}_{-73}	5.50	$-4.46^{-0.11}_{+0.11}$	2	$9.50^{+0.49}_{-0.49}$	$4.87^{+0.05}_{-0.05}$	$10.9^{+3.0}_{-3.0}$
62	2067881548771533312	1734^{+95}_{-86}	5.09	$-4.01^{-0.12}_{+0.11}$	2	$6.80^{+0.36}_{-0.39}$	$4.89^{+0.05}_{-0.06}$	$12.1^{+2.3}_{-2.4}$

Table C.4: continued.

ID	Gaia source	Distance [pc]	A_V [mag]	M_V [mag]	Group	R [$R_\odot$]	log $L/L_\odot$ [dex]	M_{sp} [$M_\odot$]
66	2067766379225921152	1556^{+70}_{-65}	5.58	$-3.59^{-0.09}_{+0.09}$	2	$5.90^{+0.26}_{-0.26}$	$4.66^{+0.04}_{-0.04}$	$14.2^{+2.2}_{-2.2}$
68	2067888218857234304	1639^{+75}_{-69}	5.23	$-6.53^{-0.10}_{+0.10}$	2	$22.60^{+1.06}_{-1.06}$	$5.90^{+0.04}_{-0.04}$	$57.4^{+7.3}_{-7.3}$
69	2067887802243913216	1549^{+69}_{-63}	5.50	$-3.75^{-0.09}_{+0.09}$	2	$6.40^{+0.28}_{-0.28}$	$4.70^{+0.04}_{-0.04}$	$14.2^{+2.8}_{-2.8}$
70	2067887840900094848	1597^{+90}_{-81}	5.56	$-4.58^{-0.12}_{+0.12}$	2	$8.90^{+0.50}_{-0.50}$	$5.12^{+0.05}_{-0.05}$	$18.4^{+2.7}_{-2.7}$
71	2067763080691028736	1660^{+91}_{-82}	6.30	$-4.12^{-0.11}_{+0.11}$	2	$8.20^{+0.43}_{-0.43}$	$4.75^{+0.05}_{-0.05}$	$15.5^{+5.2}_{-5.2}$
74	2064757698797394688	1674^{+109}_{-97}	6.92	$-5.31^{-0.13}_{+0.13}$	2	$12.60^{+0.76}_{-0.76}$	$5.38^{+0.05}_{-0.05}$	$22.4^{+3.8}_{-3.8}$
75	2064739041458261120	1499^{+87}_{-78}	6.64	$-5.90^{-0.12}_{+0.12}$	2	$20.30^{+1.16}_{-1.16}$	$5.35^{+0.05}_{-0.05}$	$15.6^{+2.3}_{-2.3}$
76	2067913164027256960	1835^{+169}_{-143}	7.51	$-5.60^{-0.18}_{+0.18}$	2	$14.50^{+1.22}_{-1.28}$	$5.50^{+0.08}_{-0.08}$	$61.4^{+18.1}_{-18.4}$
77	2064838375463800448	1704^{+128}_{-112}	6.09	$-5.03^{-0.16}_{+0.14}$	2	$10.60^{+0.71}_{-0.80}$	$5.37^{+0.06}_{-0.07}$	$19.0^{+4.6}_{-4.8}$

D

Best-fitting models

In this appendix are included all the FASTWIND best-fitting models to the observed spectra for the Cygnus OB2 O-type population analized in Chapter 6. The observed spectra (in black) is overplotted to the best-fitting models (in red) resulting from the `iacob-gbat` analysis. He I, He II and H lines are indicated with solid, dashed and dotted short vertical lines, respectively.